Table 4Comparison of the results obtained in the present study with those of Nishizawa et al. [9].

	Present work	Published work [9]	% Difference
SAR _{max} in skin	0.212	0.220	3.63
SAR _{max} in fat	0.198	0.206	3.88
SAR _{max} in muscle	0.116	0.120	3.33

model presented by Nishizawa et al. [9]. The horizontal cross section of the three layer human tissues as shown in Fig. 6 is used in the validation case. In the validation case, the leakage microwave power density of 1 mW/cm² at the electromagnetic frequency of 1300 MHz is considered. The results of the selected test case are illustrated in Fig. 7 for SAR distribution in the human body. Table 4 clearly shows a good agreement of the maximum value of the SAR of tissue between the present solution and that of Nishizawa [9]. This favorable comparison lends confidence in the accuracy of the present numerical model. It is important to note that there may be some errors occurring in the simulations which are generated by the input dielectric properties data base and the numerical scheme.

4.2. The effects of shield dielectric properties and operating frequency

Fig. 8 shows the meshes of the human model as well as the SAR and temperature distribution in the case of unshielded human model exposed to the microwave power density of $5~\text{mW/cm}^2$ at the frequency of 300~MHz. It is found that the temperature distributions are not proportional to the local SAR values. Nevertheless, these are also related to the parameters such as thermal conductivity, dielectric properties, blood perfusion rate and etc.

In the case of using dielectric shield, the dielectric properties for the shield are chosen as (low-loss; 10-j5), (medium-loss; 10-j10), and (high-loss; 20-j20). The shield gap distance and shield thickness are set to 0.5 cm and 0.3 cm, respectively. Fig. 9 and Fig. 10 show the maximum SAR and maximum temperature increase, respectively, in the human model with the test frequencies of 300 MHz, 915 MHz, 1300 MHz and 2450 MHz.

In this section, we illustrate the maximum value of SAR and temperature increase in the human model without attention to the organism. In the unshielded case, the maximum SAR value appeared at 1300 MHz as shown in Fig. 9, while the maximum temperature increase appeared at 915 MHz as shown in Fig. 10. This is because the

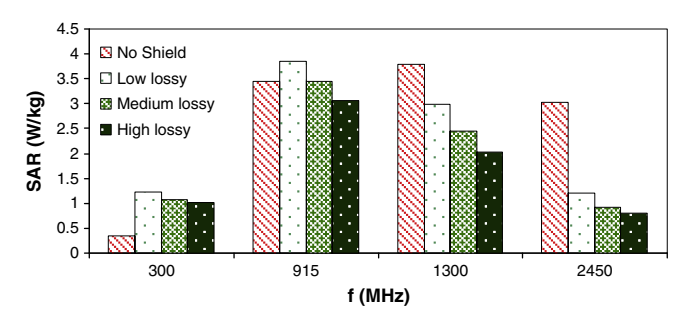


Fig. 9. Comparison of the maximum SAR in the human model at the frequencies of 300 MHz, 915 MHz, 1300 MHz and 2450 MHz.

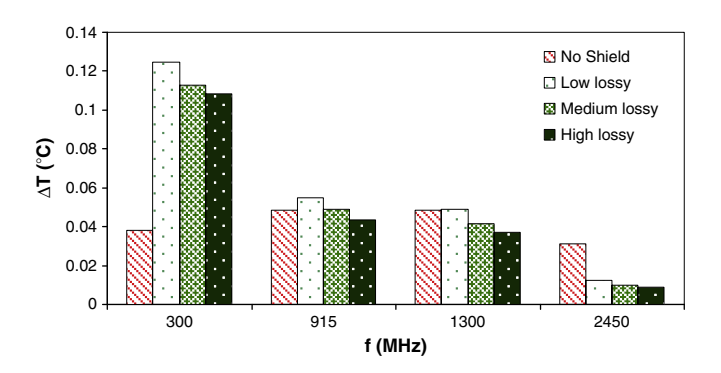


Fig. 10. Comparison of the maximum temperature increases in the human model at the frequencies of 300 MHz, 915 MHz, 1300 MHz and 2450 MHz.

differences of dielectric and thermal properties of tissues cause spatial distortions of the resonance excitation.

Since in this study, the thickness of the dielectric shield is less than the penetration depth, only a part of the supplied microwave energy is absorbed by the dielectric shield, and the other parts are allowed to penetrate further through the dielectric shield. This causes the interference of waves to penetrate further into the human model to be reflected from the human skin and travel back to the dielectric shield. Consequently, the reflection and transmission components at each interface contribute to the resonance of standing wave within the gap and the human model.

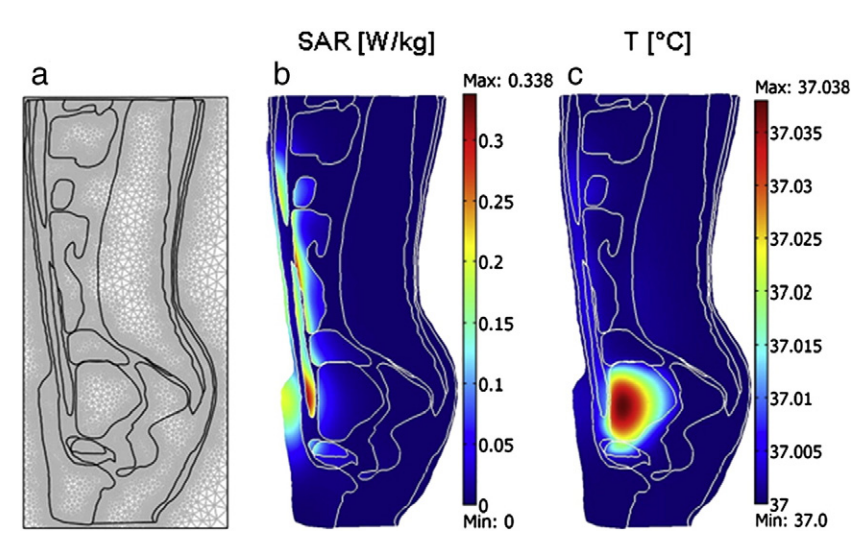


Fig. 8. Analysis of SAR and temperature distribution in the human model exposed to the microwave power density of 5 mW/cm² at the frequency of 300 MHz, (a) An initial finite element meshes of human cross section model (b) SAR distribution of the shieldless case (c) Temperature distribution of the unshield case.

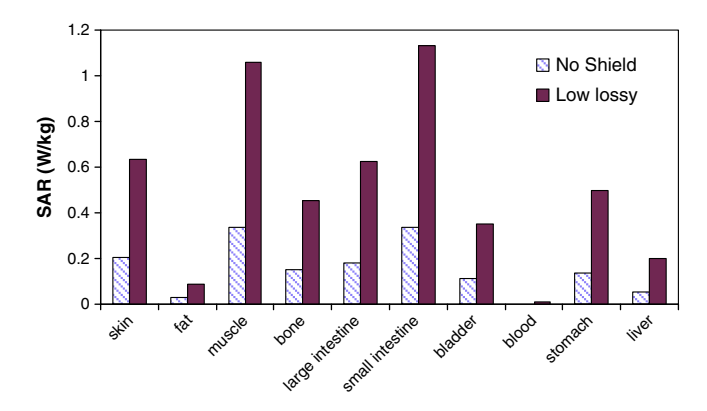


Fig. 11. Comparison of the maximum SAR in human organs of the unshielded and shielded human model at the frequency of 300 MHz.

It is evident from Fig. 9 and Fig. 10 that in the higher frequency of 1300 and 2450 MHz, when using dielectric shield, a significant reduction of SAR and temperature increase within the human model is achieved because of its smaller penetration depth. However, in the lower frequency of 300 MHz corresponding to a long wavelength, the SAR and the temperature increase have higher value than the values of the unshielded case. The reason behind this result is that the penetration depth of the dielectric shield at 300 MHz is much greater than the dielectric shield thickness. This increases a larger part of the incident wave to penetrate further through the dielectric shield and also penetrate into the human model. The great value of SAR and temperature increase in human model is caused by stronger resonance effects that occur at the low frequencies.

While in the frequency of 915 MHz, an insignificant shielding effect of medium lossy dielectric shield is illustrated. It is found that by using low lossy dielectric shield at the frequency of 915 MHz, SAR as well as temperature increase is higher compared to values of the unshielded case. This is because the resonance phenomena between the low lossy dielectric shield and human model is displayed stronger. The multiple reflections within the gap and the human model caused the accumulation of microwave energy in the gap which leads to an increase in the SAR and temperature in human organism by which the reflection rate of microwave strongly depends on the dielectric properties of the dielectric shield. By using the high lossy dielectric shield, the shielding effect is significant. This is because of a large reduction of microwave power density within the human model due to the weakness of resonance, corresponding to the lowering penetration depth of microwave. It is confirmed that the appropriate dielectric properties of the dielectric shield greatly depend on the operating frequencies.

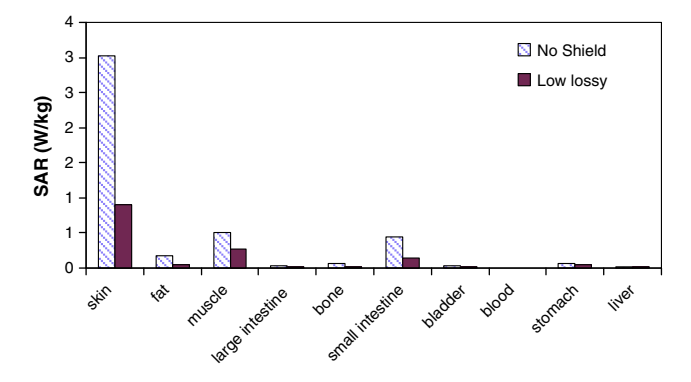


Fig. 12. Comparison of the maximum SAR in human organs of the unshielded and shielded human model at the frequency of 2450 MHz.

4.3. SAR in organs

As shown in Fig. 11, based on the results of the local maximum SAR of the unshielded case, at a low frequency of 300 MHz, peak values of SAR occurred, found both in the small intestine and the muscle. With the use of the low lossy shield, the greater values of SAR occurred as compared to the unshielded case. This is because of a larger part of the incident wave that penetrates further into the gap and human model. This caused the accumulation of microwave energy in the gap and the human model. Fig. 12 shows the maximum SAR in organs at a high frequency of 2450 MHz. It is clearly evident from Fig. 12 that a peak value of local SAR is found only at the skin due to a smaller penetration depth at high frequency range. However, large reduction of the SAR value is achieved when using the same dielectric shield (low-loss shield) with the case of 300 MHz due to the weakness of resonance.

Fig. 11 and Fig. 12 show the maximum SAR and the maximum temperature increase in the human model, while focusing on the human organism. It is found that the SAR and the temperature increase primarily depend on the penetration depth of microwave which corresponds to the operating frequency as well as the dielectric properties of the dielectric shield. As the dielectric properties of a dielectric shield vary, the penetration depth will be changed and the electric field passing through the dielectric shield is altered. If the penetration depth is changing, a fraction of the microwave energy absorbed is also changed which related to the resonance within the model. Consequently, the shielding effect of dielectric shield is changed.

5. Conclusions

This paper presents the simulations of SAR and heat transfer in the human model, where microwave energy strikes the dielectric shield in front of the human model. The SAR and temperature distributions in the human model are governed by the electric field as well as the dielectric properties of tissue.

The results show an interaction between physical parameters: operating frequencies and shield dielectric properties. For human exposure to microwave energy, the installed dielectric shield strongly affects the SAR and the temperature increase in the human body. Actually, the microwaves can transmit through the dielectric shield, and can penetrate into the human model that contribute to the resonance of standing wave within the gap and human model.

Since the frequency increases, the penetration depth for microwave gets smaller and resonance effect becomes weakness. Consequently, the shielding effect is significant. Therefore, the appropriate dielectric properties, which can effectively reduce the SAR and the temperature increase in human body of the dielectric shield, are greatly dependent on the operating frequency. Additionally, this paper presents an interesting viewpoint on the microwave shielding properties of dielectric shields at various operating frequencies, while focusing on the human organism.

Future work will extend the calculations of the SAR and the temperature increase for a three-dimensional model. Moreover, it will be carried out to study the effect of wave pattern, namely, TM wave and TE wave on a realistic model.

Acknowledgments

The authors gratefully acknowledge the financial support provided by The Thailand Research Fund (TRF), and the authors also acknowledge Thammasat University for providing the simulation facilities described in this paper.

References

- P. Ratanadecho, N. Suwannapum, W. Cha-um, Interactions between electromagnetic and thermal fields in microwave heating of hardened type I-cement paste using a rectangular waveguide (influence of frequency and sample size), ASME Journal of Heat Transfer 131 (2009) 082101–082112.
- [2] N. Makul, P. Ratanadecho, Microwave pre-curing of natural rubber-compounding using a rectangular wave guide, International Communications in Heat and Mass Transfer 37 (7) (2010) 914–923.
- [3] P. Ratanadecho, C. Serttikul, Simulation of melting of ice under a constant temperature heat source using a combined transfinite interpolation and partial differential equation methods, Journal of Porous Media 10 (7) (2007) 657–675.
- [4] M.A. Stuchly, Health effects of exposure to electromagnetic fields, IEEE Aerospace Applications Conference Proceedings, Aspen, USA, 1995, pp. 351–368.
 [5] K.L. Ryan, J.A. D'Andrea, J.R. Jauchem, P.A. Mason, Radio frequency radiation of
- [5] K.L. Ryan, J.A. D'Andrea, J.R. Jauchem, P.A. Mason, Radio frequency radiation of millimeter wave length: Potential occupational safety issues relating to surface heating, Health Physics 78 (2000) 170–181.
- [6] R.J. SPIEGEL, A review of numerical models for predicting the energy deposition and resultant thermal response of humans exposed to electromagnetic fields, IEEE Transactions on Microwave Theory and Techniques 32 (1984) 730–746.
 [7] T. Wessapan, S. Srisawatdhisukul, P. Rattanadecho, Numerical analysis of specific
- [7] T. Wessapan, S. Srisawatdhisukul, P. Rattanadecho, Numerical analysis of specific absorption rate and heat transfer in the human body exposed to leakage electromagnetic field at 915 MHz and 2,450 MHz, ASME Journal of Heat Transfer, xx (2011) xxx-xxx. (Accepted).
- [8] A.W. Guy, C.-K. Chou, J.A. McDougall, C. Sorensen, Measurement of shielding effectiveness of microwave-protective suits, IEEE Transactions on Microwave Theory and Techniques 35 (1987) 984–994.

- [9] S. Nishizawa, O. Hashimoto, Effectiveness analysis of lossy dielectric shields for a three-layered human model, IEEE Transactions on Microwave Theory and Techniques 47 (1999) 277–283.
- [10] O. Hashimoto, S. Nishizawa, Effectiveness analysis of thin resistive sheet for a three-layered elliptical human model, Microwave and Optical Technology Letters 23 (1999) 73–75.
- [11] T. Samaras, A. Christ, A. Klingenbck, N. Kuster, Worst case temperature rise in a one-dimensional tissue model exposed to radiofrequency radiation, IEEE Transactions on Biomedical Engineering 54 (2007) 492–496.
- [12] K. Shiba, N. Higaki, Analysis of SAR and current density in human tissue surrounding an energy transmitting coil for a wireless capsule endoscope, Proceedings of the 20th International Zurich Symposium on Electromagnetic Compatibility 1 (2009) 321–324, Zurich.
- [13] A. Hirata, O. Fujiwara, T. Shiozawa, Correlation between peak spatial-average SAR and temperature increase due to antennas attached to human trunk, IEEE Transactions on Biomedical Engineering 53 (2006) 1658–1664.
- [14] A. Hirata, M. Fujimoto, T. Asano, J. Wang, O. Fujiwara, T. Shiozawa, Correlation between maximum temperature increase and peak SAR with different average schemes and masses, IEEE Transactions on Electromagnetic Compatibility 48 (2006) 569–577.
- [15] D. Yang, M.C. Converse, D.M. Mahvi, J.C. Webster, Expanding the bioheat equation to include tissue internal water evaporation during heating, IEEE Transactions on Biomedical Engineering 54 (2007) 1382–1388.
- [16] T. Basak, K. Aparna, A. Meenakshi, A.R. Balakrishnan, Effect of ceramic supports on microwave processing of porous food samples, International Journal of Heat and Mass Transfer 49 (2006) 4325–4339.

Teerapot Wessapan Siramate Srisawatdhisukul Phadungsak Rattanadecho

e-mail: ratphadu@engr.tu.ac.th

Department of Mechanical Engineering, Research Center of Microwave Utilization in Engineering (RCME), Faculty of Engineering, Thammasat University (Rangsit Campus), Pathumthani 12120, Thailand

Numerical Analysis of Specific Absorption Rate and Heat Transfer in the Human Body Exposed to Leakage Electromagnetic Field at 915 MHz and 2450 MHz

In recent years, society has increased utilization of electromagnetic radiation in various applications. This radiation interacts with the human body and may lead to detrimental effects on human health. However, the resulting thermophysiologic response of the human body is not well understood. In order to gain insight into the phenomena occurring within the human body with temperature distribution induced by electromagnetic field, a detailed knowledge of absorbed power distribution is necessary. In this study, the effects of operating frequency and leakage power density on distributions of specific absorption rate and temperature profile within the human body are systematically investigated. This study focuses attention on organs in the human trunk. The specific absorption rate and the temperature distribution in various tissues, obtained by numerical solution of electromagnetic wave propagation coupled with unsteady bioheat transfer problem, are presented. [DOI: 10.1115/1.4003115]

Keywords: microwave, temperature distribution, specific absorption rate, human body

1 Introduction

Electromagnetic (EM) energy is a one heat source that is attractive over conventional heating methods because an electromagnetic wave that penetrates the surface is converted into thermal energy within the material volumetrically. High speed startup, selective energy absorption, instantaneous electric control, nonpollution, high energy efficiency, and high product quality are several advantages of microwave heating. Therefore, this technology is used in many industrial and household applications such as heating process [1] and drying process [2]. Rapid development of electromagnetic energy applications causes an increase in public concern about health risks from electromagnetic energy emitted from various sources [3].

Increasing use of high power electromagnetic energy results in the necessity to identify the limits of safe exposure with respect to thermal hazards. The amount of energy absorbed by tissue depends on many factors including frequency, dielectric property of the tissue, irradiating time exposure, intensity of electromagnetic radiation, and water content of the tissue. For this reason, public organizations throughout the world have established safety guidelines for electromagnetic wave absorption values [3]. For human exposure to electromagnetic fields, these guidelines are based on peak spatial-average specific absorption rate (SAR) for human body tissues.

The power absorption in human tissues induces temperature increase inside tissues. The severity of the physiological effect produced by small temperature increases can be expected to worsen in sensitive organs. An increase in approximate $1-5\,^{\circ}\mathrm{C}$ in

human body temperature can cause numerous malformations, temporary infertility in males, brain lesions, and blood chemistry changes. Even a small temperature increase in human body (approximately 1 °C) can lead to altered production of hormones and suppressed immune response [4].

In the past, the experimental data on the correlation of SAR levels to the temperature increases in human body are sparse. There is a research on SAR distribution of three-layer human body, which simulates three-layer physical models of skin, fat, and muscle tissues [5]. There are limited data available on thermal properties and dielectric properties of human tissues, as very few epidemiological studies have been conducted. There are some experimental studies in animals such as rat [6], cow [7], and pig [8]. However, the results may not represent the practical behavior of human tissues. Most previous studies of human body exposed to electromagnetic field did not consider heat transfer, resulting in an incomplete analysis. Therefore, modeling of heat transport in human tissues is needed in order to completely explain. The modeling of heat transfer in human tissues has been investigated. Earlier studies of heat transfer in human tissues utilized the general bioheat equation [9]; thereafter, the coupled model of general bioheat equation and Maxwell's equation were used to model human tissues exposed to electromagnetic field [10]. Other researches have been done for temperature distribution over the surface, and the various biotissues exposed to an electric field have been studied [11,12]. Furthermore, few reports have suggested thermal interactions for microwave frequency fields [13]. Researchers also carried out temperature increases in human head exposed to a handheld cellular phone [14–17].

However, most studies of temperature increases induced by electromagnetic waves have not been considered in a realistic domain of the human body with complicated organs of several types of tissues. There are few studies on the temperature and electromagnetic field interaction in realistic physical model of the human

Contributed by the Heat Transfer Division of ASME for publication in the Jour-NAL OF HEAT TRANSFER. Manuscript received January 6, 2010; final manuscript received November 17, 2010; published online January 31, 2011. Assoc. Editor: Darrell W. Pepper.

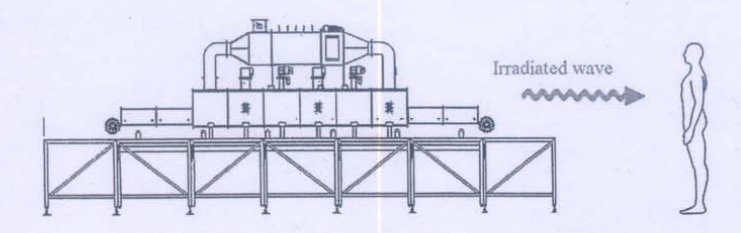


Fig. 1 Wave leakage from an electromagnetic radiation device

body due to the complexity of the problem, even though it is directly related to the thermal injury of tissues. Therefore, in order to provide information on levels of exposure and health effects from electromagnetic radiation adequately, it is essential to simulate the coupled electromagnetic field and heat transfer within an anatomically based human body model to represent the actual process of heat transfer within the human body.

This research is a pioneer work that simulates the SAR distribution and temperature distribution over an anatomically based human body. In this research, a two-dimensional human cross section model [18] was used to simulate the SAR distribution and temperature distribution over the human body at different frequencies. Electromagnetic wave propagation in tissues was investigated by using Maxwell's equations. An analysis of heat transfer in human tissues exposed to microwaves was investigated by using the bioheat equation. The effects of operating frequency (915 MHz and 2450 MHz) and leakage power density (5 mW/cm², 10 mW/cm², 50 mW/cm², and 100 mW/cm²) on distributions of specific absorption rate and temperature profile within the human body are systematically investigated. The 915 MHz and 2450 MHz frequencies were chosen for simulations in this study as they have wavelengths in the microwave band and are used most frequently in the application of industrial high power microwave heating. The obtained values provide an indication of limitations that must be considered for temperature increases due to localized electromagnetic energy absorption.

2 Formulation of the Problem

Electromagnetic fields emitted by high power radiation devices are harmful. Figure 1 shows the leakage of electromagnetic energy from the industrial microwave drying system to a human body. It is known that a human body exposed to intense electromagnetic waves can cause significant thermal damage in sensitive tissues within the human trunk. Therefore, it is necessary to investigate the temperature distributions due to exposure to electromagnetic waves in order to investigate the hot spot zones within the human body especially in abdominal and thoracic cavities.

Due to ethical consideration, exposing a live human body to electromagnetic fields for experimental purposes is difficult. It is more convenient to develop a realistic model through numerical simulation. The next section, an analysis of specific absorption rate and heat transfer in the human body exposed to electromagnetic field is illustrated. The system of governing equations as well as initial and boundary conditions are solved numerically using the finite element method (FEM).

3 Methods and Model

The first step in evaluating the effects of a certain exposure to radiation in the human body is the determination of the induced internal electromagnetic field and its spatial distribution. Thereafter, electromagnetic energy absorption, which results in temperature increases within particular parts of the human body and other interactions, can be considered.

3.1 Human Model. From Fig. 2, a two-dimensional human body model used in this study is obtained by the image processing technique from the work of Shiba and Higaki [18]. The model has

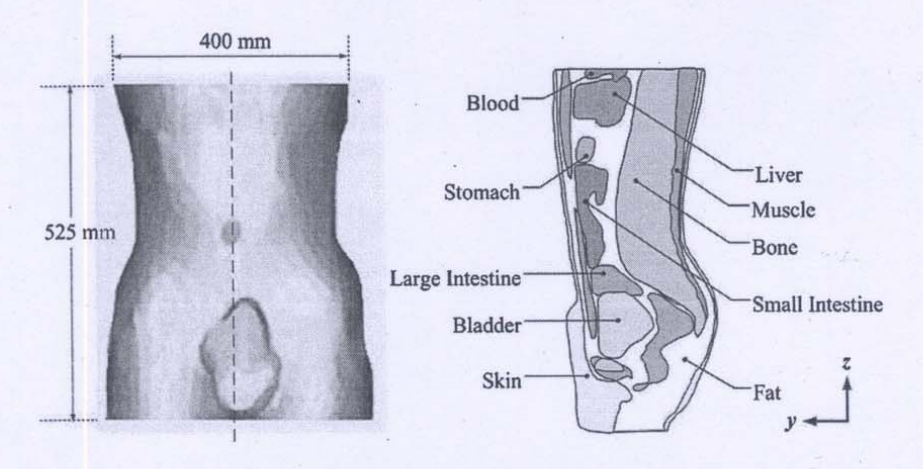


Fig. 2 Human body vertical cross section [16]

Table 1 Dielectric properties of tissues

		915 MHz		2450 MHz	
Tissue	ρ (kg/m ³)	σ (S/m)	ε_{r}	σ (S/m)	ϵ_{r}
Skin	1125	0.92	44.86	2.16	41.79
Fat	916	0.09	5.97	0.13	5.51
Muscle	1047	1.33	50.44	1.60	46.40
Bone	1038	2.10	44.80	2.10	44.80
Large intestine	1043	2.04	53.90	2.04	53.90
Small intestine	1043	3.17	54.40	3.17	54.40
Bladder	1030	0.69	18.00	0.69	18.00
Blood	1058	2.54	58.30	2.54	58.30
Stomach	1050	2.21	62.20	2.21	62.20
Liver	1030	1.69	43.00	1.69	43.00

Table 2 Thermal properties of tissues

Tissue	k (W/m K)	C _p (J/kg K)	ω_b	Q_{met} (W/m^3)
Skin	0.35	3437	0.02	1620
Fat	0.22	2300	4.58×10^{-04}	300
Muscle	0.6	3500	8.69×10^{-03}	480
Bone	0.436	1300	4.36×10^{-04}	610
Large intestine	0.6	3500	1.39×10^{-02}	9500
Small intestine	0.6	3500	1.74×10^{-02}	9500
Bladder	0.561	3900	0.00×10^{00}	
Blood	0.45	3960		
Stomach	0.527	3500	7.00×10^{-03}	
Liver	0.497	3600	0.017201	

a dimension of 400 mm in width and 525 mm in height. This model comprises ten types of tissues, which are skin, bone, muscle, fat, nerve, blood, and so forth. These tissues have different dielectric and thermal properties. The thermal properties and dielectric properties of tissues at the frequencies of 915 MHz and 2450 MHz are given in Tables 1 and 2, respectively. As very few studies associated with human tissue properties have been conducted, some of the tissue properties are not quantified. It is also difficult to directly measure tissue properties of a live human. Therefore, we used an assumption of comparing them to animal tissues (it should be noted that the properties based on animal experiments are used for most thermal parameters because no actual data are available for the parameters of the human model). Figure 2 shows a vertical cross section through the middle plane of the human trunk model.

3.2 Equations for Electromagnetic Wave Propagation Analysis. Mathematical models were developed to predict the electric field, SAR, and temperature distribution within the human body. To simplify the problem, the following assumptions were made.

- Electromagnetic wave propagation is modeled in two dimensions over the y-z plane.
- 2. The human body in which electromagnetic waves and human body interact proceeds in the open region.
- 3. The computational space is truncated by scattering boundary condition
- 4. In the human body, an electromagnetic wave is characterized by transverse electric fields (TE mode).

The model assumes that dielectric properties of tissues are constant.

The electromagnetic wave propagation in the human body is calculated by Maxwell's equations [10], which mathematically describe the interdependence of the electromagnetic waves. The general form of Maxwell's equations is simplified to demonstrate the electromagnetic field of microwaves penetrated in the human body as the following equations:

$$\nabla \times \left(\frac{1}{\mu_r} \nabla \times E\right) - k_0^2 \left(\varepsilon_r - \frac{j\sigma}{\omega \varepsilon_0}\right) E = 0 \tag{1}$$

$$\varepsilon_r = n^2$$
 (2)

where E is the electric field intensity (V/m), μ_r is the relative magnetic permeability, n is the refractive index, ε_r is the relative dielectric constant, $\varepsilon_0 = 8.8542 \times 10^{-12}$ F/m is the permittivity of free space, and σ is the electric conductivity (S/m), $j = \sqrt{-1}$.

3.2.1 Boundary Condition for Wave Propagation Analysis. Microwave energy is emitted by a microwave high power device and strikes the human body with a particular power density. Therefore, boundary condition for electromagnetic wave, as shown in Fig. 3, is considered as follows.

It is assumed that the uniform wave flux strikes the left side of the human body. Therefore, at the left boundary of the considered domain, an electromagnetic simulator employs TE wave propagation port with a specified power density,

$$S = \int (E - E_1) \cdot E_1 / \int E_1 \cdot E_1 \tag{3}$$

Boundary conditions along the interfaces between different media, for example, between air and tissue or tissue and tissue, are considered as a continuity boundary condition,

$$n \times (H_1 - H_2) = 0 \tag{4}$$

The outer sides of the tissue boundaries are considered as a scattering boundary condition,

$$n \times (\nabla \times E_z) - jkE_z = -jk(1 - k \cdot n)E_{0z} \exp(-jk \cdot r)$$
 (5)

3.3 Interaction of Electromagnetic Waves and Human Tissues. Interaction of electromagnetic fields with biological tissues can be defined in terms of SAR. Human tissues are generally lossy mediums for EM waves with finite electric conductivity. They are usually neither good dielectric materials nor good con-

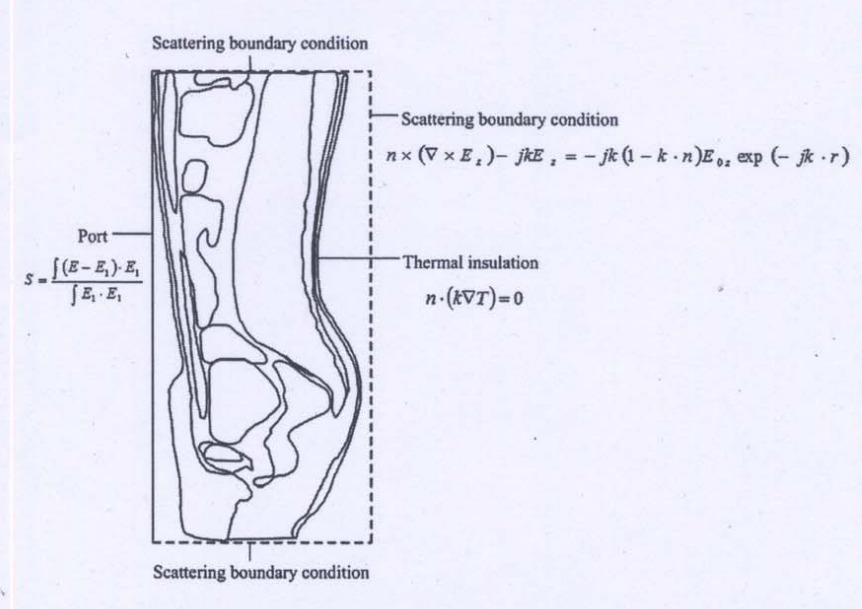


Fig. 3 Boundary condition for analysis

ductors. When EM waves propagate through the human tissues, the energy of EM waves is absorbed by the tissues. The specific absorption rate is defined as a power dissipation rate normalized by material density [8]. The specific absorption rate is given by

$$SAR = \frac{\sigma}{\rho} |E|^2 \tag{6}$$

where E is the root mean square electric field (V/m), σ is the conductivity (S/m), and ρ is the mass density of the tissue (kg/m³).

3.4 Equations for Heat Transfer Analysis. The electric field within the model attenuates due to energy absorption. The absorbed energy is converted to thermal energy, which increases the tissue temperature. To solve the thermal problem, the temperature distribution in the human body has been evaluated by the coupled bioheat and Maxwell equations. The temperature distribution corresponded to the specific absorption rate. This is because the specific absorption rate within the human body distributes, owing to energy absorption. Thereafter, the absorbed energy is converted to thermal energy, which increases the tissue temperature.

Heat transfer analysis of the human body is modeled in two dimensions over the y-z plane. To simplify the problem, the following assumptions were made.

- 1. Human tissues are biomaterial with constant thermal properties.
- 2. No phase change in substance occurs within the tissues.
- 3. There is no energy exchange throughout the human body model.
- 4. There is no chemical reactions occur within the tissues.
- 5. Local thermodynamic equilibrium is considered.

Corresponding electromagnetic field and temperature profiles can also be assumed to be two dimensional in the y-z plane. There is a continuity boundary condition between the organs within the human body. The temperature distribution inside the human model is obtained by using Pennes' bioheat equation [19]. The transient bioheat equation effectively describes how transfer occurs within the human body, and the equation can be written as

$$\rho C \frac{\partial T}{\partial t} = \nabla \cdot (k \nabla T) + \rho_b C_b \omega_b (T_b - T) + Q_{\text{met}} + Q_{\text{ext}}$$
 (7)

where ρ is the tissue density (kg/m³), C is the heat capacity of tissue (J/kg K), k is the thermal conductivity of tissues (W/m K), T is the temperature (°C), T_b is the temperature of blood (°C), ρ_b is the density of blood before entering ablation region (kg/m³), C_b is the specific heat capacity of blood (J/kg K), ω_b is the blood perfusion rate (1/s), $Q_{\rm met}$ is the metabolism heat source (W/m³), and $Q_{\rm ext}$ is the external heat source (microwave heat-source density) (W/m³).

In the analysis, heat conduction between tissues and blood flow is approximated by the term $\rho_b C_b \omega_b (T_b - T)$. The metabolism heat source is negligible, and therefore $Q_{\text{met}} = 0$.

The external heat source is equal to the resistive heat generated by electromagnetic field (microwave power absorbed), which defined as

$$Q_{\rm ext} = \frac{1}{2}\sigma_{\rm tissue}|\bar{E}|^2 \tag{8}$$

where $\sigma_{\text{tissue}} = 2\pi f \varepsilon_r' \varepsilon_0$

3.4.1 Boundary Condition for Heat Transfer Analysis. The heat transfer analysis is considered only in the human body domain, which does not include parts of the surrounding space. As shown in Fig. 3, the boundaries of the human body are considered as an insulated boundary condition,

$$n \cdot (k \nabla T) = 0 \tag{9}$$

It is assumed that no contact resistance occurs between the internal organs of the human body. Therefore, the internal boundaries are assumed to be a continuity boundary condition,

$$n \cdot (k_u \nabla T_u - k_d \nabla T_d) = 0 \tag{10}$$

3.4.2 Initial Condition for Heat Transfer Analysis. For this analysis, the temperature distribution within the human body is assumed to be uniform. Therefore, the initial temperature of the human body is defined as

$$T(t_0) = 37 \,^{\circ} \,^{\circ} C \tag{11}$$

The thermoregulation mechanisms and the metabolic heat generation of each tissue have been neglected to illustrate the clear temperature distribution. At the skin-air interface, the insulated boundary condition has been imposed to clearly illustrate the temperature distribution.

3.5 Calculation Procedure. To date, there are three principal techniques within computation electromagnetic (CEM): finite difference time domain method (FDTD) [2], method of moments (MOM) [10], and FEM. FEM has been extensively used in the simulation of electromagnetic field. Moreover, FEM models can provide users with quick and accurate solutions to multiple systems of differential equations.

In this research, the finite element method is used to analyze the transient problems. The computational scheme is to assemble finite element model and compute a local heat generation term by performing an electromagnetic calculation using tissue properties. In order to obtain a good approximation, a fine mesh is specified in the sensitive areas. This study provides a variable mesh method for solving the problem, as shown in Fig. 4. The coupled model of electromagnetic field and thermal field is solved by the FEM model, which was implemented using COMSOL™ MULTIPHYSICS 3.4, to demonstrate the phenomenon that occurs within the human body exposed to electromagnetic field. The study employs an implicit time step scheme to solve the electric field and temperature field. In this research, a time step of 10^{-2} s and 10^{-12} s are used to solve Maxwell's equations and bioheat equation, respectively. These are found to be practical to achieve each time step convergence. The temperature distribution has been evaluated by taking into account the specific absorption rate due to the electromagnetic field exposure at a particular frequency. Until the steady state is reached, the temperature at each time step is collected.

The 2D model is discretized using triangular elements, and the Lagrange quadratic is used to approximate temperature and SAR variation across each element. The convergence test of the frequency of 2450 MHz are carried out to identify the suitable number of elements required. The number of elements where solution is independent of mesh density is found to be 92,469. Higher numbers of elements are not tested due to lack of computational memory and performance. The convergence curve resulting from the convergence test is shown in Fig. 5.

4 Results and Discussion

In this study, the coupled mathematical model of bioheat transfer and electromagnetic wave propagation as well as the initial temperature of 37°C for all cases are used for the analysis. For the simulation, the thermal and dielectric properties are directly taken from Tables 1 and 2, respectively. The exposed leakage power density used in this study refers to the ICNIRP standard for safety level at the maximum SAR value of 2 W/kg [3]. However, there are frequently exceeded values of leakage power density in the industrial working area due to the leakage of microwave from the microwave high power devices [3]. In the drying industry, only two microwave frequencies of 915 MHz and 2450 MHz are available. In this analysis, the effects of operating frequency (915 MHz and 2450 MHz) and leakage power density (5 mW/cm², 10 mW/cm², 50 mW/cm², and 100 mW/cm²) on distributions of specific absorption rate and temperature profile within the hu-

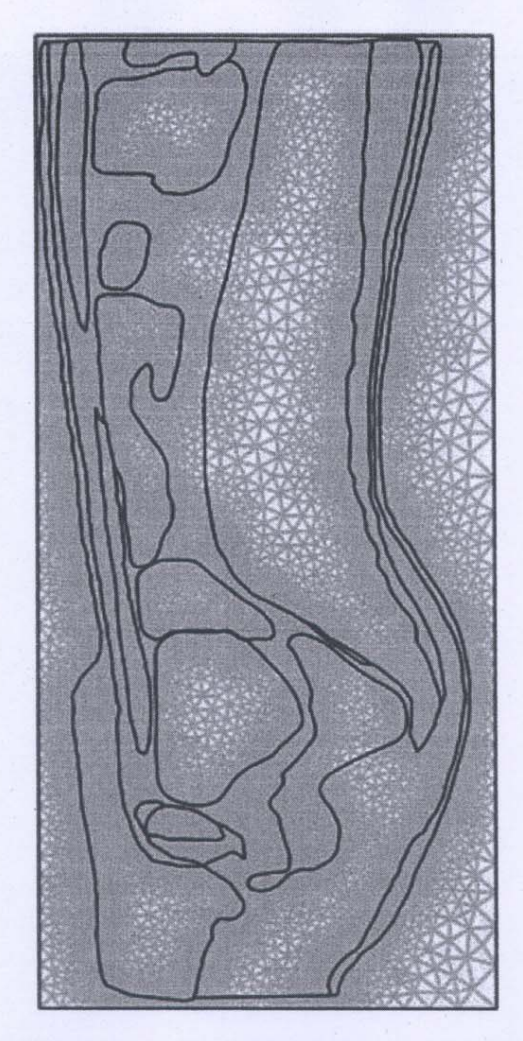


Fig. 4 An initial two-dimensional finite element mesh of human cross section model

man body are systematically investigated. The influences of frequencies and leakage power density on human body subject to electromagnetic wave are discussed in detail.

4.1 Verification of the Model. It must be noted in advance that it is not possible to make a direct comparison of the model in this study and the experimental results. In order to verify the accuracy of the present numerical model, the simple case of the simulated results is then validated against the numerical results

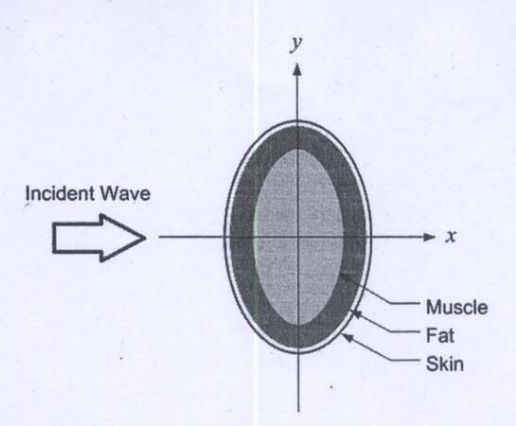


Fig. 6 Geometry of the validation model obtained from the paper [3]

with the same geometric model obtained by Nishizawa and Hashimoto [5]. The horizontal cross section of three-layer human tissues as shown in Fig. 6 is used in the validation case. In the validation case, the leakage power density exposed to the electromagnetic frequency of 1300 MHz is 1 mW/cm². The results of the selected test case are illustrated in Fig. 7 for SAR distribution in the human body. Table 3 clearly shows a good agreement in the maximum value of the SAR of tissues between the present solution and that of Nishizawa and Hashimoto. This favorable comparison lends confidence in the accuracy of the present numerical model. It is important to note that there may be some errors occurring in the simulations, which are generated by the input dielectric properties and the numerical scheme.

4.2 Distribution of Electric Field. To illustrate the distribution of penetrated electric field inside each organ of the human body, simulation analysis is required. Figure 8 shows the simulation of electric field pattern inside the human body exposed to electromagnetic field of TE mode propagation along the vertical cross section human body model at the frequencies of 915 MHz and 2450 MHz.

Figure 8(a) shows the distribution of electric field at the frequency of 915 MHz. It is found that a large part of electromagnetic wave at 915 MHz can penetrate further into the body. This electric field leads to deeper electromagnetic energy absorbed in the organs of human body in comparison to the frequency of 2450 MHz, which will be discussed later. With the lower frequency, a large part of electromagnetic wave is able to penetrate into the human body due to its long wavelength, which corresponds to a larger penetration depth.

Figure 8(b) shows the distribution of electric field at the fre-

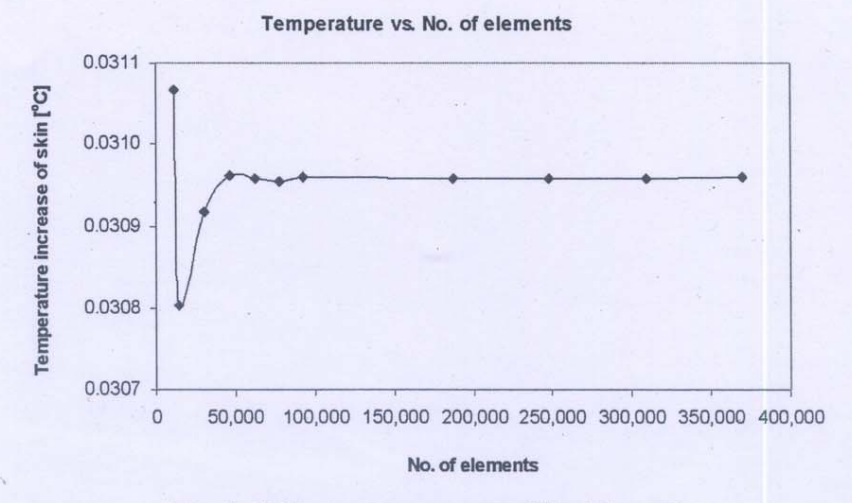


Fig. 5 Grid convergence curve of the 2D model

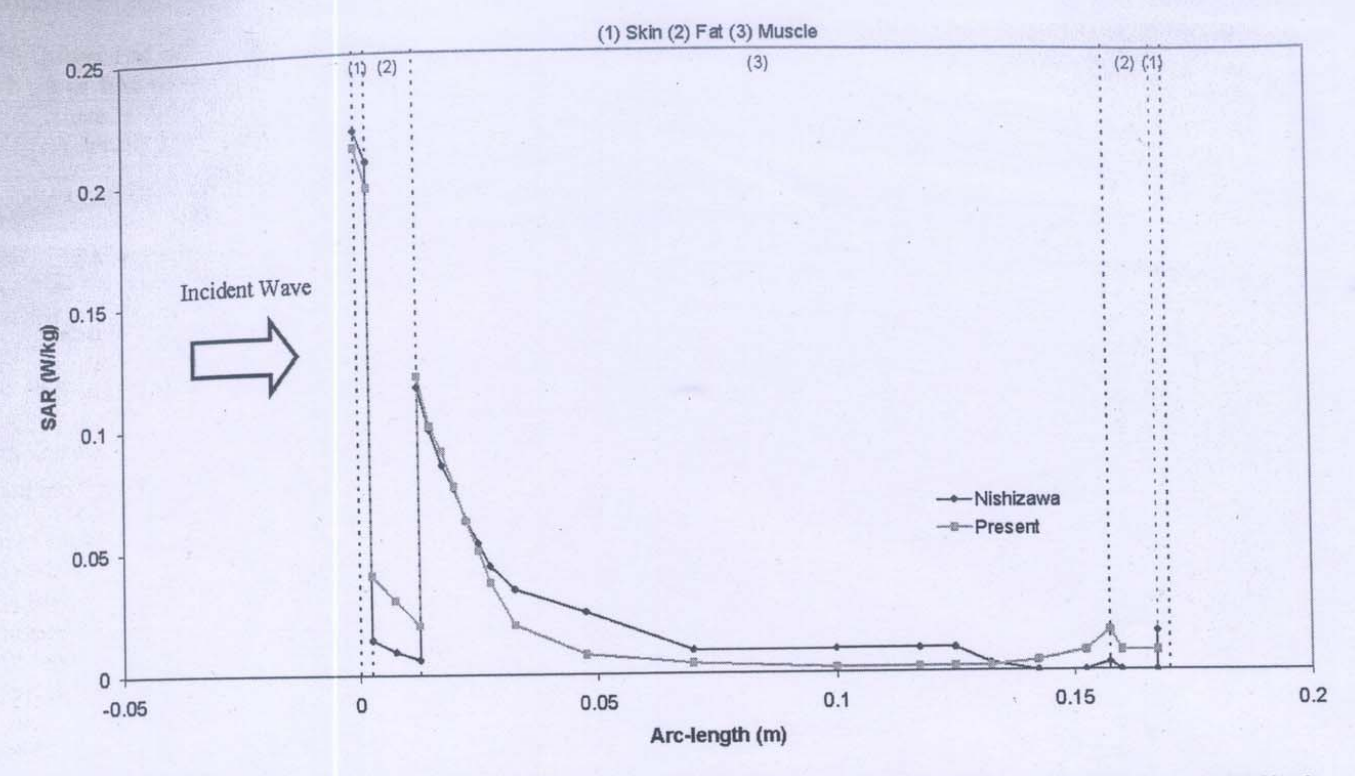


Fig. 7 Comparison of the calculated SAR distribution to the SAR distribution obtained by Nishizawa and Hashimoto [5]

quency of 2450 MHz. A high frequency wave has a short wavelength that corresponds to a small penetration depth of the electromagnetic wave. It is found that the electric field diminishes within very small distances, which results in a low specific absorption rate in organs deep inside the human trunk. This phenomenon explains why the electric field and therefore the specific absorption rate are greatest at the skin and decay sharply along the propagation direction for a short wavelength. It can be seen that the distribution of electric field for the higher frequency occurs in

Table 3 Comparison of the results obtained in the present study with those of Nishizawa and Hashimoto [5]

	Present work	Published work [5]	% Difference
SAR _{max} in skin	0.212	0.220	3.63
SAR _{max} in fat	0.198	0.206	3.88
SAR _{max} in muscle	0.116	0.120	3.33

the outer parts of the body, especially in skin, fat, and muscle. The maximum electric field intensities are 91.51 V/m at the frequency of 915 MHz and 56.12 V/m at the frequency of 2450 MHz. The electric field within the human body is extinguished where the electric field attenuates due to absorbed electromagnetic energy and is converted to heat.

4.3 SAR Distribution in Human Tissues. Figure 9 shows the SAR distribution evaluated on the vertical section of the human body in which the maximum SAR value occurs. It is evident from the results that the dielectric properties, as shown in Table 1, can become significant on SAR distribution in human tissues when microwave energy is exposed in these tissues. The magnitude of dielectric properties in each organ will directly affect the amount of SAR within the human body. The highest SAR values are obtained in the region of the skin for the frequency of 915 MHz at 3.43 W/kg and for the frequency of 2450 MHz at 3.02 W/kg. It is found that the SAR distribution in the human model is

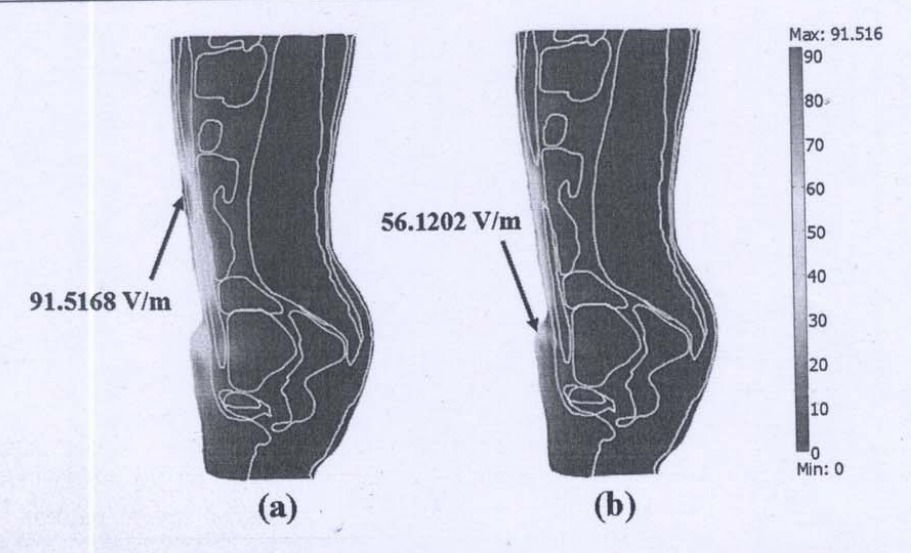


Fig. 8 Electric field distribution in human body (V/m) exposed to the leakage power density of 5 $\,$ mW/cm² at the frequencies of (a) 915 MHz and (b) 2450 MHz

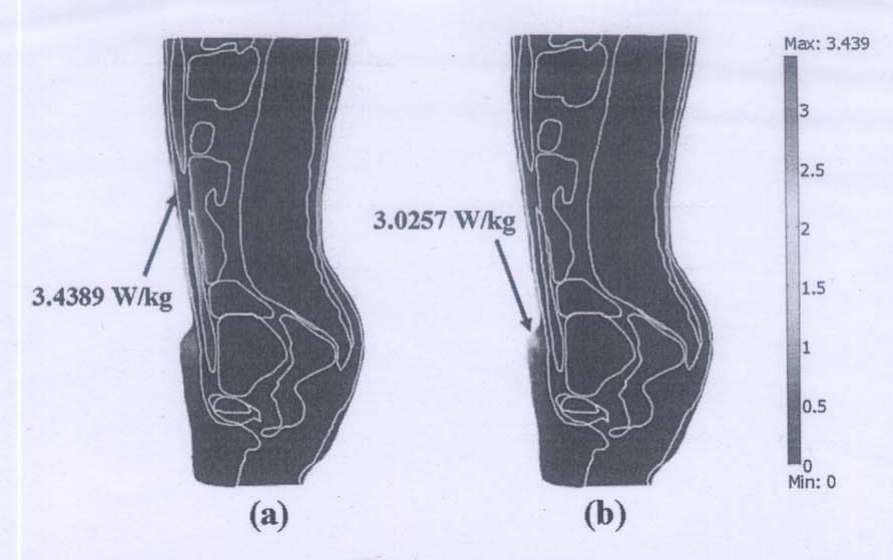


Fig. 9 SAR distribution in human body (W/kg) exposed to the leakage power density of 5 $\,$ mW/cm² at the frequencies of (a) 915 MHz and (b) 2450 $\,$ MHz

different due to the effect of the frequency and the dielectric properties of human tissues. From Fig. 9, it appears that for the frequency of 915 MHz, the highest SAR values also occur in the muscle and the small intestine due to the effect of high values of the dielectric properties. Comparing to the ICNIRP limit of SAR values (2 W/kg), the resulting SAR values are exceeded in all cases.

4.4 Temperature Distribution. Figure 10 shows the temperature increase of the organs in human body exposed to electromagnetic waves at various times. For the human body exposed to the leakage of electromagnetic wave from a high power microwave heating device at the frequency of 915 MHz or 2450 MHz for a period of time, the temperature within the human body (Fig. 10) is increased corresponding to the specific absorption rate (Fig. 9). This is because the electric field within the human body attenuates, owing to the energy absorbed, and thereafter the absorbed energy is converted to thermal energy, which increases the human body temperature. It is found that at the different frequencies, the distribution patterns of temperature at a particular time are quite different. The hot spot zone is strongly displayed at the 10 min for the frequency of 915 MHz, owing to the extensive penetration depth and different properties of tissues. To a lesser extent, at the frequency of 2450 MHz, the temperature increases in the human body are always found at the periphery of the body correlated with the electric field and SAR (Figs. 8 and 9). For the case of microwave frequency at 915 MHz, the highest temperature of 37.0487°C occurs in the fat, as shown in Fig. 10(c). A different pattern of temperature distribution is obtained at the 2450 MHz frequency, as shown in Fig. 10(c), in which the highest temperature of 37.0311°C is presented in the skin. The maximum temperature increases, with the leakage power density of 5 mW/cm², at the 915 MHz and 2450 MHz frequencies are 0.048°C and 0.031°C, respectively. These are much lower than the thermal damage temperature within the range of 1-5°C.

An electromagnetic wave exposure (for example, the leakage from microwave heating system) usually lasts only a few minutes; hence, the steady-state temperature rise is rarely reached, except for workers who work in the leakage area. Figures 11 and 12 show the temperature distributions inside the human body at the 915 MHz and 2450 MHz frequencies for different exposure times. At 915 MHz, fat tissue temperature increases slower than the other tissues due to its low lossy behavior. Fat tissue also has maximum steady-state temperature due to its low blood perfusion rate. It is found that at 915 MHz, the internal tissues (fat and bone) reach steady state slower than the external tissues (skin) due to the low thermal conductivity of the fat tissue. However, at 2450 MHz, all

of the temperature increases can reach steady state within a short period due to the high thermal conductivity of the skin tissue as well as the low heat capacity of the fat tissue.

4.5 Comparison of SAR Distribution and Temperature Distribution in Human Tissues. Consider the relation of SAR and temperature distribution at the extrusion line (Fig. 13), temperature increases of human tissues are induced by local dissipation of SAR. For a human exposed to the leakage power density of 5 mW/cm², Fig. 14 shows the maximum SAR of the 2450 MHz frequency (2.0 W/kg) in the skin region. The maximum SAR value of the 2450 MHz is approximately equal to the maximum SAR value of the 915 MHz frequency (2.0 W/kg) in the skin. However, Fig. 15 shows that the maximum temperature increase of the 2450 MHz frequency in the skin (0.02°C) is lower than the maximum temperature increase of the 915 MHz frequency in the fat (0.03°C). These different behaviors are due to the fact that for the same SAR value at different frequencies, the temperature increase is different. The maximum SAR of the 2450 MHz frequency induces the temperature increase in the skin that is lower than the temperature increase in the fat of the 915 MHz frequency. Consequently, since the interior of the fat region has a lower blood perfusion rate $(4.58 \times 10^{-4} \text{ 1/s})$ than the skin (0.02)1/s) and fat is bounded by low thermal conductivity tissue (skin), the heat transfer of fat from blood perfusion is less effective. At the same time, the high blood perfusion is present in the skin.

The localized maximum SAR for the frequencies of 915 MHz and 2450 MHz is shown in Fig. 16. For the value of localized SAR for each organ, it is found that SAR increases as the frequency decreases. For both frequencies, the three highest SARs are shown for skin, muscle, and small intestine. Furthermore, the localized SARs of the 915 MHz frequency are higher than the 2450 MHz frequency in all organs.

The maximum localized temperature increases in all tissues for the frequency of 915 MHz and 2450 MHz are shown in Fig. 17. The maximum temperature increase occurs in fat at the 915 MHz frequency, whereas the maximum temperature increase appears in the skin tissues at the 2450 MHz frequency. Since the penetration depth of the 915 MHz microwave frequency is larger than the 2450 MHz frequency and the inner organs have high dielectric properties, the larger temperature increases of the 915 MHz frequency are particularly high in the inner tissues (small intestine and bladder).

As a result, the human heterogeneous tissues greatly influence the temperature increases in the skin region exposed to the

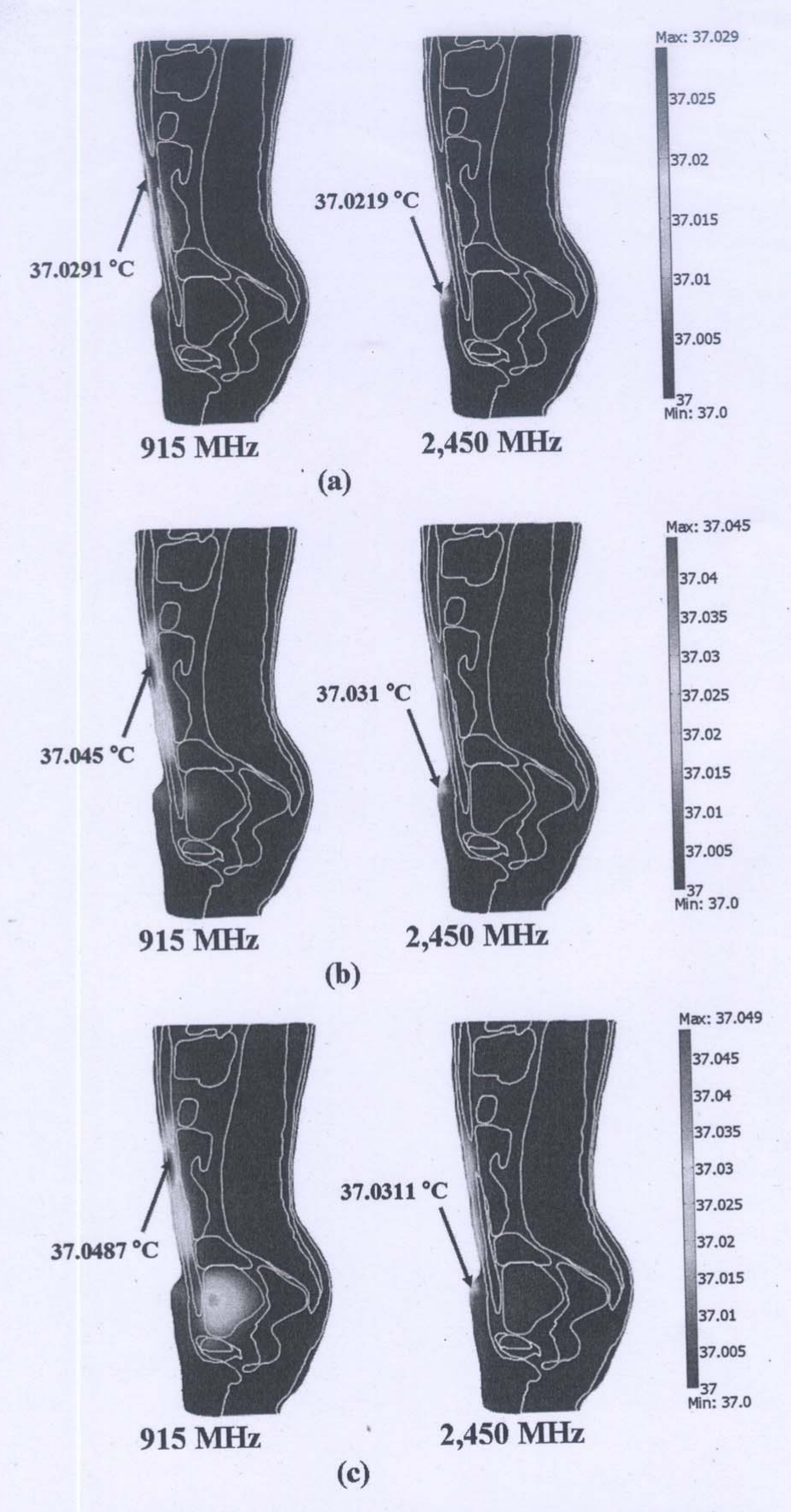


Fig. 10 The temperature distribution of human body exposed to electromagnetic wave at the frequencies of 915 MHz and 2450 MHz: (a) 1 min, (b) 10 min, and (c) steady state

frequency of 2450 MHz and in the fat region for the frequency of 915 MHz. It is found that the temperature distributions are not proportional to the local SAR values. Nevertheless, these are also related to the parameters such as thermal conductivity, dielectric

properties, and blood perfusion rate. It is therefore important to use a thermal model couple with electromagnetic wave propagation model to asses the health risk in terms of temperature increase from electromagnetic exposure.

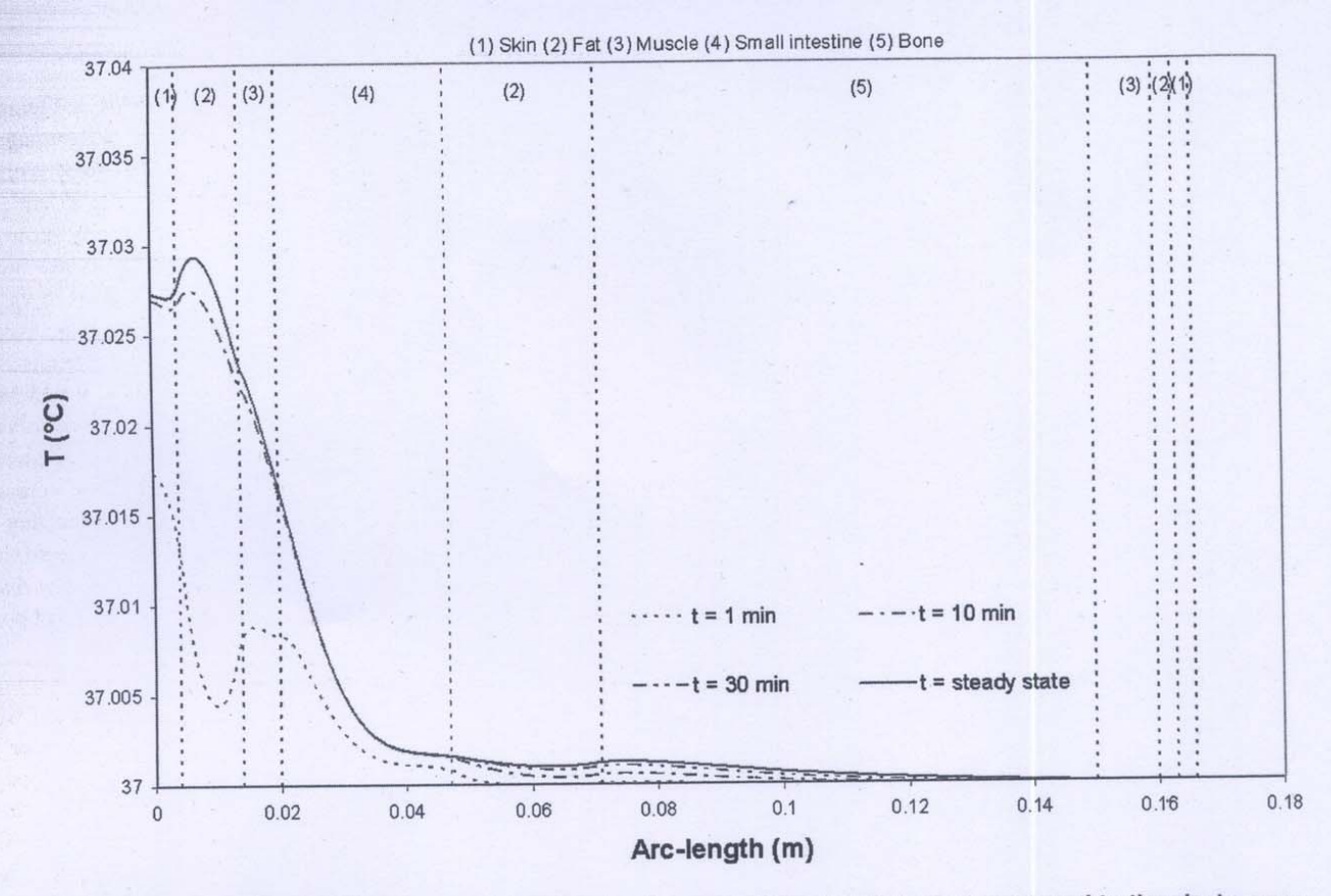


Fig. 11 Temperature distribution versus arc length of human body at various times exposed to the electromagnetic frequency of 915 MHz at the leakage power density of 5 mW/cm²

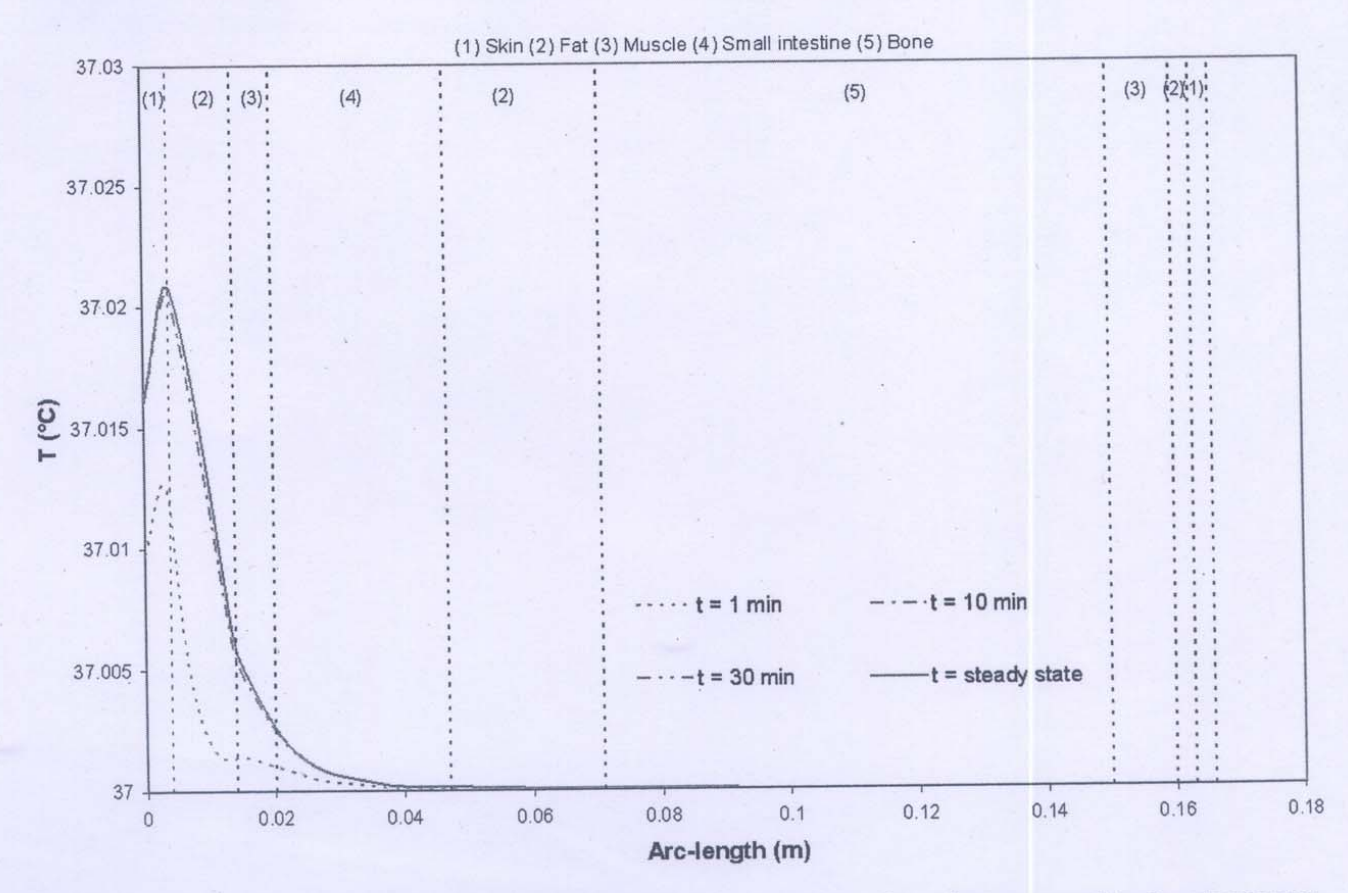


Fig. 12 Temperature distribution versus arc length of human body at various times exposed to the electromagnetic frequency of 2450 MHz at the leakage power density of 5 mW/cm²

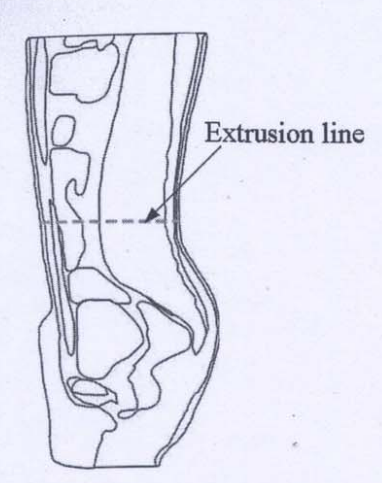


Fig. 13 The extrusion line in the human body where the SAR and temperature distribution are considered

4.6 Effect of Leakage Power Density. The effect of leakage power density (the power irradiated on the human surface) has also been investigated. The incident power and leakage power density are related, as shown in Table 4. Figure 18 shows the comparison of the temperature increase distribution within the human body at various incident powers, at t=1 min, with the frequency of 915 MHz, along the extrusion line (Fig. 13). Figure 19 shows the temperature fields of human body exposed to the electromagnetic frequency of 915 MHz at t=1 min corresponding to leakage power densities, as shown in Table 4. It is found that incident power significantly influences the rate of temperature increase. Greater power provides greater heat generation inside the human body, thereby increasing the rate of temperature rise.

5 Conclusions

This study presents the numerical simulation SAR and temperature distribution in the human body exposed to electromagnetic field at the frequencies of 915 MHz and 2450 MHz with the power densities of 5 mW/cm², 10 mW/cm², 50 mW/cm², and 100 mW/cm². The numerical simulations in this study show several important features of the energy absorption in the human body. The results show that the maximum temperatures in various organs are significantly different at different frequencies. The maximum temperature is found at the skin for the frequency of 2450 MHz and is found at the fat for the frequency of 915 MHz. While the maximum SAR value in both frequencies are found at the skin. It is found that greater leakage power density results in a greater heat generation inside the human body, thereby increasing the rate of temperature increase. Moreover, it is found that the temperature distributions in human body induced by electromagnetic fields are not directly related to the SAR distribution due to the effect of dielectric properties, thermal properties, blood perfusion, and penetration depth of the microwave power.

Therefore, health effect assessment of electromagnetic wave at various frequencies requires the utilization of the numerical simulation of SAR model along with the thermal model. However, the dielectric properties of some tissues are not indicated as a function of frequency due to the limited number of human tissue dielectric properties in the literature, and this may affect the accuracy of the simulation results. Future works will focus on the frequency-dependent dielectric properties of human tissue. A study will also be developed for 3D simulations and the study of the temperature dependency of dielectric properties. This will allow a better understanding of the realistic situation of the interaction between the electromagnetic field and the human tissues.

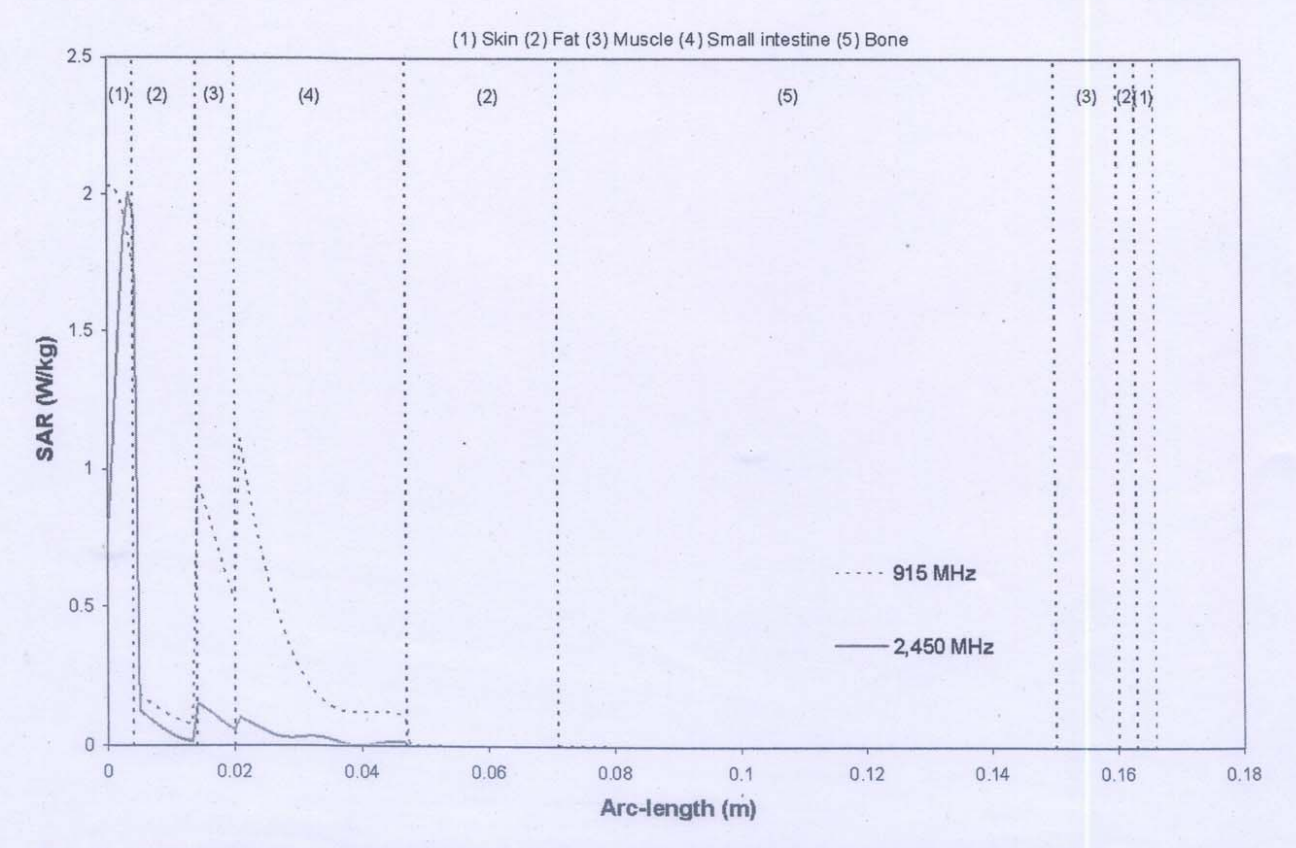


Fig. 14 SAR distribution versus arc length of human body exposed to the leakage power density of electromagnetic field at the 5 mW/cm²

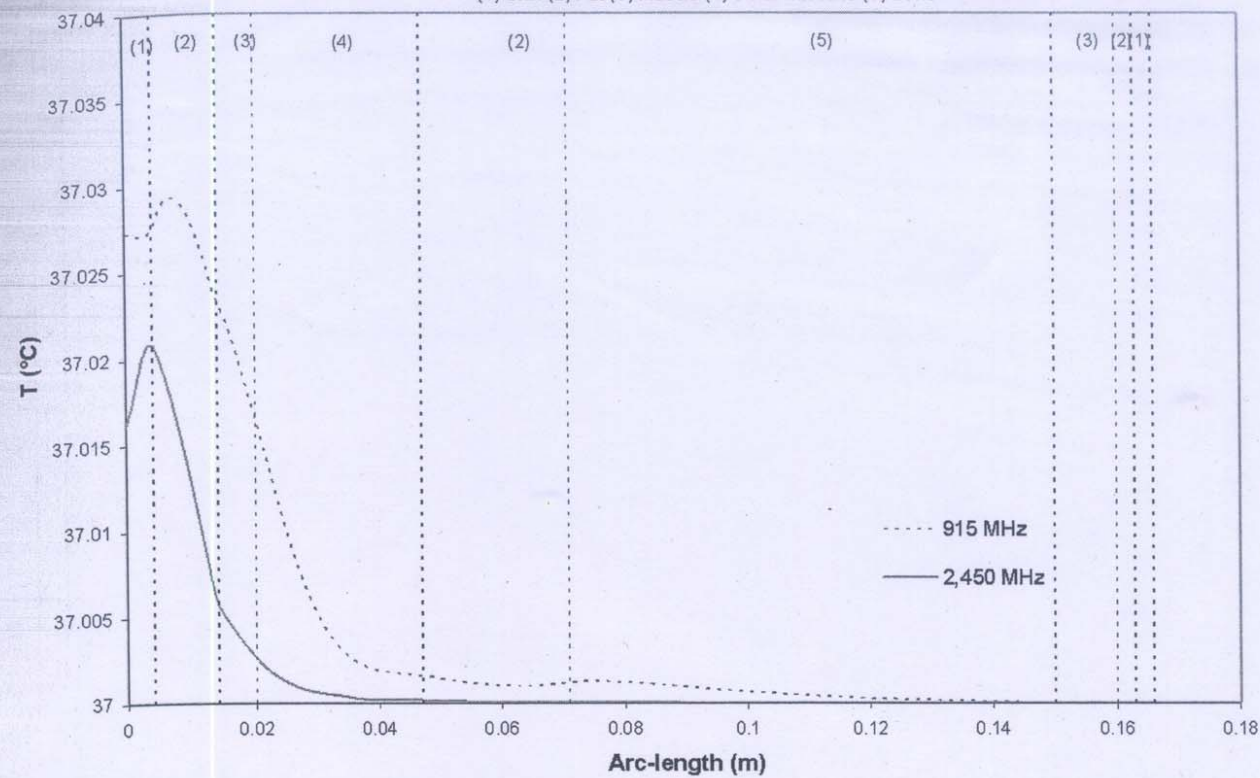


Fig. 15 Temperature distribution versus arc length of the human body exposed to the leakage power density of electromagnetic field at 5 mW/cm²

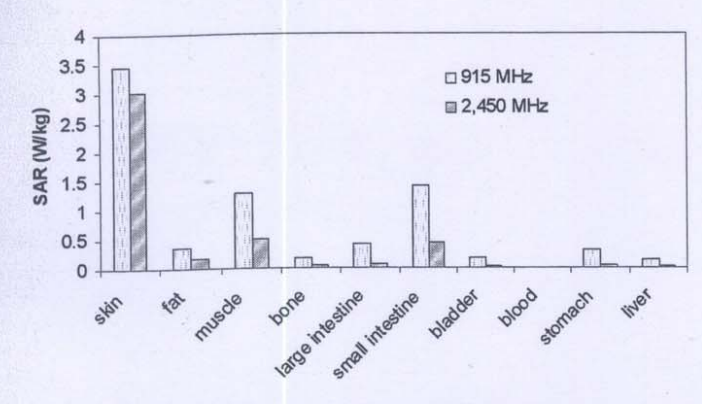


Fig. 16 Comparison of the maximum SAR in human tissues at the frequencies of 915 MHz and 2450 MHz

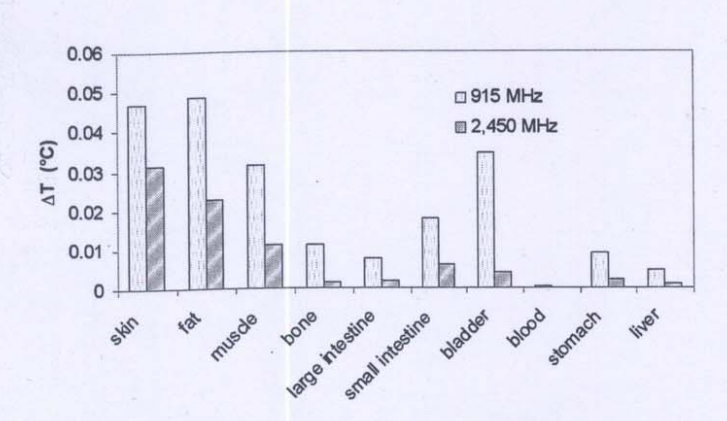


Fig. 17 Comparison of the temperature increases in human tissues at the frequencies of 915 MHz and 2450 MHz

Table 4 The relationship between the incident power and the leakage power density of microwave

Incident power (W)	Power density (mW/cm ²)
10.5	5
21.0	10
105	50
210	100

Acknowledgment

The authors would like to express their appreciation to the Thailand Research Fund (TRF) and the Thai Commission on Higher Education (CHE) for providing financial support for this study.

Nomenclature

C = specific heat capacity (J/(kg K))

E = electric field intensity (V/m)

f =frequency of incident wave (Hz)

j = current density

k = thermal conductivity (W/(m K))

n = refractive index

 $Q = \text{heat source } (W/m^3).$

T = temperature (K)

t = time

 $\tan \delta =$ loss tangent coefficient

Greek Letters

 μ = magnetic permeability (H/m)

 ε = permittivity (F/m)

 σ = electric conductivity (S/m)

 ω = angular frequency (rad/s)

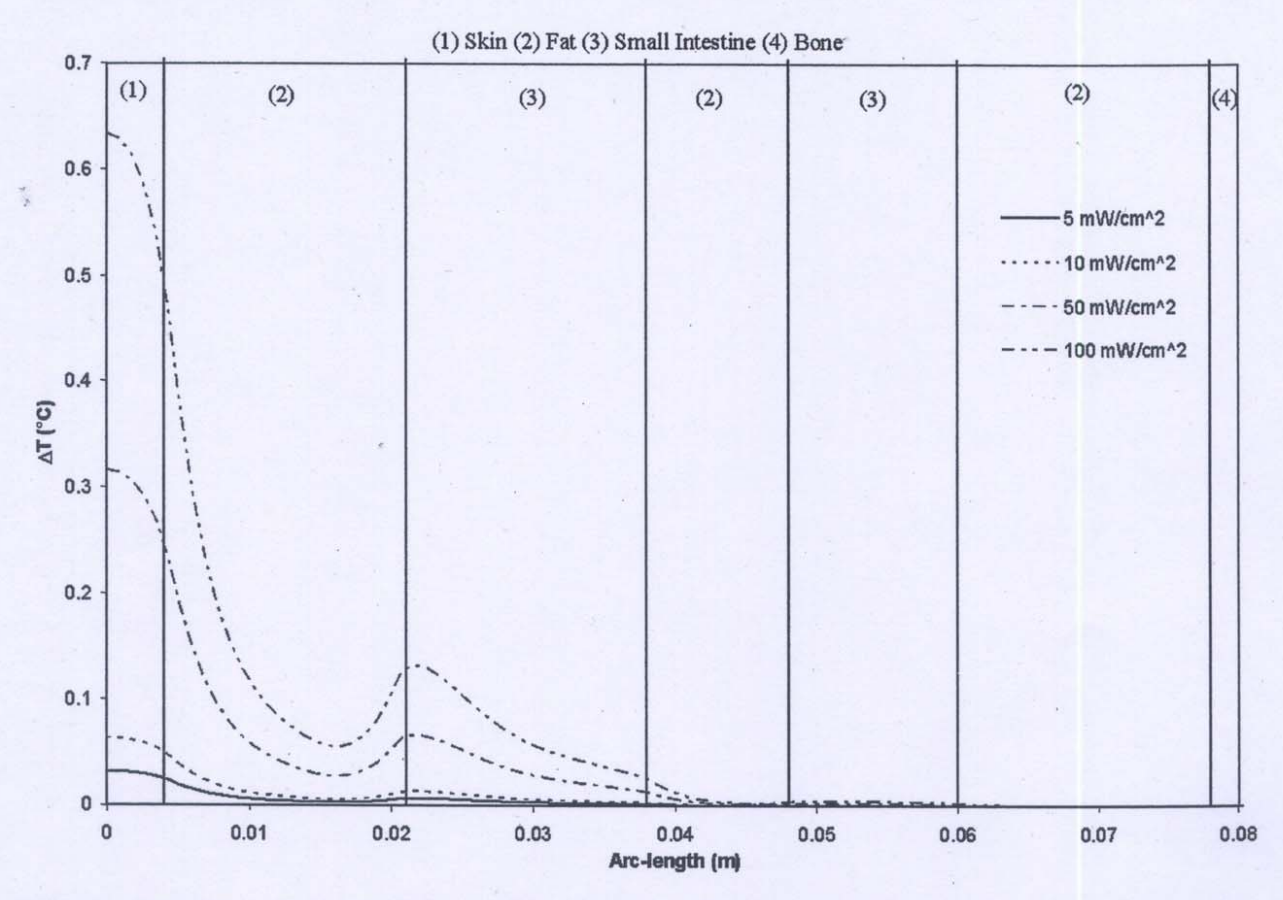


Fig. 18 Temperature increase versus arc length of human body exposed to the electromagnetic frequency of 915 MHz at various leakage power densities, at t=1 min

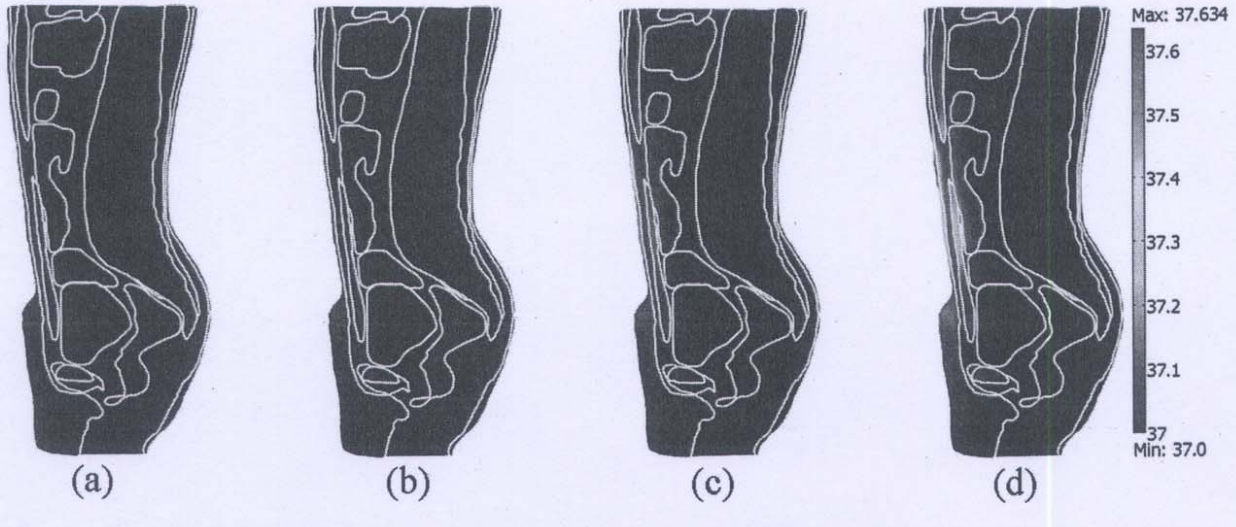


Fig. 19 Temperature distribution of human body exposed to the electromagnetic frequency of 915 MHz at t =1 min at various leakage power densities: (a) 5 mW/cm², (b) 10 mW/cm², (c) 50 mW/cm², and (d) 100 mW/cm²

 $\rho = \text{density (kg/m}^3)$

 ω_b = blood perfusion rate (1/s)

Subscripts

b = blood

ext = external

met = metabolic

r = relative

0 = free space, initial condition

References

[1] Rattanadecho, P., Suwannapum, N., and Cha-um, W., 2009, "Interactions Be-

tween Electromagnetic and Thermal Fields in Microwave Heating of Hardened Type I-Cement Paste Using a Rectangular Waveguide (Influence of Frequency and Sample Size)," ASME J. Heat Transfer, 131, p. 082101.

[2] Ratanadecho, P., Aoki, K., and Akahori, M., 2002, "Influence of Irradiation Time, Particle Sizes, and Initial Moisture Content During Microwave Drying of Multi-Layered Capillary Porous Materials," ASME J. Heat Transfer, 124, pp. 151–161.

[3] Ziegelberger, G., 2009, "ICNIRP Statement on the 'Guidelines for Limiting Exposure to Time-Varying Electric, Magnetic, and Electromagnetic Fields (up to 300 GHz)'," Health Phys., 97(3), pp. 257–258.

 [4] Stuchly, M. A., 1995, "Health Effects of Exposure to Electromagnetic Fields," IEEE Aerospace Applications Conference Proceedings, pp. 351–368.
 [5] Nishizawa, S., and Hashimoto, O., 1999, "Effectiveness Analysis of Lossy

[5] Nishizawa, S., and Hashimoto, O., 1999, "Effectiveness Analysis of Lossy Dielectric Shields for a Three-Layered Human Model," IEEE Trans. Microwave Theory Tech., 47(3), pp. 277–283. [6] Seufi, A. M., Ibrahim, S. S., Elmaghraby, T. K., and Hafez, E. E., 2009, "Preventive Effect of the Flavonoid, Quercetin, on Hepatic Cancer in Rats via Oxidant/Antioxidant Activity: Molecular and Histological Evidences," J. Exp. Clin. Cancer Res., 28(1), p. 80.

[7] Yang, D., Converse, M. C., Mahvi, D. M., and Webster, J. G., 2007, "Measurement and Analysis of Tissue Temperature During Microwave Liver Abla-

tion," IEEE Trans. Biomed. Eng., 54(1), pp. 150-155.

[8] Kanai, H., Marushima, H., Kimura, N., Iwaki, T., Saito, M., Maehashi, H., Shimizu, K., Muto, M., Masaki, T., Ohkawa, K., Yokoyama, K., Nakayama, M., Harada, T., Hano, H., Hataba, Y., Fukuda, T., Nakamura, M., Totsuka, N., Ishikawa, S., Unemura, Y., Ishii, Y., Yanaga, K., and Matsuura, T., 2007, "Extracorporeal Bioartificial Liver Using the Radial-Flow Bioreactor in Treatment of Fatal Experimental Hepatic Encephalopathy," Artif. Organs, 31(2),

[9] Pennes, H. H., 1998, "Analysis of Tissue and Arterial Blood Temperatures in the Resting Human Forearm," J. Appl. Physiol., 85(1), pp. 5–34.

- [10] Spiegel, R. J., 1984, "A Review of Numerical Models for Predicting the Energy Deposition and Resultant Thermal Response of Humans Exposed to Electromagnetic Fields," IEEE Trans. Microwave Theory Tech., 32(8), pp. 730-
- [11] Dragun, V. L., Danilova-Tret'yak, S. M., and Gubarev, S. A., 2005, "Simulation of Heating of Biological Tissues in the Process of Ultrahigh-Frequency
- Therapy," J. Eng. Phys. Thermophys., 78(1), pp. 109–114.
 [12] Ozen, S., Helhel, S., and Cerezci, O., 2008, "Heat Analysis of Biological Tissue Exposed to Microwave by Using Thermal Wave Model of Bio-Heat

Transfer (TWMBT)," Burns, 34(1), pp. 45-49.

[13] Samaras, T., Christ, A., Klingenbock, A., and Kuster, N., 2007, "Worst Case Temperature Rise in a One-Dimensional Tissue Model Exposed to Radiofrequency Radiation," IEEE Trans. Biomed. Eng., 54(3), pp. 492-496.

[14] Wang, J., and Fujiwara, O., 1999, "FDTD Computation of Temperature Rise in the Human Head for Portable Telephones," IEEE Trans. Microwave Theory Tech., 47(8), pp. 1528-1534.

[15] Hirata, A., Morita, M., and Shiozawa, T., 2003, "Temperature Increase in the Human Head Due to a Dipole Antenna at Microwave Frequencies," IEEE Trans. Electromagn. Compat., 45(1), pp. 109-116.

- [16] Hirata, A., Wang, J., Fujiwara, O., Fujimoto, M., and Shiozawa, T., 2005, "Maximum Temperature Increases in the Head and Brain for SAR Averaging Schemes Prescribed in Safety Guidelines," IEEE International Symposium on Electromagnetic Compatibility, Chicago, IL, Vol. 3, pp. 801-804.
- [17] Garcia-Fernandez, M. A., Valdes, J. F. V., Martinez-Gonzalez, A. M., and Sanchez-Hernandez, D., 2007, "Electromagnetic Heating of a Human Head Model by a Half-Wavelength Dipole Antenna," The Second European Confer-
- ence on Antennas and Propagation, pp. 1-4. [18] Shiba, K., and Higaki, N., 2009, "Analysis of SAR and Current Density in Human Tissue Surrounding an Energy Transmitting Coil for a Wireless Capsule Endoscope," 2009 20th International Zurich Symposium on Electromagnetic Compatibility, Zurich, pp. 321-324.

[19] Yang, D., Converse, M. C., Mahvi, D. M., and Webster, J. G., 2007, "Expanding the Bioheat Equation to Include Tissue Internal Water Evaporation During Heating," IEEE Trans. Biomed. Eng., 54(8), pp. 1382-1388.



Contents lists available at ScienceDirect

International Communications in Heat and Mass Transfer

journal homepage: www.elsevier.com/locate/ichmt



The method of fundamental solutions for solving free boundary saturated seepage problem[☆]

Khomgris Chaiyo, Phadungsak Rattanadecho*, Somchart Chantasiriwan

Research Center of Microwave Utilization in Engineering (R.C.M.E.), Department of Mechanical Engineering, Faculty of Engineering, Thammasat University (Rangsit Campus), Pathumthani 12120. Thailand

ARTICLE INFO

Available online 7 December 2010

Keywords: Method of fundamental solutions Seepage Free boundary Saturated porous medium

ABSTRACT

The problem of seepage flow through a dam is free boundary problem that is more conveniently solved by a meshless method than a mesh-based method such as finite element method (FEM) and finite difference method (FDM). This paper presents method of fundamental solutions, which is one kind of meshless methods, to solve a dam problem using the fundamental solution to the Laplace's equation. Solutions on free boundary are determined by iteration and cubic spline interpolation. The numerical solutions then are compared with the boundary element method (BEM), FDM and FEM to display the performance of present method.

© 2010 Elsevier Ltd. All rights reserved.

1. Introduction

The two-dimensional steady state saturated isotropic seepage flow with free boundary is described by the Laplace equation necessary boundary conditions. Previous works, the methods are to solve the unconfined seepage problem; it can be classified as analytical and numerical methods. The analytical solution can be obtained by using the theory of analytical function for liner ordinary differential equations [1,2]. It is only valid for two-dimensional problem but it cannot be used in case of complex geometrics and three-dimensional problems.

Conventionally numerical methods used to solve such problem included FDM [3] and FEM [4–8]. These methods are all mesh-dependent methods because they require boundary-fitted mesh generation. Alternative numerical methods include BEM [9] and MFS [10,11]. Both methods do not require boundary-fitted mesh, which results in considerable simplification of the preprocessing step. MFS has additional advantages over BEM in that it requires only boundary node placement instead of boundary mesh generation, and it does not require evaluation of near singular integrals [12]. The basic idea of MFS is to approximate the solution by forming a linear combination of known fundamental solutions with sources located outside the problem domain.

Previously, Chantasiriwan [13] investigated numerically both oneand two-phase Stefan problem subject to specification of boundary temperature, heat flux or energy using MFS. The numerically obtained results showed good agreement with the available analytical solutions. Kolodziej et al. [11] implemented the MFS with radial basis functions to

E-mail address: ratphadu@engr.tu.ac.th (P. Rattanadecho).

solve a heat source problem for arbitrary domains, the numerical results showed that the MFS is an accurate and reliable numerical technique for the solution of the inverse heat source problem.

In order to study seepage problem, accurately defining the position of free boundary is very important and necessary. In the past, many researchers utilized several methods to determine the location of free boundary such as Aitchison [3], and Westbrook [4] used FDM and FEM respectively, to solve the position of the free boundary, respectively. The conventional BEM was then used to study the seepage flow through the porous media by Liggett and Liu [14], and also BEM using hypersingular equations was proposed by Chen et al. [15].

In this paper, free boundary is regarded as a moving boundary with the over-specified boundary conditions, and MFS is used to find the location of free boundary. The numerical results of present method are also compared with FDM, FEM, and BEM solutions.

2. Mathematical formulations

The seepage problem of water flow through a saturated porous medium dam with tail water is shown in Fig. 1. The free boundary is defined as the boundary line or interface between the saturated-wet and dry soils. In order to reduce complexity of the phenomena to analyze flow field in the soil, several assumptions are introduced as following:

- (1) Soil in the flow field is homogeneous and isotropic.
- (2) Capillary and evaporation effects are neglected.
- (3) Two dimensional steady-state flow.
- (4) The flow follows Darcy's law.
- (5) Hydraulic conductivity or permeability of the soil is constant isotropic seepage flow.

Communicated by W.J. Minkowycz.

^{*} Corresponding author.

Nomenclatures

n direction cosine (-)G fundamental solutions (m)

p pressure (N/m²)

u component of velocity in *x* direction (m/s) *v* component of velocity in *y* direction (m/s)

x, y cartesian coordinates

Greek letters

 γ specific weight (N/m²) φ velocity potential (m²/s) ψ stream function (m²/s)

Subscripts

i, j index

Abbreviations

BEM boundary element method FDM finite difference method FEM finite element method

MFS method of fundamental solutions

The governing equation of two-dimensional steady-state isotropic seepage in terms of the velocity potential and the streamline function can be described by the Laplace's equation as

$$\nabla^2 \phi = 0 \tag{1}$$

$$\nabla^2 \psi = 0. \tag{2}$$

It is found that they are orthogonal to each other [16]. The component u-velocity and v-velocity in x- and y-direction, respectively, can be expressed as

$$u = -\frac{\partial \varphi}{\partial x}, \quad v = -\frac{\partial \varphi}{\partial y}.$$
 (3)

The velocity potential function or piezometric head can be written as

$$\varphi = y + \frac{p}{\gamma} \tag{4}$$

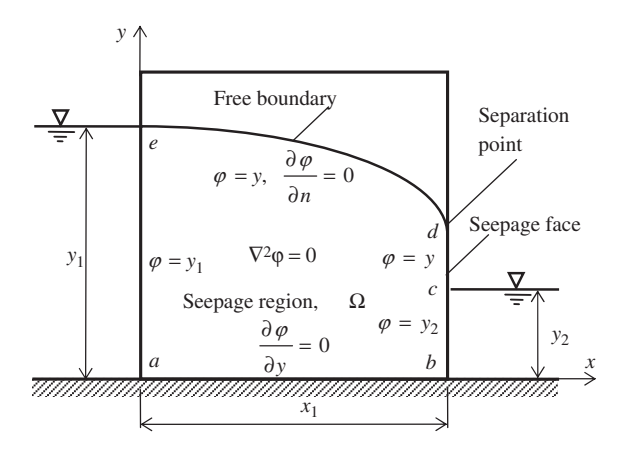


Fig. 1. Flow through a 2D rectangular dam.

where y is the position, p is the pressure, and γ is the specific gravity of fluid [16]. Therefore, the boundary conditions are presented in Fig. 1 as

$$\varphi = y_1 \quad \text{on } a - e \tag{5}$$

$$\varphi = y_2 \quad \text{on } b - c \tag{6}$$

and the remaining free boundary conditions

$$\varphi = y \quad \text{on } c - d \text{ and } d - e \tag{7}$$

$$\frac{\partial \varphi}{\partial n} = 0 \text{ on } d - e. \tag{8}$$

Boundary conditions at the free boundary are over-specified. In the following section, this boundary will be determined by using MFS with the initial guess of free boundary.

3. Numerical methods

3.1. The method of fundamental solutions

For basic idea of MFS is to express φ as linear combination of fundamental solutions [10]. Consider Fig. 1, let Ω is seepage region that be a bounded, simply connected domain in R^2 with boundary Γ . On boundary b-c, c-d, and a-e are Dirichet boundary, and boundary a-b is Neumann boundary. Boundary d-e is combined Dirichet and Neumann boundary, or is called as Robin boundary. For these boundaries can generally expressed as

$$\varphi = f(x, y) \quad \text{for } (x, y) \text{ on } \Gamma_1$$
 (9)

$$n_x \frac{\partial \varphi}{\partial x} + n_y \frac{\partial \varphi}{\partial y} = (x, y)$$
 for (x, y) on Γ_2 (10)

where direction cosine n_x and n_y are x-, and y-components, respectively, of the outward normal unit vector. The fundamental solution satisfies the solution of Laplace's equation as

$$G(P_i, Q_j) = \frac{1}{2\pi} \log r_{ij} \quad (P_i \in \Omega, , Q_j, \in \hat{S})$$
 (11)

where

$$r_{ij} = \sqrt{\left(x_i - \xi_j\right)^2 + \left(y_i - \eta_j\right)^2}$$
(12)

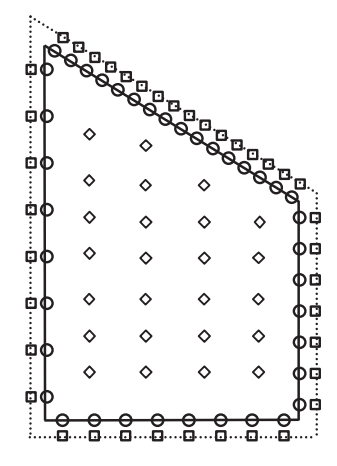


Fig. 2. The distributions of collocation points (white circles), source points (white squares), and internal domain points (white diamonds).

is a Euclidian distance between collocation point and source point, and (ξ_j, η_j) are coordinates of source points that located outside the domain shown in Fig. 2.

Since seepage problem included free boundary must be solved iteratively. Suppose that after the $n^{\rm th}$ iteration, value of $\varphi_i^{(n)}$ are known, values of $\varphi_i^{(n+1)}$ at $(n+1)^{\rm th}$ iteration are to be determined. Therefore, the approximate solution of Eq. (1) can be represented by a linear combination of fundamental solution as

$$\varphi_i^{(n+1)} = \sum_{j=1}^{N} a_j^{(n+1)} G(P_i, Q_j) \quad Q_j \in \hat{S}$$
 (13)

where N be number of nodes in boundary domain. Substituting Eq. (13) into Eqs. (9) and (10) results in a system of equations:

$$\sum_{j=1}^{N} a_j^{(n+1)} G(P_i, Q_j) = f(x_i, y_i) \qquad (i = 1, 2, ..., N_1)$$
 (14)

$$\sum_{i=1}^{N} a_{j}^{(n+1)} \left[n_{x} \frac{\partial}{\partial x} G(P_{i}, Q_{j}) + n_{y} \frac{\partial}{\partial y} G(P_{i}, Q_{j}) \right] = g(x_{i}, y_{i})$$
 (15)

where N_1 and N_2 are the number of nodes on boundary Γ_1 and Γ_2 , respectively, and $N=N_1+N_2$. Hence, $a_j^{(n+1)}$ can be determined. Direction cosine n_x and n_y in Eq. (10) or Eq. (15) on free boundary can be expressed as

$$n_{x} = \cos \alpha$$
 (16)

$$n_{y} = \cos \beta \tag{17}$$

respectively, and further details shown in Fig. 3.

Therefore, each of iteration, direction cosines of free boundary nodes are to be determined by using boundary nodes and central boundary nodes as displayed in Fig. 3. For central boundary nodes are interpolated by cubic spline interpolation (CBI) [17,18], when x-coordinate of those nodes are specifically known. Free boundary is also obtained by this interpolation technique. CBI is chosen because it uses third degree polynomials to connect the data points which often results in strikingly smooth curve fitting. For separation point is shown in Fig. 1, it is calculated by second degree polynomials after free boundary obtained for each of iteration.

Since the free boundary has over specified boundary conditions, it will be determined iteratively by using initial guess for free boundary as shown in Fig. 4. Additionally, Fig. 4 shows positions of source points in the space coordinates. It can be seen that the number of source

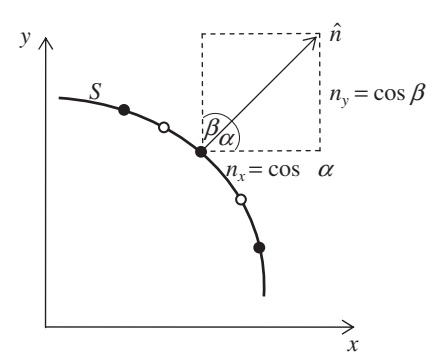


Fig. 3. Direction cosine, and locations of boundary nodes (black circles) and central boundary nodes (white circles).

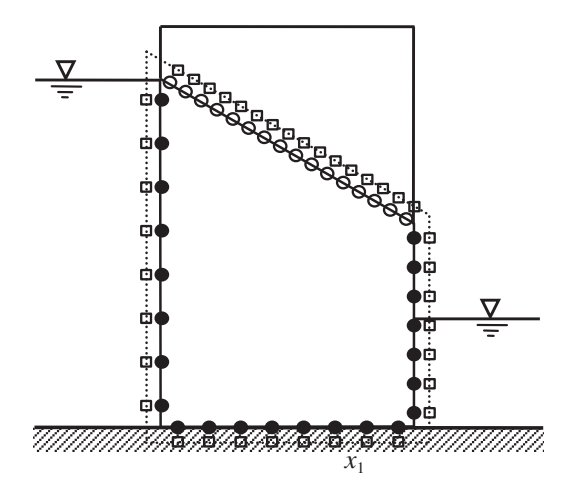


Fig. 4. Initial model: boundary nodes (black circles), initial free boundary nodes (white circles), and source points (white squares).

points is the number of boundary nodes (N). The N source points have the space coordinates as

$$(\xi_i, \eta_i) = (x_i, y_i) + BF \cdot (n_{x,i}, n_{y,i})$$

$$(18)$$

where *BF* is body factor constant, for this paper, let *BF* is equal to 1.0 to determine coordinate of source points. Each of source points is also located on an imaginary boundary, which is larger than the actual boundary. The free boundary location is determined by checking the criterion of convergence as following

$$\varepsilon = \frac{\sqrt{\sum_{i=1}^{m} (\varphi_i^{n+1} - \varphi_i^{n})^2}}{\sqrt{\sum_{i=1}^{m} (\varphi_i^{n})^2}}$$
(19)

where the symbol m is the total number of boundary nodes on the moving surface, and the allowable tolerance used in this paper is 10^{-4} as same as Chen et al. [5]. The flowchart of iteration procedure is also displayed in Fig. 5.

3.2. Finite element method

A standard finite element method is given in this section for two-dimensional seepage flow domain Ω . The weak form of Eq. (1) is obtained by multiply both sides of this equation by arbitrary continuous function $\overline{\phi}$ and integrating over the domain Ω , applying the divergence theorem [5–8] as

$$\int_{\Omega} (\nabla \overline{\varphi})^T \nabla \varphi d\Omega = 0. \tag{20}$$

It is noted that the weak form is nonlinear since the flow domain Ω is unknown such as the location of free boundary and the separation point are also unknown, although Eq. (20) is apparently linear in φ , it will be determined iteratively by using initial guess for free boundary. In finite element method the dependent variable, the velocity potential φ , is approximated by

$$\varphi = \sum_{i=1}^{n} \varphi_i N_i \tag{21}$$

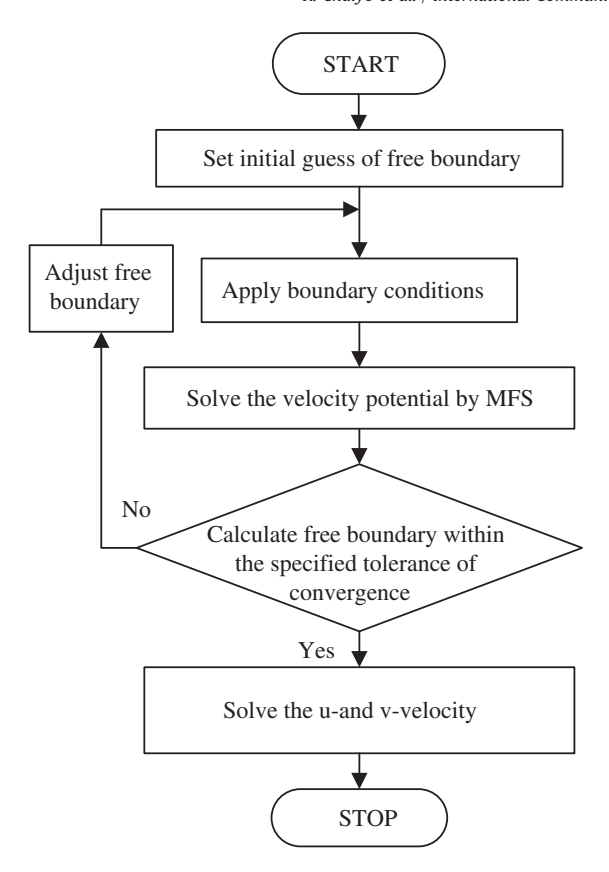


Fig. 5. Flow chart of iteration procedure

where usually the φ_i are the nodal values of φ , N_i are appropriate shape functions (interpolation function) defined piecewise element by element, and n is the total number of nodes. The linear algebraic equation system is derived by Galerkin's method as

$$K_{ij}\varphi_j = 0 \quad (i,j = 1,2, ...,n)$$
 (22)

where n is the number of nodes of finite element mesh and K_{ij} is a global matrix coefficient given by

$$K_{ij} = \int_{\Omega} \frac{\partial N_i}{\partial x_k} \frac{\partial N_j}{\partial x_l} d\Omega \quad (i, j = 1, 2, ..., n)(k, l = 1, 2, 3). \tag{23} \label{eq:23}$$

3.3. Boundary element method

The essence of a boundary element method implemented this problem is to transform the variables from area variables to boundary ones. The simplest approach is to use Green's second identity. Here one can also introduce the idea of multiplying Eq. (1) by a fundamental solution of Lapalce's equation G. Applying Green's second identity to φ and G results in the following transformation from an area integral $d\Omega$ to a line integral $d\Gamma$ [9,15] as

$$\int\limits_{\Omega} \Big(G \nabla^2 \phi - \phi \nabla^2 G \Big) d\Omega = \int\limits_{\Gamma} \bigg(G \frac{\partial \phi}{\partial n} - \phi \frac{\partial G}{\partial n} \bigg) d\Gamma \tag{24}$$

where n is the unit outward normal and $\partial/\partial n$ is the derivative in the direction of the outward normal. Using weighted residual technique, a

residual R function is set to be a fundamental solution G, Then Eq. (24) is obtained as

$$\varphi = \int_{\Gamma} G \frac{\partial \varphi}{\partial n} d\Gamma - \int_{\Gamma} \varphi \frac{\partial G}{\partial n} d\Gamma.$$
 (25)

Discretizing the boundary Γ into N_e element, it is obtained as

$$\varphi_i = \sum_{k=1}^{N_e} I_k \tag{26}$$

$$I_{k} = \int_{\Gamma_{k}} \left[\frac{\partial \varphi}{\partial n} G(s, x_{i}, y_{i}) - \varphi(s) \frac{\partial G}{\partial n} (s, x_{i}, y_{i}) \right] J(s) ds$$
 (27)

where Γ_k is a boundary element at k and N_e is a total boundary element. The velocity potential function φ can be approximated by interpolation function N_l as following:

$$\varphi(s) = \sum_{i=1}^{m} N_{l}(s)\varphi_{k,l}$$
 (28)

where it is should be m = 3 for quadratic element.

4. Analytical method

In this case, the analytical solution of the free boundary can be given in following form [1,2]

$$x = x_1 - \int_0^{\chi} \frac{\zeta(\sin^2 \chi) \sin \chi d\chi}{\sqrt{(1 - \alpha \sin^2 \chi)(1 - \beta \sin^2 \chi)}}$$
 (29)

$$y = y_1 + y_2 + \int_0^{\chi} \frac{\zeta(\cos^2\chi)\sin\chi d\chi}{\sqrt{(1-\alpha\sin^2\chi)(1-\beta\sin^2\chi)}}$$
(30)

$$0 \le \chi \le \pi/2 \tag{31}$$

where $\zeta(\chi)$ is the complete elliptic integral of the first kind; $\alpha, \beta \in (0, 1)$ are parameters that define problem; the domain parameter of y_1, y_2 and x_1 are defined as

$$y_1 = \int_0^{\pi/2} \frac{\zeta(\alpha + (\beta - \alpha)\sin^2\chi)d\chi}{\sqrt{\beta - \alpha + (1 - \beta)\sin^2\chi}}$$
(32)

$$y_{2} = \sqrt{\alpha} \int_{0}^{\pi/2} \frac{\zeta(\alpha \sin^{2}\chi) \sin \chi d\chi}{\sqrt{(1 - \alpha \sin^{2}\chi)(\beta - \alpha \sin^{2}\chi)}}$$
 (33)

$$x_1 = \int_0^{\pi/2} \frac{\zeta(\alpha + (1-\beta)\sin^2\chi)d\chi}{\sqrt{1-\alpha-(\beta-\alpha)\sin^2\chi}}.$$
 (34)

The length of the seepage surface is obtained as

$$y_0 = \int_0^{\pi/2} \frac{\zeta(\cos^2 \chi) \sin \chi \cos \chi d\chi}{\sqrt{(1 - (1 - \alpha)\sin^2 \chi) \cdot (1 - (1 - \beta)\sin^2 \chi)}}$$
(35)

5. Results and discussion

In the following, the proposed numerical technique MFS is used to solve a two-dimensional unconfined seepage flow problems of rectangular dam with tail water.

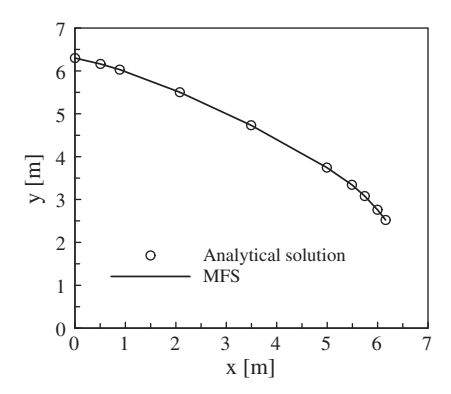


Fig. 6. Comparison of free boundary from analytical and MFS solution.

5.1. Numerical validation

In order to verify effectiveness of MFS, there two test problems of rectangular dam with tail water that are considered. The MFS results should be compared with analytical solution in first test, and conventional methods as FDM, FEM and BEM solutions in second test.

5.1.1. First test problem

In analytical method, after taking α = 0.3, β = 0.9 and performing numerical integration, the physical parameters of the problem: y_1 = 6.3014m, y_2 = 1.2359m, x_1 = 6.1592m and the length of seepage face y_0 = 1.2868m. The analytical results of the coordinates of the free boundary nodes are calculated by Eqs. (29) and (30). Fig. 6 shows the present simulated MFS results. The solutions obtained agree closely with the analytical results.

5.1.2. Second test problem

Consider seepage problem where the upper hydraulic head $y_1 = 24$ m, the lower hydraulic head $y_2 = 4$ m, and the width of dam $x_1 = 16$ m. There are 70 nodes uniformly distributed in the initial guess domain with grid spacing of 1.0 and separation point is assumed at y = 14 m. The present numerical solutions of free boundary are then compared with those of Aitchison [3], Westbrook [4], and Chen et al. [15] as shown Table 1. The number of iterations of present method is obtained by 22. It can be seen that that MFS is capable to calculate free boundary agree with other methods.

The separation point at $x = 16.0 \, m$ is interesting and important since a singular point due to the intersection of the free boundary and seepage surface. In addition, this point presents an important role in term of dam stability. It is predicted by MFS and compared with other methods as shown Table 2.

Table 1 Free boundary obtained by different methods.

	, ,			
x (m)	MFS	FDM [3]	FEM [4]	BEM [15]
1	23.75	23.74	23.64	23.74
2	23.41	23.41	23.32	23.40
3	23.03	23.02	23.06	23.01
4	22.59	22.59	22.52	22.52
5	22.12	22.12	22.12	22.09
6	21.60	21.60	21.55	21.57
7	21.04	21.04	21.07	21.00
8	20.44	20.43	20.36	20.39
9	19.79	19.78	19.81	19.73
10	19.08	19.08	19.07	19.02
11	18.32	18.31	18.26	18.24
12	17.50	17.48	17.45	17.39
13	16.59	16.57	16.45	16.45
14	15.58	15.54	15.51	15.39
15	14.40	14.39	14.33	14.09
16	12.88	12.79	Not shown	12.68

Table 2The separation point calculated by different methods.

Reference	Height (m)
Present MFS	12.88
FDM [3]	12.79
FEM [4]	Not shown
BEM [15]	12.68

5.2. Flow analysis

As in two previous test problems, the rectangular dam is homogeneous and isotropic. Water flows through the dam from a reservoir on the upstream side to the downstream side as shown in Fig. 4. Fluid particles move along a streamline always in the same direction from the upper to the lower reservoir that is the direction of x increasing in Fig. 7. Thus the fluid velocity is positive in the flow region Ω and the velocity potential φ is decreased along any streamline as display in Fig. 7. The velocity field in Fig. 7(c) shows zero normal component on the free boundary. The velocity potential function contours in Fig. 7(d) are normal to the free boundary and the bottom boundary, which are stream lines.

6. Conclusion

In this paper, it is shown how to use MFS to solve the problem of two-dimensional steady-state isotropic seepage flow. A generalized mathematical model and an effective calculation procedure are proposed. For two test problems indicate the successful implementation of numerical procedure. The free boundary and separation point can be obtained. Although it is only considered solving dam problem, MFS can be applied to more general free boundary problems.

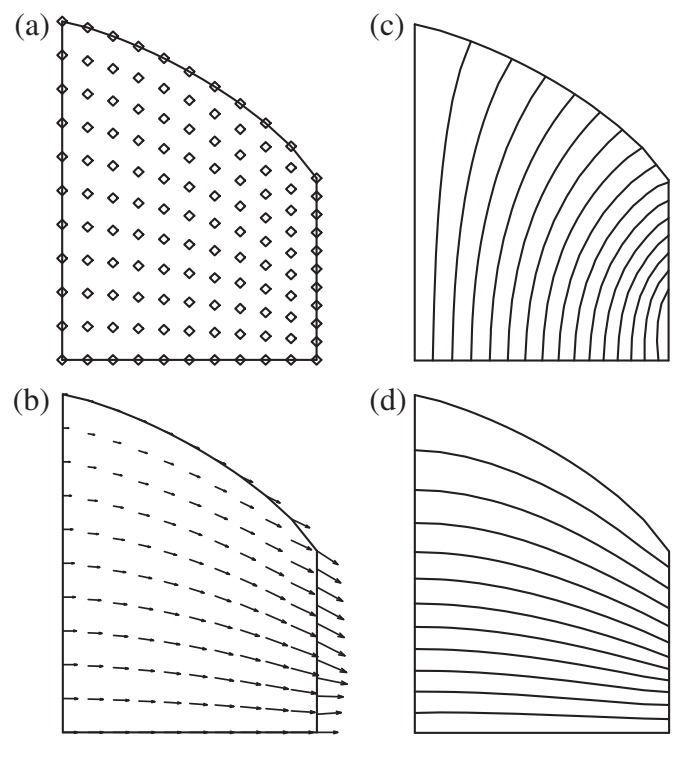


Fig. 7. Flow distribution: (a) converged shape and domain points (white diamonds); (b) velocity field in the converged shape; (c) the velocity potential distribution; and (d) the stream function distribution.

Acknowledgments

The authors gratefully acknowledge the Thailand Research Fund (TRF) for supporting this research project under the Royal Golden Jubilee Program (RGJ) contract No. PHD/0286/2550.

References

- [1] P. Ya, Polubarinova-Kochina, Theory of ground water movement, Princeton University Press, 1962.
- [2] A. Leontiev, W. Huacasi, Mathematical programming approach for unconfined seepage flow problem, Engineering Analysis with Boundary Elements 25 (2001) 49–56.
- [3] J. Aitchison, Numerical treatment of a singularity in a free boundary problem, Proceedings of the Royal Society of London. Series A 330 (1583) (1972) 573–580.
- [4] D.R. Westbrook, Analysis of inequality and residual flow procedures and an iterative scheme for free boundary seepage, International Journal for Numerical Methods in Engineering 21 (1985) 1791–1802.
- [5] K.Y. Chung, N. Kikuchi, Adaptive methods to solve free boundary problems of flow through porous media, International Journal for Numerical and Analytical Methods in Geomechanics 11 (1987) 17–31.
- [6] S.J. Lacy, J.H. Prevost, Flow through porous media: a procedure for locating the free surface, International Journal for Numerical and Analytical Methods in Geomechanics 11 (1987) 585–601.
- [7] S. Boeriu, J.C. Bruch Jr., Performance analysis tools applied to a finite element adaptive mesh free boundary seepage parallel algorithm, Computer Methods in Applied Mechanics and Engineering 194 (2005) 297–312.

- [8] J.M.M.C. Marques, J.M.P. Marado, The Influence of the permeability model in unconfined seepage problems, Proceeding of the 5th International Workshop, Guimaraes, Portugal, , 2007, pp. 143–148.
- [9] A.A. Becker, The boundary element method in engineering, McGraw-Hill Book, Singapore, pp. 41–60.
- [10] M.A. Golberg, The method of fundamental solutions for Poisson's equation, Engineering Analysis with Boundary Elements 16 (1995) 205–213.
- [11] J.A. Kolodziej, M. Mierzwiczak, M. Cialkowski, Application of the method of fundamental solutions and radial basis functions for inverse heat source problem in case of steady-state, International Communications in Heat and Mass Transfer 37 (2010) 121–124.
- [12] S. Chantasiriwan, Methods of fundamental solutions for time-dependent heat conduction problems, International Journal for Numerical Methods in Engineering 66 (2006) 147–165.
- [13] S. Chantasiriwan, The method of fundamental solutions for free surface stefan problems, Engineering Analysis with Boundary Elements 33 (2009) 529–538.
- [14] J.A. Liggett, P.L.-F. Liu, The boundary integral equation method for porous media flow, George Allen and Unwin Inc, Boston, 1983.
- [15] J.T. Chen, C.C. Hsiao, Y.T. Lee, Study of free-surface seepage problem using hypersingular equations, Communications in Numerical Methods in Engineering 23 (2007) 755–769
- 23 (2007) 755–769.
 [16] R.L. Daugherty, J.B. Franzini, E.J. Finnemore, Fluid mechanics with engineering applications, McGraw-Hill, Singapore, 1989.
- [17] P. Dechaumphai, Numerical methods in engineering, Chulalongkorn University Press, Bangkok, 1995.
- [18] S.C. Chapra, R.P. Canale, Numerical methods for engineers, McGraw-Hill, New York, 1990.

Author's personal copy

International Journal of Heat and Mass Transfer 54 (2011) 2043-2055



Contents lists available at ScienceDirect

International Journal of Heat and Mass Transfer

journal homepage: www.elsevier.com/locate/ijhmt



Numerical analysis of microwave melting of ice-saturated porous medium filled in a rectangular waveguide with resonator using a combined transfinite interpolation and PDE methods

Khomgris Chaiyo, Phadungsak Rattanadecho*

Research Center of Microwave Utilization in Engineering (R.C.M.E.), Department of Mechanical Engineering, Faculty of Engineering, Thammasat University (Rangsit Campus), Pathumthani 12120, Thailand

ARTICLE INFO

Article history:
Received 23 March 2010
Received in revised form 3 December 2010
Accepted 3 December 2010
Available online 27 January 2011

Keywords: Microwave Melting Transfinite interpolation PDE mapping Moving boundary Resonator

ABSTRACT

A numerical study is performed for the melting process of ice-saturated porous medium filled in a rectangular waveguide with a resonator subjected to electromagnetic energy. A microwave system supplies a monochromatic wave in a fundamental mode (TE_{10} mode) with operating frequency of 2.45 GHz. Focus is placed on establishing a computationally efficient approach for solving moving boundary heat transfer problem in a two-dimensional structured grid. Numerically, preliminary grids are first generated by an algebraic method, based on a transfinite interpolation method, with subsequent refinement using a PDE mapping method. A preliminary case study indicates successful implementation of the numerical procedure. The predicted results from two-dimensional melting model are then validated against available experimental results and subsequently used as a tool for efficient computational prototyping. Based on the numerical results are performed illustrating the influence of resonator and layered configuration, in case of the installed resonator has strongly affected on the microwave power absorbed, temperature distribution, and the melting front during microwave melting process.

© 2011 Elsevier Ltd. All rights reserved.

1. Introduction

The study of melting process in material exposed to microwave has been investigated by many researchers. Pangrle et al. [1] studied coupled electromagnetic and thermal model for the thawing process of frozen cylinders (water and NaCl) using a plane wave as opposed to a resonant cavity. They also developed a one-dimensional model for microwave thawing of cylindrical samples [2]. Rattanadecho [3] recently presented theoretical and experimental investigation of microwave thawing of frozen layer in a microwave oven using coordinate transformation technique based on boundary fixed grid method together with an implicit time scheme. A number of other analyses of the microwave thawing process have appeared in the literatures [4,5]. Moreover, most previous work the microwave power absorbed term was assumed to be decay exponentially into the sample following Lambert's law. This assumption is only valid for the large dimension samples where the depth of sample is much larger than the penetration depth. Otherwise in the thin samples where the depth of sample is much smaller than the penetration depth, the spatial variations of the electromagnetic field and microwave power absorbed within sample must be obtained by Maxwell's equation. The prior investigation of twodimensional microwave melting in cylinders was carried out by Zeng and Faghri [6], and their model predictions were compared with experimental data. Basak and Ayappa [7] also considered the two-dimensional microwave thawing studies with fixed grid based effective heat capacity method coupled with Maxwell's equations. The primary focus of their article is to incorporate and investigate the effect of liquid convection during thawing of a pure material with microwave. For previous work numerically results were performed using the conventional methods such as finite difference and finite element method.

In addition, Rattanadecho [8] developed two-dimensional models to predict the electromagnetic fields (TE₁₀ mode) inside the waveguide, microwave power absorbed, and temperature distributions within wood located in rectangular waveguide. In this study, the simulation results were shown to influence of irradiation time, working frequency and sample size on heating patterns were investigated in details. Rattanadecho and Klinbun [9] then recently carried out theoretically analysis of microwave heating of dielectric materials with various resonator distances. This study found that the resonator was significantly affected on a uniformity of temperature distributions depending on the penetration depth of microwave. Furthermore, Rattanadecho et al. [10] investigated numerically and experimentally the melting of frozen packed beds by a microwave with a rectangular waveguide in case of without installed resonator. However, the studied in case of

^{*} Corresponding author. Tel.: +66 2564 3001 9x3153; fax: +66 2564 3010. E-mail address: ratphadu@engr.tu.ac.th (P. Rattanadecho).

Nomenclature thermal diffusivity (m²/s) Z_{I} intrinsic impedance (Ω) *A*, *B* univariate blending function (–) specific heat capacity (J/(kg K)) C_p Greek letters Ë electric fields intensity (V/m) permittivity (F/m) ε thermal conductivity (W/m K), and wavelength (m) f frequency of incident wave (Hz), and interpolation funcλ tion (-)magnetic permeability (H/m) μ Н magnetic field intensity (A/m) υ velocity of propagation (m/s) latent heat (J/kg) L density (kg/m³) ρ Р power (W) electric conductivity (S/m) Q local electromagnetic energy term (MW/m³) transformed coordinates ξ, η S Poynting vector (W/m²) Т temperature (°C) Subscripts time (s) in input dielectric loss coefficient (-) $\tan \delta$ unfrozen u, w interpolation parameter (-) moving boundary mov Cartesian coordinates *x*, *z* S frozen wave impedance (Ω) Z_H

melting of ice-saturated porous medium including resonator effects has not been investigated before.

Transient heat transfer problem involving melting or solidification processes generally refer to as moving boundary or phase change problems. They are important topics which span a broad spectrum of scientific and engineering discipline such as thawing of freezing of soil, ice formation, food processing and numerous others. The some up to date reviews of these problems are available [11,12]. In the past, a variety of conventional numerical techniques have been developed for solving these problems, including the enthalpy [13,14], isotherm migration [15], and coordinate transformation methods [16,3]. Previous works on multidimensional moving boundary problems include Chatterjee and Prasad [17] adopted a generalized finite volume discretization scheme using a nonorthogonal curvilinear body-fitted transformation, which inherently facilitates accurated tracking of moving interfaces via adaptive grid generation in a full 3D framework, and Gong and Mujumdar [18] used the streamline Upwind/Petrov Galerkin finite element method in combination with fixed grid primitive variable method to simulate melting of a pure phase change material in 2D rectangular container.

Conventionally numerical methods have been widely used due to easy to handle numerical algorithms for phase change problem. However, in numerical approximations used in this method with discontinuous coefficients, often the largest numerical errors are introduced in a neighborhood of the discontinuities particularly for phase change in geometry complexity as well as boundary condition.

The troublesome numerical errors in conventional method are effectively reduced if the grid generation and solution procedure are separated with the discontinuities and special formulas are used to incorporate the jump conditions directly into the numerical model. This is the main idea behind this work considering moving boundary as a parameter.

To create a computational grid in body-fitted coordinates, two basic steps required: (1) define an origin point and (2) specify the distribution (number and spacing) of grid nodes along the edges of the geometric regions. The automatic grid generator then takes over, and using an algebraic technique known as transfinite interpolation, creates a grid that simultaneously matches the edge node prescription and conforms to the irregular edges of the body-fitted geometry. Grid generation by algebraic methods produces high quality numerical grids and allow for the very efficient integration of the thermal-flow field physics. Considering grid

optimization, the designed grid optimization-algorithm improves upon the transfinite interpolation method by carrying the grid generation process one step further. It uses automatically generated grid as an initial approximation to a higher quality grid system derived utilizing the technique of PDE grid generation. This technique offers advantages over purely algebraic methods:

- Good control over the skewness and spacing of the derived grid on surface interiors, while simultaneously allowing complete control over the grid spacing (node distribution) on surface edges as well as moving boundary.
- An ability to produce unique, stable, and smooth grid distributions free of interior maxima or minima (inflection points) in body-fitted coordinates.

Parabolic grid generation works well with irregularly shaped geometries and can produce grids that are highly conformal with the edges of individual computational surfaces. The means for grid generation should not be dictated by the limitations of a given specific field solution procedure and conversely the method that determines the field should accept as input an arbitrary set of coordinate points which constitutes the grid. In general, of course, these two operations can never be totally independent because the logistic structure of the information, the location of outer boundaries, the nature of coordinate and the types of grid singularities are items that have to be coordinated closely between the field solver and the grid generator [19].

Grid generation for multi-dimensional geometries using transfinite interpolation functions was studied by Cook [20], Gordon and Hall [21], Ettouney and Brown [22] successfully modeled slightly non-planar interfaces by using an algebraic grid generation system where the interface was described in terms of univariate function.

Although grid generation is the heart of most numerical algorithms for flow problems or non-phase change problem, little effort has been reported on phase change problems, particularly the problem that is to couple the grid generation algorithm with the heat transport equations.

The present paper introduces the novel numerical approach, a combined transfinite interpolation and PDE methods [23,24], for solving two-dimensional melting model under electromagnetic energy which is subjected to a monochromatic microwave TE₁₀ mode with operating frequency of 2.45 GHz. However, the effect of resonator on microwave phenomena in the case of using a rectangular waveguide with a resonator has not been clearly studied yet. The

objective of this study can be summarized as follows: (i) It is carried out to predict the melting front, the distribution of temperatures, microwave power absorbed terms, and electromagnetic fields and (ii) The influences of resonator and layered configurations on melting process are clarified in details. Furthermore, numerically in order to generate a boundary/interface fitted coordinate system, structured grids are initialized using transfinite interpolation algebraic techniques and the quality of structured grids can be significantly improved by applying parabolic-PDE methods. These methods iteratively solve unsteady conduction's equation together with moving boundary condition during the melting process considering conduction as the only mode of heat transfer in both the unfrozen layer and the frozen layer.

2. Experimental configuration

Fig. 1 shows the experimental apparatus for microwave melting system. It was developed for the melting tests to validate the model simulation. The rectangular waveguide system is operated by propagating traveling waves along the z-direction of the rectangular waveguide with the inner dimensions of 109.2×54.6 mm toward a water load that is situated at the end of the waveguide. The water load (lower absorbing boundary) ensures that only a minimal amount of microwave is reflected back to the sample. Also, an isolator (upper absorbing boundary), which is located at the upper end of waveguide, is used to trap any microwave reflected from the sample to prevent it from damaging the magnetron. In the microwave supply system a magnetron generated the monochromatic wave of TE_{10} mode with operating frequency of 2.45 GHz, and output of magnetron is adjusted as 1000 W [8].



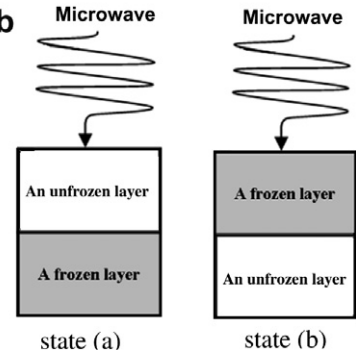


Fig. 1. Experimental apparatus: (a) microwave heating system and (b) the melting sample.

Table 1Thermal and dielectric property of the unfrozen and frozen layer.

Properties	Unfrozen layer	Frozen layer
ρ (kg/m ³)	1942.0	1910.0
$a (m^2/s)$	$0.210 imes 10^{-6}$	0.605×10^{-6}
λ (W/m K)	0.855	1.480
C_p (J/kg K)	2.099×10^3	1.281×10^{3}
$\mu_r(-)$	1.0	1.0
$\varepsilon_r (F/m)$	$88.15 - 0.414T + (0.131 \times 10^{-2})T^2 -$	5.1
	$(0.046 \times 10^{-4})T^3$	
$\tan \delta (-)$	$0.323 - (9.499 \times 10^{-3})T + (1.27 \times 10^{-4})T^2 -$	0.0124
	$(6.13 \times 10^{-7})T^3$	

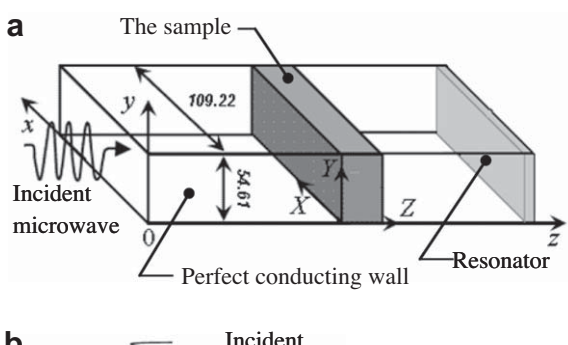
Next, the samples used for testing in microwave melting processes are considered. The sample is composed of an unfrozen layer (water and glass beads) with thickness of 50 mm and a frozen layer (ice and glass beads) with thickness of 50 mm. They are arranged in series against perpendicular to direction of irradiation via a rectangular waveguide. The unfrozen layer and the frozen layer are arranged in different configurations, as shown in state (a) and state (b) of Fig. 1(b), respectively. The dielectric properties of the each material of samples are assumed to be independent with microwave frequency. The thermal and dielectric properties of the samples are shown in Table 1.

3. Mathematical formulations

Generally, studies on the microwave melting involve solutions of the equations governing electromagnetic propagation, i.e., Maxwell's equations, either by themselves or coupled with the heat transport equation. The surface of a sample is exposed to the monochromatic wave of TE_{10} mode with operating frequency of 2.45 GHz (shown as Fig. 2(a)).

3.1. Electromagnetic field equation

Fig. 2 shows the two-dimensional analytical model for microwave melting of a sample using a rectangular waveguide with a resonator. The proposed model is based on the following assumptions:



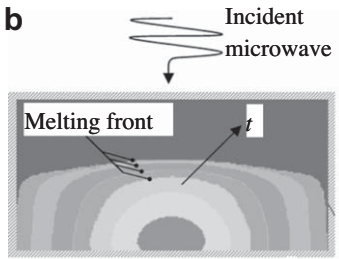


Fig. 2. The microwave system: (a) schematic of microwave system and (b) the physical model (in case of state (b)).

2046

- (1) Since the microwave field in the TE₁₀ mode has no variation of field in the direction between the broad faces, a twodimensional model over the x-z plane is applicable to analysis of electromagnetic field inside a rectangular waveguide [25].
- (2) The absorption of microwave energy by the cavity (including air) in the rectangular waveguide is negligible.
- (3) The walls of a rectangular waveguide are perfect conductors.
- (4) The effect of the sample container on the electromagnetic field can be neglected.

The electromagnetic field is solved according to the theory of Maxwell's equations. In this study, the microwave of a fundamental TE_{10} mode is considered; therefore the Maxwell's equations in terms of the electric field intensity E and magnetic intensity Hare given by:

$$\frac{\partial E_{y}}{\partial z} = \mu \frac{\partial H_{x}}{\partial t} \tag{1}$$

$$\frac{\partial E_y}{\partial x} = -\mu \frac{\partial H_z}{\partial t} \tag{2}$$

$$\begin{split} \frac{\partial E_{y}}{\partial z} &= \mu \frac{\partial H_{x}}{\partial t} \\ \frac{\partial E_{y}}{\partial x} &= -\mu \frac{\partial H_{z}}{\partial t} \\ -\left(\frac{\partial H_{z}}{\partial x} - \frac{\partial H_{x}}{\partial z}\right) &= \sigma E_{y} + \varepsilon \frac{\partial E_{y}}{\partial t} \end{split} \tag{1}$$

where the permittivity ε , magnetic permeability μ and electric conductivity σ as:

$$\varepsilon = \varepsilon_0 \varepsilon_r, \quad \mu = \mu_0 \mu_r, \quad \sigma = 2\pi f \varepsilon \tan \delta$$
 (4)

Additionally if magnetic effects are negligible, which is proven to be a valid assumption for most dielectric materials used in microwave heating applications, the magnetic permeability μ is well approximated by its value μ_0 in the free space. Let tan δ is the loss tangent coefficient. In this work, the dielectric properties are assumed to vary with temperature only.

Boundary conditions: corresponding to the analytical mode as shown in Fig. 2, can be given as follows:

(a) Perfectly conducting boundaries. Boundary conditions on the inner wall surface of a rectangular waveguide are given by using Faraday's law and Gauss's theorem:

$$E_t = 0, \quad H_n = 0 \tag{5}$$

where subscripts t and n denote the components of tangential and normal directions, respectively.

(b) Continuity boundary condition. Boundary conditions along the interface between different materials, for example between air and dielectric material surface, are given by using Ampere's law and Gauss theorem:

$$E_t = E'_t, \quad H_t = H'_t, \quad D_n = D'_n, \quad B_n = B'_n$$
 (6)

where *D* is the electric flux density and *B* is the magnetic induction. The superscript 'denotes one of the different materials.

(c) Absorbing boundary condition. At the both ends of the rectangular waveguide, the first order absorbing conditions are applied [26]:

$$\frac{\partial E_{y}}{\partial t} = \pm v \frac{\partial E_{y}}{\partial z} \tag{7}$$

where \pm represents forward or backward waves and υ is phase velocity of microwave. In case of installed resonator; the resonator boundary condition is applied at the end of rectangular waveguide:

$$E_{\nu}=0, \quad H_{z}=0 \tag{8}$$

(d) Oscillation of the electric and magnetic flied intensities by magnetron. Incident wave due to magnetron is given by the following equations:

$$E_{y} = E_{yin} \sin\left(\frac{\pi x}{L_{x}}\right) \sin(2\pi f t) \tag{9}$$

$$H_{x} = \frac{E_{yin}}{Z_{H}} \sin\left(\frac{\pi x}{L_{x}}\right) \sin(2\pi f t) \tag{10}$$

where E_{yin} is the input value of electric field intensity, L_x is the length of rectangular waveguide in x-direction and Z_H is the wave impedance defined as:

$$Z_{H} = \frac{\lambda_{g} Z_{I}}{\lambda} = \frac{\lambda_{g}}{\lambda} \sqrt{\frac{\mu}{\epsilon}}$$
 (11)

The power flux associated with a propagating electromagnetic wave is represented by the Poynting vector:

$$S = \frac{1}{2} \operatorname{Re}(\vec{E} \times \vec{H}) \tag{12}$$

The Poynting theorem allows the evaluation of the microwave power input expressed as

$$P_{\rm in} = \int_A S dA = \frac{A}{4Z_H} E_{\rm yin}^2 \tag{13}$$

where Z_I denotes intrinsic impedance depending on the properties of the material. λ and λ_g are the wave lengths of microwaves in free space and rectangular waveguide, respectively.

3.2. Heat transport equation

The schematic of microwave system as displayed in Fig. 2(a). Initially, the walls are all insulated, and the sample is composed of a water-saturated porous medium (water and glass beads) and an ice-saturated porous medium (ice and glass beads), respectively. The temperature of the sample exposed to incident wave is obtained by solving the conventional heat transport equation with the microwave power absorbed included as a local electromagnetic energy term. In order to reduce complexity of the phenomena for analyze the process of heat transport due to microwave melting of a sample, several assumptions have been introduced into the heat equations as following assumptions:

- (1) Corresponding to electromagnetic field, temperature field also can be assumed to be two-dimensional plane (x-z)plane).
- (2) The walls of sample are insulated.
- (3) The effect of the container on temperature field can be
- (4) The effect of the natural convection in the sample can be neglected.
- (5) The local thermodynamic equilibrium along each phase is assumed.
- (6) In this study, in a macroscopic sense, the pore structure within the material is assumed to be homogeneous and isotropic. Therefore, the heating model for a homogeneous and isotropic material is used in the current analysis.

The governing energy equations describing the temperature rise in a sample are the time dependent heat diffusion equation for two-dimensional heat flow with constant thermal properties for both the unfrozen and frozen layer, respectively as:

$$\frac{\partial T_l}{\partial t} = a_l \left(\frac{\partial^2 T_l}{\partial x^2} + \frac{\partial T_l}{\partial z^2} \right) + \frac{Q}{\rho \cdot C_p} + \frac{\partial T_l}{\partial z} \frac{dz}{dt}$$
 (14)

$$\frac{\partial T_s}{\partial t} = a_s \left(\frac{\partial^2 T_s}{\partial x^2} + \frac{\partial^2 T_s}{\partial z^2} \right) + \frac{Q}{\rho \cdot C_p} + \frac{\partial T_s}{\partial z} \frac{dz}{dt}$$
 (15)

where Q is local electromagnetic energy term, which is function of the electric field and defined [25] as

$$Q = 2\pi f \varepsilon_0 \varepsilon_r \tan \delta E_v^2 \tag{16}$$

Besides, last term of Eqs. (14) and (15) result from a coordinate transformation attached to moving boundary. In the unfrozen layer, internal convection can be neglected because the presence of glass beads minimizes the effect of natural convection current.

Boundary conditions:

(a) Adiabatic condition; assuming that the walls of the sample are insulate:

$$\frac{\partial T}{\partial n} = 0 \tag{17}$$

(b) Moving front boundary condition; the moving boundary between the unfrozen layer and frozen layer is described by the Stefan equation, which is obtained from a consideration of the energy balance at the interface between the unfrozen and frozen layer provides the following equation:

$$\left(\lambda_{s} \frac{\partial T_{s}}{\partial z} - q_{\text{mov}} \Delta z_{\text{mov}} - \lambda_{l} \frac{\partial T_{l}}{\partial z}\right) \left[1 + \left(\frac{\partial z_{\text{mov}}}{\partial x}\right)^{2}\right] = \rho_{s} L_{s} \frac{\partial z_{\text{mov}}}{\partial t}$$
(18)

where subscript mov denotes solid–liquid front (melting front), $\partial z_{\text{mov}}/\partial t$ is the velocity of fusion front or melting front, and L_s the latent heat of fusion. To avoid changes in the physical dimensions as the melting front progresses, $\rho_s = \rho_l$ will be specified. In this study, the thermal conductivities, λ_l and λ_s are bulk-average values for the glass beads and the water or ice, respectively.

4. Grid generation

Generally, two types of structured grid generation are in used: algebraic method, i.e., transfinite or multivariate interpolation and partial differential equation mapping (PDE mapping) methods. Transfinite interpolation provides a relatively easy way of obtaining an initial grid that can be refined and smoothed by other methods, whether algebraic, PDE (this work), or variational method. For more complex geometries, such as this work, it is preferable to construct grid initially by transfinite interpolation, and to refine the grid filled in Cartesian coordinates in the interior of a domain by PDE mapping method subsequently.

4.1. Transfinite interpolation

The present method of constructing a two-dimensional boundary-conforming grid for a phase change in microwave melting is a direct algebraic approach based on the concept of transfinite interpolation. In this method, no partial differential equations are solved to obtain the curvilinear coordinates, and the same system is used for the entire domain. The algebraic method can be easier to construct than PDE mapping methods, and give easier control over grid characteristics such as orthogonality and grid point spacing. However, this method is sometime criticized for allowing discontinuities on the boundary to propagate into the interior and for not generating grids as smooth as those generated by PDE mapping method. The main idea behind this work, prior to generation of grids by PDE mapping methods, it is preferable to obtain first preliminary grids using the algebraic method, i.e., transfinite interpolation method. The combined transfinite interpolation and PDE mapping method is used to achieve a very smoother grids point distribution and boundary point discontinuities are smoothed out in the interior domain.

For the concept of transfinite interpolation, a significant extension of the original formulation by Gordon and Hall [21] has made, it is possible to initially generate global grid system with geometry

specifications only on the outer boundaries of the computation domain and yet obtain a high degree of local control. Moreover, to successfully track the moving boundary front, the grid generation mapping must adapt to large deformations of the interface shape while maintaining as much orthogonality and smoothness as possible. Due to the generality of the method it has been possible to use more advanced mappings than conventional types and thereby improve the overall efficiency of the grid in term of computational work for a given resolution.

In Fig. 3, the present method of constructing a two-dimensional boundary-conforming grid for a system, which it is a direct algebraic approach based on the concept of transfinite or multivariate interpolation. It is possible to initially generate global single plane transformations with geometry specifications only on outer boundaries of the computational domain.

Let f(u, w) = (x(u, w), z(u, w)) denote a vector-valued function of two parameters u, w defined on the region $u_1 \le u \le u_{\text{max}}$, $w_1 \le w \le w_{\text{max}}$. This function is not known throughout the region, only on certain planes (Fig. 3). The transfinite interpolation procedure then gives the interpolation function f(u, w) by the recursive algorithm [24]:

$$f^{(1)}(u,w) = A_1(u) \cdot f(1,w) + A_2(u) \cdot f(u_{\text{max}}, w)$$

$$f(u,w) = f^{(1)}(u,w) + B_1(w) \cdot [f(u,1) - f^{(1)}(u,1)] + B_{2(w)} \cdot [f(u,w_{\text{max}}) - f^{(1)}(u,w_{\text{max}})]$$
(19)

where $A_1(u)$, $A_2(u)$, $B_1(w)$ and $B_2(w)$ are defined the set of univariate blending functions, which only have to satisfy the conditions:

$$\begin{split} A_1(1) &= 1, \quad A_1(u_{max}) = 0, \quad A_2(1) = 0, \quad A_2(u_{max}) = 1 \\ B_1(1) &= 1, \quad B_1(u_{max}) = 0, \quad B_2(1) = 0, \quad B_2(u_{max}) = 1 \end{split}$$

Further, the general form in algebraic equations can be defined as:

$$\begin{split} A_1(u) &= \frac{u_{\text{max}} - u}{u_{\text{max}} - 1}, \quad A_2(u) = 1 - A_1(u), \\ B_1(w) &= \frac{w_{\text{max}} - w}{w_{\text{max}} - 1}, \quad B_2(w) = 1 - B_1(w) \end{split} \tag{20}$$

The grid motion defined from a moving boundary motion is modeled using a Stefan equation (Eq. (18)) with a transfinite mapping method. Furthermore, the boundary fitted grid generation mapping discussed in this section forms the basis for the interface tracking mapping. However, the mapping must now match the interface curve on the interior of physical domain in addition to fitting the outer physical boundary. In addition, the system must be adaptive since the grid lines must change to follow the deforming interface while maintaining as much smoothness and orthogonality as possible.

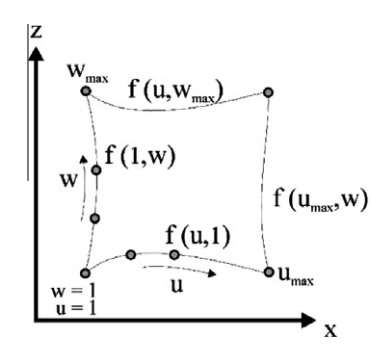


Fig. 3. The parametric domain with f(u, w) specified on planes of constant u, w.

2048

4.2. PDE mapping

In the proposed grid generation mapping, all grids discussed and displayed have been couched in terms of finite difference algorithm applications, with the understanding that whatever non-uniform grid exists in the physical space, there is exist a transformation which will recast it as a uniform rectangular grid in the computational space. The finite difference calculations are then made over this uniform grid in the computational space, after which the field results are transferred directly back to the corresponding points in the physical space. The purpose of generating a smooth grid that conforms to physical boundaries of problem is, of course, to solve the partial differential equations specified in the problem by finite difference scheme, capable of handling general non-orthogonal curvilinear coordinates.

Corresponding to Fig. 2(b), as melting proceeds, a melting front denoted here $z_{\rm mov}$ is formed. Due to the existence of this melting front, the frozen and unfrozen domains are irregular and time dependent. To avoid this difficulty, a curvilinear system of coordinates is used to transform the physical domain into rectangular region for the computational domain.

It is convenient to introduce a general curvilinear coordinate system as follows Anderson [27]:

$$x = x(\xi, \eta), \quad z = z(\xi, \eta) \text{ or } \xi = \xi(x, z), \quad \eta = \eta(x, z)$$
 (21)

The moving boundaries are immobilized in the dimensionless (ξ , η) coordinate for all times. With the details omitted, then the transformation of electromagnetic field equation (Eqs. (1), (2), (3), and (7)) can be written respectively as [10]:

$$\frac{1}{I} \left(x_{\xi} \frac{\partial E_{y}}{\partial n} \right) = \mu \frac{\partial H_{x}}{\partial t} \tag{22}$$

$$-\frac{1}{J}\left(z_{\eta}\frac{\partial E_{y}}{\partial \xi}\right) - z_{\xi}\frac{\partial E_{y}}{\partial \eta} = -\mu\frac{\partial H_{z}}{\partial t}$$
(23)

$$-\frac{1}{j}\left\{\left(z_{\eta}\frac{\partial H_{z}}{\partial \xi}-z_{\xi}\frac{\partial H_{z}}{\partial \eta}\right)-\left(x_{\xi}\frac{\partial H_{x}}{\partial \eta}\right)\right\}=\sigma E_{y}+\varepsilon\frac{\partial E_{y}}{\partial t}$$
(24)

$$\frac{\partial E_{y}}{\partial t} = \upsilon \frac{1}{I} \left(x_{\xi} \frac{\partial E_{y}}{\partial \eta} \right) \tag{25}$$

Also the heat transport equations (Eqs. (14) and (15)), and Stefan condition (Eq. (18)) can be transformed into (ξ, η) coordinate as below:

$$\frac{\partial T_{l}}{\partial t} = \frac{a_{l}}{J^{2}} \left(\alpha \frac{\partial^{2} T_{l}}{\partial \xi^{2}} - 2\beta \frac{\partial^{2} T_{l}}{\partial \xi \partial \eta} + \gamma \frac{\partial^{2} T_{l}}{\partial \eta^{2}} \right)
+ \frac{a_{l}}{J^{3}} \left[\left(\alpha \frac{\partial^{2} x}{\partial \xi^{2}} \right) \left(z_{\xi} \frac{\partial T_{l}}{\partial \eta} - z_{\eta} \frac{\partial T_{l}}{\partial \xi} \right)
+ \left(\alpha \frac{\partial^{2} z}{\partial \xi^{2}} - 2\beta \frac{\partial^{2} z}{\partial \xi \partial \eta} + \gamma \frac{\partial^{2} z}{\partial \eta^{2}} \right) \left(-x_{\xi} \frac{\partial T_{l}}{\partial \eta} \right) \right]
+ \frac{Q}{\rho \cdot C_{p}} + \frac{1}{J} \left(x_{\xi} \frac{\partial T_{l}}{\partial \eta} \right) \frac{dz}{dt}$$
(26)

$$\frac{\partial T_{s}}{\partial t} = \frac{a_{s}}{J^{2}} \left(\alpha \frac{\partial^{2} T_{s}}{\partial \xi^{2}} - 2\beta \frac{\partial^{2} T_{s}}{\partial \xi \partial \eta} + \gamma \frac{\partial^{2} T_{s}}{\partial \eta^{2}} \right) \\
+ \frac{a_{s}}{J^{3}} \left[\left(\alpha \frac{\partial^{2} x}{\partial \xi^{2}} \right) \left(z_{\xi} \frac{\partial T_{s}}{\partial \eta} - z_{\eta} \frac{\partial z}{\partial \xi} \right) \right. \\
+ \left(\alpha \frac{\partial^{2} z}{\partial \xi^{2}} - 2\beta \frac{\partial^{2} z}{\partial \xi \partial \eta} + \gamma \frac{\partial^{2} z}{\partial \eta^{2}} \right) \left(-x_{\xi} \frac{\partial T_{s}}{\partial \eta} \right) \right] \\
+ \frac{Q}{\rho \cdot C_{p}} + \frac{1}{J} \left(x_{\xi} \frac{\partial T_{s}}{\partial \eta} \right) \frac{dz}{dt} \tag{27}$$

$$\left\{ \lambda_{s} \frac{1}{J} \left(x_{\xi} \frac{\partial T_{s}}{\partial \eta} \right) - \lambda_{l} \frac{1}{J} \left(x_{\xi} \frac{\partial T_{l}}{\partial \eta} \right) \right\} \left\{ 1 + \left(\frac{1}{J} \left[z_{\eta} \frac{\partial z_{\text{mov}}}{\partial \xi} - z_{\xi} \frac{\partial z_{\text{mov}}}{\partial \eta} \right] \right)^{2} \right\} \\
= \rho_{s} L_{s} \frac{\partial z_{\text{mov}}}{\partial t}$$

where $J = x_{\xi} \cdot z_{\eta} - x_{\eta} \cdot z_{\xi}$, $\alpha = x_{\eta}^2 + z_{\eta}^2$, $\beta = x_{\xi} \cdot x_{\eta} + z_{\xi} \cdot z_{\eta}$, $\gamma = x_{\xi}^2 + z_{\xi}^2$ and, x_{ξ} , x_{η} , z_{ξ} and z_{η} denote partial derivatives, J is the Jacobian, β , α , γ are the geometric factors and η , ξ are the transformed coordinates [27].

5. Solution method

It is known that the inherent difficulties in the conventional numerical methods (pure parabolic grid generators) for melting or freezing problems suggest the use of combined transfinite interpolation and PDE methods in most instances. Although conventional numerical methods can be used to obtain satisfactory results, there are problems of large time consumption and control functions that are often difficult to determine. Therefore, the new method presented in this paper is generally preferable because it offers the highest overall accuracies and smooth grid point distribution. In addition, the boundary point discontinuities are smoothed out in the interior domain and orthogonality at boundaries can be maintained.

During the solving of a moving boundary problem including phase change in microwave melting process, complications arise due to the motion of melting front with elapsed time. In this study, the description of heat transport equations (Eqs. (14) and (15)) requires specification of the temperature T in sample layers and moving front boundary is solved. Theses equations are coupled to the Maxwell's equations (Eqs. (1)–(3)) by Eq. (16). The latter equation represents the heating effect of microwaves in both the unfrozen and frozen layer. Therefore, the numerical schemes of the microwave melting process are performed.

5.1. Electromagnetic field discretization

Generally, simulation of microwave power dissipation requires the solution of the set of three coupled scalar partial differential equations governing electromagnetic propagation, i.e., Maxwell's equation, inside a rectangular waveguide. The finite difference time-domain (FDTD) method has been used to provide a full description of electromagnetic scattering and absorption and give detailed spatial and temporal information of wave propagation.

In this study, the leapfrog scheme is applied to a set of Maxwell's equations. The electric field vector components are offset one half-cell in the direction of their corresponding components, while the magnetic field vector components are offset one half-cell in each direction orthogonal to their corresponding components [28]. The electric and magnetic fields are evaluated at alternative half time steps. For TE₁₀ mode, the electric and magnetic field components are expressed by the total field FDTD equations as

$$\begin{split} E_y^n(k,i) &= \frac{1 - \frac{\sigma(k,i)\Delta t}{2\varepsilon(k,i)}}{1 + \frac{\sigma(k,i)\Delta t}{2\varepsilon(k,i)}} E_y^{n-1}(k,i) \\ &+ \frac{1}{1 + \frac{\sigma(k,i)\Delta t}{2\varepsilon(k,i)}} \times \frac{\Delta t}{\varepsilon(k,i)J(k,i)} \left\{ \frac{z(k,i+1) - z(k,i-1)}{2\Delta \xi} \right. \\ &\times \frac{\left(H_z^{n-1/2}(k,i+1/2) - H_z^{n-1/2}(k,i-1/2)\right)}{\Delta \eta} \\ &- \frac{z(k+1,i) - z(k-1,i)}{2\Delta \eta} \\ &\times \frac{\left(H_z^{n-1/2}(k+1/2,i) - H_z^{n-1/2}(k+1/2,i)\right)}{\Delta \gamma} \end{split}$$

K. Chaiyo, P. Rattanadecho/International Journal of Heat and Mass Transfer 54 (2011) 2043-2055

$$+\frac{x(k,t+1)-x(k,t-1)}{2\Delta\xi} \times \frac{\left(H_x^{n-1/2}(k+1/2,i)-H_z^{n-1/2}(k-1/2,i)\right)}{\Delta\eta} \times \frac{\left(H_x^{n-1/2}(k+1/2,i)-H_z^{n-1/2}(k-1/2,i)\right)}{\Delta\eta}$$

$$+\frac{\Delta t}{\mu(k+1/2,i)J(k+1/2,i)}$$
(29)

$$\times \left\{ \frac{x(k+1/2,i)J(k+1/2,i)}{2\Delta\xi} \times \frac{E_{y}^{n}(k+1,i) - E_{y}^{n}(k,i)}{\Delta\eta} \right\}$$

$$(30)$$

$$H_{z}^{n+1/2}(k,i+1/2) = H_{z}^{n-1/2}(k,i+1/2)$$

$$H_{z}^{n+1/2}(k,i+1/2) = H_{z}^{n-1/2}(k,i+1/2) - \frac{\Delta t}{\mu(k,i+1/2)J(k,i+1/2)} \left\{ \frac{z(k+1,i+1/2) - z(k-1,i+1/2)}{\Delta \eta} \times \frac{E_{y}^{n}(k,i+1) - E_{y}^{n}(k,i)}{\Delta \xi} - \frac{z(k,i+3/2) - z(k,i-1/2)}{\Delta \xi} \times \frac{E_{y}^{n}(k+1,i) - E_{y}^{n}(k,i)}{\Delta \eta} \right\}$$
(31)

5.2. Heat transport discretization

The transient heat equation (Eqs. (14) and (15)) and the Stefan condition (Eq. (18)) are solved by using finite difference method. A system of nonlinear equations results whereby each equation for the internal nodes can be cast into a numerical discretization, as shown below;

In transient heat equation for unfrozen layer,

$$\begin{split} T_{l}^{n+1}(k,i) &= \frac{1}{1 + \frac{2a_{l}\Delta t}{J^{2}(k,i)}} \left(\frac{\alpha(k,i)}{\Delta\xi\Delta\xi} + \frac{\gamma(k,i)}{\Delta\eta\Delta\eta}\right) \\ &\times \left\{ T_{l}^{n}(k,i) + \frac{a_{l}\Delta t}{J^{2}(k,i)} \left[\alpha(k,i) \frac{T_{l}^{n-1}(k,i+1) + T_{l}^{n+1}(k,i-1)}{\Delta\xi\Delta\xi} \right. \right. \\ &- 2\beta(k,i) \left(\frac{T_{l}^{n-1}(k+1,i+1) - T_{l}^{n+1}(k-1,i+1)}{2\Delta\eta} \right. \\ &- \frac{T_{l}^{n-1}(k+1,i-1) - T_{l}^{n+1}(k-1,i-1)}{2\Delta\xi} \right) \bigg/ \\ &2\Delta\xi + \gamma(k,i) \frac{T_{l}^{n-1}(k+1,i) + T_{l}^{n+1}(k-1,i)}{\Delta\eta\Delta\eta} \right] \\ &+ \frac{a_{l}\Delta t}{J^{3}(k,i)} \left[\alpha(k,i) \frac{X(k,i+1) - 2X(k,i) + X(k,i-1)}{\Delta\xi\Delta\xi} \right. \\ &\times \left(\frac{Z(k,i+1) - Z(k,i-1)}{2\Delta\xi} \times \frac{T_{l}^{n-1}(k+1,i) - T_{l}^{n+1}(k-1,i)}{2\Delta\eta} \right. \\ &- \frac{Z(k+1,i) - Z(k-1,i)}{2\Delta\eta} \times \frac{T_{l}^{n-1}(k,i+1) - T_{l}^{n+1}(k,i-1)}{2\Delta\xi} \right) \\ &+ \left(\alpha(k,i) \frac{Z(k,i+1) - 2Z(k,i) + Z(k,i-1)}{\Delta\xi\Delta\xi} \right. \\ &- 2\beta(k,i) \left(\frac{Z(k+1,i+1) - Z(k-1,i+1)}{2\Delta\eta} \right) \bigg/ \\ &2\Delta\xi + \gamma(k,i) \left(\frac{Z(k+1,i-1) - Z(k-1,i-1)}{\Delta\eta\Delta\eta} \right) \\ &\times \left(- \frac{X(k,i+1) - X(k,i-1)}{2\Delta\xi} \right) \end{split}$$

$$\times \left(\frac{T_{l}^{n}(k+1,i) - T_{l}^{n}(k-1,i)}{2\Delta\eta}\right) + \frac{Q\Delta t}{\rho C_{p}}$$

$$+ \frac{1}{J(k,i)} \left(\frac{X(k,i+1) - X(k,i-1)}{2\Delta\xi}\right)$$

$$\times \left(\frac{T_{l}^{n}(k+1,i) - T_{l}^{n}(k-1,i)}{2\Delta\eta}\right) \times \Delta z$$
(32)

In transient heat equation for frozen layer,

$$\begin{split} T_s^{n+1}(k,i) &= \frac{1}{1 + \frac{2a_1\Delta t}{f^2(k,i)}} \left(\frac{x(k,i)}{\Delta t} + \frac{y(k,i)}{\Delta t} \right) \\ &\times \left\{ T_s^n(k,i) + \frac{a_l\Delta t}{f^2(k,i)} \left[\alpha(k,i) \frac{T_s^{n-1}(k,i+1) + T_s^{n+1}(k,i-1)}{\Delta \xi \Delta \xi} \right. \right. \\ &- 2\beta(k,i) \left(\frac{T_s^{n-1}(k+1,i+1) - T_s^{n+1}(k-1,i+1)}{2\Delta \eta} \right. \\ &- \frac{T_s^{n-1}(k+1,i-1) - T_s^{n+1}(k-1,i-1)}{2\Delta \xi} \right) \right/ \\ &2 \Delta \xi + \gamma(k,i) \frac{T_s^{n-1}(k+1,i) + T_s^{n+1}(k-1,i)}{\Delta \eta \Delta \eta} \right] \\ &+ \frac{a_l\Delta t}{J^3(k,i)} \left[\alpha(k,i) \frac{X(k,i+1) - 2X(k,i) + X(k,i-1)}{\Delta \xi \Delta \xi} \right. \\ &\times \left(\frac{Z(k,i+1) - Z(k,i-1)}{2\Delta \xi} \times \frac{T_s^{n-1}(k+1,i) - T_s^{n+1}(k-1,i)}{2\Delta \eta} \right. \\ &- \frac{Z(k+1,i) - Z(k-1,i)}{2\Delta \eta} \times \frac{T_s^{n-1}(k,i+1) - T_s^{n+1}(k,i-1)}{2\Delta \xi} \right) \\ &+ \left(\alpha(k,i) \frac{Z(k,i+1) + 2Z(k,i) - Z(k,i-1)}{\Delta \xi \Delta \xi} \right. \\ &- 2\beta(k,i) \left(\frac{Z(k+1,i+1) - Z(k-1,i-1)}{2\Delta \eta} \right) / 2\Delta \xi \\ &+ \gamma(k,i) \frac{Z(k+1,i-1) - Z(k-1,i-1)}{2\Delta \eta} \right) \\ &\times \left(-\frac{X(k,i+1) - X(k,i-1)}{2\Delta \eta} \right) \\ &\times \left(-\frac{X(k,i+1) - X(k,i-1)}{2\Delta \eta} \right) \\ &+ \left(\frac{T_s(k+1,i) - T_s^n(k-1,i)}{2\Delta \eta} \right) \right] + \frac{Q\Delta t}{\rho C_p} \\ &+ \frac{1}{J(k,i)} \left(\frac{X(k,i+1) - X(k,i-1)}{2\Delta \xi} \right) \\ &\times \left(\frac{T_s^n(k+1,i) - T_l^n(k-1,i)}{2\Delta \xi} \right) \times \left(\frac{T_s^n(k+1,i) - T_l^n(k-1,i)}{2\Delta \eta} \right) \times \Delta Z \right\} \end{aligned}$$

In Stefan condition,

In Stefan condition,
$$Z^{n+1}(k,i) = Z^{n}(k,i) + \frac{\Delta T}{\rho_{s}L_{s}} \left\{ \left[\frac{\lambda_{s}}{J(k+1,i)} \right] \times \left(\frac{X(k+1,i+1) - X(k+1,i-1)}{2\Delta \xi} \right) \times \left(\frac{-3T_{s}(k,i) + 4T_{s}(k+1,i) - T_{s}(k+2,i)}{2\Delta \eta} \right) - \frac{\lambda_{l}}{J(k-1,i)} \times \left(\frac{X(k-1,i+1) - X(k-1,i-1)}{2\Delta \xi} \right) \times \left(\frac{3T_{l}(k,i) - 4T_{l}(k-1,i) + T_{l}(k-2,i)}{2\Delta \eta} \right) \right] \times \left[1 + \left(\frac{Z^{n}(k+1,i) - Z^{n}(k-1,i)}{2\Delta \xi} \times \frac{Z^{n}(k+1,i) - Z^{n}(k-1,i)}{2\Delta \xi} \right)^{2} \right] \right\}$$
(34)

The details of computational schemes and strategy for solving the combined transfinite interpolation functions (Eqs. (19) and (20)) and PDE mapping (Eqs. (29)–(34)) are illustrated in Fig. 4.

5.3. The stability and accuracy of calculation

Due to dielectric properties of the most liquids are depending on temperature so it is necessary to consider the coupling model

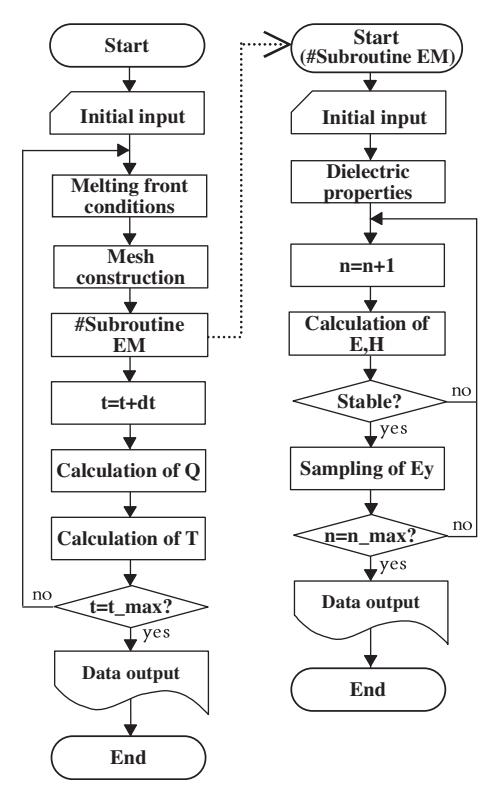


Fig. 4. The computational scheme.

for analysing the E field and the temperature distribution. For this reason, the iteration scheme (reference from Ratanadecho et al. [10]) is used to resolve the non-linear coupling of Maxwell's equations, and energy equations. Spatial and temporal resolution is selected to ensure of stability and accuracy. To insure stability of the time-stepping algorithm Δt is chosen to satisfy the courant stability condition [25]:

$$\Delta t \leqslant \frac{\sqrt{\left(\Delta x\right)^2 + \left(\Delta z\right)^2}}{D} \tag{35}$$

And the spatial resolution of each cell defines as:

$$\Delta x, \Delta z \leqslant \frac{\lambda_g}{10\sqrt{\varepsilon_r}} \tag{36}$$

where v is the velocity of an electromagnetic wave. Corresponding to Eqs. (35) and (36), the calculations are as follows:

- (1) Initial grid size: $\Delta x = 1.0922$ mm and $\Delta z = 1.0000$ mm.
- (2) Time steps: $\Delta t = 2 \times 10^{-12}$ s and $\Delta t = 1.0$ s are used corresponding to electromagnetic field, and temperature field calculations and location of melting front, respectively.
- (3) Relative error in the iteration procedures of 10^{-6} is chosen.

6. Results and discussion

The present work is to couple the grid generation algorithm with electromagnetic field and heat transport equations. The thermal analysis during melting process will be discussed in next subsection.

6.1. Physical description

The sample is composed of an unfrozen layer (water and glass bead) and a frozen layer (ice and glass bead). The unfrozen layer and the frozen layer are arranged in different configurations, as shown in state (a) and state (b) of Fig. 1(b), respectively. It is considered to illustrate microwave melting phenomena by using a rectangular waveguide incase of with and without resonator. In

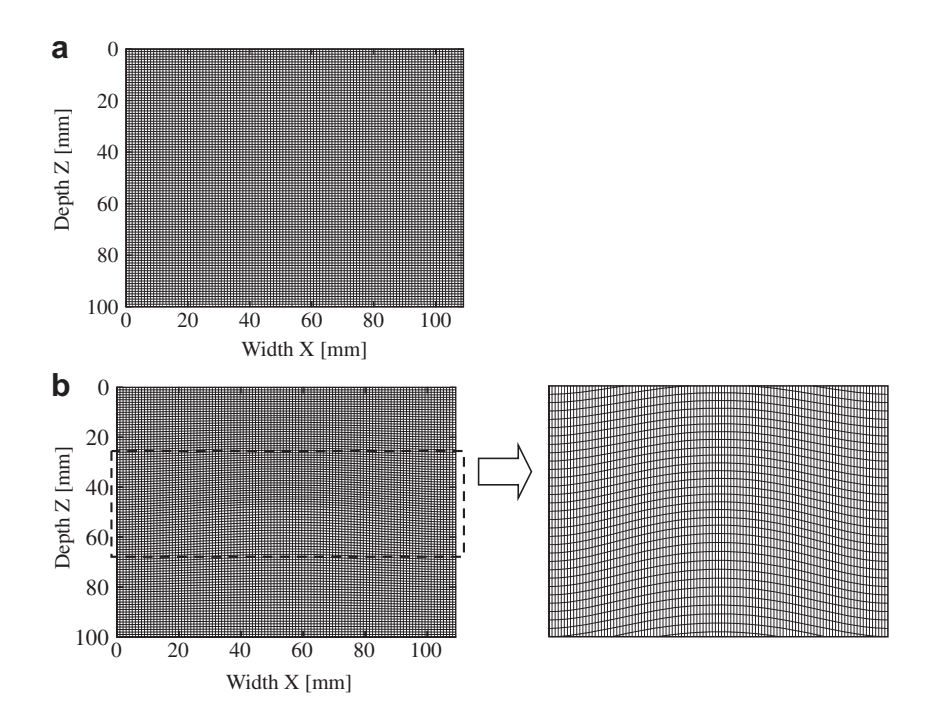


Fig. 5. Grid simulating the deformation of an interface: (a) the initial reference grid for the domain (generated by pure transfinite interpolation method) and (b) melting time of 60 s.

case of without a resonator, all transmitted waves through the sample are absorbed by fixed water load at end of the waveguide (lower boundary condition). Unlike for the case with resonator that perfectly conducting plate is installed at the end of waveguide to enhance resonance of standing wave inside a rectangular waveguide as well as the sample.

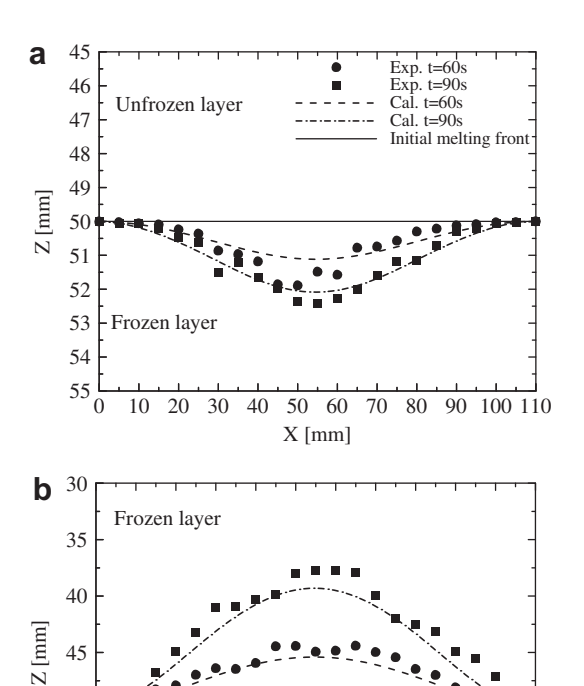


Fig. 6. The measured and predicted interface position: (a) melting front for state (a) and (b) melting front for state (b).

50 60

X [mm]

55

0

Unfrozen layer

20

10

30 40

Exp. t=60s Exp. t=90s Cal. t=60s

Cal. t=90s Initial melting front

90 100 110

70 80

6.2. A melting front tracking grid generation system

The efficiency of the grid generation system is illustrated during the melting of ice-saturated porous medium (porosity, ϕ = 0.38) subjected to electromagnetic energy. Fig. 5(a) shows the initial reference grid for the domain generated by pure transfinite interpolation method. Fig. 5(b) shows grid that fit curves that are typical of shapes seen during deformation of an interface with respect to elapsed time at t = 60 s. The calculated front locations correspond to the initial temperature of 0 °C and supplied microwave power level of 1000 W. It is found that the grid is able to maintain a significant amount of orthogonality and smoothness both within the interior and along the boundary as the grid points redistribute themselves to follow the interface. These results show the efficiency of the present method for the multi-dimensional moving boundary problem.

6.3. Numerical validation

Fig. 6(a) and (b) shows the present simulation results compared with experimental data of melting front within the layered sample without resonator in which state (a) and state (b), corresponding to the initial temperature of 0 °C for both a frozen layer and an unfrozen layer.

It is observed that the trends of results are in good agreement. However, at longer melting times (90 s) in case of state (b), the experimental data is significantly higher than that the simulation results. The source of the discrepancy is the non-uniform heating effect along the axis, which accounts for the fact that the incident microwave at the surface of a layered sample is non-uniform. Numerically, the discrepancy may be attributed to uncertainties in the thermal and dielectric property database, and the mechanism of natural convective heat transfer is not considered. On the other hand during the experiment of microwave melting process, the impact on the uncertainty of our data may cause by variations in humidity, room temperature and another effects. The uncertainty in melting kinetics was assumed to result from errors in the measured melting front of the sample.

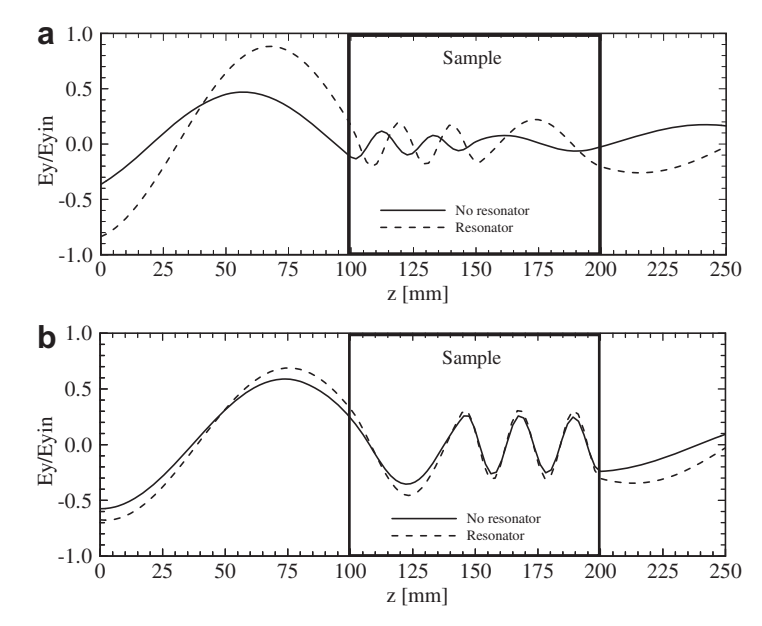


Fig. 7. Electric field distribution at t = 60 s: (a) state-a and (b) state-b.

6.4. Electric field distribution

Fig. 7(a) and (b) illustrates the electric field distribution along the center axis (x = 54.6 mm) of rectangular waveguide at t = 60 sfor different sample configuration as state (a) and state (b), in case of with and without resonator. In these figures, the vertical axis represents the intensity of the electric fields E_y , which is normalized to the amplitude of the input electric fields E_{vin} . A solid line represents the electric fields distribution inside a rectangular waveguide for the cases without resonator; all transmitted waves through the sample are absorbed by water load at the end of the waveguide. Since the sample is composed of the unfrozen layer and frozen layer. In addition, the unfrozen layer is a highly absorptive material (higher dielectric loss factor) while the frozen layer is a highly transparent material (low dielectric loss factor), where a larger part of microwave is able to transmit through this layer. For the case of state (a), the unfrozen layer considered as high lossy material has a short wavelength, which correspond to higher microwave power absorbed. It is observed from the figures that the resonance of standing wave configuration inside the sample is weak as compared to left-hand side of the sample. The some part of microwave is transmitted through the sample and then absorbed by water load at the end of the waveguide. Focusing attention of electric field distribution inside the cavity (left-hand side), a stronger standing wave with large amplitude is formed by interference between the incident and reflected waves from the surface of the sample due to the different dielectric properties of materials (air and sample) at this interface. It is evident from the results that the electric field within the sample attenuates owing to the microwave power absorbed, and thereafter the microwave power absorbed is converted to the thermal energy. In case of state (b), it is similar to state (a) that a larger part of microwaves is absorbed by the unfrozen layer. In addition, a stronger standing wave with large amplitude is formed inside the cavity (left-hand side) by interference between the incident and reflected waves from surface of the sample. Note that the amplitude of electric field inside cavity (left-hand side) of state (b) is lower than state (a) because the upper surface of the frozen layer in state (b) (exposed to incident microwaves) is a highly transparent and it protects the reflected wave from this surface.

For the cases with installed a resonator in the waveguide on both state (a) and state (b), the electric fields with small amplitude are formed within the sample, while the stronger standing wave outside the sample (left-hand side) with a lager amplitude is formed by among the forward wave, the reflected wave from the sample and the resonator. However, due to the reflections occurring at air-resonator interface, the standing wave can be also formed at the right-hand side of the sample as seen in the figure. It is interesting to observe that the electric field intensity in case of with resonator is greater than in case of without resonator for both different sample configurations as state (a) and state (b). In addition, the electric field within the sample attenuates owing to microwave power absorbed, and thereafter the microwave power absorbed is converted to thermal energy (similar to case without resonator).

6.5. Melting process without resonator

This section is presented to examine the melting characteristics of the layered sample for state (a) and state (b) configuration, respectively.

6.5.1. The temperature and microwave power absorbed distribution Fig. 8(a) shows temperature distribution of state (a). It is observed that the skin-depth heating effect causes a major part of incident waves to be absorbed within the sample, especially at

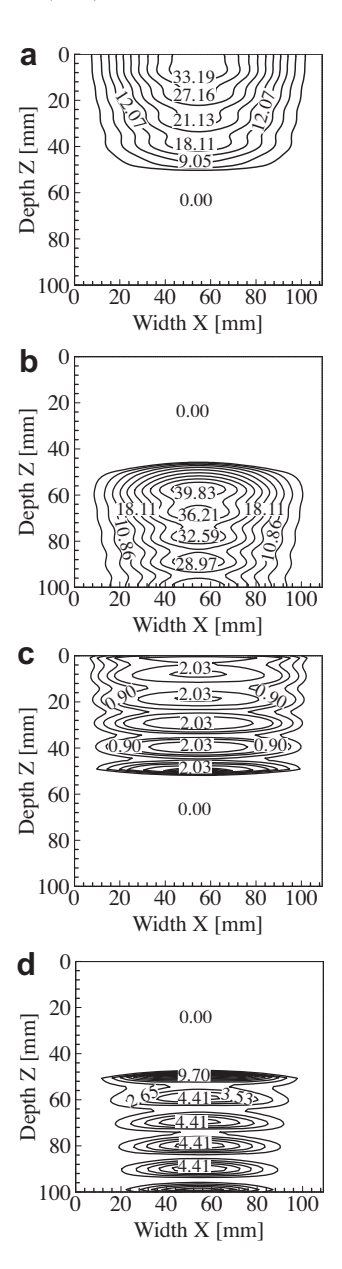


Fig. 8. Temperature and microwave power absorbed distribution at t = 60 s (without resonator): (a) temperature of state-a, (b) temperature of state-b, (c) microwave power absorbed of state-a and (d) microwave power absorbed of state-b,

the leading edge of an unfrozen layer. The temperature distribution corresponds to the electric distribution in the sample. This is because the electric field within the sample attenuates owing to microwave power absorbed, and thereafter the microwave power absorbed is converted to thermal energy where the maximum temperature occurs at leading edge of unfrozen layer. It is observed that temperature distribution within the unfrozen layer display a wavy behavior while it has no temperature gradient in the frozen layer due to this layer acts as the transparent material (very low lossy material). In addition, corresponding to the microwave power absorbed as displayed in Fig. 8(c), the temperature distribution within the unfrozen layer decays slowly along the wave propagation direction.

Fig. 8(b) and (d) illustrates the results of state (b). The incident microwave is easily further penetrated to the unfrozen layer, which forms a highly absorptive material. Since an ice in the frozen

layer is a highly transparent material to microwave where it protects the reflective wave from the expose surface. The latter arises from the fact that the larger part of microwaves can be absorbed at the leading edge of the unfrozen layer. The presence of the strength of microwave power absorbed gives to rise a hot spot at the leading edge of the unfrozen layer. This causes heat to conduct from the hotter region in unfrozen layer (higher microwave power absorbed) to the cooler region (lower microwave power absorbed) in the frozen layer. It is found that the upward movement of melting front occurs at the interface between frozen layer and unfrozen layer where the strength of the microwave power absorbed increases with increasing the melting rate. As melting proceed, the melting rate is higher in comparison to previous case (state (a)) at the same time. Nevertheless, the frozen layer stays colder due to the difference between the dielectric properties of water and ice. This is because water is a highly absorptive material, while ice is highly transparent which results in a lower microwave power

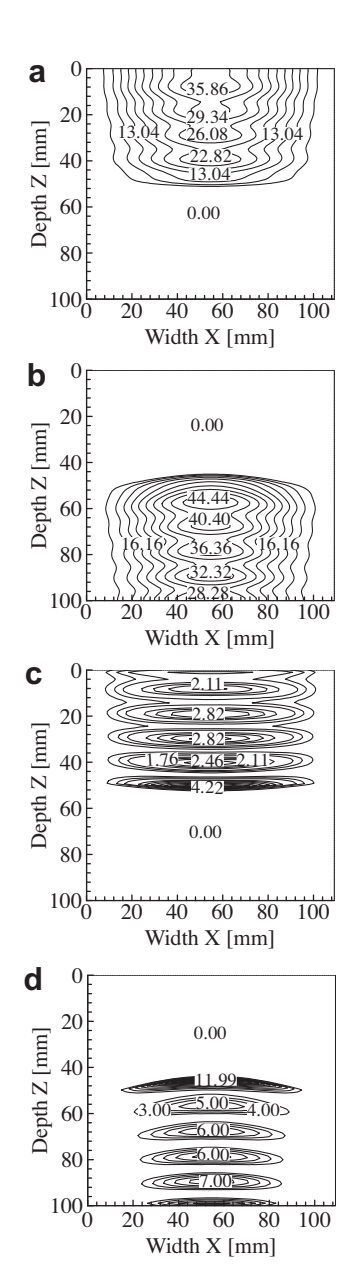


Fig. 9. Temperature and microwave power absorbed distribution at t = 60 s (with resonator): (a) temperature of state-a, (b) temperature of state-b, (c) microwave power absorbed of state-a and (d) microwave power absorbed of state-b.

absorbed within this layer. At exposure time of about 60 s, there is a difference of about 39.83 $^{\circ}\text{C}$ between the maximum and minimum temperatures.

6.5.2. Melting front

Considerately, Fig. 6 shows the melting front for the case of state (a) and state (b). For state (a), melting front moves slowly with the elapsed time along the propagation direction because the most of heat as well as microwave power absorbed take place at leading edge of unfrozen layer, which located far away from frozen layer. Consequently, a small amount of heat can conduct to the frozen layer because the water layer downstream acts as an insulator causing a slow movement of melting front. In state (b), in contrast to that state (a), the melting front moves rapidly with the elapsed time against the wave propagating direction. This is because the most of the heat directly conduct into the frozen layer due to the fact that the hot spot takes place at the leading edge of the unfrozen layer which located close to the frozen layer.

6.6. Melting process with resonator

Fig. 9 illustrates the temperature and microwave power absorbed distribution in case of with installed resonator at the end of waveguide. The temperature distribution corresponds to the electric distribution in the sample. This is because the electric field within the sample attenuates owing to microwave power absorbed, and thereafter the microwave power absorbed is converted to thermal energy as explained in previous subsection. It is observed that temperature distribution within the unfrozen layer display a stronger wavy behavior similarly case of without resonator. Since the microwaves can either transmit through sample or reflect from resonator, a standing wave or resonance is formed within the

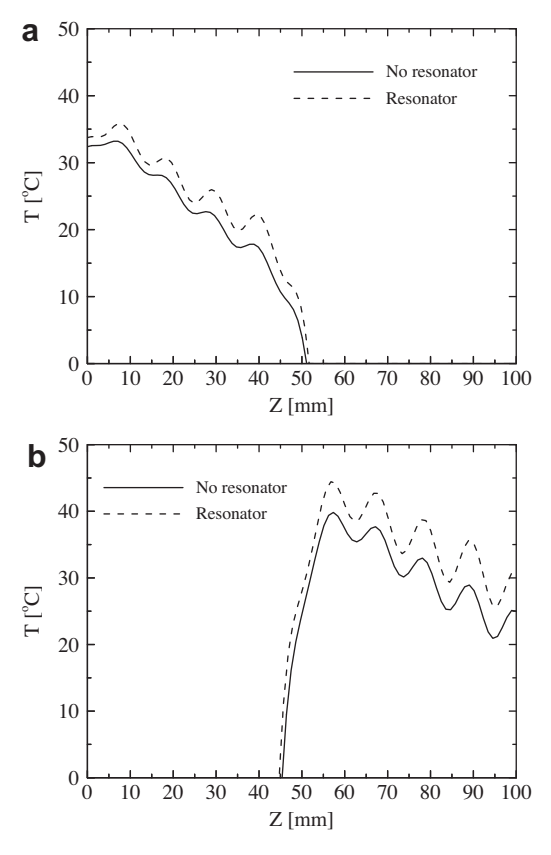
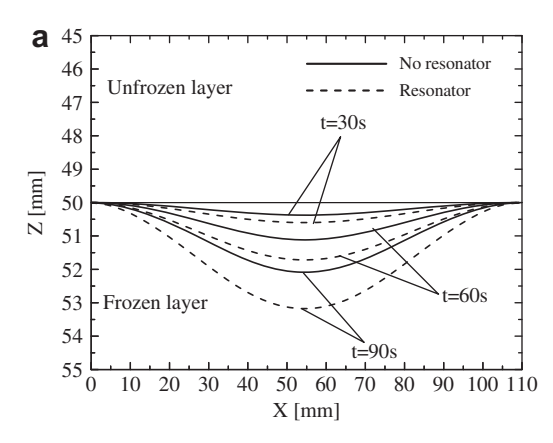


Fig. 10. Temperature profile along z-axis within the sample at t = 60 s: (a) state-a and (b) state-b.



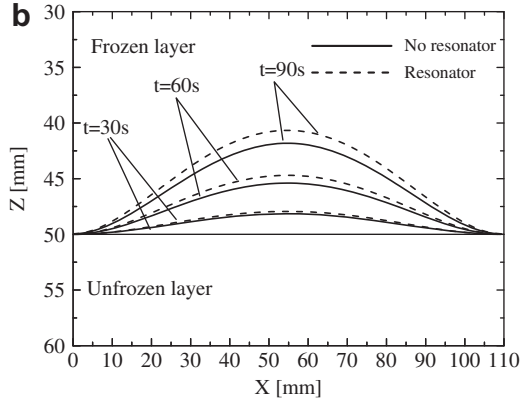


Fig. 11. Melting front at various elapsed times: (a) state-a and (b) state-b.

sample. Therefore, the microwave power absorbed as well as heat transfer rate in the sample is stronger greater than that case of without resonator. At exposure time of about 60 s, there is a difference between the maximum and minimum temperatures of about 35.86 °C and 44.44 °C, for state (a) and state (b), respectively.

Furthermore, it is interesting that the temperature profiles along the center axis (x = 54.6 mm) is greater than that case of without resonator as shown in Fig. 10. These results combined that the installation of resonator can lead to enhance a stronger standing wave or resonance.

Fig. 11 shows the results of melting front in state (a) and state (b), respectively. For the case of installed resonator, the temperature and the microwave power absorbed are always higher when compared with case of without resonator. Thus, the melting front rapidly moves with elapsed times in comparison to case of no-resonator condition. Additionally, it is interesting that melting rate of state (a) is greater than state (b) because of the difference in standing wave pattern and microwave power absorbed within sample.

This study shows the capability of the present method to correctly handle the phase change problem. With further quantitative validation of the present method, this method can be used as a tool for investigating in detail this particular melting of phase change in a porous media at a fundamental level.

7. Conclusions

Mesh quality has the largest impact on solution quality. A high-quality mesh increases the accuracy of the computational thermal flow solution and improves convergence. Therefore, it is important to provide tools for obtaining and improving a mesh. This paper present, melting of ice-saturated porous medium in a rectangular waveguide (with and without resonator) subjected to electromagnetic energy has been investigated numerically. A generalized

mathematical model and an effective calculation procedure are proposed. A preliminary case study indicates the successful implementation of the numerical procedure. A two-dimensional microwave melting model is then validated against available experimental results and subsequently used as a tool for efficient computational prototyping. Simulation results are in good agreement with available experimental results. The successful comparison with experiments should give confidence in the proposed mathematical treatment, and encourage the acceptance of this method as useful tool for exploring practical problems. Furthermore, for microwave melting, in case of installed resonator strongly affects on of temperature and microwave power absorbed distribution, and melting front rate, because the microwave can transmit through the sample and then reflect from resonator back in the sample, forming a standing wave within the sample.

The next step, which has already begun, is to couple the grid generation algorithm with the complete transport equations that determine the moving boundary front and buoyancy-driven convection in the liquid. The influence of adjusted meshes number in each layer on thermal flow solution will be investigated. Moreover, some experimental studies will be performed to completely validate numerical results.

Acknowledgments

The authors gratefully acknowledge the Thailand Research Fund (TRF) for supporting this research project.

References

- [1] B.J. Pangrle, K.G. Ayappa, H.T. Davis, E.A. Davis, J. Gordon, Microwave thawing of cylinders, Am. Inst. Chem. Eng. 37 (1991) 1789–1800.
- [2] B.J. Pangrle, K.G. Ayappa, E. Sutanto, H.T. Davis, E.A. Davis, Microwave thawing of semi-infinite slabs, Chem. Eng. Commun. 112 (1991) 39.
- [3] P. Rattanadecho, Theoretical and experimental investigation of microwave thawing of frozen layer using a microwave oven (effects of layered configurations and layer thickness), Int. J. Heat Mass Transfer 47 (2004) 937-945
- [4] A.C. Cleland, R.L. Earl, Assessment of freezing time prediction methods, J. Food Sci. 49 (1984) 1034–1042.
- [5] P. Taoukis, E.A. Davis, H.T. Davis, J. Gordon, Y. Talmon, Mathematical modeling of microwave thawing by modified isotherm migration method, J. Food Sci. 52 (1994) 455–463.
- [6] X. Zeng, A. Faghri, Experimental and numerical study of microwave thawing heat transfer for food materials, ASME J. Heat Transfer 116 (1994) 446–455.
- [7] T. Basak, K.G. Ayappa, Analysis of microwave thawing of slab with the effective heat capacity method, Am. Inst. Chem. Eng. 43 (1997) 1662–1674.
- [8] P. Rattanadecho, The simulation of microwave heating of wood using a rectangular waveguide: influence of frequency and sample size, Chem. Eng. Sci. 61 (14) (2006) 4798–4811.
- [9] P. Rattanadecho, W. Klinbun, Theoretical analysis of microwave heating of dielectric materials filled in a rectangular waveguide with various resonator distances, ASME J. Heat Transfer 133 (2011), doi:10.1115/1.4002628.
- [10] P. Rattanadecho, K. Aoki, M. Akahori, The characteristics of microwave melting of frozen packed beds using a rectangular waveguide, IEEE Trans. Microwave Theory Tech. 50 (6) (2002).
- [11] K. Charn-Jung, M. Kaviany, Numerical method for phase-change problems with convection and diffusion, Int. J. Heat Mass Transfer 35 (1992) 457–467.
- [12] S. Chellaiah, R. Viskanta, Freezing of saturated and superheated liquid in porous media, Int. J. Heat Mass Transfer 31 (1988) 321–330.
- [13] A.B. Crowley, Numerical solution of Stefan problems, Int. J. Heat Mass Transfer 21 (1978) 215.
- [14] N. Shamsundar, E.M. Sparrow, Effect of density change on multi-dimensional conduction phase change, ASME J. Heat Transfer 105 (1976) 550.
- [15] J. Crank, R.S. Gupta, Isotherm migration method in two dimensions, Int. J. Heat Mass Transfer 18 (1975) 1101.
- [16] F.B. Cheung, T.C. Chawla, D.R. Pedersen, The effect of heat generation and wall interaction on freezing and melting in finite slab, Int. J. Heat Mass Transfer 27 (1984) 29.
- [17] A. Chatterjee, V. Prasad, A full three-dimensional adaptive finite volume scheme for transport and phase-change process, Part I: formulation and validation, Numer. Heat Transfer A: Appl. 37 (2000) 801–821.
- [18] Z.X. Gong, A.S. Mujumdar, Flow and heat transfer in convention-dominated melting in rectangular cavity heated from below, Int. J. Heat Mass Transfer 41 (1998) 2573–2580.
- [19] L.E. Eriksson, Generation of boundary-conforming grid around wing-body configurations using transfinite interpolation, AIAA J. 20 (1982) 1313–1320.

- [20] W.A. Cook, Body oriented coordinates for generating 3-dimentional meshes,
- Int. J. Numer. Methods Eng. (1974) 27–43.
 [21] W.J. Gordon, C.A. Hall, Construction of curvilinear coordinate systems and applications to mesh generation, Int. J. Numer. Methods Eng. 7 (1973) 461-
- [22] H.M. Ettouney, R.A. Brown, Finite-element methods for steady solidification
- problems, J. Comput. Phys. 49 (1983) 118–150. [23] P. Rattanadecho, Simulation of melting of ice in a porous media under multiple constant temperature heat sources using a combined transfinite interpolation and PDE methods, Chem. Eng. Sci. 61 (2006) 4571-4581.
- [24] P. Rattanadecho, S. Wongwises, Moving boundary-moving mesh analysis of freezing process in water-saturated porous media using a combined transfinite interpolation and PDE mapping methods, ASME J. Heat Transfer 31 (2007) 318–333.
- [25] P. Ratanadecho, K. Aoki, M. Akahori, A numerical and experimental investigation of the modeling of microwave heating for liquid layers using a rectangular waveguide (effects of natural convection and dielectric properties), Appl. Math. Model. 26 (3) (2002) 449–472.
- [26] G. Mur, Absorbing boundary conditions for the finite-difference approximation of the time-domain electromagnetic-field equations, IEEE Trans. Electromagn. Compat. EMC-23 (4) (1981) 377-382.
- [27] J.D. Anderson, Computational Fluid Dynamics, International Editions., McGraw-Hill, New York, 1995. Chapter 5.
 [28] K.S. Yee, Numerical solution of initial boundary value problems involving
- Maxwell's equation in isotropic media, IEEE Trans. Antennas Propag. AP-14 (1966) 302-307.

ORIGINAL PAPER

Experimental and Numerical Analysis of Microwave Heating of Water and Oil Using a Rectangular Wave Guide: Influence of Sample Sizes, Positions, and Microwave Power

W. Cha-um · P. Rattanadecho · W. Pakdee

Received: 20 August 2008 / Accepted: 20 January 2009 / Published online: 13 March 2009 © Springer Science + Business Media, LLC 2009

Abstract The heating process of water and oil using microwave oven with rectangular wave guide is investigated numerically and experimentally. The numerical model is validated with an experimental study. The transient Maxwell's equations are solved by using the finite difference time domain method to describe the electromagnetic field in the wave guide and sample. The temperature profiles and velocity field within sample are determined by the solution of the momentum, energy, and Maxwell's equations. In this study, the effects of physical parameters, e.g., microwave power, the position of sample in wave guide, size, and thickness of sample, are studied. The results of distribution of electric field, temperature profiles, and velocity field are presented in details. The results show that the mathematical models are in agreement with the experimental data. Conclusively, the mathematical model presented in this study correctly explains the phenomena of microwave heating within the liquid layer.

Keywords Microwave heating · Rectangular wave guide · Mode TE_{10} · Maxwell's equation · FDTD method

Nomenclature

specific heat capacity [J/(kg K)] $C_{\mathfrak{p}}$ electric field intensity (V/m) Е frequency of incident wave (Hz) gravitational constant (m/s²) g Н magnetic field intensity (A/m) power (W)

W. Cha-um · P. Rattanadecho (⋈) · W. Pakdee Research Center of Microwave Utilization in Engineering (RCME), Department of Mechanical Engineering, Faculty of Engineering, Thammasat University (Rangsit Campus), Pathumthani 12120, Thailand

e-mail: ratphadu@engr.tu.ac.th

pressure (Pa)

췶 Springer

local electromagnetic heat generation term (W/m³) Q Poynting vector (W/m²) S Ttemperature (°C) time (s) $tan \delta$ dielectric loss coefficient (-) u,wvelocity component (m/s) wave impedance (Ω) Z_H intrinsic impedance (Ω)

Greek letters

 Z_1

thermal diffusivity (m²/s)

coefficient of thermal expansion (1/K)

 η absolute viscosity (Pa s)

permittivity (F/m) ε

wavelength (m)

magnetic permeability (H/m) μ

velocity of propagation (m/s)

kinematics viscosity (m²/s)

density (kg/m³) ρ

electric conductivity (S/m)

angular frequency (rad/s)

surface tension (N/m)

Subscripts

ambient condition

a

layer number

input in

water

Introduction

Microwave is a one heat source that is an attractive alternative over conventional heating methods because an electromagnetic wave that penetrates the surface is converted into thermal energy within the material. High speed startup, selective energy absorption, instantaneous electric control, non-pollution, high energy efficiency, and high product quality are several advantages of microwave heating. Therefore, this technology is used in many industrial and household applications. The notable application is the domestic microwave oven. In addition, it has been used in food industry for drying, pasteurization, sterilization, etc. (Chatterjee et al. 2007). Other uses include vulcanization processing, curing of concrete, medical sterilization, and process adhesives.

Referred to international journals in the past about microwave heating process, the microwave power absorbed was assumed to decay exponentially into the sample following the Lambert's law. For example, Datta et al. (1992) predicted the volumetric heat source by using Lambert's law and analyzed the temperature profiles in liquid. However, this assumption is valid for the large dimension samples where the depth of sample is much larger than the penetration depth, but for the thin samples, where the depth of sample is much smaller than penetration depth, heat transfer rate by microwave is faster. Therefore, the spatial variations of the electromagnetic field within thin samples must be obtained by solution of the Maxwell's equations. The models of the interactions between electromagnetic field and dielectric materials have been used previously to study numerous heating processes of dielectric materials in a variety of microwave applicator, such as rectangular wave guide and cavities. Jia et al. (1992), Liu et al. (1994), and Dibben and Metaxas (1997) showed the numerical modeling of microwave heating process in cavity by solving Maxwell's equation, which determines the electromagnetic field in the microwave applicator and wave guide. Ayappa et al. (1994) studied the two-dimensional natural convection of liquid in a square cavity that exposed to traveling plane microwave numerically. They found that the location, intensity, and number of power peaks influence a uniformity of temperature in liquid. Basak and Ayappa (2002) purposed the modeling to study the role of length scales on microwave thawing process in 2D cylinders. From their investigation, thawing time increased monotonically with sample diameter, and temperature gradients in the sample generally increased from regimes I to III. Tada et al. (1997) used 2D finite difference time domain (2D-FDTD) method to investigate the electromagnetic field in microwave applicator filled partially with a dielectric material. This work demonstrated the effects of the position of dielectrics on energy absorption ratio. Zhang et al. (2000) purposed 3D-FDTD to explain the distribution of microwave inside the cavity by solving the Maxwell's equation and using the finite control volume (FCV) method based on SIMPLER algorithm to obtain temperature profiles

and flow field for distilled water and corn oil. Ratanadecho et al. (2002a,b) numerically and experimentally investigated microwave heating of a liquid layer in a rectangular wave guide. Their work showed both of the electric conductivity and microwave power level that affected the degree of penetration and rate of heat generation within liquid layer. Chatterjee et al. (2007) illustrated effect of turntable rotation, natural convection, power source, and aspect ratio of container on the temperature profiles in heating of containerized liquid using microwave radiation by using numerical simulation. Zhu et al. (2007) presented numerical model of heat transfer in liquids that flow continuously in a circular duct. The results showed that the heating pattern strongly depends on the dielectric properties of the fluid in the duct and the geometry of microwave heating system. Curet et al. (2008) studied a microwave heating process in frozen and defrosted zone considering both a numerical and experimental aspects. Either Maxwell's equation or Lambert's law were used to model the microwave heat generation. Huo et al. (2004) presented a 3D finite elementboundary integral formulation. Computed results were presented for the electric field distribution, power absorption, and temperature distribution in a food load thermally treated in an industrial pilot scale microwave oven designed for food sterilization. Rattanadecho (2006) presented the modeling of microwave heating of wood using a rectangular wave guide. The influence of irradiation times, working frequencies, and sample size were examined. The presented modeling is used to identify the fundamental parameters and provide guidance for microwave heating of wood. Ratanadecho et al. (2002a,b) studied the melting of frozen packed beds by a microwave with a rectangular wave guide numerically and experimentally. They focused on the prediction of temperature, as well as the microwave energy absorbed, and the melting front within the layered packed beds. Based on the combined model of the Maxwell and heat transport equations, the results showed that the direction of melting against the incident microwave strongly depended on the structural-layered packed beds. In addition, there are many papers in this field, such as Basak (2003–2004), Ratanadecho et al. (2002a,b), Rattanadecho and Suwannapum (2009), Vadivambal and Jayas (2009), and Boyacı et al. (2009).

Nevertheless, most of the studies have concentrated on solids and focused on conduction mode heat transfer in a specimen. A few papers have investigated natural convection induced by microwave heating of liquids in a rectangular wave guide with a full comparison between mathematical modeling and experimental data. This is because of the complex distribution of electromagnetic wave in cavity that is a complicated effect on flow field.

However, this paper presents distributions of electric field, temperature profiles, and flow pattern. This work is



extended from the previous work of Ratanadecho et al. (2002a,b). The goal of this work is to analyze microwave heating processes using a mathematical model. The effects of microwave power level (300, 500, 800, and 1,000 W) and the position in wave guide are investigated. The positions of the center of the liquid layer is at the centerline of the wave guide (S0) and also at 10 mm (S10) and 20 mm (S20) away from the centerline. Moreover, effects of liquid layer size (half and equal to wave guide width) and thickness (30, 40, and 50 mm) are studied.

Experiment Setup

The experimental apparatus is shown in Fig. 1. The microwave system is a monochromatic wave of TE₁₀ mode operating at a frequency of 2.45 GHz. Magnetron generates microwave and transmits along the z-direction of the rectangular wave guide, with inside dimensions of 109.2 (X) mm \times 54.61(Y) mm² toward a water load that is situated at the end of the wave guide. On the upstream side of the sample, an isolator is used to trap any microwave reflected from the sample to prevent the microwave from damaging the magnetron. The powers of incident and the reflected and transmitted waves are measured by a wattmeter using a directional coupler (Micro Denshi., model DR-5000). Fiberoptic (Luxtron Fluroptic Thermometer., model 790, accurate to ±0.5°C) is employed for temperature measurement. The fiberoptic probes are inserted into the sample and situated on the XZ plane at Y=25 mm. Due to the symmetrical condition, temperatures are measured for only one side of the plane. An initial temperature of sample is 28°C for all cases. A sample container with a thickness of 0.75 mm is made from polypropylene, which does not absorb microwaves.

Mathematical Model Formulation

Figure 2a and b shows the schematic diagram of the problem in case of full and partial load, respectively. The case of full load is the condition in which the liquid layer cross-sectional area is $109.2(X) \times 54.61(Y)$ mm² the same as that of the wave guide, while partial load corresponds to liquid layer with a half cross-sectional area of $54.61(X) \times 54.61(Y)$ mm². Inside the wave guide, the sample is contained in a container, whose walls are insulated except the top wall.

Analysis of Electromagnetic Field

Since the electromagnetic field that is investigated is the microwave field in the TE_{10} mode, there is no variation of



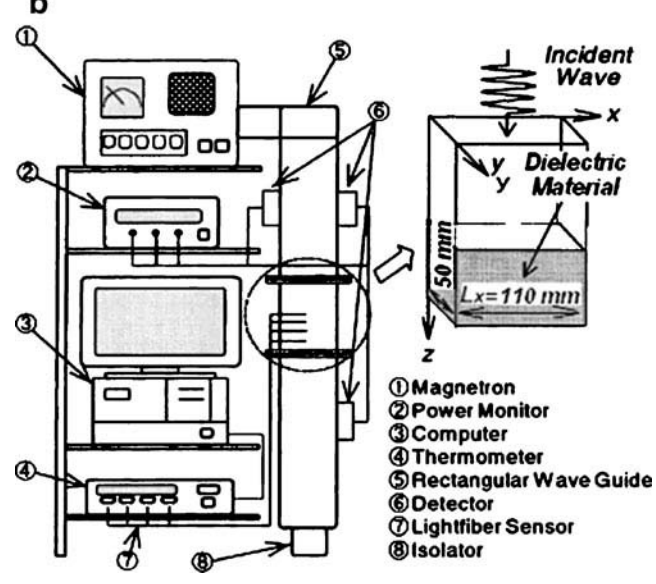


Fig. 1 Experimental apparatus of microwave heating: \mathbf{a} picture, \mathbf{b} diagram

field in the direction between the broad faces of the rectangular wave guide and is uniform in the y-direction. Consequently, it is assumed that the 2D heat transfer model in x and z-directions would be sufficient to identify the microwave heating phenomena in a rectangular wave guide



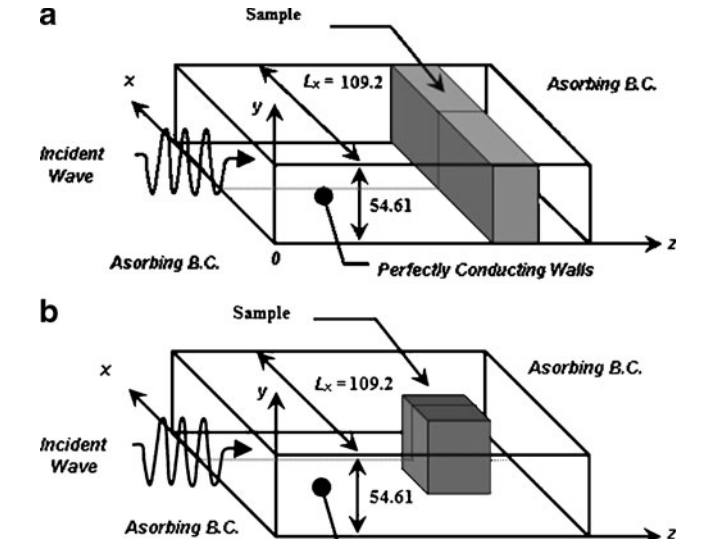


Fig. 2 Schematic diagram of the problem: a full load case, b partial load case

Perfectly Conducting Walls

(Rattanadecho et al. 2002). The other assumptions are as follows:

- 1. The absorption of microwave by air in a rectangular wave guide is negligible.
- The walls of rectangular wave guide are perfect conductors.
- 3. The effect of sample container on the electromagnetic and temperature field can be neglected.

The proposed model is considered in TE_{10} mode so that the Maxwell's equations can be written in terms of the electric and magnetic intensities

$$\varepsilon \frac{\partial E_y}{\partial t} = \frac{\partial H_x}{\partial z} - \frac{\partial H_z}{\partial x} - \sigma E_y \tag{1}$$

$$\mu \frac{\partial H_z}{\partial t} = -\frac{\partial E_y}{\partial x} \tag{2}$$

$$\mu \frac{\partial H_x}{\partial t} = \frac{\partial E_y}{\partial z} \tag{3}$$

where E and H denote electric and magnetic field intensities, respectively. Subscripts x, y, and z represent x, y, and z components of vectors, respectively. Furthermore, ε is the electrical permittivity, σ is the electrical conductivity, and μ is the magnetic permeability. These symbols are

$$\varepsilon = \varepsilon_0 \varepsilon_r \tag{4}$$

$$\mu = \mu_0 \mu_r \tag{5}$$

$$\sigma = 2\pi f \varepsilon \tan \delta \tag{6}$$

When the material is heated unilaterally, it is found that as the dielectric constant and loss tangent coefficient vary, the penetration depth and the electric field within the dielectric material vary. The penetration depth is used to denote the depth at which the power density has decreased to 37% of its initial value at the surface (Ratanadecho et al. 2002a,b).

$$D_{p} = \frac{1}{\sqrt[2\pi f]{\frac{\varepsilon_{r}'}{\sqrt{1 + \left(\frac{\varepsilon_{r}'}{\varepsilon_{r}'}\right)^{2} - 1}}}}$$

$$= \frac{1}{\sqrt[2\pi f]{\frac{\varepsilon_{r}'}{\sqrt[3]{\frac{\varepsilon_{r}'}{\sqrt{1 + (\tan \delta)^{2} - 1}}}}}$$
(7)

where $D_{\rm p}$ is penetration depth, ε''_r is relative dielectric loss factor and v is the microwave speed. The penetration depth of the microwave power is calculated according to Eq. 7, which shows how it depends on the dielectric properties of the material. It is noted that products with huge dimensions and high loss factors may occasionally overheat a considerably thick layer on the outer layer. To prevent such phenomenon, the power density must be chosen so that enough time is provided for the essential heat transfer between boundary and core. If the thickness of the material is less than the penetration depth, only a fraction of the supplied energy will become absorbed. In example, consider that the dielectric properties of water typically show moderate lousiness depending on the temperature. The water layer at low temperature typically shows slightly greater potential for absorbing microwaves. In other words, an increase in the temperature typically decreases ε''_r , accompanied by a slight increase in D_p .

The boundary conditions for TE_{10} mode can be formulated as follows:

 Perfectly conducting boundary. Boundary conditions on the inner wall surface of wave guide are given by Faraday's law and Gauss's theorem:

$$E_{\parallel} = 0, H_{\perp} = 0 \tag{8}$$

where subscripts \parallel and \perp denote the components of tangential and normal directions, respectively.

2. Continuity boundary condition. Boundary conditions along the interface between sample and air are given by Ampere's law and Gauss's theorem:

$$E_{||} = E'_{||}, H_{||} = H'_{||} \tag{9}$$

3. Absorbing boundary condition. At both ends of rectangular wave guide, the first order absorbing conditions are applied:

$$\frac{\partial E_y}{\partial t} = \pm v \frac{\partial E_y}{\partial z} \tag{10}$$

where \pm is represented forward and backward direction and v is velocity of wave.

4. Oscillation of the electric and magnetic intensities by magnetron. For incident wave due to magnetron is given by Ratanadecho et al. (2002a,b)

$$E_{y} = E_{yin} \sin\left(\frac{\pi x}{L_{x}}\right) \sin(2\pi f t) \tag{11}$$

$$H_{x} = \frac{E_{yin}}{Z_{H}} \sin\left(\frac{\pi x}{L_{x}}\right) \sin(2\pi f t) \tag{12}$$

where E_{yin} is the input value of electric field intensity, L_x is the length of the rectangular wave guide in the x-direction, Z_H is the wave impedance defined as

$$Z_{\rm H} = \frac{\lambda_{\rm g} Z_{\rm l}}{\lambda} = \frac{\lambda_{\rm g}}{\lambda} \sqrt{\frac{\mu}{\varepsilon}} \tag{13}$$

In this equation, Z_1 is intrinsic impedance depending on the properties of the material, λ and λ_g are the wave lengths of microwaves in free space and rectangular wave guide, respectively.

The power flux associated with a propagating electromagnetic wave is expressed by the Poynting vector:

$$s = \frac{1}{2} \operatorname{Re} \left(E \times H^* \right) \tag{14}$$

The Poynting theorem allows the evaluation of the microwave power input. It is represented as

$$P_{\rm in} = \int_{A} SdA = \frac{A}{4Z_{\rm H}} E_{\rm yin}^2 \tag{15}$$

Analysis of Temperature Profiles and Flow Field

The analytical model is shown in Fig. 2. To reduce complexity of the problem, several assumptions have been offered into the flow and energy equations:

- Corresponding to electromagnetic field, considering flow and temperature field can be assumed to be twodimensional plane.
- 2. The effect of the phase change for liquid layer can be neglected.
- Liquid layer is assumed when the Boussinesq approximation is valid.
- 4. The surroundings of the liquid layer are insulated except at the upper surface where energy exchanges with the ambient air.

Heat Transfer Equation

The temperature of liquid layer exposed to incident wave is obtained by solving the conventional heat transport equa-

tion with the microwave power absorbed included as a local electromagnetic heat generation term:

$$\frac{\partial T}{\partial t} + \frac{\partial (uT)}{\partial x} + \frac{\partial (wT)}{\partial z} = \frac{\partial}{\partial x} \left(\alpha \frac{\partial T}{\partial x} \right) + \frac{\partial}{\partial z} \left(\alpha \frac{\partial T}{\partial z} \right) + Q$$
(16)

where Q is the local electromagnetic heat generation term, which is a function of the electric field and defined as

$$Q = 2\pi f \,\varepsilon_0 \varepsilon'_r \tan \delta(E_y)^2 \tag{17}$$

Flow Field Equation

The governing equations for a Newtonian Boussinesq fluid are given as

Continuity equation:

$$\frac{\partial u}{\partial x} + \frac{\partial w}{\partial z} = 0 \tag{18}$$

Momentum equations:

$$\frac{\partial u}{\partial t} + u \frac{\partial u}{\partial x} + w \frac{\partial u}{\partial z} = -\frac{1}{\rho} \frac{\partial p}{\partial x} + \frac{\partial}{\partial x} \left(v \frac{\partial u}{\partial x} \right) + \frac{\partial}{\partial z} \left(v \frac{\partial u}{\partial z} \right)$$
(19)

$$\frac{\partial w}{\partial t} + u \frac{\partial w}{\partial x} + w \frac{\partial w}{\partial z} = -\frac{1}{\rho} \frac{\partial p}{\partial z} + \frac{\partial}{\partial x} \left(v \frac{\partial w}{\partial x} \right) + \frac{\partial}{\partial z} \\
\times \left(v \frac{\partial w}{\partial z} \right) + g\beta(T - T_0) \tag{20}$$

where ν and β are the kinematics viscosity and coefficient of thermal expansion of the water layer, respectively.

Boundary and initial conditions for these equations:

Since the walls of container are rigid, the velocities are zero. At the interface between liquid layer and the walls of container, zero slip boundary conditions are used for the momentum equations.

1. At the upper surface, the velocity in normal direction (w) and shear stress in the horizontal direction are assumed to be zero, where the influence of Marangoni flow (Ratanadecho et al. 2002a,b) can be applied:

$$\eta \frac{\partial u}{\partial z} = -\frac{d\xi}{dT} \frac{\partial T}{\partial x} \tag{21}$$

2. The walls, except top wall, is insulated so no heat and mass exchanges:

$$\frac{\partial T}{\partial x} = \frac{\partial T}{\partial z} = 0 \tag{22}$$



Heat is lost from the surface via natural convection and radiation:

$$-\lambda \frac{\partial T}{\partial z} = h_c (T - T_{\infty}) + \sigma_{\text{rad}} \varepsilon_{\text{rad}} T^4$$
 (23)

4. The initial condition of a water layer is defined as:

$$T = T_0 \text{ at } t = 0 \tag{24}$$

Numerical Solution

The description of heat transport and flow pattern of liquid layer Eqs. 16, 17, 18, 19, and 20 requires specification of temperature (T), velocity component (u, w), and pressure

(p). These equations are coupled to the Maxwell's equations (Eqs. 1, 2, and 3) by Eq. 17. It represents the heating effect of the microwaves in the liquid-container domain.

Electromagnetic Equations and FDTD Discretization

The electromagnetic equations are solved by using FDTD method. With this method, the electric field components (E) are stored halfway between the basic nodes, while magnetic field components (H) are stored at the center. Therefore, they are calculated at alternating half-time steps. E and E field components are discretized by a central difference method (second-order accurate) in both spatial and time domain. For TE mode, the electric and magnetic field components are discretized as

$$E_{y}^{n}(i,k) = \frac{1 - \frac{\sigma(i,k)\Delta t}{2\varepsilon(i,k)}}{1 + \frac{\sigma(i,k)\Delta t}{2\varepsilon(i,k)}} E_{y}^{n-1}(i,k) + \frac{\Delta t}{\varepsilon(i,k)} \frac{1}{1 + \frac{\sigma(i,k)}{2\varepsilon(i,k)}} \cdot \left\{ \frac{H_{z}^{n-1/2}(i+1/2,k) - H_{z}^{n-1/2}(i-1/2,k)}{\Delta x} + \frac{H_{x}^{n-1/2}(i,k-1/2) - H_{x}^{n-1/2}(i,k+1/2)}{\Delta z} \right\}$$
(25)

$$H_x^{n+1/2}(i,k+1/2) = H_x^{n-1/2}(i,k+1/2) + \frac{\Delta t}{\mu(i,k+1/2)} \left\{ \frac{E_y^n(i,k+1) - E_y^n(i,k)}{\Delta z} \right\}$$
(26)

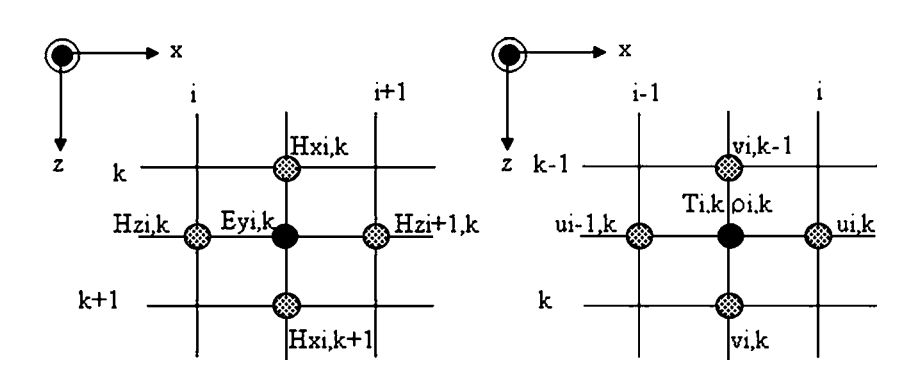
$$H_z^{n+1/2}(i+1/2,k) = H_z^{n-1/2}(i+1/2,k) - \frac{\Delta t}{\mu(i+1/2,k)} \left\{ \frac{E_y^n(i+1,k) - E_y^n(i,k)}{\Delta x} \right\}$$
(27)

Fluid Flow and Heat Transport Equations and Finite Control Volume Discretization

Equations 16, 17, 18, 19, and 20 are solved numerically by using the finite control volume along with the SIMPLE

algorithm developed by Patankar. The reason to use this method is the advantage of flux conservation that avoids generation of parasitic source. The basic strategy of the finite control volume discretization method is to divide the calculated domain into a number of control volumes and then integrate the conservation equations over this control volume over an interval of time $[t,t + \Delta t]$. At the boundaries of the calculated domain, the conservation equations are discretized by integrating over half the control volume and taking into account the boundary conditions. At the corners of the calculated domain, a quarter of control volume was used. The fully implicit time discretization finite difference scheme is used to arrive at the solution in time. Additionally, the details about numerical discretization of this method can be found in the recent literature.

Fig. 3 Grid system configurations





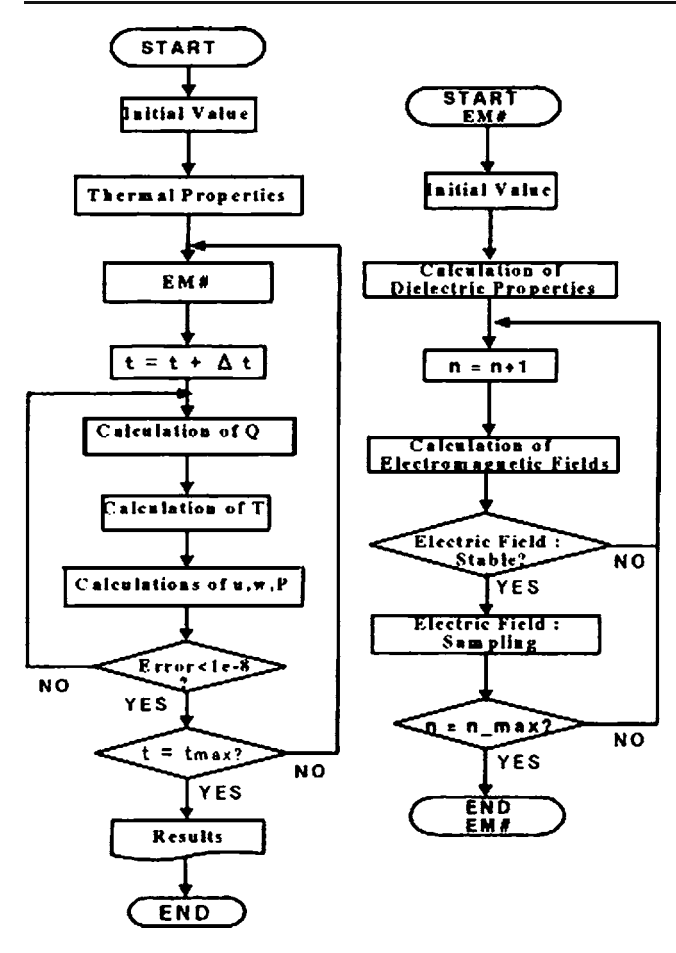


Fig. 4 Computational schemes (EM# subroutine for calculation of electromagnetic field; n calculation loop of electromagnetic field) (Ratadecho et al. 2002a,b)

The Stability and Accuracy of Calculation

The choice of spatial and temporal resolution is motivated by reasons of stability and accuracy. Spatially, as shown in Fig. 3, Eqs. 25, 26, and 27) are solved on a grid system, and temporally, they are solved alternatively for both the electric and magnetic fields. To ensure stability of the time stepping algorithm Δt must be chosen to satisfy the courant stability condition and defined as

$$\Delta t \le \frac{\sqrt{(\Delta x)^2 + (\Delta z)^2}}{v} \tag{28}$$

and the spatial resolution of each cell, defined as

$$\Delta x, \Delta z \le \frac{\lambda_{\rm g}}{10\sqrt{\varepsilon_r}}$$
 (29)

Corresponding to Eqs. 28 and 29, the calculation conditions are as follows:

- 1. Grid size: $\Delta x=1.0922$ and $\Delta z=1.0000$ mm
- 2. Time steps: $\Delta t = 2 \times 10^{-12}$ and $\Delta t = 0.01$ s are used corresponding to electromagnetic field and temperature field calculations, respectively.
- 3. Relative error in the iteration procedures of 10^{-6} was chosen.

The Iterative Computational Schemes

Since the dielectric properties of liquid layer samples are temperature dependent, to understand the influence of electromagnetic field on microwave heating of liquid layer realistically, it is necessary to consider the coupling between electric field and temperature and fluid flow fields. For this reason, the iterative computational schemes are required to resolve the coupled non-linear Maxwell's equations, momentum, and heat transport equations.

The computational scheme is to first compute a local heat generation term by running an electromagnetic calculation with uniform properties determined from initial temperature data. The electromagnetic calculation is performed until a sufficient period is reached in which representative average root mean square of the electric field at each point is computed and used to solve the time dependent temperature and velocities field. Using these temperatures, new values of the dielectric properties are calculated and used to recalculate the electromagnetic fields and then the microwave power absorption. All the steps are repeated until the required heating time is reached. The detail of computational schemes and strategy are illustrated in Fig. 4.

Results and Discussion

Two kinds of liquid are simulated in order to display physical phenomena of microwave heating in the liquid

Table 1 The electromagnetic and thermo physical properties used in the computations (Ratanadecho et al. 2002a,b and Aparna et al. 2007)

Property	Air	Water	Oil
Heat capacity, C_p (J kg ⁻¹ K ⁻¹)	1,007	4,190	2,000
Thermal conductivity, λ (W m ⁻¹ K ⁻¹)	0.0262	0.609	0.168
Density, ρ (kg m ⁻³)	1.205	1000	900
Dielectric constant, ε'_r	1.0	$88.15 - 0.414 T + (0.131 \times 10^{-2})T^2 - (0.046 \times 10^{-4})T^3$	2.8
Loss tangent, tan δ	0.0	$0.323 - (9.499 \times 10^{-3}) T + (1.27 \times 10^{-4}) T^2 - (6.13 \times 10^{-7}) T^3$	0.05



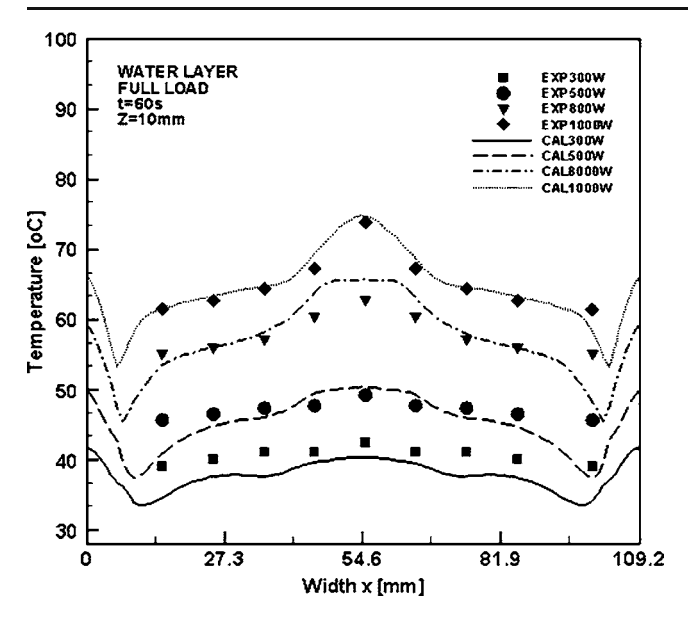


Fig. 5 comparison of the temperature distribution within the water layer between the predicted and experimental results at various microwave power, at t=60 s, along with the horizontal axis (z=10 mm) of a rectangular wave guide

layers with different dielectric properties. Water and oil are chosen for this purpose. Dimensions of the rectangular wave guide are $109.2(X) \times 54.61(Y)$ mm². Microwave frequency is operated at 2.45 GHz. Thermal and dielectric properties used for mathematical calculations are shown in Table 1.

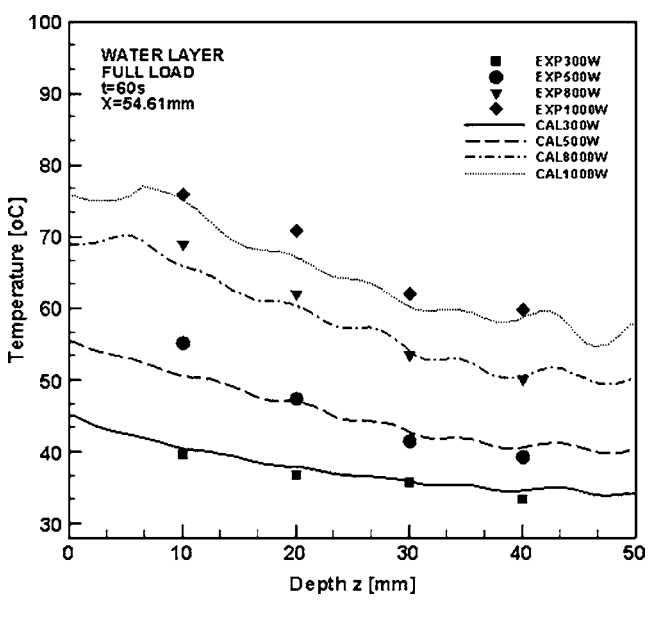


Fig. 6 Comparison of the temperature distribution within the water layer between the predicted and experimental results at various microwave power, at t=60 s, along with the vertical axis (x=54.61 mm) of a rectangular wave guide

The Effect of Microwave Power

Figures 5 and 6 show the comparison of the temperature distribution within the water layer between the predicted and experimental results at various microwave power, at t=60 s, along with the horizontal axis (z=10 mm) and vertical axis (x=54.61 mm) of a rectangular wave guide, respectively. Dimensions of water layer are $109.2(X) \times 54.61(Y)$ mm², which is equal to the size of wave guide. Thickness (Z) is 50 mm. It is found that power significantly influences the rate of temperature rise. Greater power provides greater heat generation rate inside the medium, thereby increasing the rate of temperature rise. Figure 5 shows the greatest temperature in the center of heating layer with the temperature decreasing toward the side walls of the water layer corresponding to the characteristic of TE₁₀ mode. However, the results from calculation at the side walls are increasing, which is due to the walls being insulated and low rate of heat loss. In Fig. 6, the temperature within the water layer closest to the incoming microwave is shown. The region close to the top surface heats up with a faster rate than elsewhere within the water layer. Nevertheless, the temperature decays slowly along the propagation direction due to the skin depth heating effect. The predicted results are in a reasonable agreement with the experimental results.

Figure 7a and b shows simulation of electric field. Figure 7a is the case of empty wave guide. Figure 7b is the

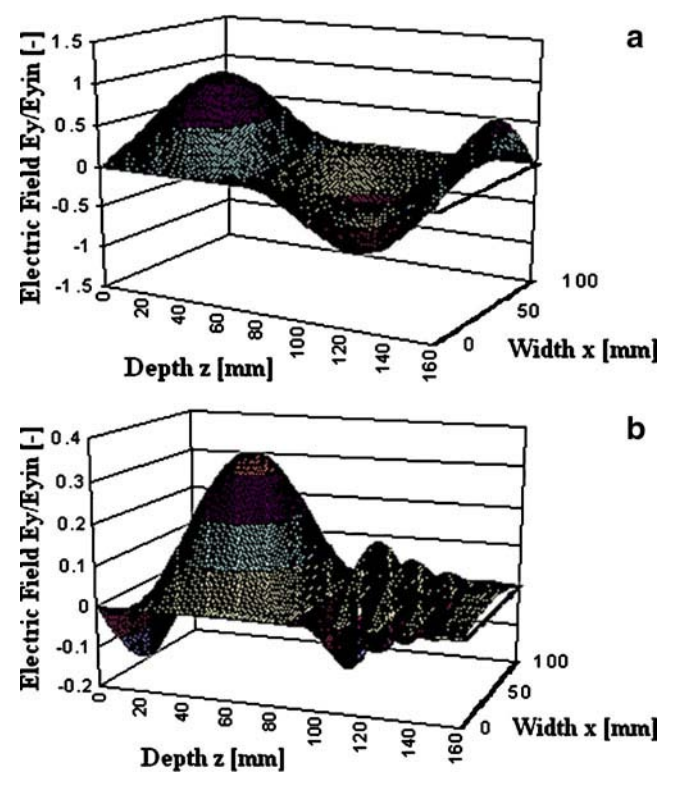


Fig. 7 Distribution of electric field (*P*=300 W): **a** wave guide is empty, **b** insert water layer



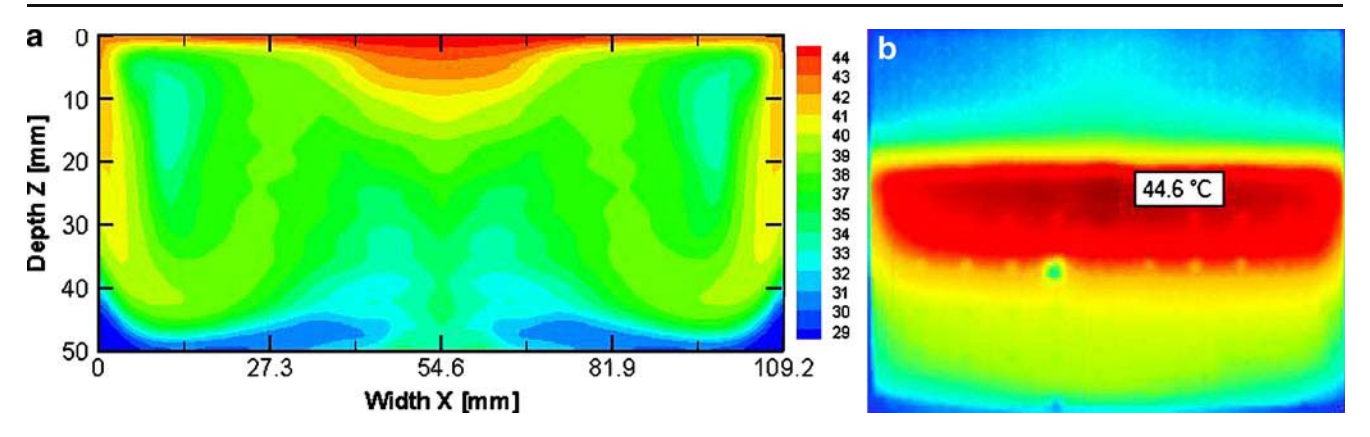


Fig. 8 Temperature profiles within water layer on X-Z plane (P=300 W, t=60 s): a from calculation, b captured by infrared camera

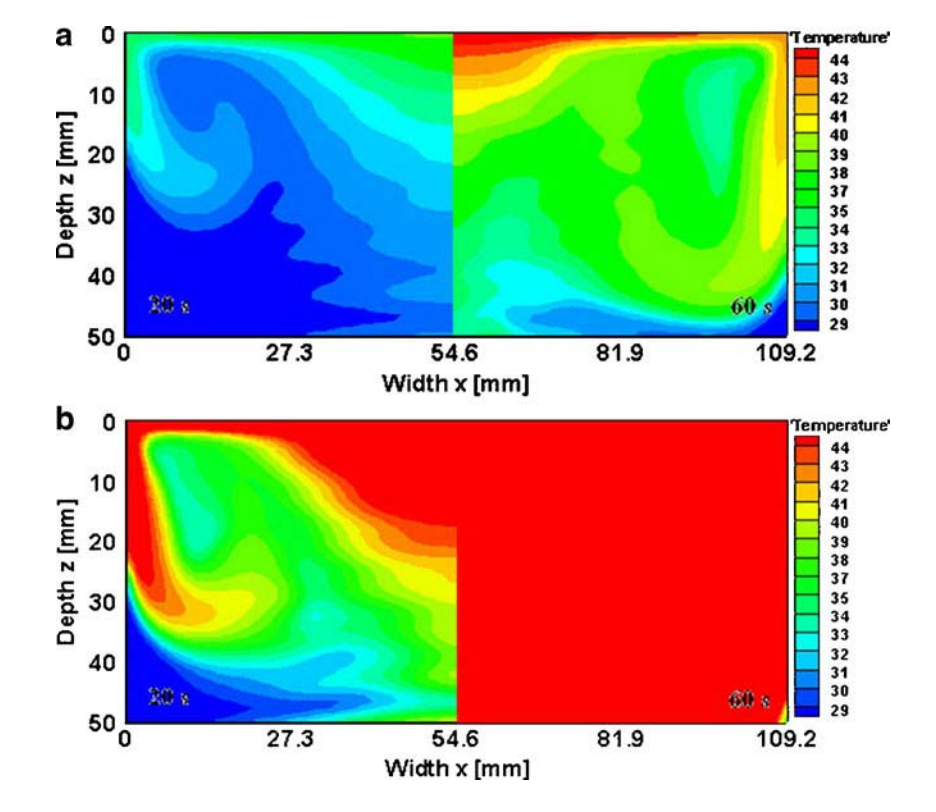
case of water layer inside wave guide. The vertical axis represents the intensity of the electric field E_{yy} , which is normalized to the amplitude of the input electromagnetic wave E_{yin} . Figure 7a is the simulated electric field of TE_{10} mode along the center axis x=54.61 mm of a rectangular wave guide. For this case, the inside of the wave guide is empty, and the incident wave is chosen to be 9.565×10^3 V/m (300 W). A uniform static wave of TE_{10} mode inside wave guide is shown. Figure 7b shows a stronger standing wave with a larger amplitude forms in the cavity forward to the water layer, while the electric field within the water layer is extinguished. Since the incident wave passing through the cavity having low permittivity is directly

irradiated with the water layer having high permittivity, the major part of incident wave is reflected and resonated, while other part that is minor is transmitted.

Figure 8a and b shows temperature profiles from calculation and that captured by infrared camera, respectively. Microwave power is 300 W (t=60 s). The results agree reasonably well.

Figures 9a and b shows temperature profiles within a water layer on X–Z plane at various microwave power (300 and 1,000 W). In the case of a full load, a temperature profile is symmetric. The left figure shows early state (t= 20 s), and the right figure shows final state (t=60 s). The highest temperature in the upper region of heating water

Fig. 9 Temperature profiles within water layer on *X–Z* plane at various microwave power: **a** 300 W, **b** 1,000 W





layer with the temperature decreasing towards the lower wall is shown.

Figures 10a and c are velocity fields within water layer on X-Z plane, corresponding to temperature fields in Fig. 9a and b. At the early stage of heating (t=20 s), the effect of conduction plays the greatest role than convection mode. As the heating proceeds, the local heating on the surface water layer causes the difference of surface tension on the surface of water layer, which leads to the convective flow of water (Marangoni flow). This causes water to flow from the hot region (higher power absorbed) at the central region of water layer to the colder region (lower power absorbed) at the side wall of container. In the stage of heating (t=60 s), the effect of convective flow becomes stronger and plays a more important role, especially at the upper portion of the side walls of container. However, at the bottom region of the walls where the convection plays the smallest, temperature distributions are primarily governed by the conduction mode. In the case of microwave power level of 300 W, the temperature within water layer is greater closer to the incoming microwave and has a trend corresponding to those of velocity fields.

In the case of microwave power level of 1,000 W, overall, temperature is greater near the top surface and locally high inside the layer. Furthermore, it is evident that the heating rate is higher in this case than in 300 W. This is because of the penetration depth heating effect, which increases a larger part of the incident wave to penetrate further into the water layer.

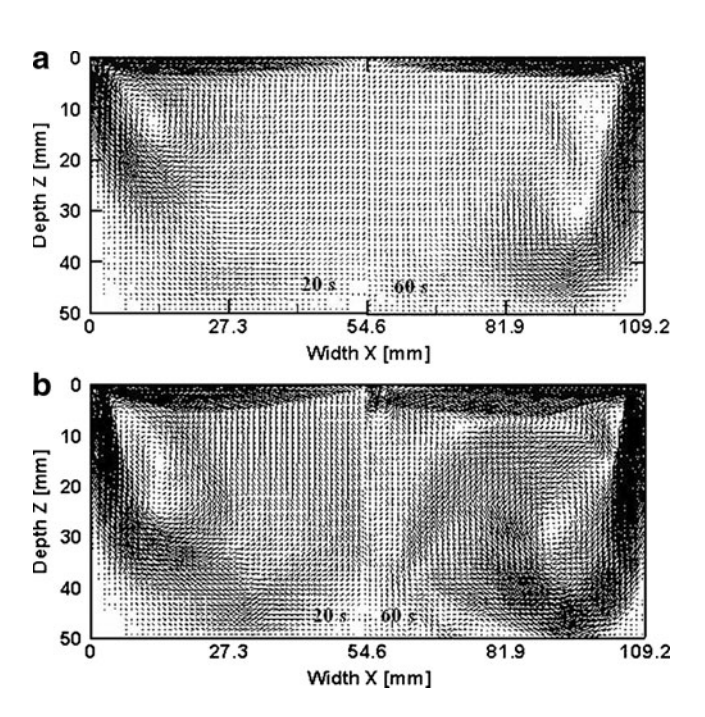


Fig. 10 Velocity field within water layer on $X\!-\!Z$ plane at various microwave power: a 300 W and b 1,000 W

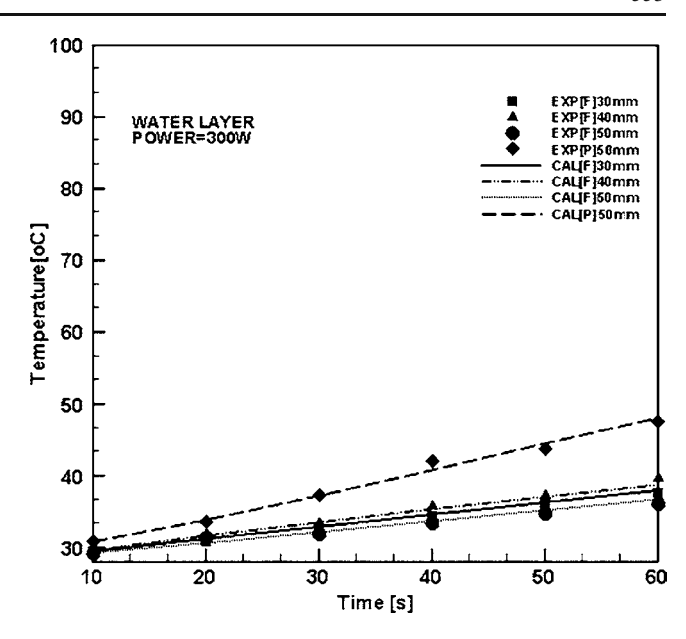


Fig. 11 The comparison of the temperature distribution within the water layer between the predicted and experimental results at various sample sizes

The Effect of Liquid Layer Size

Figure 11 shows the comparison of the temperature distribution within the water layer between the predicted and experimental results at various sample sizes. Microwave power is 300 W. From the figure, dimensions of water layer are $54.61(X) \times 54.61(Y) \times 50(Z)$ mm³, providing the highest heat generation rate within sample. This is because water that has a smaller volume has a higher rate change of

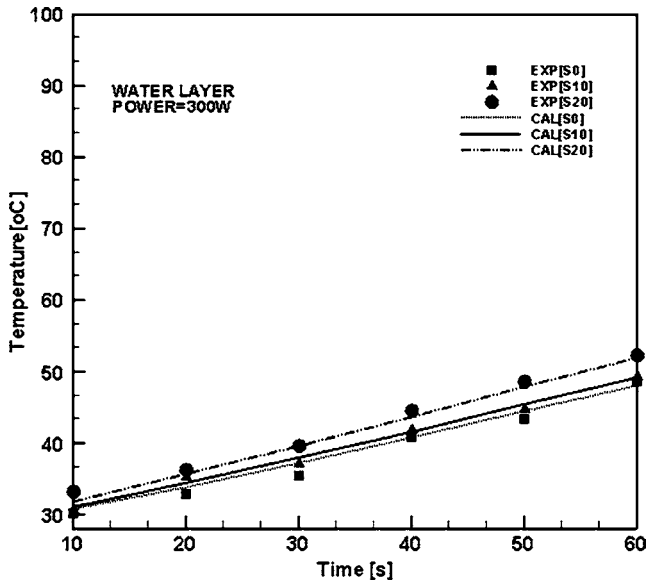
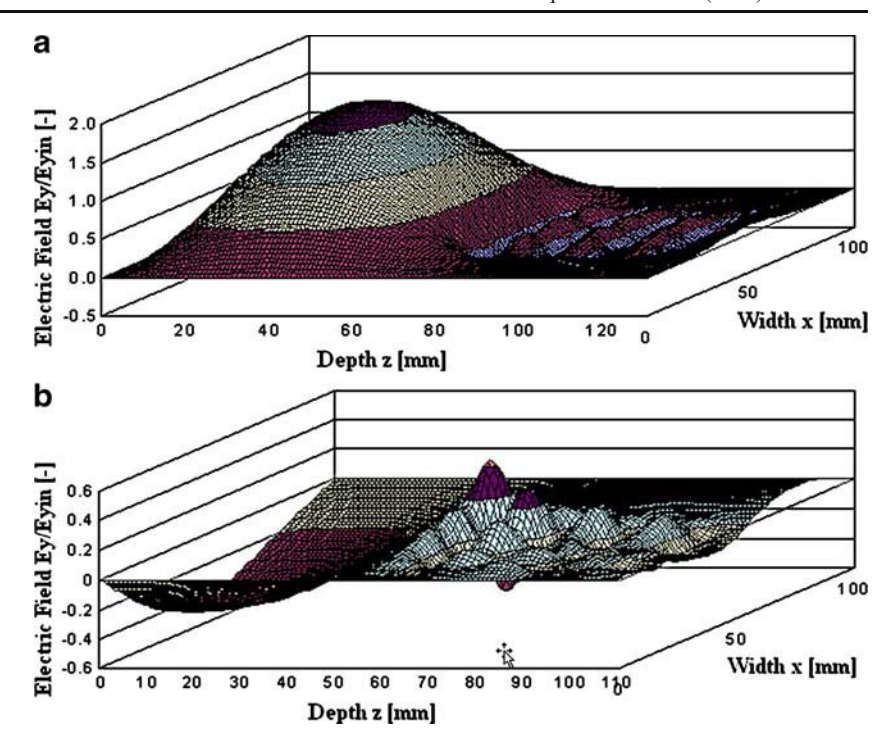


Fig. 12 The comparison of the temperature distribution within the water layer between the predicted and experimental results at various positions inside wave guide



Fig. 13 Distribution of electric field at various positions inside wave guide: a S0, b S20



temperature due to larger heat generation rate per unit volume. However, the exception is observed. Although the water in a $109.2(X) \times 54.61(Y) \times 40(Z)$ -mm³ container has larger volume than that in a $109.2(X) \times 54.61(Y) \times 30$

(Z)-mm³ container, the water with the larger volume has greater rate of temperature rise. The reason behind this result is that the penetration depth of water that is greater than its thickness causes the interference of waves reflected

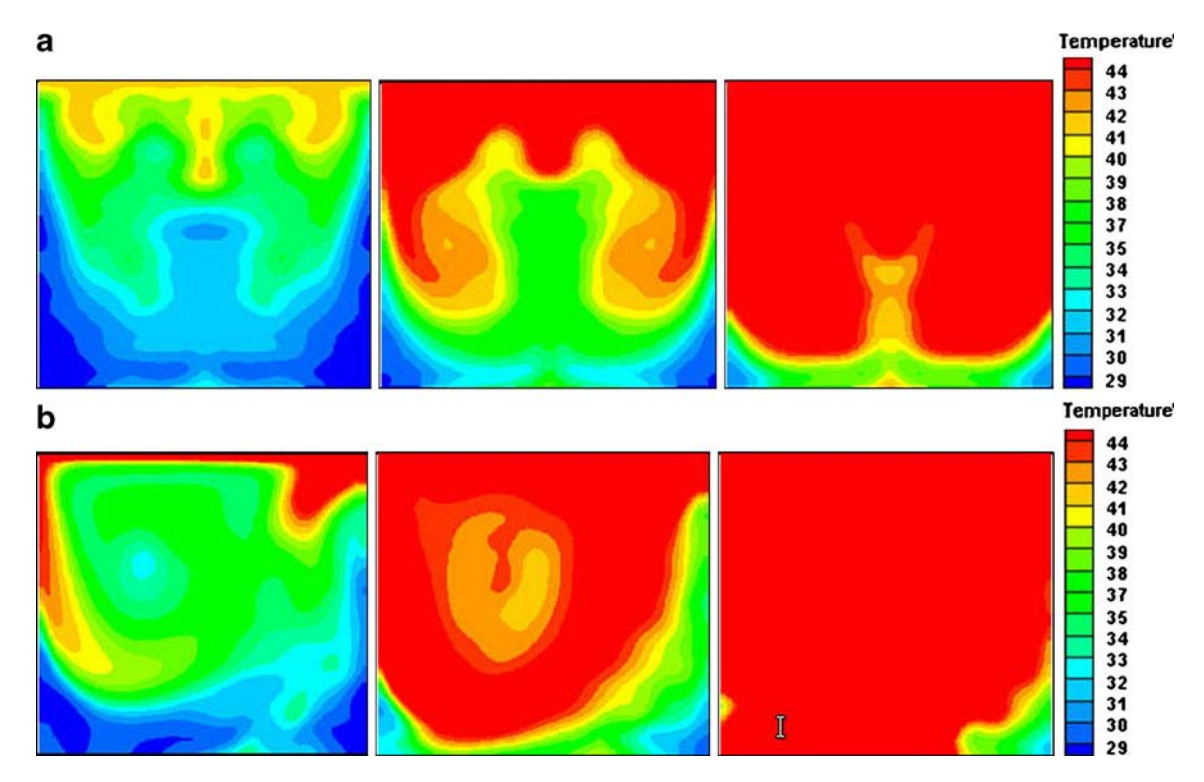


Fig. 14 Temperature profiles within water layer in case of partial load at various positions inside wave guide (P=300 W, thickness=50 mm): a S0, b S20



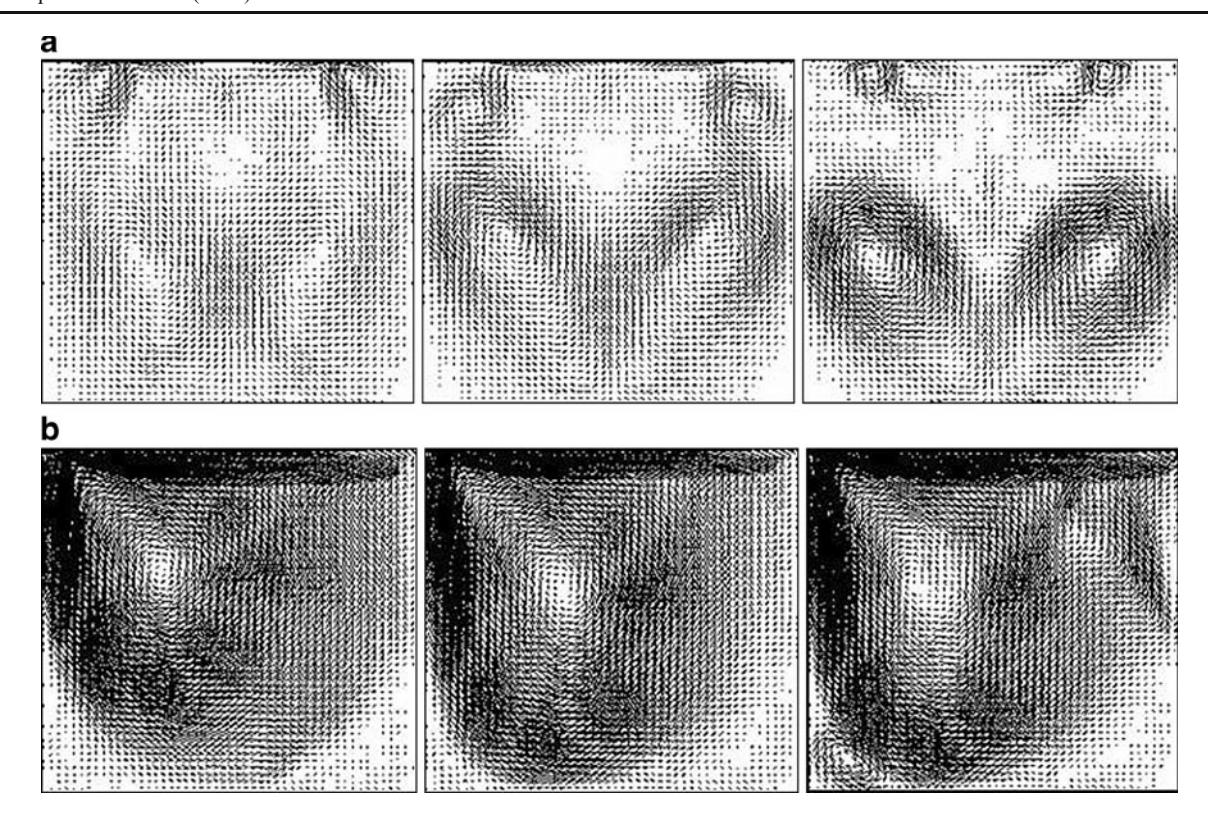


Fig. 15 Velocity field within water layer in case of partial load at various positions inside wave guide (P=300 W, thickness=50 mm); a S0, b S20

from the interface of water and air at the lower side due to the difference of dielectric properties of water and air. Consequently, the reflection and transmission components at each interface contribute to the resonance of standing wave inside the water sample. Therefore, the field distribution does not poses an exponential decay from the surface.

The Effect of Position of Liquid Layer Inside Wave Guide

This section discusses the effects of positions of the water layer in the rectangular wave guide. Three different locations of the water layer are investigated. The dimension of the water layer is $54.61(X) \times 54.61(Y)$ mm² and is 50(Z) mm in thicknesses.

Figure 12 shows the comparison of the temperature distribution within the water layer between the predicted and experimental results at various positions inside wave guide. Microwave power is 300 W. From these figure, the rate change of temperature is highest when the location of the sample is shifted to 20 mm away from the center, whereas the rate is lowest when the sample is located at the center.

Figures 13, 14, and 15 show phenomena of microwave heating of water layer in case of partial load at various positions (P=300 W).

Figure 13a and b shows the distribution of electric field within water layer. It shows considerably uniform distribu-

tion of electric field when the sample is located at the center (S0), whereas distribution of electric field is relatively not uniform when location of the sample is shifted to 20 mm away from the center, which is denoted by S20.

Figure 14a and b presents temperature profiles within the water layer on *X*–*Z* plane. Figure 14a shows the distribution of temperature when the sample is located at the center (S0). Temperature profile is symmetrical and is similar in the case of full load. The upper region of heating is a high temperature and decreases towards the lower wall. However, the wall side has temperature greater than the center of

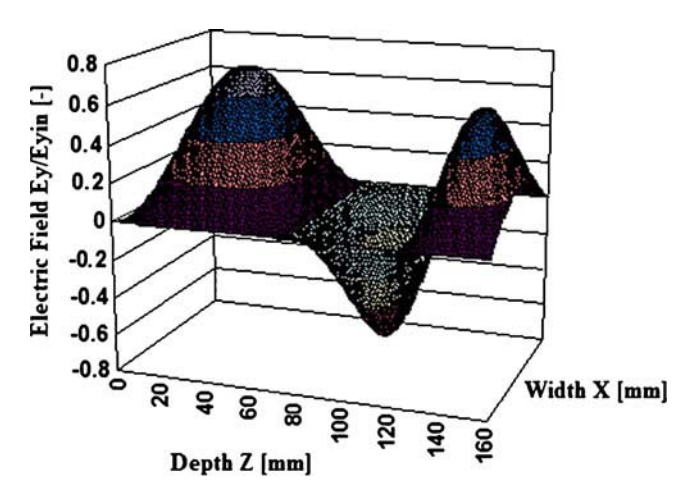


Fig. 16 Distribution of electric field inside wave guide and oil

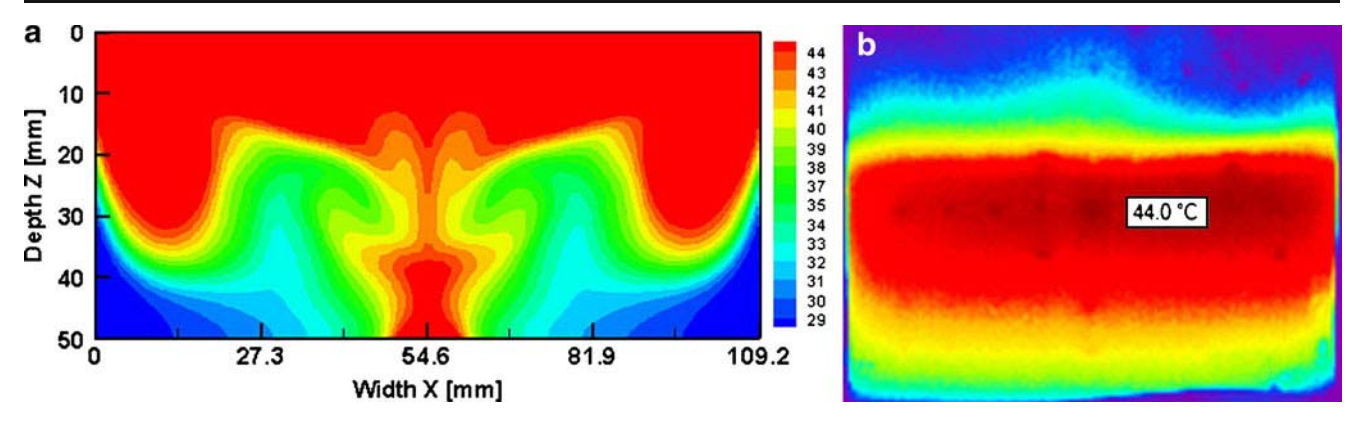


Fig. 17 Temperature profiles within oil on X-Z plane at 60 s; a from calculation, b captured by infrared camera

water layer. Figure 14b shows the distribution of temperature when location of the sample is shifted to 20 mm away from the center. Temperature profile is not symmetrical. The temperature distributes from the corner of the sample toward the lower side. In addition, it is interesting that the rate change of temperature becomes greatest when the sample is displaced 20 mm from the center. This result is attributed to the size of sample that is smaller than the wave guide; therefore, waves reflect disorder resulting in a multimode of field pattern.

Velocity fields within water layer on X–Z plane are shown in Fig. 15a and b. Several circulations are observed in Fig. 14a and b. When location of the sample is shifted to 20 mm away from the center, there appears the transition from several circulations to one larger circulation. The vectors are rigorous near the upper left corner. The velocity fields have a trend corresponding to that of temperature profiles.

The Effect of Dielectric Properties

Microwave-heating process within water layer and oil are examined in this section. The samples used are water and cooking oil. For the water layer, the physical phenomena of microwave heating are shown in the preceding sections. Temperature is highest at the center since the density of the electric field of the microwave field in the TE₁₀ mode is high around the center region in the wave guide. The temperature is higher closer to the surface of water since water is a high lossy dielectric material, which has a small penetration depth causing the field to decay rapidly. The penetration depth is computed using Eq. 7 based on the dielectric properties of water.

Next, the result of oil can be observed in Fig. 16, 17, and 18, which respectively present the electric field distribution, contours of temperature, and velocity field. The dimension of oil layer is $109.2(X) \times 54.61(Y) \times 50(Z)$ mm³. Figure 16 depicts the surface plots of simulation of electric field inside wave guide and oil along the center axis x=

54.61 mm of a rectangular wave guide. Microwave power is 300 W $(9.565 \times 10^3 \text{ V/m})$. Figure 17a and b shows temperature profiles from the calculation and that captured by infrared camera, respectively. The results agree reasonably well. The temperature is highest in the upper region of the heating oil, with the temperature decreasing towards the lower wall. This oil is considered a low lossy material in which the fields can penetrate farther than in the water layer, causing high temperature at the lower region of the layer. Furthermore, the temperature distribution of oil (Fig. 17) and water (Fig. 8) are compared. It is found that temperature in the X–Z plane is more uniform in water than in oil, since more convection mechanism exists in water. The convection mode of heat transfer helps in distributing temperature throughout the layer. Figure 18 depicts flow pattern within the oil layer. The flow motions are induced by temperature gradients. The flow directions are indicated by the overwritten arrows significantly controlling overall heat transfer directions.

Conclusion

The numerical analysis in this paper describes many of the important interactions within a water layer and oil during

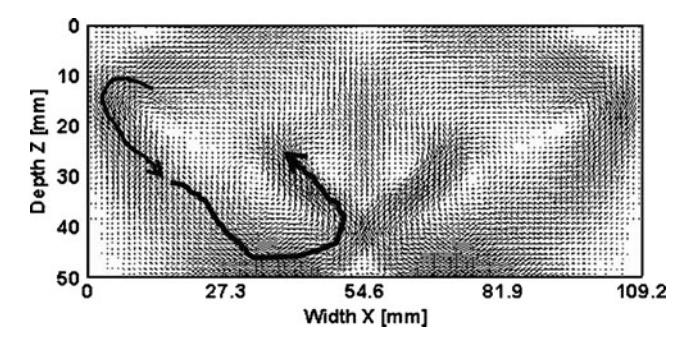


Fig. 18 Velocity field within oil layer in case of full load at 60 s (P= 300 W, thickness=50 mm)



microwave heating using a rectangular wave guide. The following summarizes the conclusions of this work:

- A mathematical model of microwave heating by using rectangular wave guide is presented, which is in relatively good agreement with the results of the experiment. The model used successfully describes the heating phenomena of water layers and oil under various conditions.
- 2. The temperature profiles and velocity fields in the water layer and oil are governed by the electric field as well as dielectric properties of water.
- 3. The distribution of heating location primarily depends on the penetration depth of liquid layer.
- 4. Size and thickness of water layer have an effect on phenomena of microwave heating. Water layer that is small and has thickness close to penetration depth has greater distribution of temperature due to larger heat generation rate per unit volume, and the reflection and transmission components at each interface contribute to a stronger resonance of standing wave inside the sample.
- 5. The position of water layer inside the wave guide is proven to have an important effect on microwave heating process. When the layer is placed off the center, it reveals unsymmetrical heating and flow patterns, which enhance the rate of temperature rise.
- Natural convection due to buoyancy force strongly affects flow pattern within water layer during microwave heating process and clearly enhances temperature distribution in the layer.

The next steps of this research will be to investigate more associated parameters and more details of position inside wave guide and develop the 3D mathematical model.

Acknowledgement The authors gratefully acknowledge the financial support provided by The Thailand Research Fund for the simulation facilities described in this paper.

References

- Aparna, K., Basak, T., & Balakrishnan, A. R. (2007). Role of metallic and composite (ceramic–metallic) supports on microwave heating porous dielectrics. *International Journal of Heat and Mass Transfer*, 50, 3072–3089. doi:10.1016/j.ijheatmasstransfer.2006.11.021.
- Ayappa, K. G., Brandon, S., et al. (1994). Microwave driven convection in a square cavity. AIChE Journal, 40(7), 1268– 1272. doi:10.1002/aic.690400718.
- Basak, T. (2003). Analysis of resonance during microwave thawing of slabs. *International Journal of Heat and Mass Transfer*, 46, 4279–4301. doi:10.1016/S0017-9310(03)00212-6.
- Basak, T. (2004). Role of resonance on microwave heating of oil—water emusions. *AIChE Journal*, 50, 2659–2675. doi:10.1002/aic.10207.
- Basak, T., & Ayappa, K. G. (2002). Role of length scales on microwave thawing dynamics in 2D cylinders. *International*

- Journal of Heat and Mass Transfer, 45(23), 4543–4559. doi:10.1016/S0017-9310(02)00171-0.
- Boyacı, İ. H., Sumnu, G., & Sakiyan, O. (2009). Estimation of dielectric properties of cakes based on porosity, moisture content, and formulations using statistical methods and artificial neural networks. Food Bioprocess Technology. doi:10.1007/s11947-008-0064-z
- Chatterjee, S., Basak, T., & Das, S. K. (2007). Microwave driven convection in a rotating cylindrical cavity, A numerical study. *Journal of Food Engineering*, 79, 1269–1279. doi:10.1016/j. jfoodeng.2006.04.039.
- Curet, S., Rouaud, O., & Boillereaux, L. Microwave tempering and heating in a single-mode cavity: Numerical and experimental investigations. *Chemical Engineering and Processing*, 47, 1656– 1665.
- Datta, A. K., Prosetya, H., & Hu, W. (1992). Mathematical modeling of batch heating of liquids in a microwave cavity. *Journal of Microwave Power and Electromagnetic Energy*, 27, 38–48.
- Dibben, D. C., & Metaxas, A. C. (1997). Frequency domain vs. time domain finite element methods for calculation of fields in multimode cavities. *IEEE Transactions on Magnetics*, 33(2), 1468–1471. doi:10.1109/20.582537.
- Huo, Y., Li, B. Q., & Tang, J. (2004). Boundary/finite edge element modeling of 3-D microwave thermal food processing. ASME, Heat Transfer Division, (Publication) HTD 375 (1), Art. No. IMECE2004-59670, pp. 687–694.
- Jia, X., & Bialkowski, M. (1992). Simulation of microwave field and power distribution in a cavity by a three dimension finite element method. *Journal of Microwave Power and Electromagnetic* Energy, 27(1), 11–22.
- Liu, F., Turner, I., & Bialowski, M. (1994). A finite-difference time-domain simulation of power density distribution in a dielectric loaded microwave cavity. *Journal of Microwave Power and Electromagnetic Energy*, 29(3), 138–147.
- Mur, G. (1981). Absorbing boundary conditions for the finitedifference approximation of the time-domain electromagneticfield equations. *IEEE Transactions on Electromagnetic Compatibility EMC-23*, 4, 377–382. doi:10.1109/TEMC.1981.303970.
- Patankar, S. V. (1980). *Numerical heat transfer and fluid flow*. New York: Henisphere.
- Ratanadecho, P., Aoki, K., & Akahori, M. (2002a). A numerical and experimental investigation of the modeling of microwave heating for liquid layers using a rectangular wave guide (effects of natural convection and dielectric properties). *Applied Mathematical Modelling*, 26, 449–472. doi:10.1016/S0307-904X(01)00046-4.
- Ratanadecho, P., Aoki, K., & Akahori, M. (2002b). Experimental validation of a combined electromanetic and thermal model for a microwave heating of multi-layered materials using a rectangular wave guide. ASME Journal of Heat and Transfer, 124(5), 992– 996. doi:10.1115/1.1495521.
- Rattanadecho, P. (2006). The simulation of microwave heating of wood using a rectangular wave guide: Influence of frequency and sample size. *Chemical Engineering Science*, 61, 4798–4811. doi:10.1016/j.ces.2006.03.001.
- Rattanadecho, P., Kazuo, A., & Masatoshi, A. (2002). The characteristics of microwave melting of frozen packed beds using a rectangular wave guide. *IEEE Transactions on Microwave Theory and Technique*, 50(6), 1487–1494. doi:10.1109/TMTT.2002.1006410.
- Rattanadecho, P., & Suwannapum, N. (2009). Interactions between electromagnetic and thermal fields in microwave heating of hardened type I-cement paste using a rectangular wave guide (influence of frequency and sample size). ASME Journal of Heat and Transfer (in press).
- Tada, S., Echigo, R., & Yoshida, H. (1997). Numerical analysis of electromagnetic wave in a partially loaded microwave applicator.



- International Journal of Heat and Mass Transfer, 41, 709–718. doi:10.1016/S0017-9310(97)00164-6.
- Vadivambal, R., & Jayas, D. S. (2009). Non-uniform temperature distribution during microwave heating of food materials—A review. Food Bioprocess Technology. doi:10.1007/s11947-008-0136-0
- Yee, K. S. (1996). Numerical solution of initial boundary value problems involving Maxwell's equation in isotropic media. *IEEE Transactions on Antennas and Propagation*, 14, 302–307.
- Zhang, Q., Jackson, T. H., & Ungan, A. (2000). Numerical modeling of microwave induced natural convection. *International Journal* of Heat and Mass Transfer, 43, 2141–2154. doi:10.1016/S0017-9310(99)00281-1.
- Zhu, J., Kuznetsov, A. V., & Sandeep, K. P. (2007). Mathematical modeling of continuous flow microwave heating of liquid (effect of dielectric properties and design parameters). *International Journal of Thermal Sciences*, 46, 328–341. doi:10.1016/j. ijthermalsci.2006.06.005.





Contents lists available at ScienceDirect

International Communications in Heat and Mass Transfer

journal homepage: www.elsevier.com/locate/ichmt



Energy and exergy analyses in convective drying process of multi-layered porous packed bed to analyse in convective drying process of multi-layered porous

Ratthasak Prommas, Pornthip Keangin, Phadungsak Rattanadecho*

Research Center of Microwave Utilization in Engineering (R.C.M.E.), Faculty of Engineering, Thammasat University, Khlong Luang, Pathumthani, Thailand 12120

ARTICLE INFO

Available online 9 July 2010

Keywords:
Energy utilization
Exergy efficiency
Convective drying
Multi-layered porous

ABSTRACT

This paper is concerned with the investigation of the energy and exergy analyses in convective drying process of multi-layered porous media. The drying experiments were conducted to find the effects of multi-layered porous particle size and thermodynamics conditions on energy and exergy profiles. An energy analysis was performed to estimate the energy utilization by applying the first law of thermodynamics. An exergy analysis was performed to determine the exergy inlet, exergy outlet, exergy losses during the drying process by applying the second law of thermodynamics. The results show that the energy utilization ratio (EUR) and the exergy efficiency depend on the particle size as well as the hydrodynamic properties and the layered structure, by considering the interference between capillary flow and vapor diffusion in the multi-layered packed bed.

© 2010 Elsevier Ltd. All rights reserved.

1. Introduction

Drying is a thermal process in which heat and moisture transfer occur simultaneously. Heat is transferred by convection from heated air to the product to raise the temperatures of both the solid and moisture that is present. Moisture transfers occurs as the moisture travels to the evaporative surface of the product and then it evaporate into the circulating air as water vapor, are necessary for process design, optimization, energy integration, and control [1,2]. The heat and moisture transfer rates are therefore related to the velocity, temperature and type of product with the circulating drying air. Thermal drying has been recognized as an important unit operation as it is energy intensive and has a decisive effect on the quality of most products that are dried commercially [3,4].

Drying of porous solids is a subject of significant scientific and technological interest in a number of industrial applications including coatings, food, paper, textile, wood, ceramics, building materials, granular materials, electronic devices and pharmaceuticals [5].

Drying of porous materials is a problem of coupled heat and mass transport in a multiphase system which undergoes structural changes and shrinkage during the process. As drying proceeds, the mechanisms of water migration and all the transport properties change [6]. Nevertheless, most of the models describing the drying of foodstuffs are constructed on the basis of theories commonly used in dealing with

E-mail address: ratphadu@engr.tu.ac.th (P. Rattanadecho).

conventional porous materials, and without acknowledging the features which make this particular problem unusual.

The traditional thermodynamics method of assessing processes involving the physical or chemical processing of materials with accompanying transfer and transformation of energy is by the completion of an energy balance which is based on the first law of thermodynamics. The first law analysis is used to reduce heat losses or enhance heat recovery. Meanwhile, it gives no information on the degradation of the useful energy that occurs within the process equipment [7]. The exergy of an energy form or a substance is a measure of its usefulness or quality or potential change [8]. Exergy is defined as the maximum work, which can be produced by a system or a flow of matter or energy and it comes to equilibrium with a specified reference environment (dead state) [9]. Unlike energy, exergy is conserved only during ideal processes and destroyed due to irreversibilities in real processes [10].

The features of exergy are identified to highlight its importance in a wide range of applications [11]. Exergy analysis has been increasingly useful as a tool in the design, assessment, optimization and improvement of energy systems. It can be applied on both system and component levels. Exergy analysis leads to a better understanding of the influence of thermodynamics phenomena on effective process, comparison of the importance of different thermodynamics factors, and the determination of the most effective ways of improving the process [12]. As regards the exergy analyses of drying processes, some work has been carried out in recent years. Kanoglua and et al. [13] analyzed a thermodynamics aspect of the fluidized bed drying process of large particles for optimizing the input and output conditions by using energy and exergy models. The effects of the hydrodynamic and thermodynamics conditions were also analyzed such as inlet air

Communicated by W.J. Minkowycz.

^{*} Corresponding author.

Nomenclature

 c_p

mean specific heat, (kJ/kg K) \bar{c}_p EUR energy utilization ratio, (%) Ex exergy, (kJ/kg) gravitational acceleration, m/s² g constant in Newton's law g h enthalpy, (kJ/kg) joule constant I ṁ mass flow rate, (kg/s) N number of species Р pressure, (kPa) Q net heat, (kJ/s)

specific heat, (kJ/kg K)

 Q_u useful energy given by heater, (kJ/s)

s specific entropy, (kJ/kg K)

T temperature, (K)

u specific internal energy, (kJ/kg)

v specific volume, m³/s V velocity, (m/s)

 $egin{array}{ll} w & specific humidity, (g/g) \\ \dot{W} & energy utilization, (J/s) \\ z & altitude coordinate, (m) \\ \end{array}$

Subscripts

a air da drying air dc drying chamber f fan

i inlet
L loss

mp moisture of product

o outlet

pb porous packed bed

sat saturated

∞ surrounding or ambient

Greek symbols

 $\begin{array}{ll} \phi & \quad \text{relative humidity, (\%)} \\ \eta_{\text{ex}} & \quad \text{exergetic efficiency, (\%)} \\ \mu & \quad \text{chemical potential, (kJ/kg)} \end{array}$

temperature, fluidization velocity and initial moisture content on energy efficiency and exergy efficiency. Syahrul and et al. [14] and Dincer [15] used a model to analyze exergy losses of a air drying process. Their work demonstrated that the usefulness of exergy analysis in thermodynamics assessments of drying processes and providence the performances and efficiencies of these processes. Akpinar and et al. [16,17] studied energy and exergy of the drying of red pepper slices in a convective type dryer, with potato slices in a cyclone type dryer and pumpkin slices in a cyclone type dryer. The type and magnitude of exergy losses during drying was calculated. Colak [18] performed an exergy analysis of thin layer drying of green olive in a tray dryer. In Colak's study the effects of the drying air temperature, the mass flow rate of drying air and olives on the system performance were discussed. Ceylan et al. [19] carried out energy and exergy analyses during the drying of two types of timber. The effects of ambient relative humidity and temperature were taken into

Typical applications of non-uniform material include the tertiary oil recovery process, geothermal analysis, asphalt concrete pavements

process and preservation process of food stuffs. Therefore, knowledge of heat and mass transfer that occurs during convective drying of porous materials is necessary to provide a basis for fundamental understanding of convective drying of non-uniform materials. From research on energy and exergy analysis of the drying process the analysis on the phenomenon of evaporation in porous materials is relatively small. Prommas [20] analyzed the energy and exergy in drying process of porous media using hot air. Due to the limited amount of experimental work on convective drying of multi-layered material, the various effects are not fully understood and a number of critical issues remain unresolved. The effects of particle size and the layered configuration on the overall drying kinetics have not been systematically studied. Although most previous investigations consider single-layered material, little effort has been reported on convective drying of multi-layered material (non-uniform structure) at a fundamental level.

From macroscopic point of view, the effects of the particle sizes, hydrodynamic properties, and the layered configuration on the overall drying kinetics must be clarified in detail. Therefore, the specific objectives of this work are to extend the previous work of Prommas to discuss the effect of particle size and the layered configuration on the overall drying kinetics include the convective drying of multi-layered porous packed bed.

The objectives of this work are described of multi-layered to effect of particle size and capillary pressure for evaluate the exergy losses of two operations multi-layered porous packed bed, the exergy losses and exergy input for the different drying operations and the influences of operating parameters on exergy losses. The knowledge gained will provide an understanding in multi-layered porous media and the parameters which can help to reduce energy consumptions and losses.

2. Experimental apparatus

Fig. 1(a) shows the experimental convective drying system. The hot air, generated electrically travels through a duct toward the upper surface of two samples situated inside the test section. The outside walls of test section are covered with insulation to reduce heat loss to the ambient. The flow outlet and temperature can be adjusted at a control panel.

As shown in Fig. 1(b), the samples are unsaturated packed beds composed of glass beads, water and air. The samples are prepared in the two configurations in the: a single-layered porous packed bed (uniform packed bed) with bed depth $\delta = 40 \text{ mm}$ (d = 0.15 mm (F bed) and d = 0.4 mm (C bed)) and a two-layered porous packed bed, respectively. The two-layered porous packed bed are arranged in different configurations in the: F-C bed (fine particles (d = 0.15 mm, $\delta = 20 \text{ mm}$) overlay the coarse particles (d = 0.4 mm, $\delta = 20 \text{ mm}$)), and C-F bed (coarse particles (d = 0.4 mm, δ = 20 mm) overlay the fine particles (d = 0.15 mm, δ = 20 mm)), respectively. The width and total length of all samples used in the experiments are 25 mm and 40 mm, respectively. The temperature distributions within the sample are measured using fiberoptic sensors (LUXTRON Fluroptic Thermometer, Model 790, accurate to 0.5), which are placed in the center of the sample at 5 mm form surface in Fig. 2. In each test run, the weight loss of the sample is measured using a high precision mass balance.

The uncertainty in the results might come from the variations in humidity and room temperature. The uncertainty in drying kinetics is assumed to result from errors in the measuring weight of the sample. The calculated uncertainties in weight in all tests are less than 2.8%. The uncertainty in temperature is assumed to result from errors in adjusting input power, ambient temperature and ambient humidity. The calculated uncertainty associated with temperature is less than 2.85%.

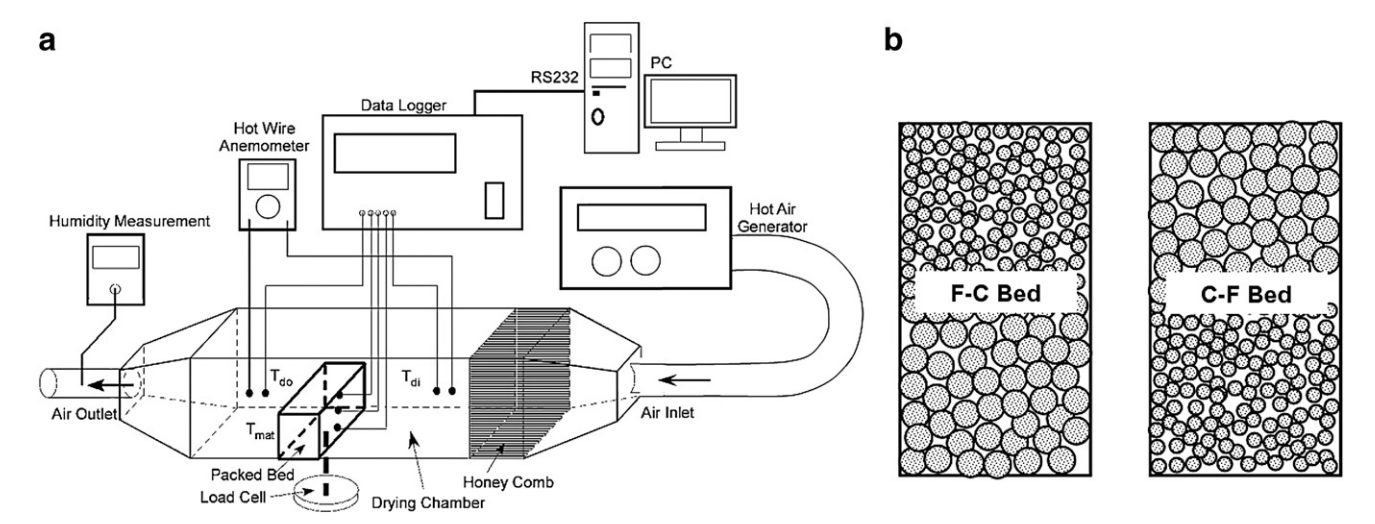


Fig. 1. Schematic of experimental facility: (a) Equipment setup; (b) Multi-layered porous packed bed (Sample).

${\bf 3.} \ The \ characteristic \ of \ moisture \ transport \ in \ multi-layered \ porous \ packed \ beds$

As shown in Fig. 3 shows the typical multi-layered packed bed to be stated. The multi-layered packed beds are arranged in different configurations as follows:

- (a) F–C bed, the fine particles (average diameter of 0.15 mm) is over the coarse particles (average diameter of 0.4 mm).
- (b) C–F bed, the coarse particles (average diameter of 0.4 mm) is over the fine particles (average diameter of 0.15 mm).

It is observed that the moisture content profiles are not uniform in multi-layered packed beds. During convective drying, higher moisture content occurs in the fine bed while the moisture content inside coarse bed remains lower compared with the initial state. This is a result of capillary action.

From a macroscopic point of view, we will consider liquid water transport at the interface between two beds where the difference in particle size is considered. Fig. 4 shows typical moisture characteristic curve (relationship between capillary pressure (p_c) and water saturation (s)) for the different particle sizes. In the case of the same capillary pressure, a smaller particle size corresponds to higher moisture content. Considering the case where two particle sizes having the same capillary pressure at the interface of different particle sizes are justified, as shown in Fig. 5. Since the capillary pressure has the same value at the interface between two beds the moisture content becomes discontinuous at the interface. This is a result of the differences in capillary pressure for the two particle layer. The physical and transport properties of the two sizes of particles composing the bed are shown in Table 1.

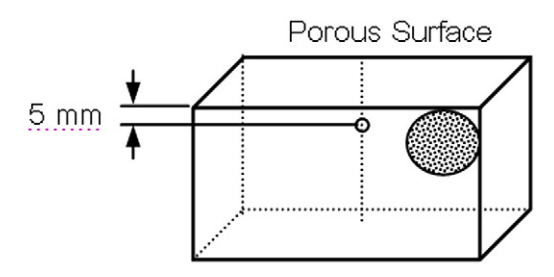


Fig. 2. The positions of temperature measurement in porous packed bed.

4. Mathematical formulation of problem

Schematic diagram of the convective drying model for multilayered porous packed bed is shown in Fig. 6 [21]. When a porous packed bed is heated by hot air flowing over its upper surface, the heat is transferred from the top of porous packed bed into the interior. Therefore, the temperature gradient is formed in the bed, and the

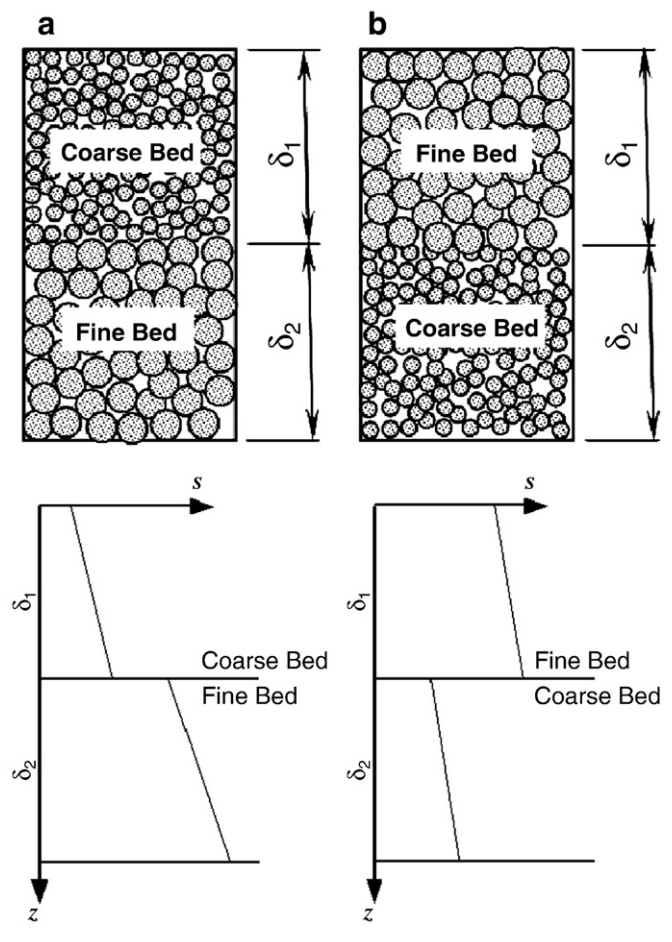


Fig. 3. Shows the typical profile of moisture content in multi-layered porous packed bed during convective drying in the cases of: (a) C–F bed (b) F–C bed.

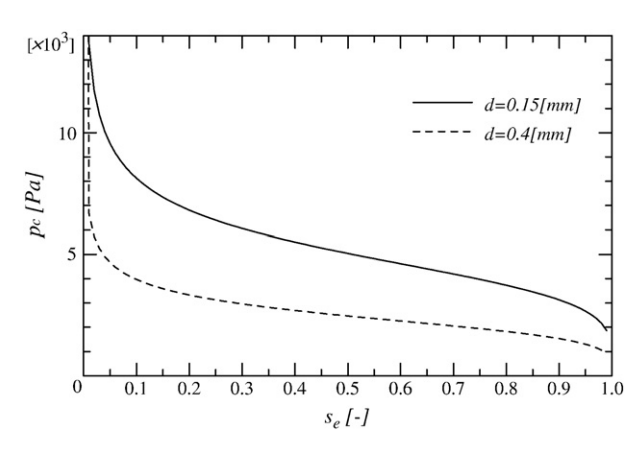
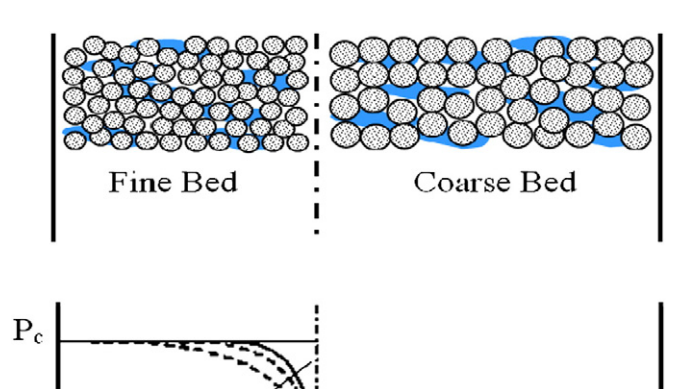


Fig. 4. Typical relationship between capillary pressure and water saturation [21].

liquid phase at the upper surface of porous packed bed evaporates by the variation of saturated vapor concentration corresponding to this temperature gradient as long as the surface remains wetted. In analysis, the main assumptions involved in the formulation of the transport model are:

- 1. The capillary porous material is rigid and no chemical reactions occur in the sample.
- 2. Local thermodynamics equilibrium is reached among each phase.
- 3. The gas phase is ideal in the thermodynamics sense.
- 4. The process can be modeled as steady-flow.
- 5. The multi-layered porous packed bed sample side wall is perfectly except the top surface insulated, hence adiabatic.
- In a macroscopic sense, the porous packed bed is assumed to be homogeneous and isotropic, and liquid water is not bound to the solid matrix.



t=0

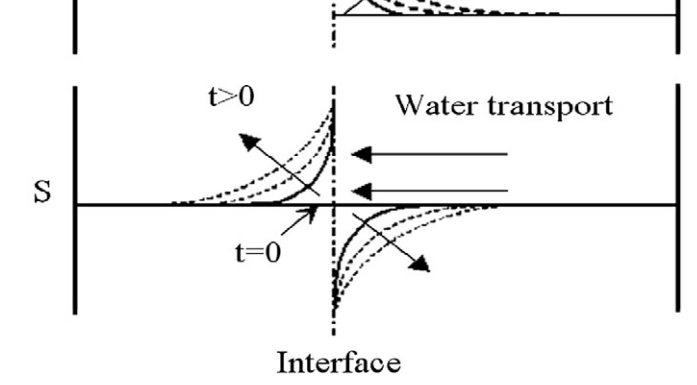


Fig. 5. Schematic diagram of water transport at the interface of multi-layered porous packed bed during convective drying process.

Table 1The characteristic of water transport in porous packed bed [21].

Diameter, d (mm)	Porosity, ϕ	Permeability, k (m ²)
0.15	0.387	8.41×10^{-12}
0.4	0.371	3.52×10^{-11}

- 7. A dry layer (evaporation front) is formed immediately after water saturation approaches the irreducible value.
- 8. The volumes of the upper layer and lower layer are equal.
- 9. The distributions of water saturation in the layered porous packed beds differ greatly depending on the structure of layered porous packed beds even if the total volume of water that exists among the pores in the porous packed beds is identical.

By energy and exergy analyses in drying process of multi-layered porous packed bed using hot air, the main basic equations are given as follows:

4.1. Energy analysis

A schematic diagram of the model is shown in Fig. 6. By applying the principle of conservation of mass and energy in the sample, the governing equation of mass and energy for all phases can be derived by using the volume average technique. The main transport mechanism describes moisture movement during drying by means of convection mode within the sample including liquid flow driven by capillary pressure gradient and gravity while the vapor is driven by the gradient of the partial pressure of the evaporating species. The traditional methods of thermal system analysis are based on the first law of thermodynamics. These methods use an energy balance on the control volume to determine heat transfer between the system and its environment. The first law of thermodynamics introduces the concept of energy conservation, which states that energy entering a thermal system with fuel, electricity, flowing streams of matter, and so on is conserved and cannot be destroyed. In general, energy balances provide no information on the quality or grades of energy crossing the thermal system boundary and no information about internal losses.

The drying process includes the process of heating, cooling and humidification. The process can be modeled as steady-flow processes by applying the steady-flow conservation of mass (for both dry air and moisture) and conservation of energy principles, General equation of mass conservation of drying air:

$$\sum \dot{m}_{ai} = \sum \dot{m}_{ao} \tag{1}$$

General equation of mass conservation of moisture:

$$\sum_{i} (\dot{m}_{wi} + \dot{m}_{mp}) = \sum_{i} \dot{m}_{wo}$$
or
$$\sum_{i} (\dot{m}_{ai} w_i + \dot{m}_{mp}) = \sum_{i} \dot{m}_{ai} w_o$$
(2)

General equation of energy conservation:

$$\dot{Q} - \dot{W} = \sum \dot{m_o} \left(h_o + \frac{V_o^2}{2} \right) - \sum \dot{m_i} \left(h_i + \frac{V_i^2}{2} \right)$$
 (3)

where the changes in kinetic energy of the fan were taken into consideration while the potential and kinetic energy in other parts of the process were neglected. During the energy and exergy analyses of porous packed bed drying process, the following equations were used to compute the enthalpy of drying air.

$$h = c_{pda}T + wh_{sat@T}$$
 (4)

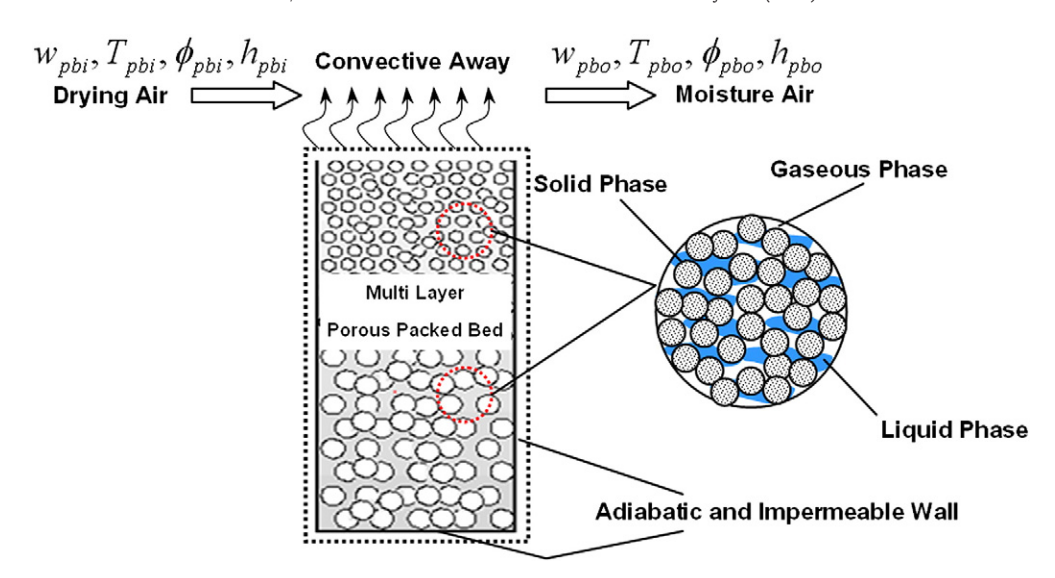


Fig. 6. Physical model of multi-layered porous packed bed.

The enthalpy equation of the fan outlet was obtained Bejan [22] using Eq. (5) as below:

$$h_{fo} = \left[\left(\dot{W}_f - \frac{V_{fo}^2}{2^*1000} \right) \left(\frac{1}{\dot{m}_{da}} \right) \right] + h_{f_i}$$
 (5)

where, h_{f_i} characterizes the enthalpy of drying air at the inlet of the fan, h_{fo} the enthalpy at the outlet of the fan, V_{fo} the drying air velocity at the outlet of the fan, W_f fan energy and \dot{m}_{da} mass flow of drying air. Considering the values of dry bulb temperature and enthalpy from Eq. (5), the specific and relative humidity of drying air at the outlet of the fan were determined Akpinar [16]. The inlet conditions of the heater were assumed to be equal to the outlet conditions of the fan. The useful energy gained from the heater enters the drying chamber as the convection heat source, which was defined as:

$$\dot{Q}_u = \dot{m}_{da} C p_{da} (T_{ho} - T_{hi}) \tag{6}$$

where T_{ho} , T_{hi} are the outlet and inlet temperature of air at the heating section. The inlet conditions of the drying chamber were determined depending on the inlet temperatures and specific humidity of drying air. It was considered that the mass flow rate of drying air was equally passed throughout the chamber. The specific humidity at the outlet of the chamber can be defined as:

$$w_{pbo} = w_{pbi} + \frac{\dot{m}_{wpb}}{\dot{m}_{da}} \tag{7}$$

where, w_{pbi} denotes the specific humidity at the inlet of the porous packed bed chamber, \dot{m}_{wpb} the mass flow rate of the moisture removed from porous packed bed samples. The heat utilized during the humidification process at the chamber, can be estimated by

$$\dot{Q}_{pb} = \dot{m}_{da} \left(h_{pbi@T} - h_{pbo@T} \right) \tag{8}$$

where, $h_{pbi@T}$ and $h_{pbo@T}$ identify orderly the enthalpies at the inlet and outlet of porous packed bed chamber. The enthalpy of moisture air outlet of porous packed bed chamber can be defined as:

$$h_{pbo@T} = h_{pbi@T} - w_{pbo}h_{sat@T}$$
 (9)

where w_{pbo} is the amount of product moisture evaporated. The energy utilization ratio for the drying chamber can be obtained using the following expression Akpinar [16]:

$$EUR_{dc} = \frac{\dot{m}_{da}(h_{pbi@T} - h_{pbo@T})}{\dot{m}_{da}Cp_{da}(T_{ba} - T_{bi})}.$$
(10)

4.2. Exergy analysis

The second law of thermodynamics introduces the useful concept of exergy in the analysis of thermal systems is show in Fig. 6. As known, exergy analysis evaluates the available energy at different points in a system. Exergy is a measurement of the quality or grade of energy and it can be destroyed in the thermal system. The second law states that part of the exergy entering a thermal system with fuel, electricity, flowing streams of matter, or other sources is destroyed within the system due to irreversibilities. The second law of thermodynamics uses an exergy balance for the analysis and the design of thermal systems. In the scope of the second law analysis of thermodynamics, total exergy of inflow, outflow and losses of the drying chamber are estimated. The basic procedure for exergy analysis of the chamber is determined the exergy values at steadystate points and the reason of exergy variation for the process. The exergy values are calculated by using the characteristics of the working medium from a first law energy balance. For this purpose, the mathematical formulations used to carry out the exergy balance are as show below Ahern [23].

$$\begin{split} \textit{Exergy} &= (u - u_{\scriptscriptstyle{\infty}} \) - T_{\scriptscriptstyle{\infty}}(s - s_{\scriptscriptstyle{\infty}}) + \frac{P_{\scriptscriptstyle{\infty}}}{J}(v - v_{\scriptscriptstyle{\infty}}) + \frac{V^2}{2gJ} + (z - z_{\scriptscriptstyle{\infty}})\frac{g}{g_cJ} \\ & \textit{internal entropy} \quad \textit{work} \quad \textit{momentum gravity} \\ & \textit{energy} \\ & + \sum_{c} (\mu_c - \mu_{\scriptscriptstyle{\infty}}) N_c + E_i A_i F_i (3T^4 - T_{\scriptscriptstyle{\infty}}^4 - 4T_{\scriptscriptstyle{\infty}}T^3) + \dots \\ & \textit{chemical} \quad \textit{radiation emission} \end{split}$$

The subscript ∞denotes the reference conditions. In the exergy analyses of many systems, only some of the terms shown in Eq. (11) are used but not all. Since exergy is energy available from any source, it can be developed using electrical current flow, magnetic fields, and

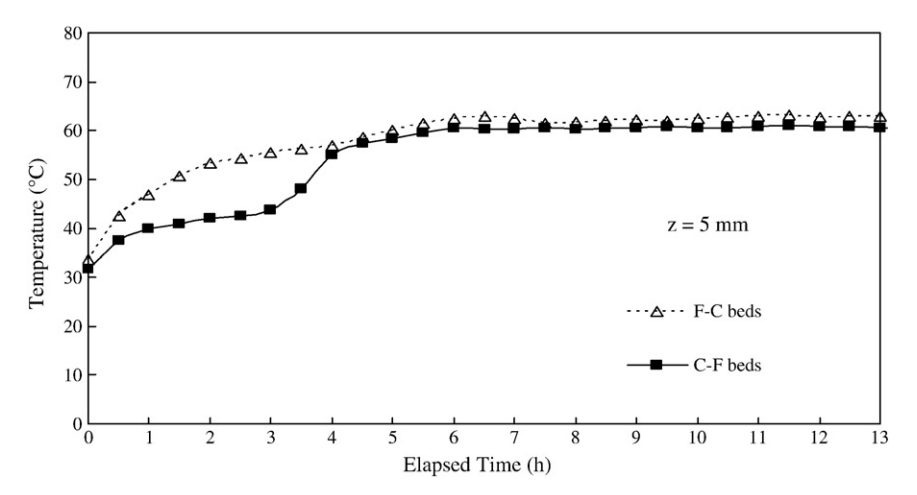


Fig. 7. The variation of temperature profiles with respect to time.

diffusion flow of materials. One common simplification is to substitute enthalpy for the internal energy and PVterms that are applicable for steady-flow systems. Eq. (11) is often used under conditions where the gravitational and momentum terms are neglected. In addition to these, the pressure changes in the system are also neglected because of $v \cong v_\infty$, hence Eq. (11) is reduced as:

$$\textit{Exergy} = \bar{c}_p \left[(T - T_{\infty}) - T_{\infty} \ln \frac{T}{T_{\infty}} \right] \tag{12}$$

The inflow and outflow of exergy can be found using the above expression depending on the inlet and outlet temperatures of the drying chamber. Hence, the exergy loss is determined as:

Exergy loss = Exergy inflow – Exergy outflow
$$\sum Ex_i = \sum Ex_i - \sum Ex_o$$
(13)

The exergy inflow for the chamber is stated as below

$$Ex_{dci} = Ex_{pbi} = \overline{c}_{p_{da}} \left[(T_{dci} - T_{\infty}) - T_{\infty} \ln \frac{T_{dci}}{T_{\infty}} \right]$$
 (14)

The exergy outflow for the drying chamber is stated as:

$$Ex_{dco} = Ex_{pbo} = \bar{c}_{pda} \left[(T_{dco} - T_{\infty}) - T_{\infty} \ln \frac{T_{dco}}{T_{\infty}} \right]$$
 (15)

The exergetic efficiency can be defined as the ratio of the product exergy to exergy inflow for the chamber as outlined below:

$$Exergy \, Efficiency = \frac{Exergy \, inflow - Exergy \, loss}{Exergy \, inflow}$$
 (16)

$$\eta_{Ex} = 1 - \frac{Ex_L}{Ex_i}. \tag{17}$$

5. Results and discussion

Fig. 7 shows the measured temperature profiles within the multi-layered porous packed beds for $s_0 = 0.5$, $T_a = 70(^{\circ}\text{C})$, $U_{\infty} = 1.2 \text{ (m/s)}$ and bed depth (z) at a level of 5 mm in cases of F–C and C–F beds as a function of elapsed time. The physical properties are given in Table 1. It can be observed that at the early stage of the drying process the temperature increase in both cases are nearly the same profiles. It is well-known that the temperature increases as drying progresses. This is because the latent heat transfer in evaporation process is retained due to the decline of the mass transfer rate together with the decreases of average moisture content. Nevertheless the temperature profile of the F–C bed increases with a higher rate than the C–F bed. This is because the dry layer formed earlier in the F–C bed and abrupt temperature rise occurs as the dry bulb temperature is approached. On the other hand, in the case of the C–F bed the temperature slowly increases in comparison with the F–C bed due to the late formation of

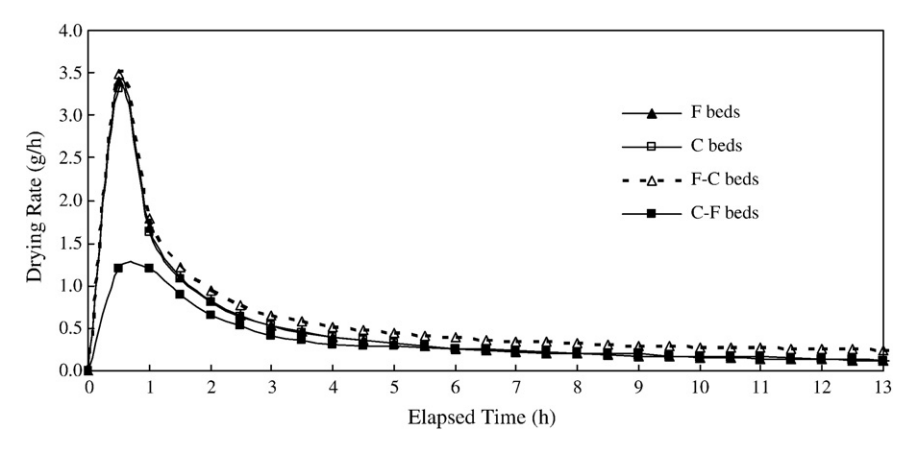


Fig. 8. The variation of drying rate with respect to time.

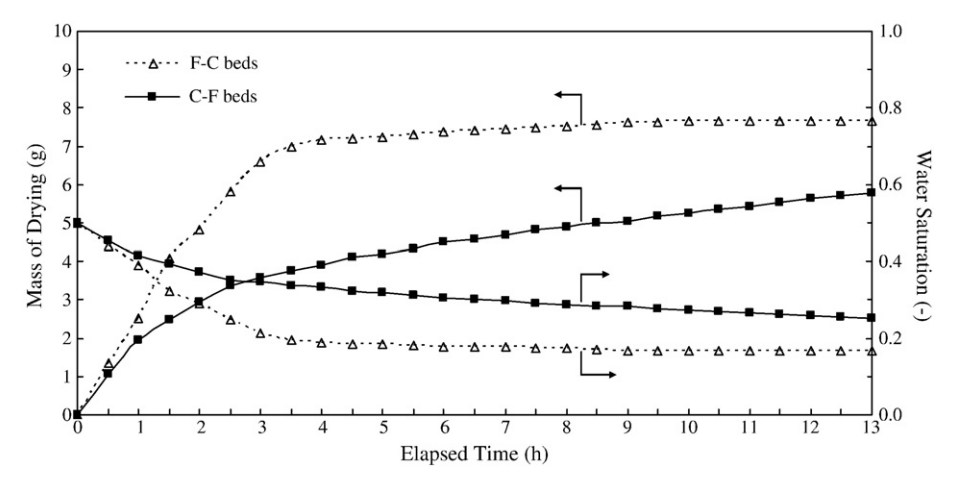


Fig. 9. The variation of water saturation and mass of drying in multi-layered porous packed bed with respect to time.

dry layer. In this regime [21], the liquid flows due to the gradient in the capillary pressure, and gravity can induce this flow. In addition, the presence of temperature gradient within the medium and the consecutive existence of surface tension gradient move the liquid away from the heated surface (opposing the capillary effect). Thus, capillarity, gravity, and thermo-capillarity flow are the most significant forces governing the liquid motion [24]. As the liquid flows out of the medium, the local saturation throughout the sample decreases with increasing heating time, where the saturation at the heated permeable surface decreased faster (because the liquid flow towards the lowest saturation and also the resistance to liquid flow increases with decreasing in saturation thus requiring large saturation gradients). At the end of the funicular regime the surface saturation drops to the irreducible saturation. The time at which this occurs is called the critical time. For a short period after heating, the heated surface will be intermittently dry. This is associated with a decrease in the drying rate. After this intermittent surface-drying period, the moving interface regime begins. The surface becomes completely dry, the surface temperature increases rapidly, and the heat transferred to the porous medium results in penetration of the evaporation front (a moving interface) into the medium.

At the longer drying time, the temperature profile at any instant tends to be constant shape throughout the region. In this period, the vapor diffusion effect plays an important role in the moisture migration mechanism because of the sustained vaporization that is generated within the sample. The vapor is superheated in the dry region (temperature distribution in the dry region is shown in Fig. 7) and in equilibrium with the liquid in the wet region. As the elapsed

time increases, the total pressure in the wet region increases indicating significant bulk evaporation as a consequence of a rise in the temperature of the wet region.

Figs. 8 and 9 show the variations of drying mass and drying rate with respect to time for the two packed packed beds (F–C and C–F beds). It is observed that the variations of drying mass and drying rate and temperature are interrelated. The drying speed is greatly different although the initial water saturation is the same. The F–C bed dries faster than C–F bed. This is due to the difference in the moisture content in the neighborhood of the drying surface. Since the driving force of heat and mass transfer is very large when moisture content and temperature in neighborhood of the drying surface is high. Consequently, the drying is very fast in case of F–C bed.

In the microscopic sense, the drying rate rises quickly in the early stages of drying (which corresponds to higher moisture content at the upper surface) and then decreases and reaches a plateau before decreasing again when the formation of a drying front is established. It is evident from the figure that the increase in drying rate can become significant when the F–C bed is utilized. This is a result of the strong effect of capillary pressure in F–C bed. For this case the capillary pressure easily overcomes the resistance caused by the lower permeability and maintains a supply of liquid water near the surface.

In the case of two-layered packed beds (F–C bed and C–F bed), the moisture content profiles become discontinuous at the interface between the two layers, namely, the moisture content in the upper layer is higher than that for the lower layer in F–C bed, while the moisture content in the upper layer is lower than that for the C–F bed. This is because the equilibrium water saturation under the same

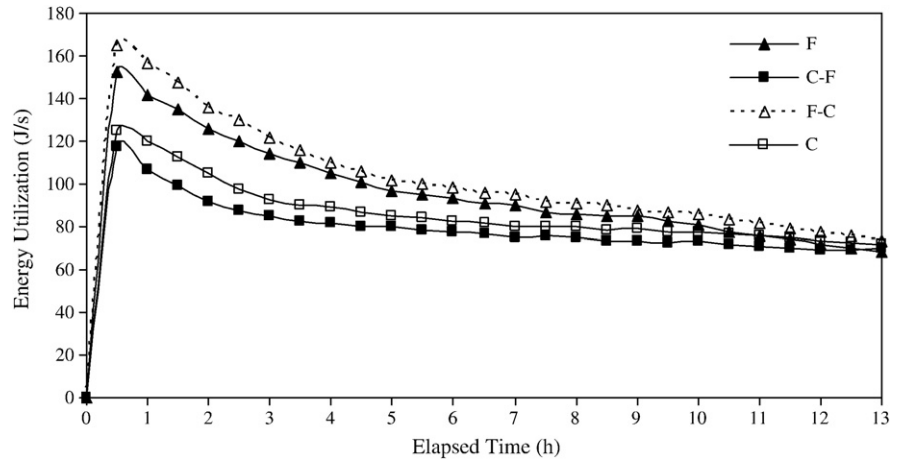


Fig. 10. Variation of energy utilization and drying time with different porous packed bed.

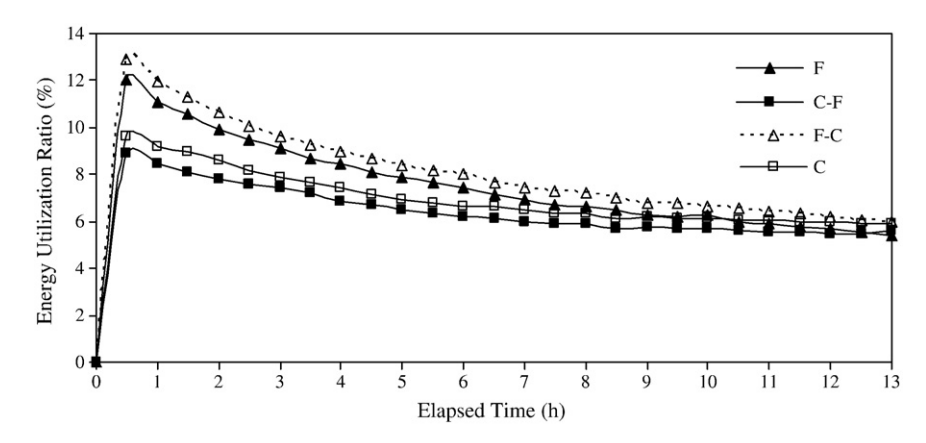


Fig. 11. Variation of energy utilization ratio with different porous packed bed.

capillary pressure differs according to the particle sizes smallest particle size corresponding to higher water saturation. Therefore, the drying kinetics is strongly influenced by the difference in water saturation. Continuing the drying process (Fig. 9) causes the average water saturation inside the F–C bed to decrease quickly in comparison with the C–F bed. In the case of the C–F bed, in contrast to that F–C bed, the moisture content in the upper layer (C bed) is very low and the dry layer is formed rapidly while the moisture content in the lower layer (F bed) remains high. This is due to the C bed (which corresponds to a lower capillary pressure) located above the F bed retards the upward migration of liquid water through the interface between two layers and also due to the effect of gravity.

According to the experimental results from Figs. 7–9, these results can be used as the input parameters for analyzing the energy utilization (Eqs. (8) to (10)) and exergy efficiency (Eqs. (11) to (17)) as follows:

Fig. 10 shows the variation of energy utilization as a function of drying time of different configurations and drying time. The energy utilization is relatively high at the beginning of drying process due to the high moisture content of the sample, and consequently gradually decrease because the low moisture content of the samples at the end of the process.

Fig. 11 shows the variation of energy utilization ratio against drying time of F–C and C–F packed bed. Energy balance is analyzed to evaluate the energy utilization ratio. The values of energy utilization ratio in drying chamber are calculated by using Eq. (10). When velocity and the temperature of hot air are kept constantly, the energy utilization ratio values are seem to be similar to energy utilization due to energy inlet of drying process to be constant.

In order to calculate the exergetic efficiency of the drying process, exergy analysis is taken into consideration. The exergy inflow rates

were calculated by using Eq. (14) as function of the ambient and inlet temperatures. The exergy inflow during the drying of multi-layered porous packed bed is attracted by drying layered of porous packed bed. The exergy outflows are calculated by using Eq. (15) and during the experiments which varied. It was observed that the exergy outflow from the drying chamber slowly increases with an increase of the drying time.

The exergetic efficiency of the drying chamber increases with an increase of drying time as shown in Fig. 12. The variation of exergy efficiency with respect to time is inversely with energy utilization ratio. This is because during drying process the available energy in the drying chamber increases as an increase of drying time, since moisture content decreases with time. The effect of the multi-layered on the drying time as well as the exergy efficiency of the drying system is also presented. The exergy efficiencies in case of C–F bed are higher than that of the F–C bed approximate 10% after 1 h of drying time thought the drying process. The results show that the energy utilization and exergy efficiency in Figs. 10–12 are strongly depended of layered configuration and particle size as described in Figs. 1–9.

6. Conclusion

The experimental analysis presented in this paper describes many important interactions within multi-layered porous materials during convective drying. The following paragraph summarizes the conclusions of this study:

The effects of particle sizes and layered configuration on the overall drying kinetics are clarified. The drying rate in the F–C bed is slightly higher than that of the C–F bed. This is because the higher capillary pressure for the F–C bed results in to maintain a wetted drying surface for a longer period of time. The F–C bed displays the

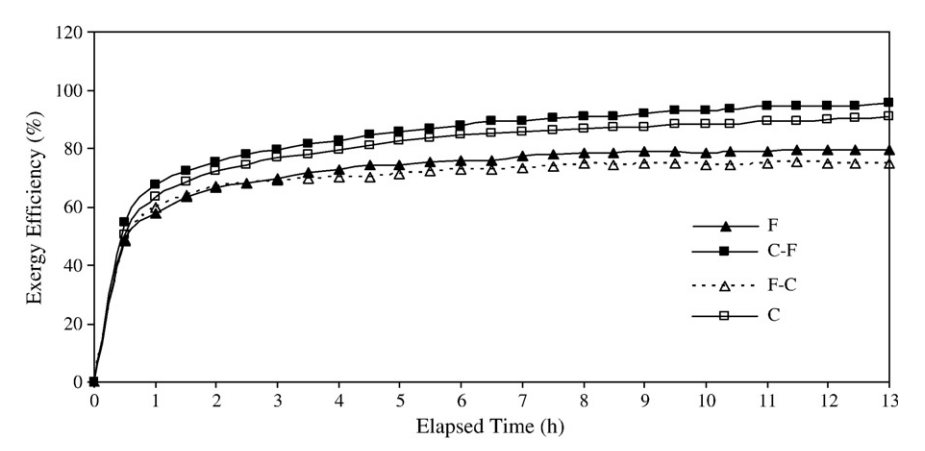


Fig. 12. Variation of exergy efficiency with different porous packed bed.

drying curve which differentiates it from the others. It has a shorter drying time due to the strong effect of capillary action.

Energy and exergy of the drying process of the multi-layered porous packed bed were analyzed. It can be concluded that energy utilization, energy utilization ratio and exergy efficiency strongly depend on particle size and multi-layered configurations

Acknowledgment

The authors would like to express their appreciation to the Commission on Higher Education, Thailand and Thailand Research Fund (TRF) for providing financial support for this study.

References

- I. Dincer, M.A. Rosen, Energy, environmental and sustainable development, Applied Energy 46 (1999) 427–440.
 I. Dincer, A.Z. Sahin, Incorporation of the dincer number into the moisture
- [2] I. Dincer, A.Z. Sahin, Incorporation of the dincer number into the moisture diffusion equation, International Communications in Heat and Mass Transfer 3 (2004) 109–119.
- [3] A.S. Mujumdar, An overview of innovation in industrial drying: current status and R&D needs, Transport in Porous Media 66 (2007) 3–18.
- [4] I. Białobrzewski, M. Zielińska, A.S. Mujumdar, M. Markowski, Heat and mass transfer during drying of a bed of shrinking particles — simulation for carrot cubes dried in a spout-fluidized-bed drier, International Journal of Heat and Mass Transfer 51 (2008) 4704–4716.
- [5] N.M. Panagiotou, A.K. Stubos, G. Bamopoulos, Z.B. Maroulis Drying, kinetics of a multi-component mixture of organic solvents, Drying Technology 17 (1999) 2107–2122.
- [6] A.G. Yiotis, A.K. Stubos, A.G. Boudouvis, Y.C. Yortsos, A 2-D pore-network model of the drying of single-component liquids in porous media, Advances in Water Resources 24 (2001) 439–460.
- [7] R.G. Carbonell, S. Whitaker, Dispersion in pulsed systems II Theoretical developments for passive dispersion in porous, Chemical Engineering Science 38 (1983) 1795–1802.
- [8] T. Tekcin, M. Bayramogilu, Exergy loss minimization analysis of sugar production process from sugar beet, Food and Bioproducts Processing 76 (1998) 149–154.

- [9] M.A. Rosen, I. Dincer, On exergy and environmental impact, International Journal of Energy Research 21 (1998) 643–654.
- [10] M.A. Rosen, D.S. Scott, Entropy production and exergy destruction: Part I hierarchy of earth's major constituencies, International Journal Hydrogen Energy 28 (2003) 1307–1313.
- [11] A.I. Liapis, R. Bruttini, Exergy analysis of freeze drying of pharmaceuticals in vials on trays, International Journal of Heat and Mass Transfer 51 (2008) 3854–3868.
- [12] Y. Liu, Y. Zhao, X. Feng, Exergy analysis for a freeze-drying process, Applied Thermal Engineering 28 (2008) 675–690.
- [13] M. Kanoglua, I. Dincer, M.A. Rosen, Understanding energy and exergy efficiencies for improved energy management in power plants, Energy Policy 35 (2007) 3967–3978.
- [14] S. Syahrul, I. Dincer, F. Hamdullahpur, Thermodynamics modeling of fluidized bed drying of moist particles, International Journal of Thermal Sciences 42 (2003) 691–701.
- [15] I. Dincer, A.Z. Sahin, A new model for thermodynamics analysis of a drying process, International Journal of Heat and Mass Transfer 47 (2004) 645–652.
- [16] E.K. Akpinar, Energy and exergy analyses of drying of red pepper slices in a convective type dryer, International Communication in Heat and Mass Transfer 31 (2004) 1165–1176.
- [17] E.K. Akpinar, A. Midilli, Y. Bicer, Energy and exergy of potato drying process via cyclone type dryer, Energy Conversion and Management 46 (2005) 2530–2552.
- [18] N. Colak, A. Hepbasli, Performance analysis of drying of green olive in a tray dryer, Journal of Food Engineering 80 (2007) 1188–1193.
- [19] I. Ceylan, M. Aktas, H. Dogan, Energy and exergy analysis of timber dryer assisted heat pump, Applied Thermal Engineering 27 (2007) 216–222.
- [20] R. Prommas, P. Rattanadecho, D. Cholaseuk, Energy and exergy analyses in drying process of porous media using hot air, International Communications in Heat and Mass Transfer 37 (2010) 372–378.
- [21] P. Ratanadecho, K. Aoki, M. Akahori, Experimental and numerical study of microwave drying in unsaturated porous material, International Communications in Heat and Mass Transfer 28 (2001) 605–616.
- [22] A. Bejan, Advanced Engineering Thermodynamics, John Wiley and Sons, New York, 1998.
- [23] J.E. Ahern, The Exergy Method of Energy Systems Analysis, John Wiley, New York, 1980.
- [24] M. Kaviany, J. Rogers, Funicular and evaporative-front regimes in convective drying of granular beds, International Journal of Heat and Mass Transfer 35 (1992) 469–480.

Natural Convection in a Saturated Variable-Porosity Medium Due to Microwave Heating

Watit Pakdee¹

e-mail: pwatit@engr.tu.ac.th e-mail: wpele95@yahoo.com

Phadungsak Rattanadecho

Department of Mechanical Engineering, Research Center of Microwave Utilization in Engineering (RCME), Thammasat University, Klong Luang, Pathumthani, Thailand Microwave heating of a porous medium with a nonuniform porosity is numerically investigated based on a proposed numerical model. A two-dimensional variation of porosity of the medium is considered. The generalized non-Darcian model developed takes into account the presence of a solid drag and the inertial effect. The transient Maxwell's equations are solved by using the finite difference time domain method to describe the electromagnetic field in the waveguide and medium. The temperature profile and velocity field within a medium are determined by solution of the momentum, energy, and Maxwell's equations. The coupled nonlinear set of these equations is solved using the SIMPLE algorithm. In this work, a detailed parametric study is conducted on heat transport inside a rectangular enclosure filled with a saturated porous medium of constant or variable porosity. The numerical results agree well with the experimental data. Variations in porosity significantly affect the microwave heating process as well as the convective flow pattern driven by microwave energy. [DOI: 10.1115/1.4003535]

Keywords: microwave heating, variable porosity, natural convection, saturated porous media, rectangular waveguide

1 Introduction

Microwave heating of a porous medium is widely implemented in industries, such as heating food, ceramics, biomaterials, concrete manufacture, etc., since microwave energy has many advantages such as short time process, high thermal efficiency, environmentally friendly credentials, and high product quality. Microwave radiation penetrates into a material and heats it by a dipolar polarization that occurs million times per second.

A number of previous works have focused on the drying of unsaturated porous media in which heat and mass transfers were modeled [1-6]; however, most of these dealt with solid materials and focused on heat conduction within a medium. Some works studied a natural convection induced by microwave heating of fluids since a complex distribution of electromagnetic waves is shown to be a complicated effect on flow field [7–11]. The effects of natural convection and dielectric properties on liquid layers were studied numerically and experimentally. The heating kinetics strongly depended on the dielectric properties [7]. Natural convection due to buoyancy force strongly affects flow patterns within the water layer during the microwave heating process and clearly enhances temperature distribution in the layer [8]. Recently, Cha-um et al. [8] experimentally investigated the heating process within a packed bed filled with glass beads and water and found that the location of the sample relative to that of heat source had an important effect on the pattern of heating. Other recent works focused on microwave driven convection in pure liquids [9–11]. While the previous studies were based on pure liquids, we pay attention to a natural convection induced by microwave energy in a fluid-saturated porous medium.

Furthermore, all the previous investigations referred did not account for the effect of variable porosity in the vicinity of the impermeable wall. A region of higher porosity near the wall that forms due to the packing of the porous spheres near the column

¹Corresponding author.

Contributed by the Heat Transfer Division of ASME for publication in the JOURNAL OF HEAT TRANSFER. Manuscript received May 11, 2010; final manuscript received January 14, 2011; published online March 8, 2011. Assoc. Editor: William P. Klinzing.

wall is not as efficient as that away from the wall toward the column center [12]. Benenati and Brosilow [13] found a distinct porosity variation with a high porosity region close to the wall in packed beds. Values of porosity that are highly close to an impermeable wall decrease to an asymptotic value at about four to five sphere diameters away from it [14,15]. Many researchers found that the variation of porosity might significantly affect flow patterns as well as heat transfer features [13,16–18]. The porosity of the bed exhibits sinusoidally damping decay especially at locations near the wall [13]. This phenomenon leads to the channeling effect that could significantly modify flow patterns [14,19–21]. Hsiao et al. [17] showed that including the effects of variable porosity and thermal dispersion on natural convection in the region of the heated horizontal cylinder in an enclosed porous medium increases the average Nusselt number and reduces the error between the experimental data and their solutions. Thus, the effects of porosity variation should be taken into account in practice [16,17,22,23].

Therefore, in the present study, we propose a numerical model for the microwave heating of a saturated porous packed bed in which the porosity variation is considered. The non-Darcian boundary and inertial effects are taken into account. Heating characteristic and flow pattern are numerically investigated. The numerical model is validated with experimental data obtained using a rectangular waveguide operated under the microwave of ${\rm TE}_{10}$ mode.

2 Experimental Setup

Figure 1 shows the experiment apparatus for microwave heating of a saturated porous medium using a rectangular waveguide. Actual image of the apparatus is shown in Fig. 1(a). The microwave system is a monochromatic wave of TE_{10} mode operating at a frequency of 2.45 GHz. From Fig. 1(b), magnetron (No. 1) generates microwaves and transmits them along the z-direction of the rectangular waveguide (No. 5) with inside cross-sectional dimension of $109.2 \times 54.61 \text{ mm}^2$ that refers to a testing area (circled) and a water load (No. 8) that is situated at the end of the waveguide. On the upstream side of the sample, an isolator is used to trap any microwaves reflected from the sample to prevent dam-

Journal of Heat Transfer

Copyright © 2011 by ASME

JUNE 2011, Vol. 133 / 062502-1

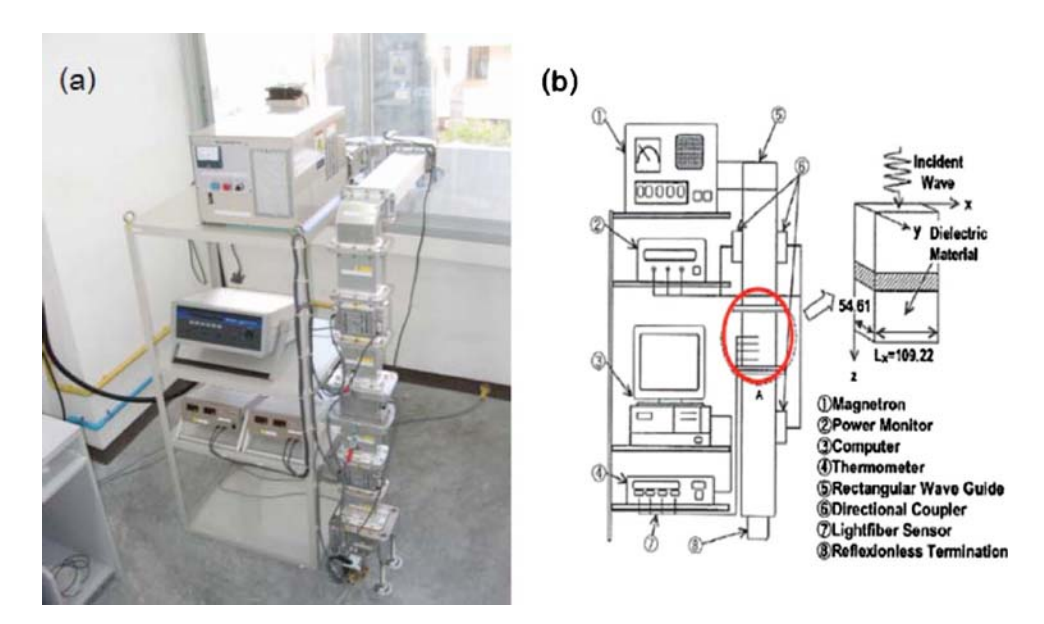


Fig. 1 The microwave heating system with a rectangular waveguide

age to the magnetron. The powers of incident, reflected, and transmitted waves are measured by a wattmeter using a directional coupler (No. 6) (Micro Denshi, Saitama, Japan, model DR-5000). Fiberoptic probes (No. 7) (Luxtron Fluroptic thermometer (model 790, accurate to $\pm 0.5\,^{\circ}$ C)) are employed for temperature measurement. The probes are inserted into the sample and positioned on the XZ plane at Y=25 mm (see Fig. 2). Due to the symmetry, temperatures are only measured on one side of the plane. The samples are saturated porous packed beds composed of glass beads and water. The container, with a thickness of 0.75 mm, is made of polypropylene, which does not absorb microwave energy.

In our present experiment, a glass bead of 0.15 mm in diameter is examined. The averaged (freestream) porosity of the packed bed corresponds to 0.385. The dielectric and thermal properties of water, air, and glass bead are listed in Table 1.

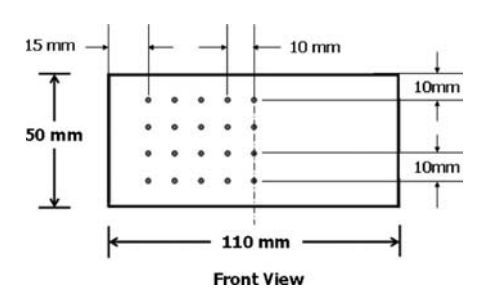


Fig. 2 Locations of temperature measurement in the symmetrical xz plane

3 Mathematical Formulation

3.1 Analysis of Electromagnetic Field. Electromagnetic waves are formed with a combination of electric waves and magnetic waves. The magnetic and electric fields of an electromagnetic wave are perpendicular to each other and to the direction of the wave. Microwave is a part of an electromagnetic spectrum that has a particular range of wavelengths. Since the electromagnetic field that is investigated is the microwave field in the TE₁₀ mode, there is no variation of field in the direction between the broad faces of the rectangular waveguide and it is uniform in the y-direction. Consequently, it is assumed that a two-dimensional heat transfer model in x- and z-directions will be sufficient to identify the microwave heating phenomena in a rectangular waveguide [7]. Further assumptions are as follows.

- The absorption of microwaves by air in a rectangular waveguide is negligible.
- (2) The walls of a rectangular waveguide are perfect conductors.
- (3) The effect of the sample container on the electromagnetic and temperature fields can be neglected.

The proposed model is considered in the TE_{10} mode so the Maxwell's equations can be written in terms of the electric and magnetic intensities:

$$\varepsilon \frac{\partial E_y}{\partial t} = \frac{\partial H_x}{\partial z} - \frac{\partial H_z}{\partial x} - \sigma E_y \tag{1}$$

Table 1 The electromagnetic and thermophysical properties used in the computations [24]

Property	Water	Glass bead
Heat capacity c_p (J kg ⁻¹ K ⁻¹)	4190	800
Thermal conductivity λ (W m ⁻¹ K ⁻¹)	0.609	1.0
Density ρ (kg m ⁻³)	1000	2500
Dielectric constant, a ε'.	$88.15 - 0.414T + (0.131 \times 10^{-2})T^2 - (0.046 \times 10^{-4})T^3$	5.1
Loss tangent, a tan δ	$0.323 - (9.499 \times 10^{-3})T + (1.27 \times 10^{-4})T^2 - (6.13 \times 10^{-7})T^3$	0.01

^aT is in °C.

062502-2 / Vol. 133, JUNE 2011

Transactions of the ASME

$$\mu \frac{\partial H_z}{\partial t} = -\frac{\partial E_y}{\partial x} \tag{2}$$

$$\mu \frac{\partial H_x}{\partial t} = \frac{\partial E_y}{\partial z} \tag{3}$$

where E and H denote electric field intensity and magnetic field intensity, respectively. Subscripts x, y, and z represent the x-, y-, and z-components of vectors, respectively. Finally, ε is the electrical permittivity, σ is the electrical conductivity, and μ is the magnetic permeability. These variables can be defined as follows:

$$\varepsilon = \varepsilon_0 \varepsilon_r \tag{4}$$

$$\mu = \mu_0 \mu_r \tag{5}$$

$$\sigma = 2\pi f \varepsilon \tan \delta \tag{6}$$

The dielectric properties of porous material depend on the temperature in which fractions of fluid and solid are considered based on porosity ϕ as follows [23]:

$$\varepsilon_r(T) = \varepsilon_r'(T) - j\varepsilon_r''(T) \tag{7}$$

where

$$\varepsilon_r'(T) = \phi \varepsilon_{rf}'(T) + (1 - \phi)\varepsilon_{rp}' \tag{8}$$

$$\varepsilon_r''(T) = \phi \varepsilon_{rf}''(T) + (1 - \phi)\varepsilon_{rp}'' \tag{9}$$

where ϵ' and ϵ'' represent the dielectric constant and the dielectric loss, respectively.

The loss tangent coefficient can be written as

$$\tan \delta(T) = \frac{\varepsilon_r''(T)}{\varepsilon_r'(T)} \tag{10}$$

When the material is heated unilaterally, it is found that as the dielectric constant and loss tangent coefficient vary, the penetration depth and the electric field within the dielectric material vary. Penetration depth is a measure of how deep the electromagnetic radiation can penetrate into a material. A number of factors can influence penetration depth including properties of the material, intensity, and frequency of the electromagnetic wave. The penetration depth is used to denote the depth at which the power density has decreased to 37% of its initial value at the surface [6].

$$D_{p} = \frac{1}{\frac{2\pi f}{v} \sqrt{\frac{\varepsilon_{r}' \left(\sqrt{1 + \left(\frac{\varepsilon_{r}''}{\varepsilon_{r}'}\right)^{2} - 1\right)}{2}}}$$

$$= \frac{1}{\frac{2\pi f}{v} \sqrt{\frac{\varepsilon_{r}' (\sqrt{1 + (\tan \delta)^{2}} - 1)}{2}}}$$
(11)

where D_p is the penetration depth, ε_r'' is the relative dielectric loss factor, and v is the microwave speed. The penetration depth of the microwave power is calculated according to Eq. (11), which demonstrates how it depends on the dielectric properties of the material. It is noted that products of huge dimensions and with high loss factors may occasionally overheat a considerably thick layer of the outer surface. To prevent such a phenomenon, the power density must be chosen so that enough time is provided for the essential heat transfer between boundary and core. If the thickness of the material is less than the penetration depth, only a fraction of the supplied energy will become absorbed. For example, the dielectric properties of water show that water moderately dissipate electromagnetic energy into heat. This characteristic depends on the temperature. The water layer at low temperature typically shows a slightly greater potential for absorbing microwaves. In other words, an increase in the temperature typically decreases ε_r''

accompanied by a slight increase in ${\cal D}_p.$ The boundary conditions for the ${\rm TE}_{10}$ mode can be formulated as follows.

(1) Perfectly conducting boundary. Boundary conditions on the inner wall surface of waveguide are given by Faraday's law and Gauss's theorem:

$$E_{\parallel} = 0, \quad H_{\perp} = 0 \tag{12}$$

where subscripts \parallel and \perp denote the components of tangential and normal directions, respectively.

Continuity boundary condition. Boundary conditions along the interface between sample and air are given by Ampere's law and Gauss's theorem:

$$E_{\parallel} = E'_{\parallel}, \quad H_{\parallel} = H'_{\parallel}$$
 (13)

(3) The first-order absorbing boundary condition applied at both ends of rectangular waveguide:

$$\frac{\partial E_y}{\partial t} = \pm v \frac{\partial E_y}{\partial z} \tag{14}$$

where \pm represents forward and backward directions and vis the velocity of the wave.

The incident wave due to magnetron is given in Ref. [7], showing an oscillation of the electric and magnetic intensities by the magnetron:

$$E_{y} = E_{y_{\text{in}}} \sin\left(\frac{\pi x}{L_{x}}\right) \sin(2\pi f t) \tag{15}$$

$$H_{x} = \frac{E_{y_{\text{in}}}}{Z_{H}} \sin\left(\frac{\pi x}{L_{x}}\right) \sin(2\pi f t)$$
 (16)

where $E_{y_{in}}$ is the input value of electric field intensity, L_x is the length of the rectangular waveguide in the x-direction, and Z_H is the wave impedance defined as

$$Z_{H} = \frac{\lambda_{g} Z_{l}}{\lambda} = \frac{\lambda_{g}}{\lambda} \sqrt{\frac{\mu}{\varepsilon}}$$
 (17)

Here, Z_l is the intrinsic impedance dependent on the properties of the material and λ and λ_g are the wavelengths of microwaves in free space and the rectangular waveguide, respectively.

The power flux associated with a propagating electromagnetic wave is expressed by the Poynting vector:

$$s = \frac{1}{2} \operatorname{Re}(E \times H^*) \tag{18}$$

The Poynting theorem allows the evaluation of the microwave power input, which is represented as

$$P_{\rm in} = \int_{A} S dA = \frac{A}{4Z_H} E_{y_{\rm in}}^2$$
 (19)

3.2 Analysis of Temperature Profile and Flow Field. The physical problem and coordinate system are depicted in Fig. 3. The microwave is propagating to the xy plane while the transport phenomena on the xz plane are currently investigated. To reduce the complexity of the problem, several assumptions have been offered into the flow and energy equations.

- Corresponding to the electromagnetic field, the flow and temperature fields can be assumed to be a two-dimensional
- The effect of the phase change is neglected.
- (3) Boussinesq approximation is used to account for the effect of the density variation on the buoyancy force.

JUNE 2011, Vol. 133 / 062502-3

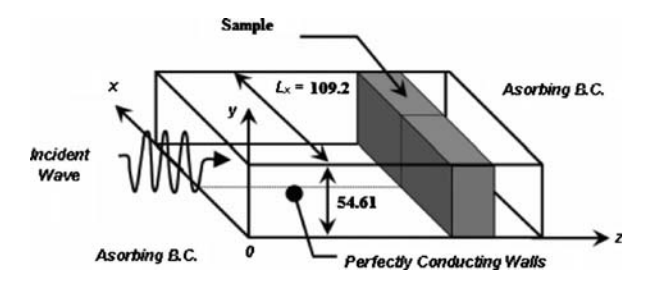


Fig. 3 Schematic of the physical problem

(4) The surroundings of the porous packed bed are insulated except at the upper surface where energy exchanges with the ambient air.

3.2.1 Flow Field Equation. The porous medium is assumed to be homogeneous and thermally isotropic. The saturated fluid within the medium is in a local thermodynamic equilibrium (LTE) with the solid matrix [25–27]. The validity regime of local thermal equilibrium assumption has been established [28]. The fluid flow is unsteady, laminar, and incompressible. The pressure work and viscous dissipation are all assumed to be negligible. The thermophysical properties of the porous medium are taken to be constant; however, the Boussinesq approximation takes into account the effect of density variation on the buoyancy force. The Darcy-Forchheimer-Brinkman model was used to represent the fluid transport within the porous medium [28,29]. The Brinkman's and the Forchheimer's extensions treat the viscous stresses at the bounding walls and the nonlinear drag effect due to the solid matrix, respectively [29]. Furthermore, the solid matrix is made up of spherical particles, while the porosity and permeability of the medium are varied depending on the distance from the wall. Using standard symbols, the governing equations describing the heat transfer phenomenon are given as follows.

Continuity equation:

$$\frac{\partial u}{\partial x} + \frac{\partial w}{\partial z} = 0 \tag{20}$$

Momentum equations:

$$\frac{1}{\varepsilon} \frac{\partial u}{\partial t} + \frac{u}{\varepsilon^2} \frac{\partial u}{\partial x} + \frac{w}{\varepsilon^2} \frac{\partial u}{\partial z} = -\frac{1}{\rho_f} \frac{\partial p}{\partial x} + \frac{v}{\varepsilon} \left(\frac{\partial^2 u}{\partial x^2} + \frac{\partial^2 u}{\partial z^2} \right) - \frac{\mu u}{\rho_f \kappa} - F(u^2 + w^2)^{1/2}$$
(2)

$$\frac{1}{\varepsilon} \frac{\partial w}{\partial t} + \frac{u}{\varepsilon^2} \frac{\partial w}{\partial x} + \frac{w}{\varepsilon^2} \frac{\partial w}{\partial z} = -\frac{1}{\rho_f} \frac{\partial p}{\partial z} + \frac{v}{\varepsilon} \left(\frac{\partial^2 w}{\partial x^2} + \frac{\partial^2 w}{\partial z^2} \right) - \frac{w\mu}{\rho_f \kappa} - F(u^2 + w^2)^{1/2} + g\beta(T - T_0)$$
(22)

where ε , ν , and β are the porosity, kinematics viscosity, and coefficient of thermal expansion of the water layer, respectively. The permeability κ and geometric F function are [16,30]

$$\kappa = \frac{d_p^2 \varepsilon^3}{175(1 - \varepsilon)^2} \tag{23}$$

$$F = \frac{1.75(1 - \varepsilon)}{d_p \varepsilon^3} \tag{24}$$

The porosity is assumed to vary exponentially with the distance from the wall [13,15,21]. Based on these previous studies, we proposed the variation of porosity within three confined walls of the bed: a bottom wall and two lateral walls. The expression that considers the variation of porosity in two directions in the xz plane is given by

$$\varepsilon = \varepsilon_s \left[1 + b \left\{ \exp\left(-\frac{bx}{d_p}\right) + \exp\left(-\frac{b(W - x)}{d_p}\right) + \exp\left(-\frac{bz}{d_p}\right) \right\} \right]$$
(25)

where d_p is the diameter of glass beads, ε_s known as the freestream porosity is the porosity far away from the walls, W is the width of the packed bed, and b and c are empirical constants. The dependencies of b and c to the ratio of the bed to bead diameter are small, and b and c were suggested to be 0.98 and 1.0, respectively [14].

3.2.2 Heat Transfer Equation. The temperature of the liquid layer exposed to the incident wave is obtained by solving the conventional heat transport equation with the microwave power absorbed included as a local electromagnetic heat generation term:

$$\sigma \frac{\partial T}{\partial t} + u \frac{\partial T}{\partial x} + w \frac{\partial T}{\partial z} = \alpha \left(\frac{\partial^2 T}{\partial x^2} + \frac{\partial^2 T}{\partial z^2} \right) + Q \tag{26}$$

where the specific heat ratio $\sigma = [\varepsilon(\rho c_p)_f + (1-\varepsilon)(\rho c_p)_s]/(\rho c_p)_f$ and $\alpha = k_e/(\rho c_p)_f$ is the thermal diffusivity.

The local electromagnetic heat generation term that is a function of the electric field is defined as

$$Q = 2\pi f \varepsilon_0 \varepsilon_r' \tan \delta (E_v)^2$$
 (27)

Boundary and initial conditions for these equations. Since the walls of the container are rigid, the velocities are zero. At the interface between the liquid layer and the walls of the container, zero slip boundary conditions are used for the momentum equations

At the upper surface, the velocity in the normal direction (w) and the shear stress in the horizontal direction are assumed to be zero, where the influence of Marangoni flow [7] can be applied:

$$\eta \frac{\partial u}{\partial z} = -\frac{d\xi}{dT} \frac{\partial T}{\partial x} \tag{28}$$

(2) The walls, except for the top wall, are insulated so no heat or mass exchanges:

$$\frac{\partial T}{\partial x} = \frac{\partial T}{\partial z} = 0 \tag{29}$$

(3) Heat is lost from the surface via natural convection and radiation:

$$-\lambda \frac{\partial T}{\partial z} = h_c (T - T_{\infty}) + \sigma_{\text{rad}} \varepsilon_{\text{rad}} (T^4 - T_{\infty}^4)$$
 (30)

(4) The initial condition of a medium is defined as

$$T = T_0 \quad \text{at } t = 0 \tag{31}$$

4 Numerical Procedure

The description of heat transport and flow pattern of liquid layer equations (20)–(24) and (26) requires specification of temperature (T), velocity components (u,w), and pressure (p). These equations are coupled to the Maxwell's equations (Eqs. (1)–(3)) by Eq. (27), which represents the heating effect of the microwaves in the liquid-container domain.

4.1 Electromagnetic Equations and FDTD Discretization. The electromagnetic equations are solved by using the finite difference time domain (FDTD) method. With this method, the electric field components (E) are stored halfway between the basic nodes while the magnetic field components (H) are stored at the center. Thus, they are calculated at alternating half-time steps. E and E field components are discretized by a central difference method (second-order accurate) in both spatial and time domains.

062502-4 / Vol. 133, JUNE 2011

Transactions of the ASME

4.2 Fluid Flow and Heat Transport Equations and Finite Control Volume Discretization. Equations (20)–(24) are solved numerically by using the finite control volume along with the semi-implicit method for pressure-linked equations (SIMPLE) algorithm developed by Patankar. The reason for using this method is the advantage provided by the flux conservation that avoids the generation of a parasitic source. The basic strategy of the finite control volume discretization method is to divide the calculated domain into a number of control volumes and then integrate the conservation equations over this control volume and over an interval of time $[t, t+\Delta t]$. At the boundaries of the calculated domain, the conservation equations are discretized by integrating over half the control volume, taking into account the boundary conditions. At the corners of the calculated domain, we used a quarter of the control volume. The fully Euler implicit time discretization finite difference scheme is used to arrive at the solution in time. Additionally, the details about numerical discretization of this method can be found in the recent literature.

4.2.1 The Stability and Accuracy of Calculation. The choice of spatial and temporal resolutions is motivated by reasons of stability and accuracy. To ensure stability of the time stepping algorithm, Δt must be chosen to satisfy the Courant stability condition and is defined as

$$\Delta t \le \frac{\sqrt{(\Delta x)^2 + (\Delta z)^2}}{v} \tag{32}$$

and the spatial resolution of each cell is defined as

$$\Delta x, \Delta z \le \frac{\lambda_g}{10\sqrt{\varepsilon_r}} \tag{33}$$

Corresponding to Eqs. (32) and (33), the calculation conditions are as follows.

- (1) Grid resolution is $100(x) \times 200(z)$.
- (2) Grid size: $\Delta x = 1.0922$ mm and $\Delta z = 1.0000$ mm.
- (3) Time steps: $\Delta t = 2 \times 10^{-12}$ s and $\Delta t = 0.01$ s are used corresponding to the electromagnetic field and temperature field calculations, respectively.
- (4) Relative error in the iteration procedures of 10⁻⁶ was chosen.

The mesh of 100×200 was found to be sufficient for the simulations carried out in the present study. Independence of the solutions on the grid size was examined through a number of test cases. The results indicate that negligible difference of solutions was achieved above the resolution of 80×160 [7].

4.2.2 The Iterative Computational Schemes. Since the dielectric properties of liquid layer samples are temperature dependent, to understand the influence of the electromagnetic fields on the microwave heating of a liquid layer, it is necessary to consider the coupling between electric field and temperature and fluid flow fields. For this reason, iterative computational schemes are required to resolve the coupled nonlinear Maxwell's equations, momentum, and heat transport equations.

The computational scheme is to first compute a local heat generation term by running an electromagnetic calculation with uniform properties determined from initial temperature data. The electromagnetic calculation is performed until a sufficient period is reached in which the representative average root mean square (rms) of the electric field at each point is computed and used to solve the time dependent temperature and velocity field. Using these temperatures, new values of the dielectric properties are calculated and used to recalculate the electromagnetic fields and then the microwave power absorption. All the steps are repeated until the required heating time is reached.

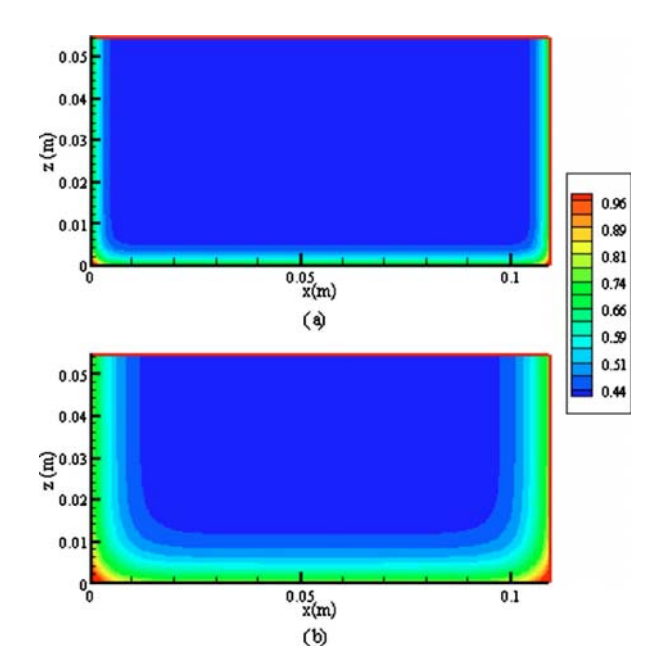


Fig. 4 Porosity distributions with the bead diameters: (a) 1 mm and (b) 3 mm

5 Results and Discussion

In the current simulations, the formulation that computes the variation of porosity in two directions given by Eq. (25) is employed to describe the two-dimensional porosity variation. The glass bead diameters of 1.0 mm and 3.0 mm are examined with which the freestream porosity is 0.385. The resulting calculations are illustrated in Fig. 4 on the x-z plane. Variations of the bed porosity were considered since it was proved that the porosity decayed from the wall [13,14]. As is clearly seen in the figure, the porosity is high in the vicinity of an impermeable boundary and reduces to a freestream value at about four to five bead diameters from the boundary [15]. The computed porosities vary according to the distances from the walls in two directions. Porosities are largest at the corners because it is not efficient to pack spherical beads at bed corners. The gradients of porosity are found to be lower with larger particle diameters.

To examine the validity of the mathematical model, the numerical results were compared with the experimental data. The description with regard to the experimental setup and associated

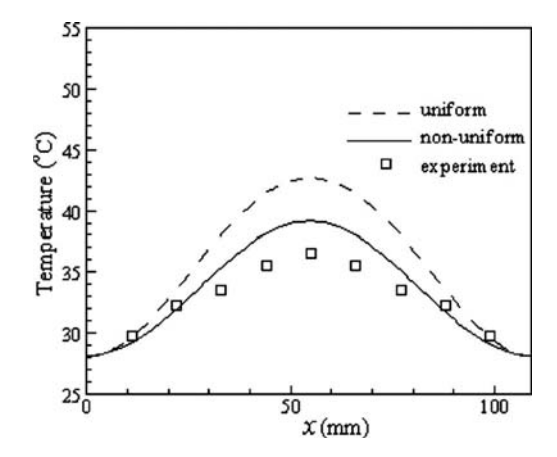


Fig. 5 The temperature distributions taken at 30 s are shown to compare the numerical solutions with the experimental result

Journal of Heat Transfer

JUNE 2011, Vol. 133 / 062502-5

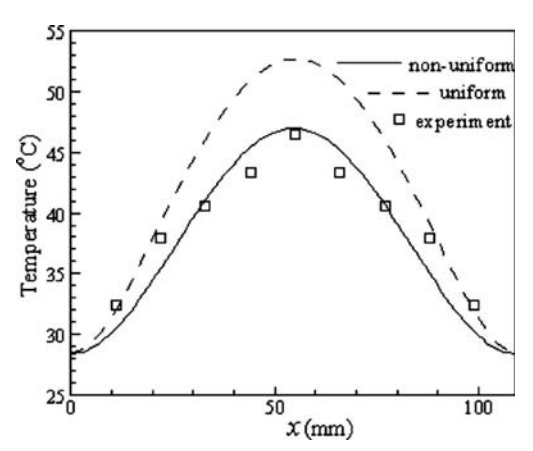


Fig. 6 The temperature distributions taken at 50 s are shown to compare the numerical solutions with the experimental result

parameters is given in Sec. 2. The diameter of glass beads and the freestream porosity are 0.15 mm and 0.385, respectively. With respect to the model simulation, the computed data for both uniform and nonuniform (variable) cases were extracted at 30 s and

50 s. The comparisons of temperature distributions on the x-z-plane at the horizontal line z=21 mm are shown in Figs. 5 and 6 at 30 s and 50 s, respectively. The results show an appreciably improved agreement when the variation of porosity within the packed bed is considered. For the uniform case, the peak temperature is about 40°C at 30 s and reaches 50°C at a later time, while the temperatures are lower in the case of variable porosity. However, it is clear in both the figures that the temperature is highest at the middle location since the density of the electric field in the TE₁₀ mode is high around the center region in the waveguide.

Figure 7 displays temperature contours as a function of time of the two cases, which exhibit a wavy behavior corresponding to the resonance of electric field. For the nonuniform porosity, the heating rate is noticeably slower than that for the uniform porosity. The reason behind this is that in the nonuniform-porosity medium, greater water content exists near the bottom wall attributed to a higher water-filled pore density. Since water is very lossy, large amounts of energy can be absorbed as both the incoming waves and the reflected waves particularly attenuate at the bottom area. This occurrence results in a resonance of a weaker standing wave with smaller amplitude throughout the packed bed. The weaker standing wave dissipates less energy, which is in turn converted into less thermal energy, giving a relatively slow heating rate. This explains why nonuniform porosity gives an overall lower temperature. Furthermore, a greater amount of water present in the

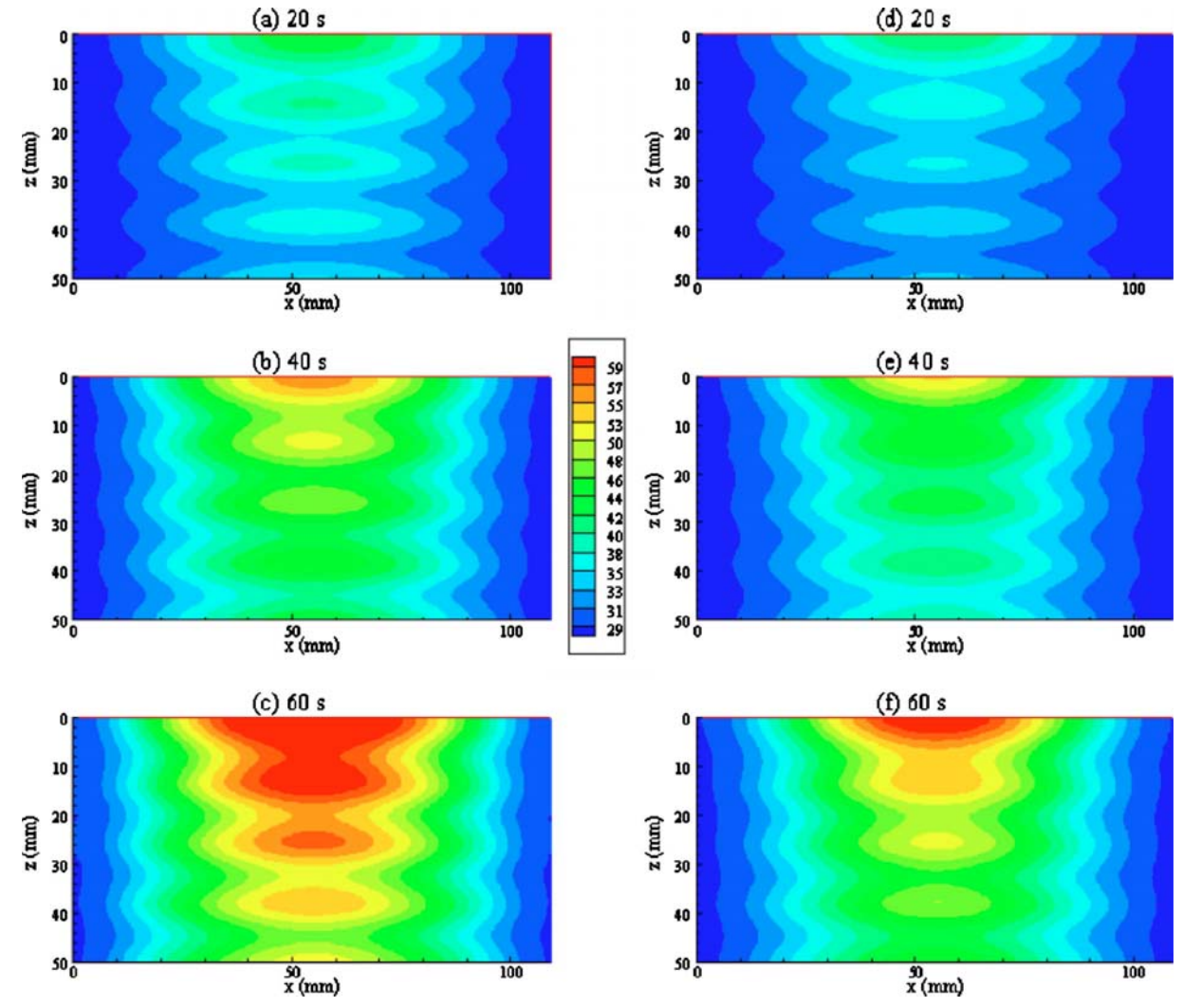


Fig. 7 Time evolutions of temperature contour (°C) within the porous bed at 20 s, 40 s, and 60 s for uniform case ((a)-(c)) and nonuniform case ((d)-(f))

062502-6 / Vol. 133, JUNE 2011

Transactions of the ASME

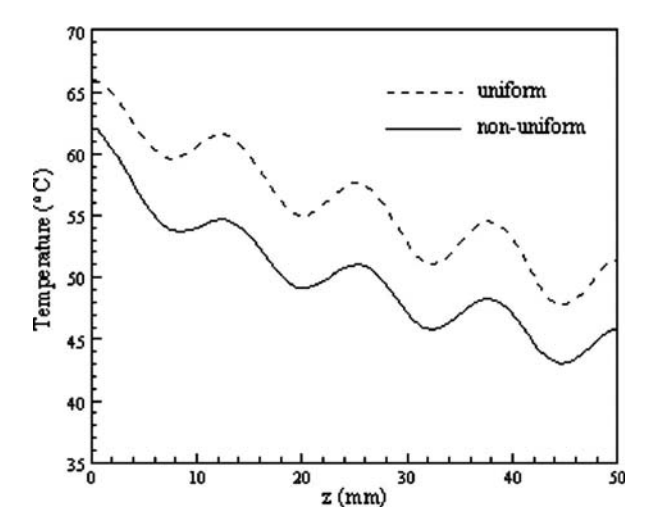


Fig. 8 Centerline temperature along the z axis for uniform (dashed line) and nonuniform (solid line) porous packed beds

nonuniform medium causes a smaller depth of penetration since water has relatively high values of dielectric constant and a high loss tangent. Figure 8 shows variations of centerline temperature vertically along the z axis at the different times of the two bed types. The resulting plots confirm the wavy behavior shown in Fig. 7. Moreover, it is obvious that the bed temperature is higher in the uniform-porosity porous bed.

In terms of flow characteristic, the instantaneous velocity vectors at 60 s are displayed in Fig. 9. The fluid flows as it is driven by the effect of buoyancy that overcomes the retarding viscous force. The nonuniform temperature distribution evident in Fig. 7 leads to an unstable condition. Temperature gradients, which exist in both transverse and axial directions, result in circulated flows. The velocities are higher close to the top boundary since there exist higher temperature gradients, thereby higher density gradi-

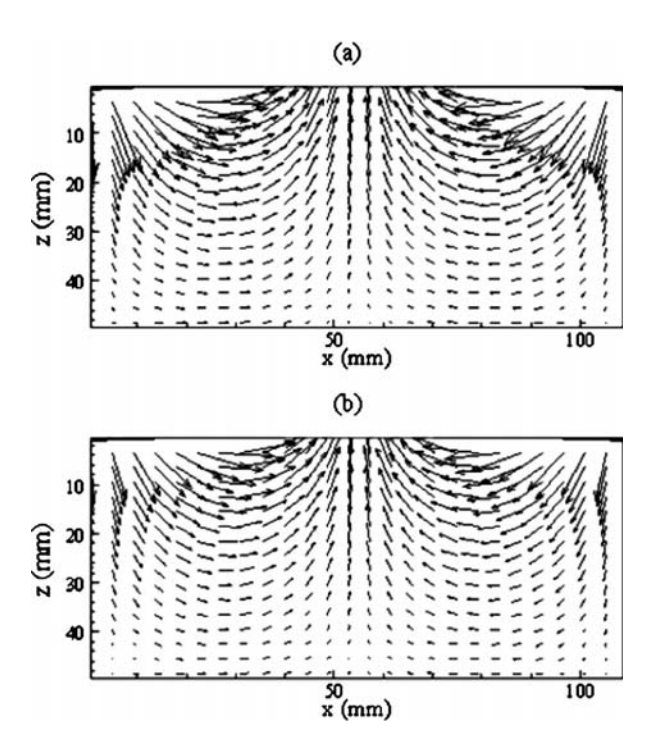


Fig. 9 Velocity vectors from the two cases of porous medium: (a) nonuniform and (b) uniform

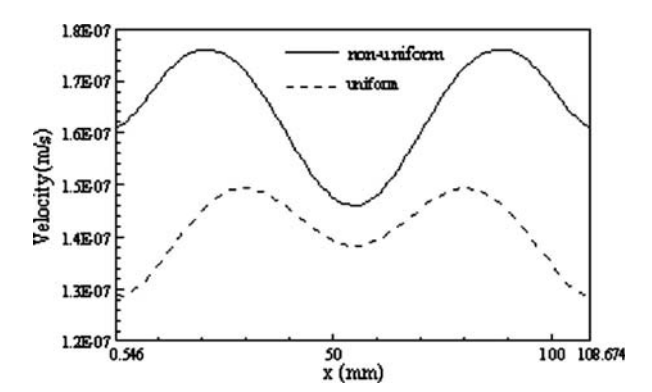


Fig. 10 Variations of velocity magnitudes along the \boldsymbol{x} axis for uniform (dashed line) and nonuniform (solid line) porous packed beds

ents leading to stronger buoyancy-induced flows. It is seen that flow velocities in the variable-porosity medium are lower than those in the uniform-porosity medium. This result is attributed to higher porosities near walls in the nonuniform case. Higher porosity media correspond to higher permeability, which allows greater flow velocity due to smaller boundary and inertial effects. The difference is clear in the vicinity of walls where high velocities carry energy from the wall toward the inner area.

To gain further insight in flow phenomena, the centerline velocity magnitudes along the *x*-direction are depicted in Fig. 10. It is clear that the nonuniform porosity gives larger magnitudes. Two peaks are seen spatially in both the cases. The peak values are at the same locations, as observed in Fig. 9. More importantly, the gradient of magnitude is larger in the nonuniform case due to the presence of porosity gradients. It is worthwhile comparing a *u*-component velocity shown in Fig. 11 along the *x* axis. The sign of the value reflects the direction of flow along the *x* axis. Relatively cold fluid flows toward the center domain from both sides to replace a hot fluid portion that expands toward the top boundary. This result is consistent with the flow behaviors depicted in Fig. 9.

6 Conclusions

The microwave heating of a porous medium with a nonuniform (variable) porosity is carried out based on the proposed numerical model. The two-dimensional variation of porosity of the medium is considered to be a function of the distance from the bed walls. Transient Maxwell's equations are employed to solve for the description of the electromagnetic field in the waveguide and medium. The generalized non-Darcian model that takes into account

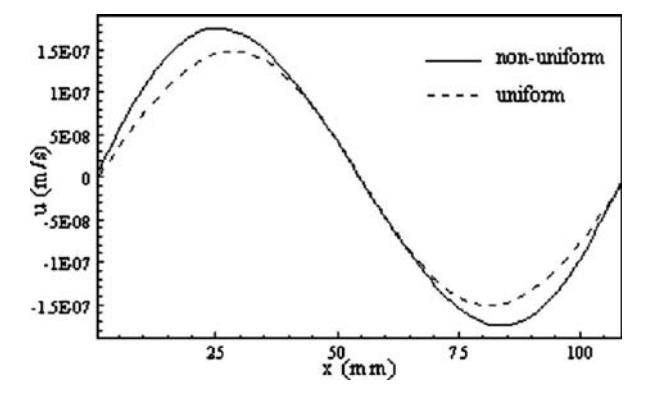


Fig. 11 Variations of u-component velocity along the x axis for uniform (dashed line) and nonuniform (solid line) porous packed beds

Journal of Heat Transfer

JUNE 2011, Vol. 133 / 062502-7

the presence of a solid drag and the inertial effect is included. The numerical results are in good agreement with the experimental data. In addition to the effect on the convective flow velocity that is larger in the nonuniform case, it is found that the variation of porosity near the wall has an important influence on the dielectric properties of the porous packed bed and markedly affects the heating process.

Acknowledgment

This work was supported by the National Research University Project of Thailand Office of Higher Education Commission and by the Thailand Research Fund.

Nomenclature

 c_p = specific heat capacity (J/(kg K) E = electric field intensity (V/m)

f =frequency of incident wave (Hz)

 $g = \text{gravitational constant } (m/s^2)$

H = magnetic field intensity (A/m)

P = power(W)

p = pressure (Pa)

Q = local electromagnetic heat generation term (W/m^3)

 $s = Poynting vector (W/m^2)$

 $T = \text{temperature } (^{\circ}\text{C})$

t = time (s)

 $\tan \delta = \text{dielectric loss coefficient } (-)$

u, w = velocity component (m/s)

 Z_H = wave impedance (Ω)

 Z_l = intrinsic impedance (Ω)

Greek Letters

 $\phi = \text{porosity } (\text{m}^3/\text{m}^3)$

 α = thermal diffusivity (m²/s)

 β = coefficient of thermal expansion (1/K)

 η = absolute viscosity (Pa s)

 $\varepsilon = \text{permittivity (F/m)}$

 ε' = dielectric constant (F/m)

 ϵ'' = dielectric loss factor (F/m)

 λ = wavelength (m)

 μ = magnetic permeability (H/m)

v = velocity of propagation (m/s)

 $\nu = \text{kinematics viscosity } (\text{m}^2/\text{s})$

 $\rho = \text{density (kg/m}^3)$

 σ = electric conductivity (S/m)

 ω = angular frequency (rad/s)

 ξ = surface tension (N/m)

Subscripts

0 = free space

 ∞ = ambient condition

a = air

f = fluid

j = layer number

 $in \ = \ input$

p = particle

r = relative

References

- [1] Wei, C. K., Davis, H. T., Davis, E. A., and Gordon, J., 1985, "Heat and Mass Transfer in Water-Laden Sandstone: Microwave Heating," AIChE J., 31(5),
- [2] Ni, H., Datta, A. K., and Torrance, K. E., 1999, "Moisture Transport in Intensive Microwave Heating of Biomaterials: Porous Media Model," Int. J. Heat Mass Transfer, 42, pp. 1501-1512.

- [3] Feng, H., Tang, J., Cavalieri, R. P., and Plumb, O. A., 2001, "Heat and Mass Transport in Microwave Drying of Porous Materials in a Spouted Bed," AIChE J., 47, pp. 1499–1512.
- [4] Ratanadecho, P., Aoki, K., and Akahori, M., 2002, "Influence of Irradiation Time, Particle Sizes, and Initial Moisture Content During Microwave Drying of Multi-Layered Capillary Porous Materials," ASME J. Heat Transfer, 124(1), pp. 151-161.
- [5] Dinčov, D. D., Parrot, K. A., and Pericleous, K. A., 2004, "Heat and Mass Transfer in Two-Phase Porous Materials Under Intensive Microwave Heating,'
- J. Food Eng., **65**, pp. 403–412. [6] Rattanadecho, P., 2006, "The Simulation of Microwave Heating of Wood Using a Rectangular Wave Guide: Influence of Frequency and Sample Size," Chem. Eng. Sci., 61, pp. 4798–4811.
- [7] Ratanadecho, P., Aoki, K., and Akahori, M., 2002, "A Numerical and Experimental Investigation of Modelling of Microwave Heating for Liquid Layers Using a Rectangular Wave Guide (Effects of Natural Convection and Dielectric Properties)," Appl. Math. Model., 26, pp. 449-472.
- [8] Cha-um, W., Rattanadecho, P., and Pakdee, W., 2009, "Experimental Analysis of Microwave Heating of Dielectric Materials Using a Rectangular Wave Guide (MODE: TE10) (Case Study: Water Layer and Saturated Porous Me-
- dium)," Exp. Therm. Fluid Sci., 33(3), pp. 472–481.

 [9] Ayappa, K. G., and Brandon, S., 1994, "Microwave Driven Convection in a Square Cavity," AIChE J., 40(7), pp. 1268–1272.
- [10] Franca, A. S., and Haghighi, K., 1996, "Adaptive Finite Element Analysis of Microwave Driven Convection," Int. Commun. Heat Mass Transfer, 23(2), pp. 177-186.
- [11] Chatterjee, S., Basak, T., and Das, S. K., 2007, "Microwave Driven Convection in a Rotating Cylindrical Cavity: A Numerical Study," J. Food Eng., 79, pp. 1269–1279.
- [12] Liu, S., and Masliyah, J. H., 1996, "Single Fluid Flow in Porous Media," Chem. Eng. Commun., 148, pp. 653–732.
 [13] Benenati, R. F., and Brosilow, C. B., 1962, "Void Fraction Distribution in Pack
- Beds," AIChE J., 8, pp. 359-361.
- [14] Vafai, K., 1984, "Convective Flow and Heat Transfer in Variable-Porosity Media," J. Fluid Mech., 147, pp. 233–259. [15] Amiri, A., and Vafai, K., 1994, "Analysis of Dispersion Effects and Non-
- Thermal Equilibrium, Non-Darcian, Variable Porosity Incompressible Flow Through Porous Media," Int. J. Heat Mass Transfer, 37(6), pp. 939–954.
- [16] Khaled, A.-R. A., and Chamkha, A. J., 2001, "Variable Porosity and Thermal Dispersion Effects on Coupled Heat and Mass Transfer by Natural Convection From a Surface Embedded in a Non-Metallic Porous Medium," Int. J. Numer. Methods Heat Fluid Flow, 11(5), pp. 413-429.
- [17] Hsiao, S.-W., Cheng, P., and Chen, C.-K., 1992, "Non-Uniform Porosity and Thermal Dispersion Effects on Natural Convection About a Heated Horizontal Cylinder in an Enclosed Porous Medium," Int. J. Heat Mass Transfer, 35(12), pp. 3407-3418.
- [18] Sakamoto, H., and Kulacki, F. A., 2008, "Effective Thermal Diffusivity of Porous Media in the Wall Vicinity," ASME J. Heat Transfer, 130(2), p. 022601.
- [19] Vafai, K., 1986, "Analysis of the Channeling Effect in Variable Porosity Me-
- dia," ASME J. Energy Resour. Technol., 108, pp. 131–139. [20] Hunt, M. L., and Tien, C. L., 1998, "Non-Darcian Convection in Cylindrical
- Packed Beds," ASME J. Heat Transfer, 110, pp. 2523–2532.
 [21] Poulikakos, D., and Renken, K., 1987, "Forced Convection in a Channel Filled With Porous Medium, Including the Effects of Flow Inertia, Variable Porosity and Brinkman Friction," ASME J. Heat Transfer, 109, pp. 880-888.
- [22] Chai, Z., and Guo, Z., 2007, "Study of Electro-Osmotic Flows in Microchannels Packed With Variable Porosity Media via Lattice Boltzmann Method," J. Appl. Phys., 101, p. 104913.
- [23] Akbal, S., and Baytas, F., 2008, "Effects of Non-Uniform Porosity on Double Diffusive Natural Convection in a Porous Cavity With Partially Permeable Wall," Int. J. Therm. Sci., 47(7), pp. 875-885.
- [24] Ratanadecho, P., Aoki, K., and Akahori, M., 2001, "Experimental and Numerical Study of Microwave Drying in Unsaturated Porous Material," Int. Commun. Heat Mass Transfer, 28(5), pp. 605–616.
- [25] El-Refaee, M. M., Elsayed, M. M., Al-Najem, N. M., and Noor, A. A., 1998, "Natural Convection in Partially Cooled Tilted Cavities," Int. J. Numer. Methods Fluids, 28, pp. 477-499.
- [26] Nield, D. A., and Bejan, A., 1999, Convection in Porous Media, Springer, New
- [27] Al-Amiri, A. A., 2002, "Natural Convection in Porous Enclosures: The Application of the Two-Energy Equation Model," Numer. Heat Transfer, Part A, 41, pp. 817-834.
- [28] Marafie, A., and Vafai, K., 2001, "Analysis of Non-Darcian Effects on Temperature Differentials in Porous Media," Int. J. Heat Mass Transfer, 44, pp. 4401–4411.
- [29] Nithiarasu, P., Seetharamu, K. N., and Sundararajan, T., 1997, "Natural Convective Heat Transfer in a Fluid Saturated Variable Porosity Medium," Int. J. Heat Mass Transfer, 40, pp. 3955-3967.
- [30] Chamkha, A. J., Issa, C., and Khanafer, K., 2002, "Natural Convection From an Inclined Plate Embedded in a Variable Porosity Porous Medium Due to Solar Radiation," Int. J. Therm. Sci., 41, pp. 73–81.



Contents lists available at ScienceDirect

International Communications in Heat and Mass Transfer

journal homepage: www.elsevier.com/locate/ichmt



Energy and exergy analyses in drying process of porous media using hot air

Ratthasak Prommas, Phadungsak Rattanadecho*, Dulyachot Cholaseuk

Research Center of Microwave Utilization in Engineering (R.C.M.E.), Department of Mechanical Engineering, Faculty of Engineering, Thammasat University; (Rangsit Campus), Pathumthani 12120, Thailand

ARTICLE INFO

Available online 24 February 2010

Keywords: Energy Exergy Drying porous medium Capillary pressure

ABSTRACT

In this paper the energy and exergy analyses in drying process of porous media using hot air was investigated. Drying experiments were conducted to find the effects of particle size and thermodynamics conditions on energy and exergy profiles. An energy analyses was performed to estimate the energy utilization by applying the first law of thermodynamics. An exergy analyses was performed to determine the exergy inlet, exergy outlet, exergy losses and efficiency during the drying process by applying the second law of thermodynamics. The results show that energy utilization ratio (EUR) and exergy efficiency depend on the particle size as well as hydrodynamic properties. Furthermore, the results of energy and exergy presented here can be applied to other porous drying processes which concern effect of porosity as well as grain size.

© 2010 Elsevier Ltd. All rights reserved.

1. Introduction

Drying is widely used to preserve porous medium products. It is a complicated process involving heat and mass transfer between the material surface and its surroundings [1]. Thermal drying in solids might be regarded as a result from two simultaneous actions: a heat transfer process by which the moisture content of the solid is reduced and a mass transfer process that implies fluid displacement within the structure of the solid towards its surface. Such motion depends on medium structure, moisture content and characteristics of the material. Furthermore the separation of vapor from solid substrate depends also on external pressure and temperature distribution on the total area of solid surface and the moisture content of drying air. Provided that thermal drying occurs in slow rate at ambient conditions, thus drying plants are designed and developed in order to accelerate appropriate drying rates for example, to supply the product is more heat those of ambient conditions [2]. Transferring in porous media is an important research subject that can be applied to various industrial applications, such as chemical reactors, heat exchangers, thermal insulations, electronic cooling and etc. Two distinguish approaches are taken into consideration to study transfer mechanisms in porous media [3]. One of the main goals in designing and optimizing of industrial drying processes is to use as little to reduce moisture from the product to the desired value. Consequently,

The features of exergy are identified to highlight its importance in a wide range of applications [6]. Exergy analysis has been increasingly as a useful tool in the design, assessment, optimization and improvement of energy systems [7]. It can be applied on both system and component levels. Exergy analysis leads to a better understanding of the influence of thermodynamic phenomena on effective process, comparison of the importance of different thermodynamic factors, and the determination of the most effective ways of improving the process [8]. As regards the exergy analyses of drying processes, some work has been carried out in recent years. Dincer and et. al [9] analyzed a thermodynamic aspect of the fluidized bed drying process of large particles for optimizing the input and output conditions by using energy and exergy models. The effects of the hydrodynamic and thermodynamic conditions were also analyzed such as inlet air temperature, fluidization velocity and initial moisture content on energy efficiency and exergy efficiency. Dincer and Sahin [10] used a model to analyze exergy losses of air drying process. Their work demonstrated that the usefulness of exergy analysis in thermodynamic assessments of drying processes and providence the performances and efficiencies of these processes. Akpinar [11,12] studied energy and exergy of the drying of red pepper slices in a convective

E-mail address: ratphadu@engr.tu.ac.th (P. Rattanadecho).

energy quantity and quality as well as heat and mass transfer should be investigated throughout progressive drying process [4]. The concepts of exergy destruction, exergy consumption, irreversibility, and lost work are importance. Exergy is a measurement of the maximum useful work that can be done by a system interacting with an environment at a constant pressure and temperature. The simplest is that of a reservoir with heat source of infinite capacity and invariable temperature. The maximum efficiency of heat withdrawal from a reservoir that can be converted into work is called the Carnot efficiency [5].

[☆] Communicated by W.J. Minkowycz.

^{*} Corresponding author.

Nomenclature

 c_p specific heat, (kJ/kg K) C_p mean specific heat, (kJ/kg K) EUR energy utilization ratio, (%) Ex exergy, (kJ/kg)

g gravitational acceleration, m/s² constant in Newton's law

h enthalpy, (kJ/kg)
J joule constant
m mass flow rate, (kJ/s)
N number of species
P pressure, (kPa)
Q net heat, (kJ/s)

 Q_{tt} useful energy given by heater, (kJ/s)

s specific entropy, (kJ/kg K)

T temperature, (K)

U specific internal energy, (kJ/kg)

v specific volume, m³/s V velocity, (m/s)

w specific humidity, (g/g) \dot{W} energy utilization, (J/s) z altitude coordinate, (m)

Subscripts

a air
da drying air
d drying chamber
f fan

f fan inlet L loss

mp moisture of product

o outlet

pb porous packed bed

sat saturated

∞ surrounding or ambient

Greek symbols

 $\begin{array}{ll} \varphi & \quad \text{relative humidity, (\%)} \\ \eta_{\text{ex}} & \quad \text{exergetic efficiency, (\%)} \\ \mu & \quad \text{chemical potencial, (kJ/kg)} \end{array}$

type dryer, with potato slices in a cyclone type dryer and pumpkin slices in a cyclone type dryer. The type and magnitude of exergy losses during drying was calculated. Colak and Hepbasli [13] performed an exergy analysis of thin layer drying of green olive in a tray dryer. In Colak's [14] study the effects of the drying air temperature, the mass flow rate of drying air and olives on the system performance were discussed. Ceylan et al. [15] carried out energy and exergy analyses during the drying of two types of timber. The effects of ambient relative humidity and temperature were taken into account.

The drying of porous media has been interested by many researchers and become complex, coupled, and multiphase processes with a wide range of applications in industry. In addition, as a result of high cost of energy, an operation with a high potential for optimizing with respect to energy savings has been realized. For many years, it has been studied experimentally for measuring drying kinetics on the macro-scale.

Typical applications of non-uniform material include the tertiary oil recovery process, geothermal analysis, asphalt concrete pavements

process and preservation process of food stuffs. Therefore, knowledge of heat and mass transfer that occurs during convective drying of porous materials is necessary to provide a basis for fundamental understanding of convective drying of non-uniform materials.

The fore mentioned works concerned mainly with, energy and exergy analyses of drying process. Normally, most of materials in the drying process are porous materials. In the recent works the authors were mention about porous materials structure, with are concern with energy and exergy analyses of drying process.

The objectives of this work are to evaluate (i) the exergy losses of two operations porous packed bed, (ii) the distributions of the exergy losses and exergy input of the different drying operations and (iii) the influences of operating parameters on exergy losses. The knowledge gained will provide an understanding in porous media and the parameters which can help to reduce energy consumptions and losses.

2. Experimental apparatus

Fig. 1(a) shows the experimental convective drying system. The hot air, generated electrically travels through a duct toward the upper surfaces of two samples situated inside the test section. The outside walls of test section are covered with insulation to reduce heat loss to the ambient. The outlet flow and temperature can be adjusted at a control panel.

As shown in Fig. 1(b), the samples are unsaturated packed beds composed of glass beads, water and air. The samples are prepared in the two configurations: a single-layered packed bed (uniform packed bed) with bed depth 50 mm (d=0.15 mm (F bed) and d=0.4 mm (C bed)). The width and total length of all samples used in the experiments are 50 mm and 100 mm, respectively. The temperature distributions within the sample are measured using fiberoptic sensors (LUXTRON Fluroptic Thermometer, Model 790, accurate to 0.5), which are placed in the center of the sample at inserted into the packed bed at 5, 15 and 25 mm. form surface in Fig. 2. In each test run, the weight loss of the sample is measured using a high precision mass balance.

The uncertainty in the results might come from the variations in humidity and room temperature. The uncertainty in drying kinetics is assumed to result from errors in the measuring weight of the sample. The calculated uncertainties in weight in all tests are less than 2.8%. The uncertainty in temperature is assumed to result from errors in adjusting input power, ambient temperature and ambient humidity. The calculated uncertainty associated with temperature is less than 2.85%

3. Mathematical formulation of problem

Schematic diagram of the convective drying model for porous packed bed is shown in Fig. 3. When a packed bed is heated by hot air flowing over its upper surface, the heat is transferred from the top of packed bed into the interior. Therefore, the temperature gradient is formed in the bed, and the liquid phase at the upper surface of packed bed evaporates by the variation of saturated vapor concentration corresponding to this temperature gradient as long as the surface remains wetted. In analysis, the main assumptions involved in the formulation of the transport model are:

- 1. The capillary porous material is rigid and no chemical reactions occur in the sample.
- 2. Local thermodynamic equilibrium is reached among each phase.
- 3. The gas phase is ideal in the thermodynamic sense.
- 4. The process can be modeled as steady-flow.
- 5. Packed bed sample side wall is perfectly insulated, hence adiabatic.

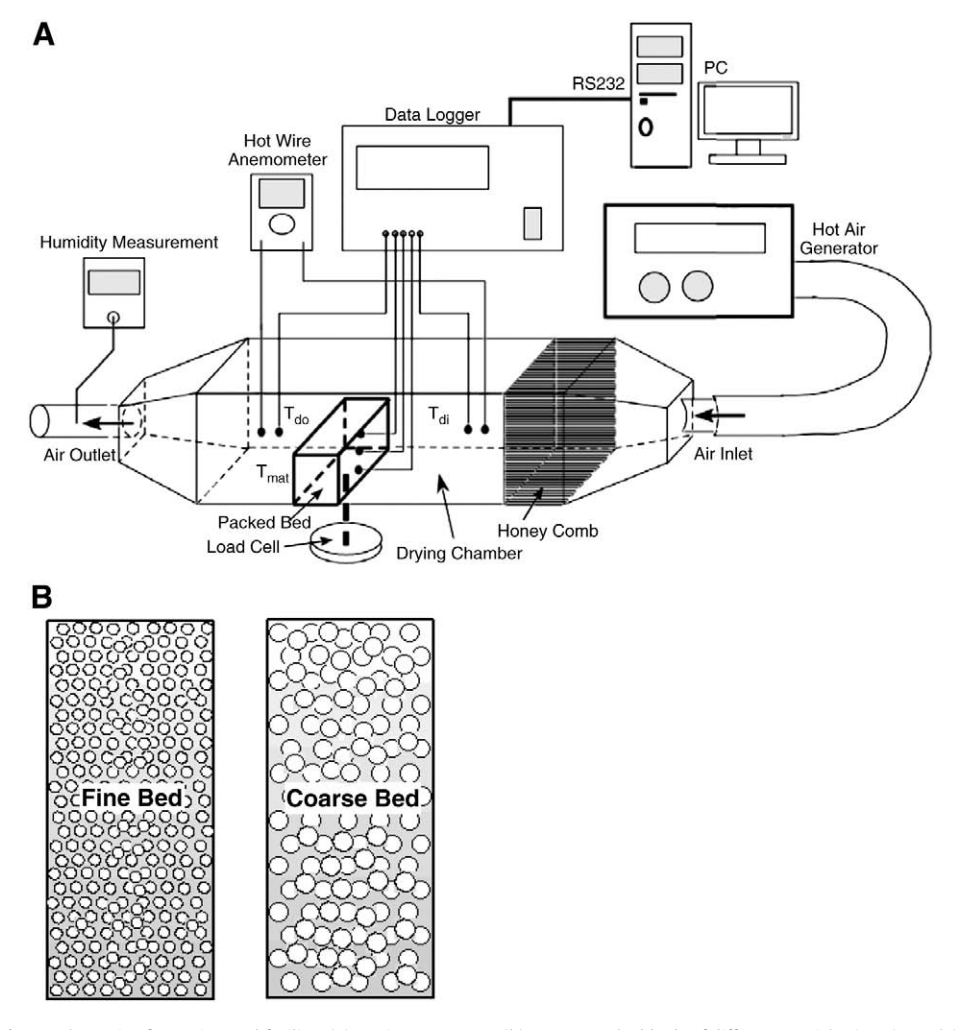


Fig. 1. Schematic of experimental facility: (a) Equipment setup; (b) Porous packed beds of different particle sizes (sample).

- In a macroscopic sense, the packed bed is assumed to be homogeneous and isotropic, and liquid water is not bound to the solid matrix.
- 7. A dry layer (evaporation front) is formed immediately after water saturation approaches the irreducible value.

By energy and exergy analyses in drying process of single-layered packed bed using hot air, the main basic equations are given as follows:

3.1. Energy analysis

The traditional methods of thermal system analysis are based on the first law of thermodynamics. These methods use an energy balance on the system to determine heat transfer between the system and its environment. The first law of thermodynamics introduces the

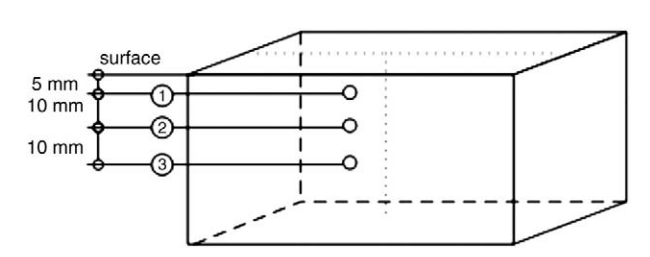


Fig. 2. The positions of temperature measurement in porous packed bed.

concept of energy conservation, which states that energy entering a thermal system with fuel, electricity, flowing streams of matter, and so on is conserved and cannot be destroyed. In general, energy balances provide no Information on the quality or grades of energy crossing the thermal system boundary and no information about internal losses (Fig. 4).

The drying process includes the process of heating, cooling and humidification. The process can be modeled as steady-flow processes by applying the steady-flow conservation of mass (for both dry air and

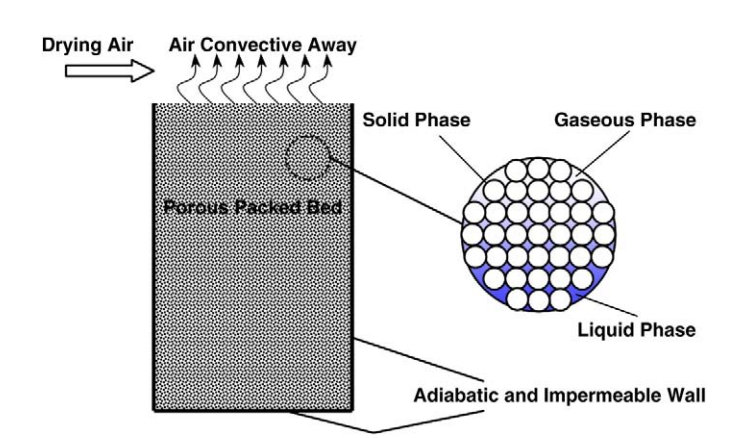


Fig. 3. Configuration of porous packed bed.

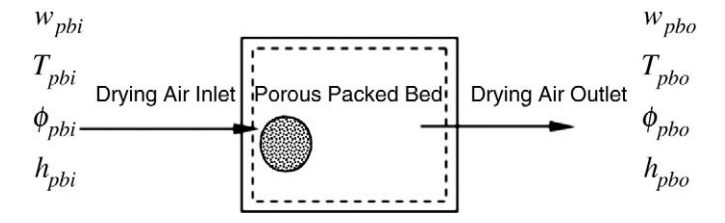


Fig. 4. Properties of porous packed bed in drying chamber.

moisture) and conservation of energy principles. General equation of mass conservation of drying air:

$$\sum \dot{m}_{\rm ai} = \sum \dot{m}_{\rm ao} \tag{1}$$

General equation of mass conservation of moisture:

$$\sum \left(\dot{m}_{wi} + \dot{m}_{mp} \right) = \sum \dot{m}_{wo} \tag{2}$$

$$\sum \left(\dot{m}_{ai}w_i + \dot{m}_{mp}\right) = \sum \dot{m}_{ai}w_o$$

General equation of energy conservation:

$$\dot{Q} - \dot{W} = \sum \dot{m_0} \left(h_0 + \frac{V_0^2}{2} \right) - \sum \dot{m_i} \left(h_i + \frac{V_i^2}{2} \right) \tag{3}$$

where the changes in kinetic energy of the fan were taken into consideration while the potential and kinetic energy in other parts of the process were neglected. During the energy and exergy analyses of packed bed drying process, the following equations were used to compute the enthalpy of drying air.

$$h = c_{\rm pda}T + wh_{\rm sat@T} \tag{4}$$

The enthalpy equation of the fan outlet was obtained Bejan [16] using Eq. (5) as below:

$$h_{\rm fo} = \left[\left(\dot{W}_{\rm f} - \frac{V_{\rm fo}^2}{2^* 1000} \right) \left(\frac{1}{\dot{m}_{\rm da}} \right) \right] + h_{f_i}$$
 (5)

where, $h_{\rm fi}$ characterizes the enthalpy of drying air at the inlet of the fan, $h_{\rm fo}$ the enthalpy at the outlet of the fan, $V_{\rm fo}$ the drying air velocity at the outlet of the fan, $W_{\rm f}$ fan energy and $\dot{m}_{\rm da}$ mass flow of drying air. Considering the values of dry bulb temperature and enthalpy from Eq. (5), the specific and relative humidity of drying air at the outlet of the fan were determined Akpinar [11]. The inlet conditions of the heater were assumed to be equal to the outlet conditions of the fan. The useful energy gained from the heater enters the drying chamber as the convection heat source, which was defined as:

$$\dot{Q}_{u} = \dot{m}_{da} c_{pda} (T_{ho} - T_{hi}) \tag{6}$$

where $T_{\rm ho}$, $T_{\rm hi}$ are the outlet and inlet temperature of air at the heating section. The inlet conditions of the drying chamber were determined depending on the inlet temperatures and specific humidity of drying air. It was considered that the mass flow rate of drying air was equally passed throughout the chamber. The specific humidity at the outlet of the chamber can be defined as:

$$w_{\rm pbo} = w_{\rm pbi} + \frac{\dot{m}_{\rm wpb}}{\dot{m}_{\rm rla}} \tag{7}$$

where $\dot{w}_{\rm dci}$ denotes the specific humidity at the inlet of the chamber, $\dot{m}_{\rm wpb}$ the mass flow rate of the moisture removed from packed bed samples. The heat utilized during the humidification process at the chamber, can be estimated by

$$\dot{Q}_{\rm pb} = \dot{m}_{\rm da} \left(h_{\rm pbi@T} - h_{\rm pbo@T} \right) \tag{8}$$

$$h = c_{\text{pda}}T + wh_{\text{sat@T}} \tag{9}$$

where $w_{\rm pbo}$ is the amount of product moisture evaporated. The energy utilization ratio for the drying chamber can be obtained using the following expression Akpinar [11]:

$$EUR_{dc} = \frac{\dot{m}_{da}(h_{dci@T} - h_{dco@T})}{\dot{m}_{da}C_{rdc}(T_{bo} - T_{bi})}$$
(10)

4. Exergy analysis

The second law of thermodynamics introduces the useful concept of exergy in the analysis of thermal systems. As known, exergy analysis evaluates the available energy at different points in a system. Exergy is a measurement of the quality or grade of energy and it can be destroyed in the thermal system. The second law states that part of the exergy entering a thermal system with fuel, electricity, flowing streams of matter, or other sources is destroyed within the system due to irreversibilities. The second law of thermodynamics uses an exergy balance for the analysis and the design of thermal systems. In the scope of the second law analysis of thermodynamics, total exergy of inflow, outflow and losses of the drying chamber were estimated. The basic procedure for exergy analysis of the chamber is to determine the exergy values at steady-state points and the reason of exergy variation for the process. The exergy values are calculated by using the characteristics of the working medium from a first law energy balance. For this purpose, the mathematical formulations used to carry out the exergy balance are as show below Ahern [17].

$$\begin{split} \textit{Exergy} &= (u - u_{\scriptscriptstyle \infty}) - T_{\scriptscriptstyle \infty}(s - s_{\scriptscriptstyle \infty}) \, + \, \frac{P_{\scriptscriptstyle \infty}}{J}(v - v_{\scriptscriptstyle \infty}) \, + \, \frac{V^2}{2gJ} \, + \, (z - z_{\scriptscriptstyle \infty}) \frac{g}{g_cJ} \\ & \text{internal entropy work momentum gravity} \\ & \text{energy} \end{split} \tag{11} \\ & + \, \sum_{c} \, (\mu_c - \mu_{\scriptscriptstyle \infty}) N_c \, + \, E_i A_i F_i \Big(3T^4 - T_{\scriptscriptstyle \infty}^4 - 4T_{\scriptscriptstyle \infty} T^3 \Big) \, + \, \dots \\ & \text{chemical radiation emission} \end{split}$$

The subscript ∞ denotes the reference conditions. In the exergy analyses of many systems, only some of the terms shown in Eq. (11) are used but not all. Since exergy is energy available from any source, it can be developed using electrical current flow, magnetic fields, and diffusion flow of materials. One common simplification is to substitute enthalpy for the internal energy and PV terms that are applicable for steady-flow systems. Eq. (11) is often used under conditions where the gravitational and momentum terms are neglected. In addition to these, the pressure changes in the system are also neglected because of $v \cong v_\infty$, hence Eq. (11) is reduced as

$$Exergy = \overline{c}_p \left[(T - T_{\infty}) - T_{\infty} \ln \frac{T}{T_{\infty}} \right]$$
 (12)

The inflow and outflow of exergy can be found using the above expression depending on the inlet and outlet temperatures of the drying chamber. Hence, the exergy loss is determined as:Exergy

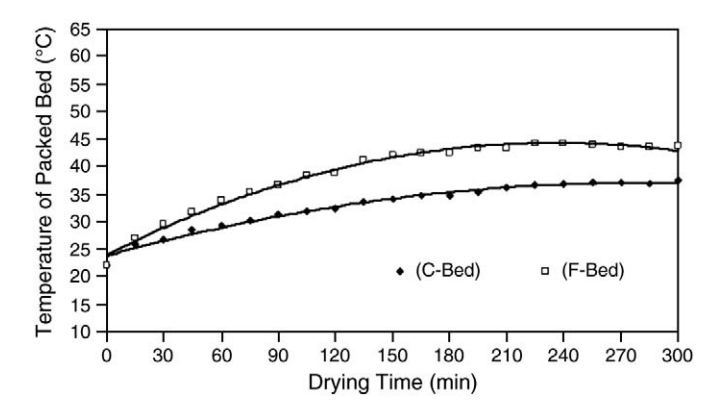


Fig. 5. The temperature profiles with respect to time.

loss = Exergy inflow - Exergy outflow

$$\sum Ex_{L} = \sum Ex_{i} - \sum Ex_{o} \tag{13}$$

The exergy inflow for the chamber is stated as below

$$Ex_{\rm dci} = Ex_{\rm pbi} = \overline{c}_{\rm p_{da}} \left[(T_{\rm dci} - T_{\infty}) - T_{\infty} \ln \frac{T_{\rm dci}}{T_{\infty}} \right]$$
 (14)

The exergy outflow for the drying chamber is stated as:

$$Ex_{\rm dco} = Ex_{\rm pbo} = \overline{c}_{\rm pda} \left[(T_{\rm dco} - T_{\infty}) - T_{\infty} \ln \frac{T_{\rm dco}}{T_{\infty}} \right]$$
 (15)

The exergetic efficiency can be defined as the ratio of the product exergy to exergy inflow for the chamber as outlined below:

$$\textit{Exergy Efficiency} = \frac{\textit{Exergy inf low-Exergyloss}}{\textit{Exergy inf low}} \tag{16}$$

$$\eta_{EX} = 1 - \frac{Ex_L}{Ex_i} \tag{17}$$

5. Results and discussions

Drying experiments were conducted by varying operating parameters which are temperature, air velocity, packed beds thickness and air humidity. For porous packed beds of two different sizes, 0.15 and 0.45 mm. drying air temperatures 50 °C and air velocities 2.5 m/s, energy and exergy analyses were carried out.

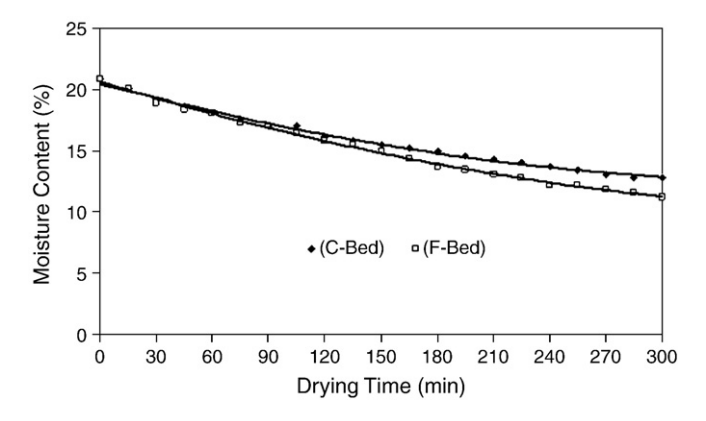


Fig. 6. The variation of moisture content with respect to time.

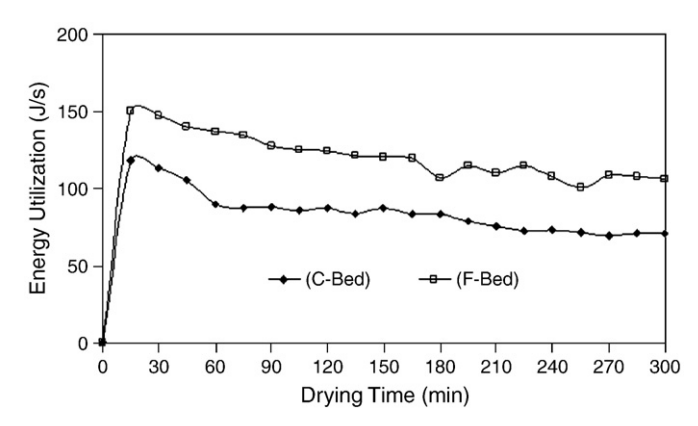


Fig. 7. Variation of energy utilization and drying time with different packed bed.

It is observed that at the early stage of the drying process the temperature profiles in both cases are nearly the same. As drying progresses, the temperature increases. This is because the latent heat transfer due to evaporation is retained due to the decline of the mass transfer rate together with the decreasing of average moisture content. Nevertheless, the temperature profile in F bed rises at a higher rate than that in the C bed. This is because the dry layer formed earlier in the F bed and an abrupt temperature rise occurs as the dry bulb temperature is approached. On the other hand, in the case of the C bed the temperature increases more slowly in comparison to F bed due to the late formation of dry layer. The prediction of the formation of a dry layer estimated from the drop in the surface mass of drying and rise in the drying temperature is marked in Fig. 5.

In the single-layered packed bed, the moisture content continuously decreases toward the surface. The decrease in surface saturation, this set up a saturation gradient, which draws liquid water toward the surface through capillary action while water vapor moves towards the surface due to a gradient in the vapor partial pressure. However, the internal moisture transport is mainly attributable to capillary flow of liquid water through the voids during the initial stage of drying.

Fig. 6. show the variation of moisture content and drying time. It is observed that at the early stage of the drying process the moisture content profiles in both cases are nearly the same. As drying progresses, the moisture content decreases. The following discussion is concerned with the effect of particle size on moisture migration mechanism under the same conditions for the single-layered packed bed. In Fig. 6, the observed moisture content profiles at the leading edge of the sample in the case of fine bed (F bed) are higher than those in the case of coarse bed (C bed). This is because of the fine bed or small particle size (corresponding to a higher capillary pressure) can cause moisture to reach the surface at a higher rate than in the case of

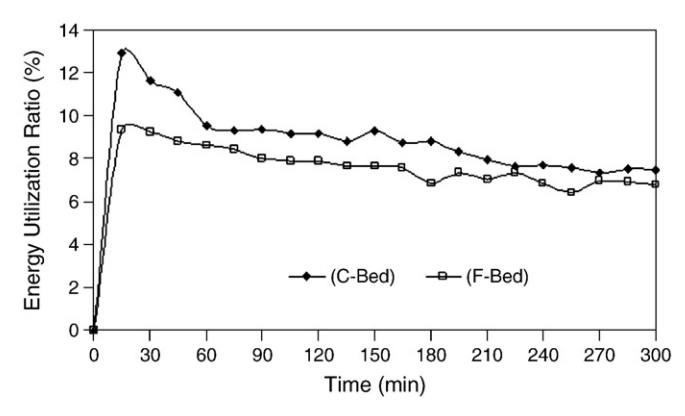


Fig. 8. Variation of energy utilization ratio with different packed bed.

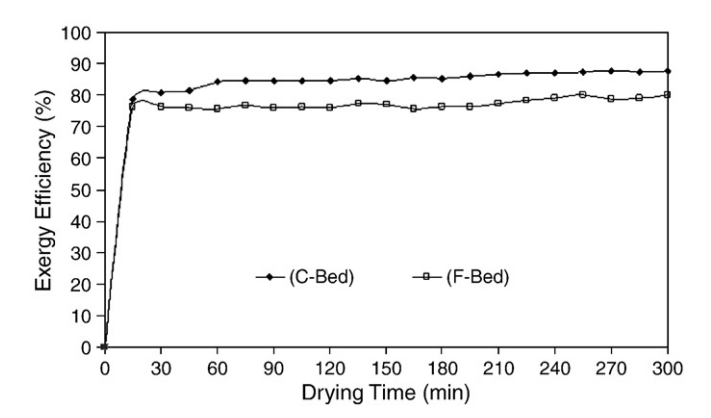


Fig. 9. Variation of exergy efficiency with different packed bed.

the coarse bed, i.e., large particle size. On the other hand, in the case of coarse bed, the moisture profiles at the leading edge of the sample are always lower as compared with the small particle size due to the lower capillary pressure inside the sample and the gravitational effect. Continued drying eventually causes the average moisture level inside the packed bed to decrease, especially at the leading edge of the upper layer (Fig. 6). When the moisture content at the upper surface (surface saturation) approaches the irreducible where the liquid water becomes discontinuous (pendular state), the liquid water supply to the surface by capillary action becomes insufficient to replace the liquid being evaporated. The latter arises from the fact that the dry layer takes place over small effective surface or on a front retreating from the surface into the interior of the sample dividing it into two layers, a dry layer and a two-phase layer. The discontinuity of the temperature gradient close to the drying front is a result of heat flux necessary for evaporation Pakdee and Rattanadecho [18]. In addition the effective thermal conductivity falls considerably resulting in a resistance of the heat flow rate. A further consequence of premature drying of the outer dry layer is that the local temperature of the sample will reach that of drying medium (hot air).

Fig. 7. shows the variation of energy utilization as a function of drying time for different particle sizes of particle and drying time. The energy utilization was high and getting higher at the beginning of drying process due to the high moisture of the sample while it quickly decreased because of the low moisture content of the samples towards the end of the process.

Fig. 8. shows the variation of energy utilization ratio (EUR) as a function of drying time for F bed and C bed. Energy balance analysis was carried to estimate the Energy Utilization Ratio (EUR). The values of the energy utilization in the drying chamber were calculated using Eq. (10). From the results it is observed that for a given particular air velocity during packed beds drying the EUR increases as particle size of packed bed decreases. These variations were more at the beginning of the drying and gradually the difference reduced Ratanadecho, Aoki and Akahori [19], this is because the large raise in particle size of packed bed significantly influences drying rate, hence at elevated particle size the EUR decreases with drying time. Consequently it was noticed that the EUR of drying chamber decreases with increase of drying time, it is because during the drying process the moisture content of the product decreases for the same energy input. Furthermore, at the beginning of the drying process, the energy efficiencies were observed to be higher than at the final stage and were found to be very low at the end of drying process.

Exergy analysis was carried to find the exergetic efficiency of the drying process Lampinen [20] by varying the drying parameters. The exergy inflow rates were calculated using Eq. (15) depending on the ambient and inlet temperatures. The exergy inflow during the drying of packed bed depending on drying particle size of packed bed. The exergy outflows were calculated using Eq. (16) and during the

experiments which varied. It was observed that the exergy outflow from the drying chamber increased slowly with the drying time.

From the results it was noticed that the exergy outflow and the exergy loss increased with the increase of particle size. The exergetic efficiency of the drying chamber increased with the increase of drying time as shown in Fig. 9. This is because during the drying process the available energy in the drying chamber increases with drying time, since the amount of moisture decreases with time. Then, the effect of the other particle size on the drying time as well as the exergy efficiency of the drying system is presented. Furthermore, the exergy efficiencies of C-bed were observed to be higher than the F-bed about 10 % after 60 min of drying time with parallel to the end of drying process.

6. Conclusion

Energy and exergy analysis of the drying process of the packed bed were carried out in this study. Taking in to considerations the result from these analyses, the following conclusion may be drawn on energy utilization, energy utilization ratio and exergy efficiency decreased with increasing drying time, both energy utilization and energy utilization ratio increased with large particle size of packed bed.

The effects of particle sizes on the overall drying kinetics are clarified. The drying rate in the case of the F bed (fine particles) is slightly higher than that case of the C bed (coarse particles). This is because the higher capillary pressure for the F bed results in the maintenance of a wetted drying surface for a longer period of time.

It is also found that the drying rate depends strongly on the moisture content at the heating surface.

Our future aim is to validate the investigation of drying process of multi-layered packed beds. The comparisons of drying source between hot air and microwave energy.

Acknowledgments

The authors would like to express their appreciation to the Thailand Research Fund (TRF) for providing financial support for this study.

References

- K. Dutta, V.K. Nema, R.K. Bhardwaj, Drying behavior of spherical grains, Int. J. Heat Mass Transf. 31 (1988) 855–861.
- [2] I. Dincer, A.Z. Sahin, A new model for thermodynamic analysis of a drying process, Int. J. Heat Mass Transf. 47 (2004) 645–652.
- [3] B. Lyes, B. Azeddine, Mathematical description of heat and mass transfer during deep bed drying: effect of product shrinkage on bed porosity, Appl. Therm. Eng. 28 (2008) 2236–2244.
- [4] E.K. Akpinar, A. Midilli, Y. Bicer, The first and second law analyses of thermodynamic of pumpkin drying process, J. Food Eng. 72 (2006) 320–331.
- [5] M.A. Rosen, M.N. Le, I. Dincer, Efficiency analysis of a cogeneration and district energy system, Apply Therm. Eng. 25 (2005) 147–159.
- [6] Yongzhong Liu, Yanfei Zhao, Xiao Feng, Exergy analysis for a freeze-drying process, Appl. Therm. Eng. 28 (2008) 675–690.
- [7] M. Kanoglua, I. Dincer, M.A. Rosen, Understanding energy and exergy efficiencies for improved energy management in power plants, Energy Policy 35 (2007) 3967–3978.
- [8] J. Szargut, D.R. Morris, F.R. Steward, Exergy Analysis of Thermal, Chemical and Metallurgical Processes, Hemisphere Publishing Corporation, New York, 1998.
- [9] S. Syahrul, I. Dincer, F. Hamdullahpur, Thermodynamic modeling of fluidized bed drying of moist particles, Int. J. Therm. Sci. 42 (2003) 691–701.
- I. Dincer, A.Z. Sahin, A new model for thermodynamic analysis of a drying process, Int. J. Heat Mass Transf. 47 (2004) 645–652.
- [11] E.K. Akpinar, Energy and exergy analyses of drying of red pepper slices in a convective type dryer, Int. Commun. Heat Mass Transf. 31 (8) (2004) 1165–1176.
- [12] E.K. Akpinar, A. Midilli, Y. Bicer, Energy and exergy of potato drying process via
- cyclone type dryer, J. Food Eng. 46 (2005) 2530–2552.
 [13] E.K. Akpinar, A. Midilli, Y. Bicer, The first and second law analyses of thermodynamic of pumpkin drying process, J. Food Eng. 72 (2006) 320–331.
- [14] N. Colak, A. Hepbasli, Performance analysis of drying of green olive in a tray dryer, J. Food Eng. 80 (2007) 1188–1193.

- [15] I. Ceylan, M. Aktas, H. Dogan, Energy and exergy analysis of timber dryer assisted heat pump, Appl. Therm. Eng. 27 (2007) 216–222.
 [16] A. Bejan, Advanced Engineering Thermodynamics, John Wiley and Sons, New
- York, 1998.
- [17] J.E. Ahern, The Exergy method of Energy Systems Analysis, John Wiley, New York, 1980.
- [18] W. Pakdee, P. Rattanadecho, Unsteady effects on natural convective heat transfer through porous media in cavity due to top surface partial convection, Appl. Therm. Eng. 26 (2006) 2316–2326.
- [19] P. Ratanadecho, K. Aoki, M. Akahori, Experimental and numerical study of microwave drying in unsaturated porous material, Int. Commun. Heat Mass Transf. 28 (2001) 605–616.
- [20] M.J. Lampinen, M.A. Heikkinen, Exergy analysis for stationary flow systems with several heat exchange temperatures, Int. J. Energy Res. 19 (1995) 407–418.



Contents lists available at ScienceDirect

Experimental Thermal and Fluid Science

journal homepage: www.elsevier.com/locate/etfs



Analysis of heat and mass transfer enhancement in porous material subjected to electric fields (effects of particle sizes and layered arrangement)

Chainarong Chaktranond*, Phadungsak Rattanadecho

Department of Mechanical Engineering, Faculty of Engineering, Thammasat University, Rangsit Campus, Pathumthani 12121, Thailand

ARTICLE INFO

Article history: Received 23 September 2009 Received in revised form 3 February 2010 Accepted 5 February 2010

Keywords: Electrohydrodynamics Drying process Heat and mass transfer

ABSTRACT

This research experimentally investigates the influences of electrical voltage, particle sizes and layer arrangement on the heat and mass transfer in porous packed bed subjected to electrohydrodynamic drying. The packed bed consists of a single and double layers of glass beads, water and air. Sizes of glass beads are 0.125 and 0.38 mm in diameter. Electric fields are applied in the range of 0–15 kV. Average velocity and temperature of hot airflow are controlled at 0.33 m/s and 60 °C, respectively. The results show that the convective heat transfer coefficient and drying rate are enhanced considerably with a Corona wind. In the single-layered case, due to effects of porosity, the packed bed containing small beads has capillary pressure higher than that with big beads, resulting in higher removal rate of water and higher rate of heat transfer. Considering the effect of capillary pressure difference, temperature distribution and removal rate of moisture in the double-layered case appear to be different than those observed in the single-layered case. Moreover, in the double-layered case, the fine-coarse packed bed gives drying rate higher than that given by the coarse–fine packed bed.

© 2010 Elsevier Inc. All rights reserved.

1. Introduction

There has been a continuous effort to achieve a better technological performance in drying processes, which provide high quality products and minimize the energy cost. Hot-air drying technique is widely used in agricultural industries for removing the moisture content from products. However, its drying period is long, resulting in large energy consumption. In order to improve the drying rate, many researchers have paid much attention in a development of hot-air drying by cooperating the conventional method with the other methods, e.g., microwave [1-6], infrared [7–10], and electric fields (Electrohydrodynamics, EHD) [11–13]. In order to increase the removal rate of moisture within materials, microwave irradiation penetrates in the bulk of material, and creates a heat source at a certain location. However, microwave drying is known to result in a poor quality product if it is not properly applied [2,3]. To heat the surface region, infrared radiation is transmitted through water at a short wavelength, while it is absorbed on the surface at a long wavelength [8]. This way of drying process is suitable to dry thin layers of material with large surface exposed to radiation. In electrohydrodynamic drying, highintensity electric field is applied to airflow in order to induce the secondary flow or circulating flow, so-called Corona wind. The net effect of this secondary flow is additional mixing of fluids and destabilization of boundary layer, therefore leading to a substantial increase in mass transfer coefficients [11].

Due to simultaneous heat and mass transfer taking place during drying process, mechanisms of drying in porous materials are complicated, and still have been investigated by many researchers. Schröder et al. [14] measured heat transfer between particles and nitrogen gas flow in packed bed. They reported that increasing gas flow led to higher heat transport coefficient. Alem-Rajabif and Lai [11] experimentally investigated the drying rate of partially wetted glass bead subjected to electric field. In their experiments, a wire electrode and a copper plate were located on the upper and lower of a packed bed, respectively. The results showed that EHD drying was most effective at the surface of the packed bed. In addition, the rate of drying with the positive Corona was generally greater than that with the negative Corona. This result was consistent with the experimental setup by Alem-Rajabif and Lai [11], Lai and Lai [12] who examined the influence of electric field parameters on the drying rate of a packed bed. Their results showed that drying rate depended on the strength of the electric field and the velocity of the cross flow. Without cross flow, the drying rate increased linearly with the applied voltage, while the influence of Corona wind was suppressed by high cross-flow velocity.

To explain the drying mechanisms, Ratanadecho et al. [4] experimentally and numerically studied the microwave drying in unsaturated material with different porosities. They found that packed bed with a small bead size had capillary forces and drying rate higher than that with a big bead size. From the above literatures,

^{*} Corresponding author. Tel.: +66 02 564 3001x3144; fax: +66 02 564 3010. E-mail address: cchainar@engr.tu.ac.th (C. Chaktranond).

Nome	nclature		
С	coarse bead	Greek l	etters
d	diameter of glass bead (mm)	δ	depth of packed bed (mm)
D_h	hydraulic diameter (m)	λ_{eff}	the effective thermal conductivity (W/m K)
F	fine bead	μ $$	viscosity (Pa s)
h_c	convective heat transfer coefficient (W/m ² K)	ϕ	porosity (m ³ /m ³)
h_v	latent heat of vaporization (J/kg)	ρ	density (kg/m³)
K	permeability (m ²)	σ	surface tension (Pa m)
M	mass (kg)		
m	mass flux of evaporation (kg/m ² s)	Subscri	pts
p	pressure (Pa)	а	air
R_e	Reynolds number	С	capillary
S	saturation	eff	effective
S_{eff}	effective water saturation associated with the irreduc-	EHD	air with electric fields
-33	ible water saturation	free	free air
T	temperature (°C)	g	gas
∇T	temperature gradient in packed bed (°C)	Ī	liquid
V	volume (m³)	S	solid
Χ	moisture content	sur	surface
Z	distance from surface of packed bed	w	water

only the researches by Ratanadecho et al. [4–6] had studied the mechanisms of heat and mass transfer in the packed bed. However, behaviour of microwave heating is different from hot-air heating. To get further understanding in the mechanisms of drying with surface heating, this study experimentally investigates and analyzes the heat and mass transfer within single- and double-layered porous packed bed subjected to hot-air flow and electric fields. Moreover, effects of particle sizes and layered arrangement are also examined.

2. Theory

2.1. Drying enhancement with Corona wind

For drying with hot-air flow, the idea of heat-and-mass transfer enhancement by utilizing EHD is shown in Fig. 1. When hot-air flow exposes to high-voltage electric fields, the flow is circulated. Then this secondary flow enhances the convective heat transfer and depresses the influence of boundary layer on the packed-bed surface. This causes much of moisture on surface to vaporize towards the hot-air flow, and allows larger amount of heat to transfer into the packed bed. Consequently, the drying rate is substantially enhanced.

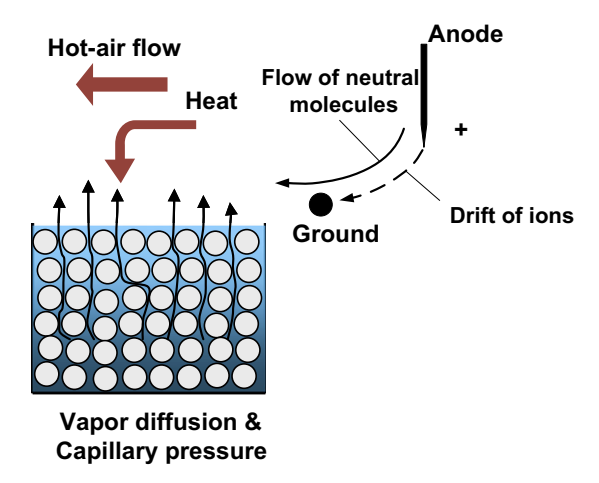


Fig. 1. Idea of enhancement of heat and mass transfer with corona wind.

2.2. Related equations

Water saturation (S) of a porous medium with respect to a particular fluid is defined as

$$S = \frac{\text{Volume of fluid}}{\text{Total volume of voids}} = \frac{V_{\text{water}}}{V_{\text{void}}}$$
 (1)

Moisture content (X) in porous material is the ratio of total mass of water (M_w) to total mass of dry solid (M_s), i.e.

$$X = \frac{M_w}{M_s} \tag{2}$$

Eq. (2) can be written in term of water saturation as,

$$X = \frac{\phi \rho_{w}}{(1 - \phi)\rho_{s}} S \tag{3}$$

where ϕ is porosity of material (m³/m³), $\rho_{\rm w}$ and $\rho_{\rm s}$ are density of water and solid (kg/m³), respectively.

From Fourier's law, heat flux through porous material is computed by

$$q = -\lambda_{eff} \nabla T \tag{4}$$

where λ_{eff} is effective thermal conductivity (W/m K), and ∇T is temperature gradient in packed bed (°C/m).

Based on the experimental results of Aoki et al. [15], the effective thermal conductivity is further assumed to be a function of water saturation and is defined as

$$\lambda_{eff} = \frac{0.8}{1 + 3.7e^{-5.95S}} \tag{5}$$

Exchange of energy at surface of packed bed exposed to airflow can be calculated by

$$\lambda_{eff} \frac{\partial T}{\partial z} = -h_c (T_a - T_{sur}) + \dot{m}_w h_v \tag{6}$$

where h_c is convective heat transfer coefficient (W/m² K), \dot{m}_w is mass flux of evaporation (kg/m² s) or rate of weight loss of water from porous media, h_v is latent heat of vaporization (J/kg), T_{sur} is temperature on material surface (°C), and T_a is air-flow temperature (°C).

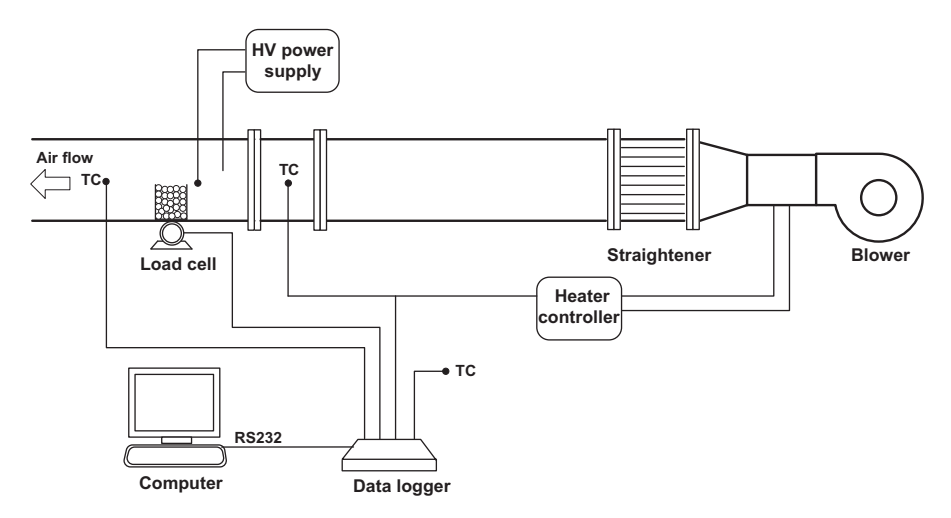
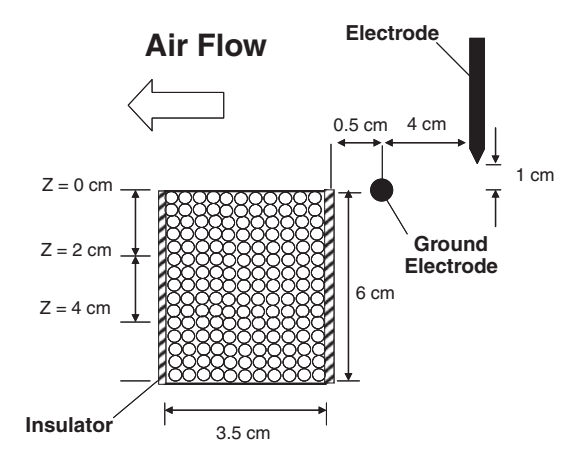


Fig. 2. Schematic diagram of experimental setup.

The relationship between the capillary pressure (p_c) and the water saturation is defined by using Leverett functions $J(S_{eff})$ [2,3], i.e.

$$p_c = p_g - p_l = \frac{\sigma}{\sqrt{K/\phi}} J(S_{eff})$$
 (7)

where S_{eff} is effective water saturation associated with the irreducible water saturation, K is permeability (m^2) , and σ is surface tension (Pa m). Subscripts of g and l denote as gas and liquid phases, respectively.



 $\textbf{Fig. 3.} \ \ \textbf{Dimensions of packed bed and locations of electrodes}.$

3. Experimental setup and apparatus

Schematic diagram of experimental setup is shown in Fig. 2. The rig is an open system. Air is supplied from a blower and its temperature is increased by an electric heater. In order to control temperature of hot air, a thermocouple sensor (TC) is placed in front of the test section, where the cross-sectional area is $15 \times 15 \text{ cm}^2$. The high voltage power supply (LEYBOLD 521721) is used to create high-voltage electric fields.

As shown in Fig. 3, electrode wires are comprised of four copper positive discharge electrodes and a copper ground electrode. The discharge electrode wires are suspended from the top wall and are placed in the front of packed bed. Diameter of each discharge electrode is 0.025 mm and the space between each wire is 26 mm. Ground electrode is suspended horizontally across the test section, and its diameter is 0.25 mm.

Fig. 4 shows the configuration of the packed beds composed of glass bead, water and air. As shown in Fig. 4, the samples are prepared in the two configurations in the: a single-layered packed bed (uniform packed bed) with bed depth δ = 60 mm (d = 0.125 (F bed) and d = 0.38 (C) bed), and a double-layered packed bed, respectively. The double-layered packed beds are arranged in different configurations in the: F–C bed (fine beads (d = 0.125, δ = 30 mm) overlaying the coarse beads (d = 0.38 mm, δ = 30 mm)), and C–F (coarse beads (d = 0.38 mm, δ = 30 mm) overlaying the fine beads (d = 0.125, δ = 30 mm)), respectively. The width and total length of all samples used in the experiments are 35 mm and 120 mm, respectively. The container of glass beads is made of acrylic plate with a thickness of 0.5 mm. Moreover, to control heat transfer from

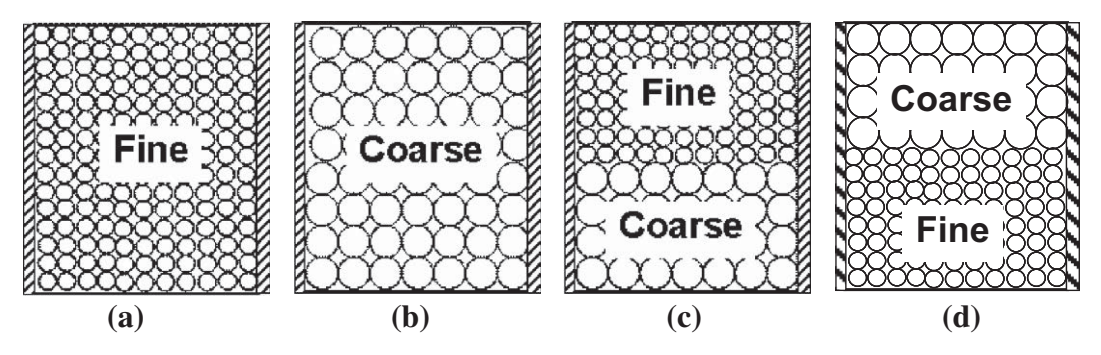


Fig. 4. Configuration of packed bed: (a) and (b) single layer, (c) F-C layer, and (d) C-F layer.

Table 1 Testing conditions.

Condition	Symbol	Value
Initial moisture	$X_{db,i}$	22-38%db
Drying temperature	T	50–60 °C
Ambient temperature	T_a	25 °C
Mean air velocity	U_b	0.33 m/s
Applied voltage	V	0, 10, 15 kV
Drying time	t	24-48 h
Glass beads	d	0.125, 0.38 mm

Table 2 Characteristics of water transport in porous media.

Diameter, d (mm)	Porosity, ϕ	Permeability, K (m ²)
0.125	~0.385	$\sim 8.41 \times 10^{-12}$
0.38	~0.371	$\sim 3.52 \times 10^{-11}$

hot air towards only the upper surface of packed bed, other sides are insulated by rubber sheet.

Temperature distribution within the sample are measured using fiber optic sensors (LUXTRON Fluroptic Thermometer, Model 790, Santa Clara, Canada, accurate to ± 0.5 °C), which are placed in the middle plane of the sample at depth z = 0, 2, and 4 cm, which are measured away from the surface of the packed bed. In each test run, the weight loss of the sample is measured by a load cell.

In the experiments, the maximum electrical voltage is tested so that breakdown voltage will not occur. The details of testing conditions and characteristics of water transport in porous media are shown in Tables 1 and 2, respectively.

4. Results and discussion

In measuring the temperature in the packed bed, it is assumed that temperature is in state of thermodynamic equilibrium, thus temperatures of all phases, i.e. solid, liquid, and gas, are same. The average temperature of hot air measured at the front of test section is approximately 60 °C. Reynolds number ($R_e = U_b D_h/$) of airflow is 3049.

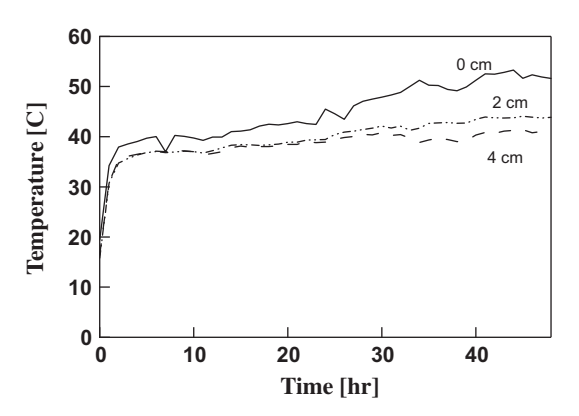


Fig. 6. Surface temperature (z = 0 cm) of packed bed with 0.125-mm bead in various voltages.

4.1. Effects of EHD on air flow

In order to observe the motion of airflow subjected to the electric fields, this study utilizes the incense smoke technique. A spotlight of 500 W is placed at the outlet of channel, and the light direction is opposite to the flow direction. Due to high speed of flow, the bulk mean velocity is reduced to 0.1 m/s. In addition, the motion of flow is continuously captured by a digital video camera recorder (SONY DCR-PC108/PC109E). As shown in Fig. 5, under the influence of EHD, airflow neighboring electrodes is induced by electric fields, and is circulated near the ground electrode. Moreover, it is observed that strength of vortex is proportional to the magnitude of electrical voltage applied.

4.2. Effects of heat and mass transfer on packed bed

Figs. 6 and 7 show the influence of EHD on temperature in packed bed with 0.125-mm bead at z = 0 and 4 cm, respectively. Clearly, when electric fields are applied, the temperature in packed bed increases faster. In addition, higher voltage applied gives rise to higher temperature. Moreover, EHD influences the surface temperature more than the inside. This is because EHD induces a sec-

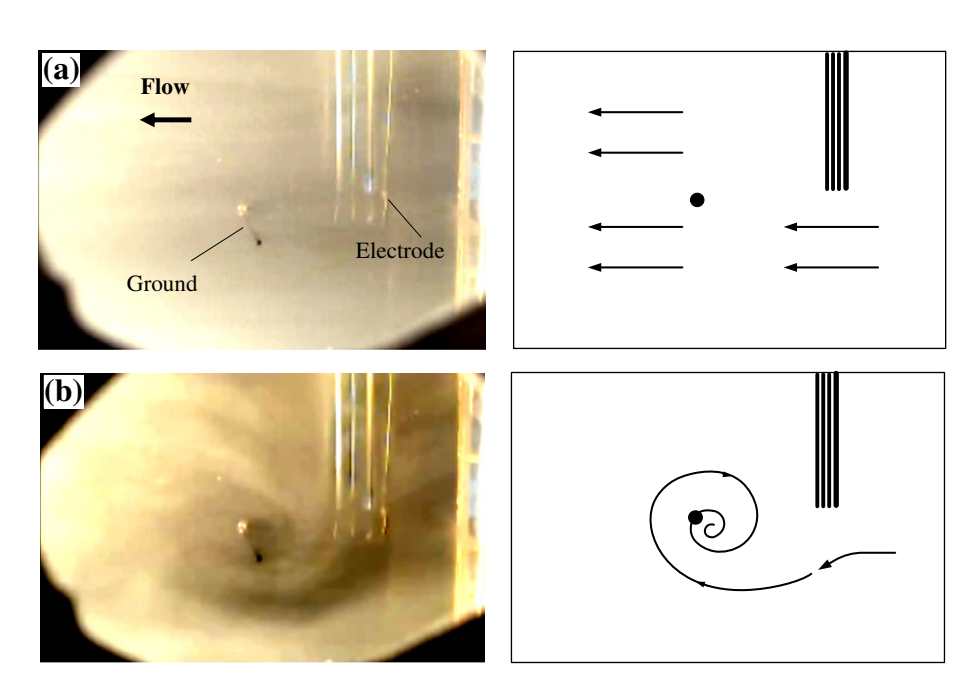


Fig. 5. Motion of air flow: (a) without electric fields, and (b) with electric fields at V = 10 kV.

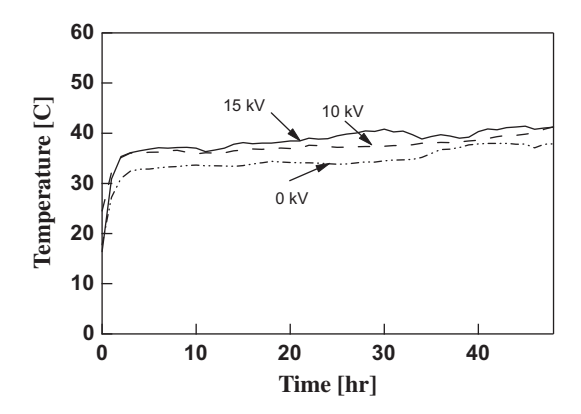


Fig. 7. Temperature of packed bed with 0.125-mm bead at z = 4 cm.

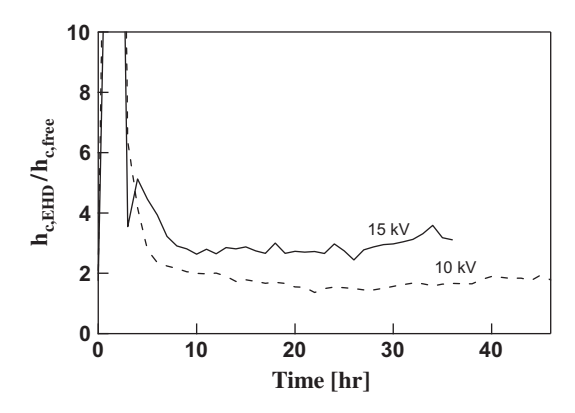
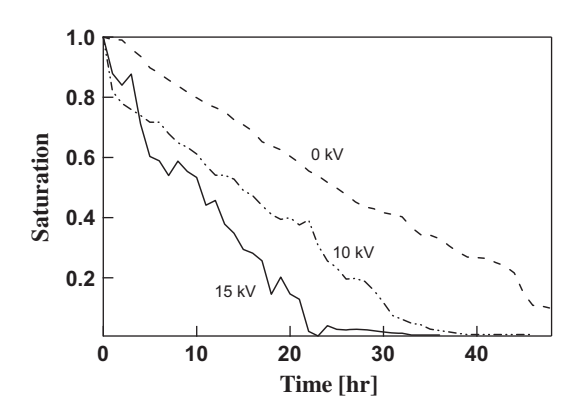


Fig. 8. Enhancement of heat transfer coefficient in case of packed bed with $0.125 \, \mathrm{mm}$ bead.



 $\begin{tabular}{ll} \textbf{Fig. 9.} Comparison on water saturation of packed bed with 0.125-mm bead in various voltages. \end{tabular}$

ondary flow, so-called Corona wind. The effect of this Corona wind circulating above packed bed enhances the mass transfer, and destabilizes the boundary layer on the surface. Consequently, convective heat transfer coefficient is enhanced, and then heat from hot-air flow can much transfers into packed bed. Therefore, the temperature of the cases with EHD is higher than that without EHD.

In this study, the augmentation of heat transfer due to EHD is defined as the ratio convective heat transfer coefficient with EHD to convective heat transfer coefficient with free air, i.e. $h_{c,EHD}/h_{c,free}$. As shown in Fig. 8, in warm-up period, this ratio increases rapidly. In addition, in constant drying period (constant surface temperature), the ratios are about 2 and 3 for cases with V = 10 and 15 kV, respectively.

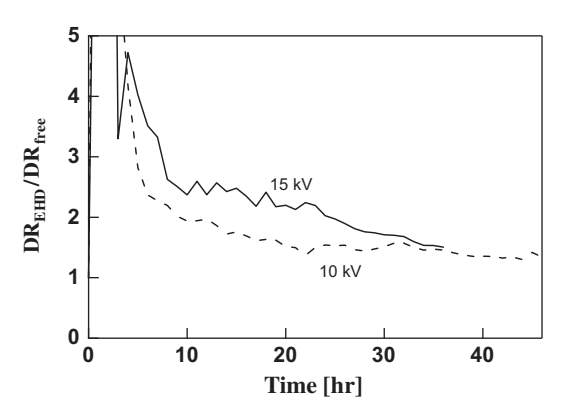


Fig. 10. Enhancement of rate of mass transfer in case of packed bed with 0.125-mm bead.

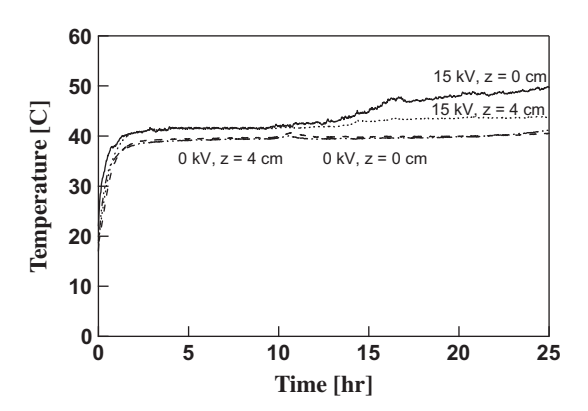


Fig. 11. Temperature of packed bead with 0.38-mm bead in various voltages at z = 0 and 4 cm.

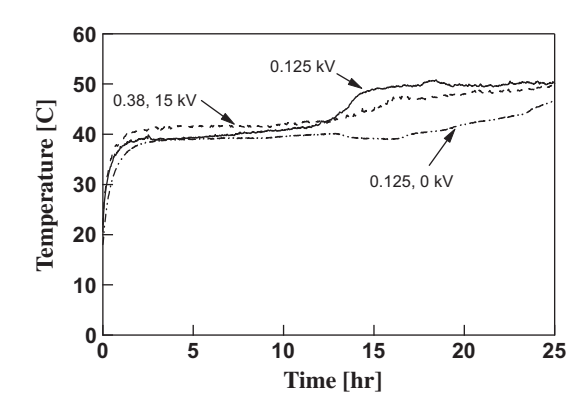


Fig. 12. Comparison on surface temperature (z = 0 cm) of packed bead with 0.38-mm and 0.125-mm beads.

As shown in Fig. 9, with voltage applied, water saturation in packed bed is much more reduced, due to enhancement of mass transfer. In constant rate of drying period, the drying rate with EHD approximately being 2–2.5 higher than that with hot-air flow only, as shown in Fig. 10.

Heat transfer in packed bed with big beads (0.38 mm) is shown in Fig. 11. Without EHD, difference of temperature between surface and inside is very small. Due to the influence of EHD, temperature difference is clearly observed. In addition, an increase in temperatures is much higher than that in the case without electric fields.

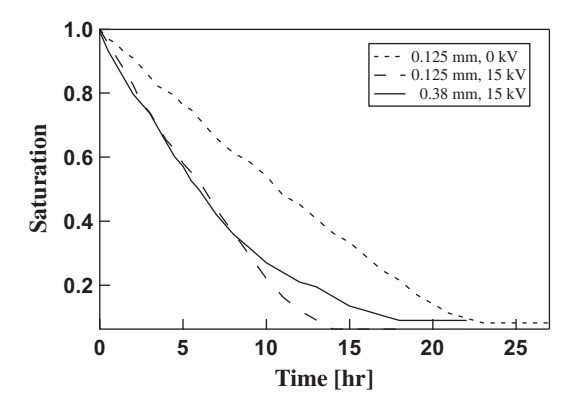


Fig. 13. Comparison on saturation in packed bead with different glass bead sizes.

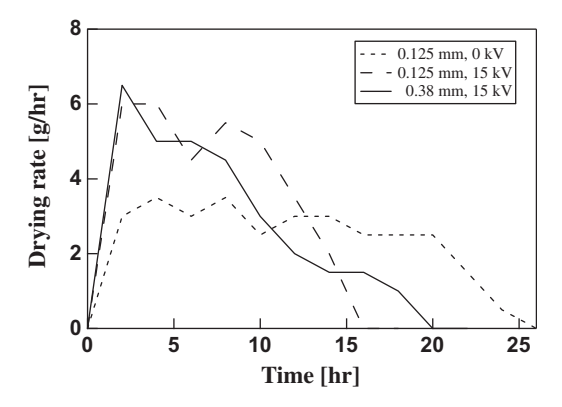


Fig. 14. Comparison on drying rate in packed bead with different glass bead sizes.

4.3. Effect of glass bead size

In the case of a single-layered packed bed, the moisture content continuously decreases towards the surface. The decrease in surface saturation leads to a saturation gradient, which draws liquid water towards the surface through capillary action while water vapor moves towards the surface due to a gradient in the vapor partial pressure.

The following results are concerned with the effect of particle size on moisture migration mechanism and heat transfer under the same conditions for the single-layered packed bed. As shown in Fig. 12, after a constant rate of drying period, surface temperature in packed bed with small bead (0.125 mm) rapidly increases, while the case in packed bed with big bead (0.38 mm), temperature gradually increases. As clearly seen in Fig. 13, saturation in small bead case decreases faster than that in big bead case. In addition, high rate of drying in small bead case remains longer than that in big bead case, as shown in Fig 14. This is because effect of capillary pressure in small bead case is higher than that in the big bead case. As shown in Table 2, porosity of packed bed with small bead is larger than that of packed bed with big bead. In addition, from Eq. (7), if $(\sigma J(S_{eff}))_{fine} \sim (\sigma J(S_{eff}))_{coarse}$ then $p_{c,fine} > p_{c,-}$ coarse. It means that in the case of same saturation, a smaller particle size corresponds to a higher capillary pressure. With higher capillary pressure, it can cause moisture to reach the surface at a higher rate. Therefore, more moisture is transferred from inside packed bed towards the surface.

In fact, in drying period, heat flux from hot-air flow transfers to water in packed bed for evaporation. If packed bed contains a high saturation level, then an increase of its temperature will be slow. This causes temperature in big bead case to be lower than that in small bead case.

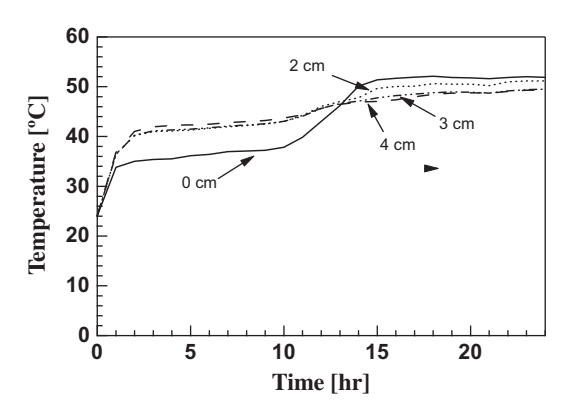


Fig. 15. Temperature in F–C packed bed when V = 15 kV.

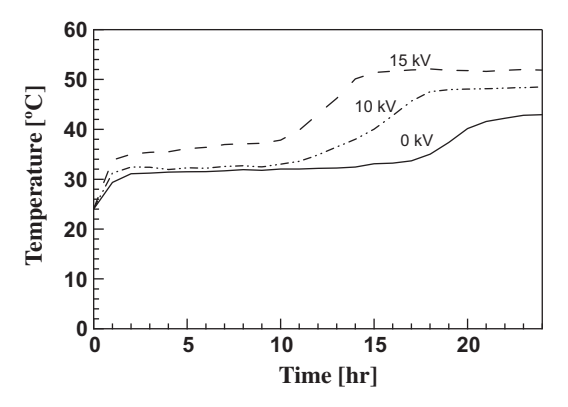


Fig. 16. Temperature at z = 0 cm in F–C packed bed in various voltages.

4.4. Effects of layered arrangement

In case of double-layered packed bed, in order to measure the temperature on the interface layer, one more fiber optic wire is placed at z = 3 cm.

Temperature distributions in the case of double-layered packed bed (F-C bed and C-F bed) are quite different from the results in single-layered cases. Figs. 15 and 16 show temperature in packed bead of F-C case. As shown in Fig. 15, in the warm-up period, all temperatures in this packed bed rise up steadily. Later, they remain constant, and the surface temperature of packed bed is lowest. Until a certain time, the temperature on surface increases rapidly, and is higher than temperature in the other layers due to the effect of capillary pressure difference. From the above discussion, capillary pressure in small bead case is higher than that in big bead case. In the initial period, if both layers have the same amount of saturation, then there will be the difference of capillary pressure. Therefore, effect of capillary action in the fine bead layer (upper layer) will induce the moisture from the coarse bead layer (the lower layer) to the fine bead layer. This causes void in the lower layer to be filled with more of the vapor phase. Therefore, with a same heat flux, temperature in the lower layer becomes higher. As moisture evaporating process proceeds, temperatures of porous packed are constant, while heat is used for changing phase. Until a certain time, the surface becomes dry as heat will mainly transfer with conduction. Consequently, temperature in the upper layer rises up again when drying zone starts to appear, and the temperature of surface layer is higher than the other layers. Effect of voltage applied on heat transfer in F–C packed bed is shown in Fig. 16. With higher voltage, surface temperature of packed bed reaches a certain temperature faster.

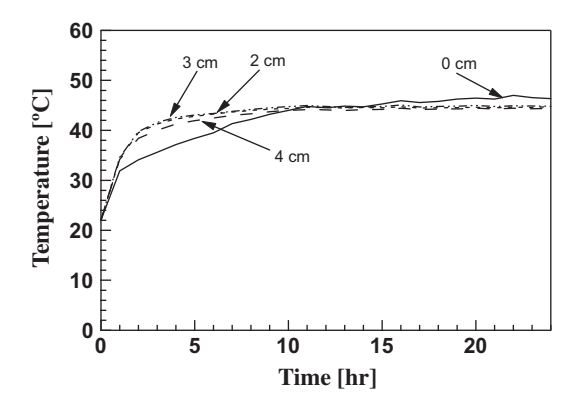


Fig. 17. Temperature in C–F packed bed when V = 15 kV.

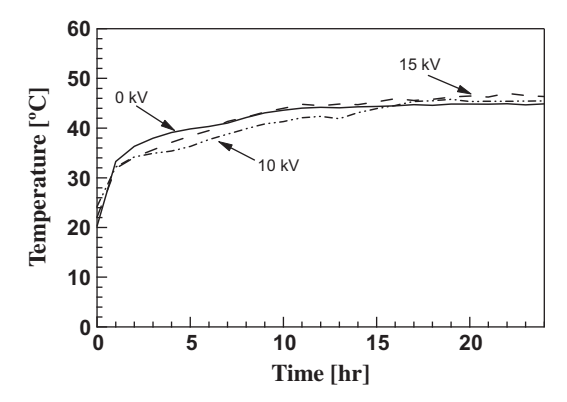


Fig. 18. Temperature at z = 0 cm in C–F packed bed in various voltages.

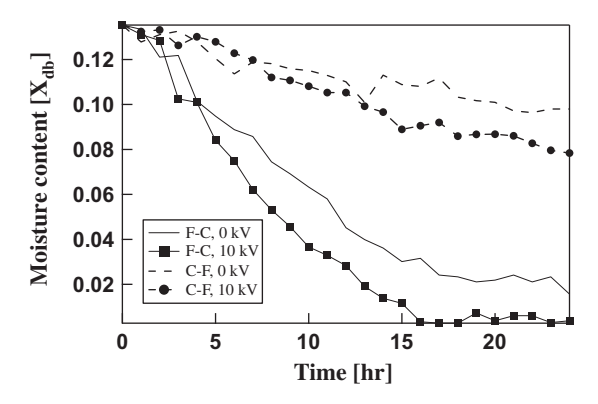


Fig. 19. Comparison on moisture content in double-layered packed bed in various cases.

Figs. 17 and 18 show the results when coarse beads overlay fine beads. Unlike F–C case, without and with electric fields, the temperature in each depth is not much different. In addition, the surface temperature is highest. This is because moisture in the coarse layer (the upper layer) slowly transfers to the surface, and this effect retards the moisture transfer from the lower layer towards the upper.

It is evidenced in Fig. 19 that when the drying process reaches a certain time, moisture content in F-C packed bed is in low level, while the moisture content in C-F packed bed is still high. In other words, the moisture removed from C-F cases is much lower than that from F-C cases. As mentioned above, effect of capillary pressure difference suppresses a certain amount of moisture in C-F

cases to transfer toward the surface. With influence of EHD, the drying rate is increased. In addition, rate of drying of F–C cases is about 3.13–3.67 times higher than that of C–F case. Moreover, with voltage applied, the drying rate is improved about 1.5–1.97 times.

5. Conclusions

Effect of electrical voltage, particle sizes, and layered arrangement on heat and mass transfer in the porous packed beds are experimentally investigated and analyzed in this paper. The following paragraph summarizes the conclusions of this study:

- 1. Effects of Corona wind circulating above packed bed enhance the convective heat transfer coefficient and evaporation rate on the packed-bed surface exposed to hot-air flow, resulting in enhancement of heat and mass transfer in the packed bed. In addition, the degree of enhancement of heat and mass transfer is dependent on the magnitude of voltage applied.
- 2. The effects of particle size are clarified. The drying rate in the small bead case is higher than that in the big bead case. This is because of the higher capillary pressure for the packed bed with small bead: moisture in packed bed can be substantially removed towards the material surface.
- 3. Due to the effect of capillary pressure difference, heat and mass transfer in double-layered case and the single-layered case behave differently. With retarding effect on moisture motion to the upper layer of the C–F case, relatively small amount of moisture moves to the upper layer, resulting in a low temperature. In F–C cases, effect of capillary pressure difference enhances moisture in the lower layers to move towards the upper layers. With voltage applied, the drying rate is improved about 1.5–1.97 times. In addition, the drying rate of F–C cases is about 3.13–3.67 higher than that of C–F cases.

Acknowledgement

The authors are pleased to acknowledge Thailand Research Fund (TRF) for supporting this research work.

References

- [1] F. Gori, G. Gentili, L. Matini, Microwave heating of porous media, ASME J. Heat Transfer 109 (1987) 522–525.
- [2] A.E. Drouzasam, H. Dchubert, Microwave application in vacuum drying of fruits, J. Food Eng. 28 (1996) 203–209.
- [3] J. Yongsawatdigul, S. Gunasekaran, Microwave-vacuum drying of cranberries: part I. Energy use and efficiency, J. Food Process. Preserv. 20 (1996) 121–143.
- [4] P. Ratanadecho, K. Aoki, M. Akahori, Experimental and numerical study of microwave drying in unsaturated porous material, Int. Commun. Heat Mass Transfer 28 (5) (2001) 605–616.
- [5] P. Ratanadecho, K. Aoki, M. Akahori, Influence of irradiation time, particle sizes, and initial moisture content during microwave drying of multi-layered capillary porous materials, J. Heat Transfer 124 (2002) 151–161.
- [6] W. Cha-um, P. Rattanadecho, W. Pakdee, Experimental analysis of microwave heating of dielectric materials using a rectangular wave guide (MODE: TE10) (Case study: water layer and saturated porous medium), Exp. Therm. Fluid Sci. 33 (2009) 472–481.
- [7] C. Sandua, Infrared radiative drying in food engineering: a process analysis, Biotechnol. Prog. 2 (3) (1986) 109–119.
- [8] N. Sakai, T. Hanzawa, Application and advances in infrared heating in Japan, Trends Food Sci. Technol. 5 (11) (1994) 357–362.
- [9] D. Nowak, P.P. Lewicki, Infrared drying of apple slices, Innov. Food Sci. Emerg. Technol. 5 (2004) 353–360.
- [10] J. Wang, K.C. Sheng, Modeling of multi-layer far-infrared dryer, Drying Technol. 22 (2004) 809–820.
- [11] A. Alem-Rajabif, F.C. Lai, EHD-enhancement drying of partially wetted glass beads, Drying Technol. 23 (1995) 597–609.
- [12] F.C. Lai, K.W. Lai, EHD-Enhanced drying with wire electrode, Drying Technol. 20 (7) (2002) 1393–1405.
- [13] T.I.J. Goodenough, P.W. Goodenough, S.M. Goodenough, The efficiency of corona wind drying and its application to the food industry, J. Food Eng. 80 (2007) 1233–1238.

- [14] E. Schröder, A. Class, L. Krebs, Measurements of heat transfer between particles and gas in packed bed at low to medium Reynolds numbers, Exp. Therm. Fluid Sci. 30 (2006) 545–558.
- [15] K. Aoki, M. Hattori, M. Kitamura, N. Shiraishi, Characteristics of heat transport in porous media with water infiltration, ASME/JSME Therm. Eng. Proc. 4 (1991) 303–308.